SPECTRAL DOMAIN OCT DOPPLER ASSESSES AQUEOUS OUTFLOW

by

Lawrence E. Kagemann

B.S Biomedical Engineering, University of Iowa, 1986

M.S. Biomedical Engineering, University of Miami, 1989

Submitted to the Graduate Faculty of

Swanson School of Engineering in partial fulfillment

of the requirements for the degree of

Doctor of Philosophy

University of Pittsburgh

2012

UNIVERSITY OF PITTSBURGH

SWANSON SCHOOL OF ENGINEERING

This dissertation was presented

by

Lawrence E. Kagemann

It was defended on

March 26, 2012

and approved by

George Stetten, MD, PhD, Professor, Department of Bioengineering

Gadi Wollstein, MD, Associate Professor, Department of Ophthalmology

Hiroshi Ishikawa, MD, Assistant Professor, Department of Ophthalmology

John Galeotti, PhD, Senior Project Scientist, CMU Robotics Institute

Dissertation Director: Joel S. Schuman, MD, Professor, Department of Ophthalmology, and Department of Bioengineering

SPECTRAL DOMAIN OCT DOPPLER ASSESSES AQUEOUS OUTFLOW

Lawrence E. Kagemann, Ph.D.

University of Pittsburgh, 2012

Glaucoma is the second leading cause of blindness worldwide, affecting approximately 67 million people and costing the US healthcare system an estimated $2.5 billion annually. The greatest risk factor for the diagnosis and progression of glaucoma is high eye pressure. All glaucoma medications and procedures are designed to reduce eye pressure, slowing disease progression and preserving vision.

The eye's aqueous humor nourishes avascular tissues in the anterior segment. It also maintains the eye's geometry by pressurizing the globe, facilitating its ability to focus light on the retina. The balance between aqueous humor production and uptake is responsible for the pressure within the eye. Most glaucoma medications are designed to reduce pressure by increasing aqueous humor outflow, and surgeries are designed to enhance or bypass exiting outflow pathways. But, the effects of medications and procedures on a patient by patient basis on outflow remain speculative.

Here, techniques for the non-invasive direct mapping and measurement of aqueous humor outflow in the living human eye are proposed. Mapping provides morphometric insights and measurements of the components of the outflow system, while the flow technique is the first to provide direct measurements of outflow, free of the assumptions plaguing other modalities. "Virtual casting" of the outflow system yields 3D maps from which terminal branches are identified. Doppler measurements quantify velocity within those branches. Total aqueous humor outflow is determined by integrating calculated flow across all identified terminal branches. These technologies can be adapted to existing FDA approved OCT clinical scanners. Clinical application of these technologies may improve the management of glaucoma by reducing the time needed to determine and implement optimal therapeutic strategies, thereby preserving vision in glaucoma patients.

TABLE OF CONTENTS

LIST OF TABLES

LIST OF FIGURES

LIST OF EQUATIONS

LIST OF ABBREVIATIONS

2D	two-dimensional or two dimensions
3D	three-dimensional or three-dimensions
AC	anterior chamber
ALT	argon laser trabeculoplasty
ANOVA	analysis of variance
A-scan	axial scan
C	Celsius
CC	collector channel
CoV	coefficient of variability
Δ	offset distance between two mirrors
GNR	gold nanorod
GNR/ml	gold nanorods per milliliter
I	intensity of light
i.e.	id est “that is”
IOP	intraocular pressure
ISVP	intrascleral venous plexus
IV	intravenous
k	wavenumber of light

kn	portion of total intensity in pathway n
λ	wavelength of light
LLC	limited liability corporation
mM	millimolar
mmHg	millimeters of mercury
μ	micron
μl/min	microliter per minute
μm	micrometer
N	sample size
OCT	optical coherence tomography
SC	Schlemm’s canal
SC/CC	SC ostium (or ostia) at a collector channel
SD	standard deviation
SD-OCT	spectral domain OCT
SLT	selective laser trabeculoplasty
St. Dev.	standard deviation
τ	wave number
TM	trabecular meshwork
UPMC	University of Pittsburgh Medical Center

PREFACE

Joel and George: "Here is what I have seen: It is good and fitting for one to eat and drink, and to enjoy the good of all his labor in which he toils under the sun all the days of his life which God gives him; for it is his heritage. As for every man to whom God has given riches and wealth, and given him power to eat of it, to receive his heritage and rejoice in his labor—this is the gift of God*."* *Ecclesiastes 5:18-19* Being able to rejoice in my labors and share that pleasure with men that I respect has makes me doubly blessed. Thank you!!

Gadi: "And these words which I command you today shall be in your heart. You shall teach them diligently to your children, and shall talk of them when you sit in your house, when you walk by the way, when you lie down, and when you rise up. You shall bind them as a sign on your hand, and they shall be as frontlets between your eyes. You shall write them on the doorposts of your house and on your gates." *Deuteronomy 6:6-9* You will always be an example and reminder to me that an honorable man that loves and leads his family can also be an internationally recognized and honored scientist. Your life is an example for everyone around you!

Hiroshi: "As iron sharpens iron, so a man sharpens the countenance of his friend." *Proverbs 27:17* Thank you for NEVER taking anything that I say at face value, but making me demonstrate everything that I find. You have made me think, and improved the quality or my work and clarity of my thinking immeasurably.

John: "Wisdom is the principal thing; therefore get wisdom. And in all your getting, get understanding. Exalt her, and she will promote you; she will bring you honor, when you embrace her. She will place on your head an ornament of grace; a crown of glory she will deliver to you." *Proverbs 4:7-12* It looks good on you! I hope we have numerous opportunities to collaborate in the future.

What good is a dissertation without the meaning of life?

"Of making many books there is no end, and much study is wearisome to the flesh. Let us hear the conclusion of the whole matter:

Fear God and keep His commandments,
For this is man's all."

Ecclesiastes 12:12-13

"Jesus answered, "I AM the way and the truth and the life. No one comes to the Father except through Me. If you really know Me, you will know My Father as well. From now on, you do know Him and have seen Him."

John 14:6-7

I must also acknowledge and thank my most wonderful wife Janice for her love and support throughout this project. Besides doing everything in her power to facilitate me taking 3 months out of our life to write, she also increased my knowledge and abilities with the scanner, and spend several of her own weekends serving as an independent masked observer making heretofore unheard of measurements of the outflow system.

I'd be remiss if I failed to thank Alon Harris. He took me, a person searching for his professional self (albeit a capable engineer), and taught me to be a scientist. He provided a platform for my training, promoted my abilities, and put me on the world stage. The frustrations that he suffered trying to learn to communicate with and manage an engineer defy description. Without him, Joel would have never heard of me, and I would not be where I am today. Alon, I will forever credit you for giving me my career. I found myself as a scientist under your guidance, care, and knowledge. Thank you!

"At last, after our long journey, we have reached the beginning." —ancient Mentat conundrum

1.0 AQUEOUS HUMOR AND GLAUCOMA

1.1 INTRODUCTION: FOR THE PAGES WE ARE ABOUT TO READ…

The work described herein comprises a newly developed technique for the mapping of the conventional aqueous humor outflow system, and the measurement of aqueous humor outflow in the eye. The importance of this mapping and measurement, beyond the utter Star-Trek'esque awesomeness of reaching into a living organ and mapping a system non-inversely, is the preservation of vision in persons with glaucoma. Knowledge of where and how aqueous humor is leaving the eye, and how medications and invasive procedures are affecting changes to that outflow are of vital importance in the management of glaucoma, but are currently unavailable to the glaucoma specialist.

The eye is a pressurized vessel that focuses images onto light-sensitive tissue, where image data is converted to electrochemical signals.[1] These signals are transmitted to the brain by the optic nerve. Light passes through the cornea, aqueous humor, lens, and vitreous before reaching the light-sensitive tissues of the retina. After passing through the retinal ganglion and bipolar cell layers, light reaches the photoreceptors where it is converted to an electrochemical signal. This signal is transmitted to the brain via the axons of the retinal ganglion cells, which gather to form the optic nerve. (Figure 1).[2]

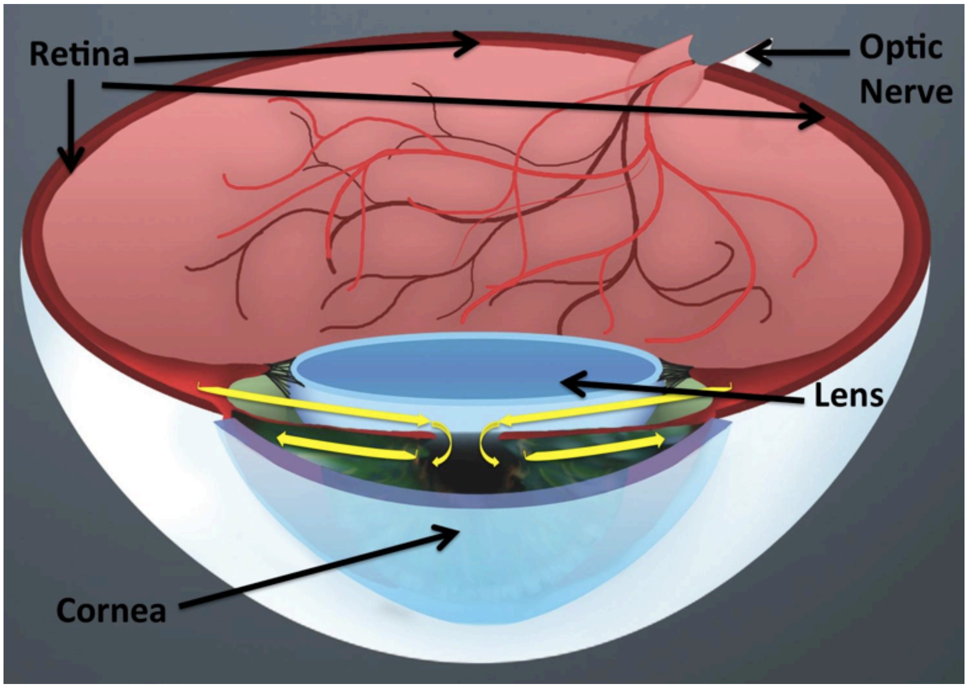

Figure 1. Gross anatomy of the eye

The structural integrity of the eye, and therefore, relative position of its optical elements are maintained by the pressure within the eye.[3]

Aqueous humor is a fluid produced (inflow) in the epithelial cells of the ciliary body (Figure 1, yellow arrows). [3] It exits the eye (outflow) through one of two paths, as will be described below, each with inherent resistance to outflow.[3] Pressure in the eye (intraocular pressure, IOP) is created by the flow of aqueous humor against outflow resistance.[3] It is possible to manipulate IOP through medical and surgical intervention by either altering the resistance to outflow, or reducing inflow.[3]

Primary open angle glaucoma is the most common of the 4 sub-types of glaucoma, and is an optic neuropathy in which retinal ganglion cells die at an accelerated rate relative to that in healthy eyes.[4] The primary risk factor for both the presence and progression of glaucoma is elevated IOP.[4] For this reason, the goal of all therapeutic and surgical interventions in glaucoma is the reduction of intraocular pressure, either through the reduction of resistance to outflow, or the reduction in inflow rates. A technique to map the conventional outflow system and a technique to measure volumetric outflow in living eyes would be of tremendous value to glaucoma specialists. The goal of the following work is the development of such a measurement using spectral domain optical coherence tomography (SD-OCT) three-dimensional (3D) imaging.

1.2 AQUEOUS HUMOR: DYNAMICS AND FUNCTION

1.2.1 The Source of Aqueous Humor: Functional Anatomy

Aqueous humor is the clear liquid filling the anterior segment of the eye.[5] The source of aqueous humor in the eye has long been thought to be the ciliary body,[6] though the exact mechanism of production remained elusive until recently. Aqueous humor is similar to blood plasma, and is a solution of Na^+ and Cl^- ions (approximately 150 and 130 millimolar respectively), though the protein content of aqueous humor is less than 1% of that of serum.[7,8] Previously thought to be an ultrafiltrate of blood[9], the protein content of aqueous humor makes it a hyperosmotic fluid that could not be produced by filtration.[10] Further, aqueous humor formation levels are independent of blood pressure.[11,12] Metabolic inhibitors reduce the rate of aqueous humor production.[13] If the mechanism of aqueous humor production were purely a filtration process, blood pressure level would alter the rate of production, and metabolic inhibition would not. It is generally accepted that aqueous humor formation is a more than a paracellular ultrafiltration process, but an ultrafiltrate of blood actively secreted by the ciliary epithelium through a process of transcellular transport.[9]

Since the cornea and lens are part of the optical pathway of the eye and must be clear to facilitate light transmission, they are avascular tissues (Figure 2).[14] Circulating aqueous humor takes on the roles of nutrition delivery and waste removal for the cornea and lens, as well as delivering neurotransmitters.[14] In disease, the same circulating aqueous humor facilitates transport of inflammatory cells as well as drugs to the anterior ocular structures.[14]

Aqueous humor flows (Yellow arrows, Figure 2) from the posterior chamber through the pupil into the anterior chamber. It exits the anterior chamber via the trabecular meshwork (TM), into Schlemm's canal (SC, the conventional outflow pathway) or into the supraciliary space (uveoscleral pathway).[15] In normal healthy eyes, aqueous humor is secreted by the ciliary epithelium[16] at a rate of 2.75 +/- 0.63 microliters per minute (µl/min) during waking hours.[17] The rate varies throughout the day, and is highest in the morning and slightly lower in the afternoon. Rates during sleep drop to approximately half of those of the morning peak flow rate.[15,17]

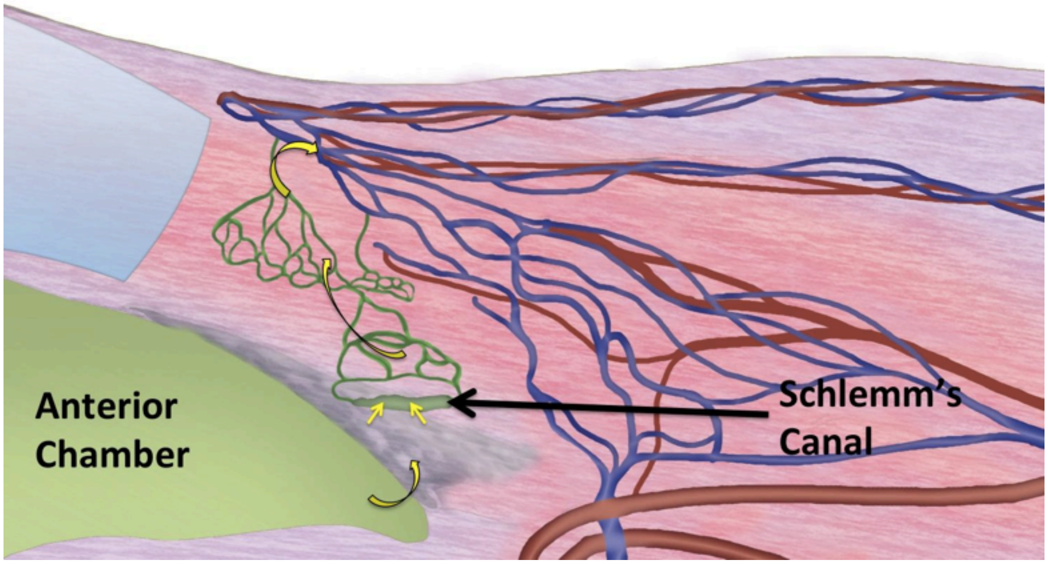

Figure 2. Anatomy of the conventional outflow pathway

Aqueous humor flows from the posterior chamber, around the lens, through the pupil and into the anterior chamber. A temperature gradient creates convective flow streams, with aqueous humor rising in the warmer region near the lens, and falling in the area of the anterior chamber close to the cooler cornea[18] (of course, these models assume a stationary open eye, and once an eye is blinking and changing direction of gaze in a body that is walking around, other factors may come into play).

1.2.2 Aqueous Humor Outflow

Aqueous humor leaves the anterior chamber via one of two pathways. The majority of aqueous outflow passes through the conventional pathway in adult humans, in which it passes through the TM, passes into SC, and flows out via a meshwork of collector channels and aqueous veins, which empty into episcleral veins.[19-29] Pressure within the episcleral veins is approximately 9 millimeters of mercury (mmHg), requiring a minimal level of IOP to maintain the pressure gradient that drives outflow.[30,31] The conventional outflow pathway is pressure-dependent; specifically, as IOP increases, resistance to outflow increases.[32] The conventional outflow pathway has a flow-dependent resistance of 3 to 4 mmHg per µl/min of flow, producing a normal IOP of approximately 16mmHg.[30,31,33-36] Most of this resistance (~75%) is produced by flow through the TM, with the remaining resistance generated by flow distal to SC.[37] Disorders in the conventional outflow system may result in IOP elevation, which is the greatest risk factor for glaucoma.[38] For this reason, medications and procedures for glaucoma are designed to reduce resistance to outflow.

In the non-conventional outflow pathway, aqueous humor flows into the connective tissue between the muscle bundles of the ciliary body, through the suprachoroidal space, and out through the sclera.[39-44] Flow through the non-conventional pathway is essentially unaffected by IOP, though flow through this pathway decreases with age, making outflow via the conventional pathway increasingly important in the elderly.[45,46]

1.3 GLAUCOMA

1.3.1 Introduction

Glaucoma is the second leading cause of irreversible blindness worldwide (after age related macular degeneration), affecting approximately 67 million people worldwide (2.2 million people in the United States) and costing the US healthcare system an estimated $2.5 billion annually.[47] The greatest risk factor for the diagnosis and progression of glaucoma is high IOP. All glaucoma medications and procedures are designed to reduce IOP, slowing disease progression and preserving vision. Most glaucoma medications are designed to increase aqueous humor outflow, and most surgeries are designed to reduce resistance to outflow by enhancing or replacing exiting outflow pathways. But, the effects of these medications and procedures on outflow remain speculative and occur without direct observation.

1.3.2 Definition and Epidemiology

The American Academy of Ophthalmology defines primary open angle glaucoma as "a progressive, chronic optic neuropathy in adults in which intraocular pressure (IOP) and other currently unknown factors contribute to damage, and in which, in the absence of other identifiable causes, there is a characteristic acquired atrophy of the optic nerve and loss of retinal ganglion cells and their axons. This condition is associated with an anterior chamber angle that is open by gonioscopic appearance." [4] As retinal ganglion cells are lost, the retinal nerve fiber layer (consisting of the axons of the retinal ganglion cells) thins, and cupping appears in the optic nerve head. Retinal ganglion cell loss presents functionally as a reduced sensitivity to light throughout the field of vision.

Approximately 45 million people have open-angle glaucoma worldwide.[48] The prevalence of primary open angle glaucoma for adults 40 and older in the United States was estimated to be 2% in 2004,[49] though it varies among ethnic groups. The prevalence of open angle glaucoma in African Americans is approximately three times higher than in Caucasians in the United States.[49-52] Open angle glaucoma is the leading cause of blindness in African Americans.[52]

1.3.3 Intraocular Pressure and Glaucoma

The prevalence of primary open angle glaucoma increases with IOP.[35,36,51,53-56] Reducing IOP reduces the risk of progression of glaucoma.[57-62] To that end, the reduction and control of IOP is the primary goal of disease management in glaucoma.[4] The initial goal (target IOP) for IOP reduction is 25% below baseline.[4] If retinal nerve fiber layer thickness, optic nerve head appearance, or visual fields continue to degenerate, the target IOP can be further reduced. IOP is reduced either by medical therapy, or invasive procedures, which include either laser or incisional procedures.

1.3.3.1 Pharmaceutical Pressure Reduction

There are currently six classes of anti-glaucoma medications, each indicated for the reduction of IOP. Beta-blockers block activation of beta-adrenergic receptors, reducing IOP by decreasing the production of aqueous humor.[63] Carbonic anhydrase inhibitors also act by decreasing aqueous humor production. Unlike beta-blockers, which inhibit metabolic activity in the ciliary epithelium by reducing cyclic adenosine monophosphate, carbonic anhydrase inhibitors reduce production of bicarbonate ion, which is a critical component in the production of aqueous humor.[63] Alpha-2 adrenergic agonists selectively activate the alpha-2 adrenergic receptors in the ciliary body. As with beta-blockers, activation of the alpha-2 adrenergic receptors leads to a reduction of cyclic adenosine monophosphate, reducing production of aqueous humor. Unlike beta-blockers, alpha-2 adrenergic agonists may also increase conventional and uveoscleral outflow.[63]

Muscarinic cholinergic compounds, such as pilocarpine, increase aqueous humor outflow. The actual mechanism remains unclear, but it is hypothesized that they cause the contraction of smooth muscle within the ciliary body and iris, pulling on TM and mechanically opening passages within.[63] Epinephrine and epinephrine analogs bind to multiple receptor subtypes within the eye, reducing aqueous humor production and increasing aqueous humor outflow; however the mechanisms of each are poorly understood.[63] Finally, prostaglandins and their analogs reduce IOP by increasing uveoscleral outflow.[63] This occurs without significantly altering outflow in the conventional pathway.

A meta-analysis of the literature found that of all classes of IOP lowering medications, beta-blockers alone present evidence of maintaining visual fields.[64] Despite the performance of the class as a whole, no other individual compound had a sufficient body of work to demonstrate the same ability to stabilize visual fields.[64] But, a more recent study suggests that alpha-agonists may be more effective in stabilizing visual fields than beta-blockers in POAG patients with normal IOP's.[65]

The actual effect of all of these classes of glaucoma medications on flow through the conventional outflow pathway in the living eye remains unobservable and cannot be measured. Neither the exact morphology of the pathway nor the flow velocities within individual eyes could previously be measured. One important goal of the work described in the following chapters was to provide these important missing clinical measurements.

1.3.3.2 Laser Trabeculoplasty

There are currently two laser trabeculoplasty procedures to lower IOP; argon laser trabeculoplasty (ALT) and selective laser trabeculoplasty (SLT).[66] Both deliver laser energy to the TM without ablating the tissue, producing a reduction of outflow resistance. ALT produces a reduction of IOP greater than 75% in eyes with no previous surgeries.[4] Theories hypothesizing the mechanism of action resulting in the drop of outflow resistance fall into three broad categories: mechanical effect, metabolic effect, and cell regrowth effects. The mechanical theory is based on observations of morphometric changes in tissues exposed to laser energy.[67] Tissue shrinkage in the TM may be associated with enlarged outflow pathways and reduced resistance.[66] The biological theory proposes that the cascade of healing events triggered by the laser injury create a decrease in outflow resistance as a second-order effect, specifically via macrophage activation producing extracellular matrix and upregulation of interleukin I and tumor necrosis factor triggering metalloproteinase expression.[66,68] The cell regrowth theory proposes that newly grown cells in the TM replacing those damaged by the laser produce different extracellular matrix, enhancing the aqueous outflow.[69]

SLT differs from ALT in that the wavelength used delivers energy selectively to the pigment (melanin) of the TM. With brief pulse durations of 3ns, thermal effects in and energy transfer to the TM are approximately 1,000 times less that those of ALT, reducing or eliminating photocoagulation-induced damage.[67]

All of these procedures are performed with no knowledge of the condition of the outflow pathway distal to the locations of laser injury. It is possible that a foreknowledge of locations of patent collector channel ostia within SC would allow the surgeon more precise placement of laser treatments, increasing the efficacy of the procedures.

1.3.3.3 Trabeculectomy

Filtering surgery lowers IOP by providing an alternative outflow pathway with lower resistance than that of the physiological pathways.[70-73] A passage through sclera into the anterior chamber is created, removing a small portion of the trabecular meshwork tissue.[70-73] A conjunctival bleb is created to receive aqueous humor exiting the eye through the new passage, while providing some degree of outflow resistance to avoid hypotony. Placement of the new outflow passage is currently made with no knowledge of the morphology of the existing physiological outflow pathway. It is possible that providing the glaucoma surgeon knowledge of the patent conventional outflow system could allow him or her to devise surgical that spare functional tissues.

1.3.3.4 Glaucoma Implant Devices

Trabeculectomies can fail for a number of reasons including angle closure, vitreous loss, fibroblast proliferation and scarring in the bleb leading to elevated outflow resistance.[74-77] Eliminating the possibility of growth into the artificial outflow pathway, and controlling the level of outflow resistance therein could eliminate a number of these modes of failure. This can be accomplished by implanting an artificial mechanical outflow pathway, or shunt.[78-80] In general, there are two types of shunts; those with and without valves limiting outflow.[81-84] In either case, outflow devices are currently placed with no knowledge of the prominent outflow pathways in individual eyes. If the locations of the prominent outflow pathways were known before surgery, it might be possible to augment and not destroy existing ostia and large collector channels.

1.3.3.5 Non-Penetrating Glaucoma Procedures

As stated above, 75% of resistance to outflow occurs proximal to Schlemm's canal.[37] Surgical procedures that penetrate into the anterior chamber (trabeculectomy and glaucoma shunts) bypass the source of greatest resistance. However; those procedures also carry the risk of infection and other damage to interior tissues associated with penetration into the anterior chamber.[85,86] Non-penetrating deep sclerectomy is a procedure similar to a trabeculectomy, except that the incision stops at the inner wall of SC, allowing anterior segment fluids to percolate into the newly formed outflow pathway.[87,88] Canaloplasty is another non-penetrating procedure surgical procedure in which SC is mechanically opened by a forcing a microcatheter through its full circumference.

It is possible that the efficacy of each of these procedures would improve if the surgeon had foreknowledge of the location of prominent collector channels and aqueous veins, and was able to plan the procedure so that the entry wound avoided their damage.

1.4 CONCLUSIONS

Glaucoma is a blinding disease associated with elevated IOP. Both medical and surgical treatments for glaucoma are designed to reduce IOP, often by reducing resistance to aqueous outflow. At present, procedures are performed with no knowledge of the "outflow landscape", blindly destroying areas of tissue containing outflow structures, while sparing others, all with no appreciation of which areas might be patent and carrying a higher volume of aqueous humor than others, and which are quiescent. The ability to visualize and map the outflow pathways within the living eye may greatly benefit surgical planning. If those maps of the outflow system contained Doppler information, the effects of glaucoma medications on aqueous humor outflow might be determined rapidly on a patient-by-patient basis. Further, should the maps and Doppler data suggest that system capacity limits the potential for high outflow, it may be possible that failure of medical therapy may be bypassed completely in favor of surgical enhancement or replacement of the natural outflow system. Finally, should a vast aqueous venous outflow network exist, but present with low velocities, SLT or ALT may be indicated, but the presence of a limited aqueous venous outflow network may indicate the need for either a shunt or other procedure creating an alternative outflow pathway. In either case, better surgical planning would be possible if the aqueous humor outflow pathway could be visualized in each patient, enabling more personalized medicine.

2.0 OPTICAL COHERENCE TOMOGRAPHY

2.1 INTRODUCTION: FROM SIMPLICITY TO REALITY

The heart of SD-OCT technology is an optical device dating back more than 130 years. The Michelson interferometer splits a single beam of light into two beams with a partial mirror, each of those beams back-reflected by a mirror, meeting at the partial mirror, and forming an interference pattern in a detector (Figure 3).[89] The intensity of light reaching a detector (I) is a function of the wavelength of the light and the offset (Δ) between the two mirrors.

The use of a Michelson interferometry-based thickness measurements in thin films with micron (μ) level accuracy was described 40 years ago.[90] The technique featured a low-coherence light source projecting into a Michelson interferometer with one moving mirror, and provided the description of intensity at the detector, the long-known fundamental relationships that are the basis of time-domain OCT.[90,91] In this chapter, the relationship between the intensity of a monochromatic source beam and the intensity detected as a single point as a function of mirror offset is presented, and that relationship expanded to the special case of a wide-bandwidth source split by a into two paths with different intensities and detected in a spectrometer.

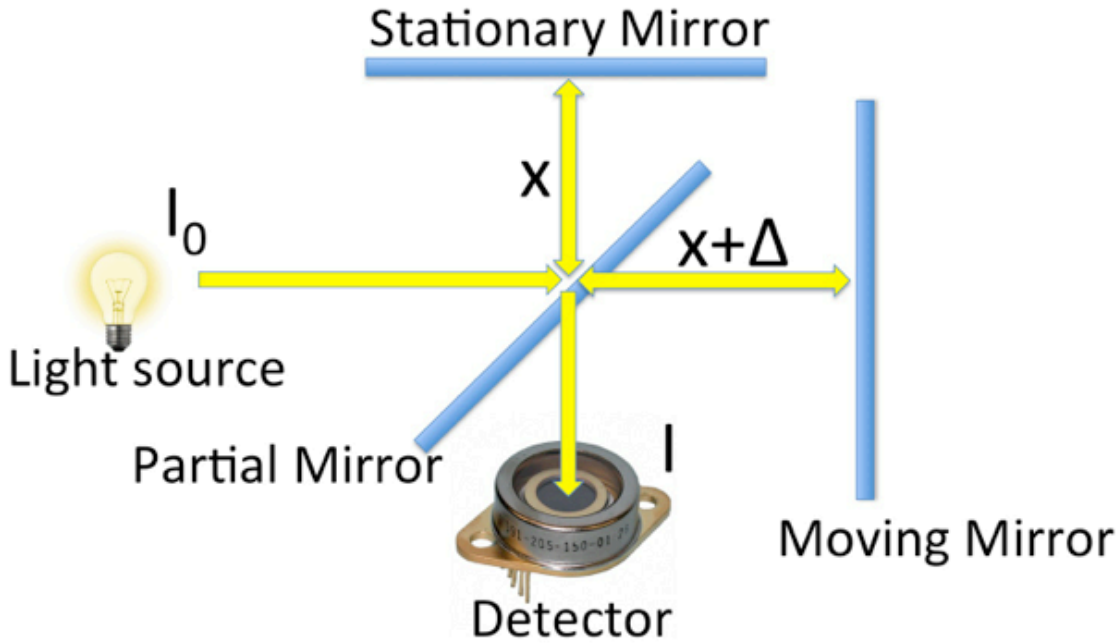

Figure 3. Michelson interferometer

2.2 INTERFEROMETRY AND TIME DOMAIN OCT

In the case of monochromatic light, intensity varies as the cosine of the offset between the two mirrors (Figure 3) and the wavelength of the light (λ, Equation 1),

Equation 1. Monochromatic light in a Michelson interferometer

$$I = 4I_0 \, cos^2\left(\frac{\delta}{2}\right)$$

with $\delta = (2\pi/\lambda)\Delta$, λ = the wavelength, and Δ equal to to the offset between the two mirrors in the interferometer (Figure 3).[90] Expanding this description for low-coherence (wide bandwidth) light sources, intensity at the detector is only detectable when the offset between the two mirrors (Δ,

Figure 3) is near zero, eliminating the cosine term of equation 2, as a function of wavenumber (τ).[90]

Equation 2. Broad spectrum light in an interferometer

$$\boldsymbol{I(\Delta) = 4\int_{\tau_0}^{\tau_n} i(\tau)\, cos^2\left(\frac{\tau\Delta}{2}\right) d\tau}$$

A broadband source is used in OCT because the intensity reaching the detector in equation 2 becomes 0 at all mirror locations away from $\Delta=0$. Equation 2 assumes that the partial mirror in Figure 3 is perfect, with no loss of light and perfect balance between the two paths. OCT systems use a fiber optic beam splitter in place of the partial mirror (Figure 4) with different intensities of light (I_1 and I_2) going to each optical path. Time domain OCT has a moving reference mirror. The depth of tissue in the sample arm being interrogated by the OCT beam is determined by the location of the moving reference mirror at the time of data acquisition.[92]

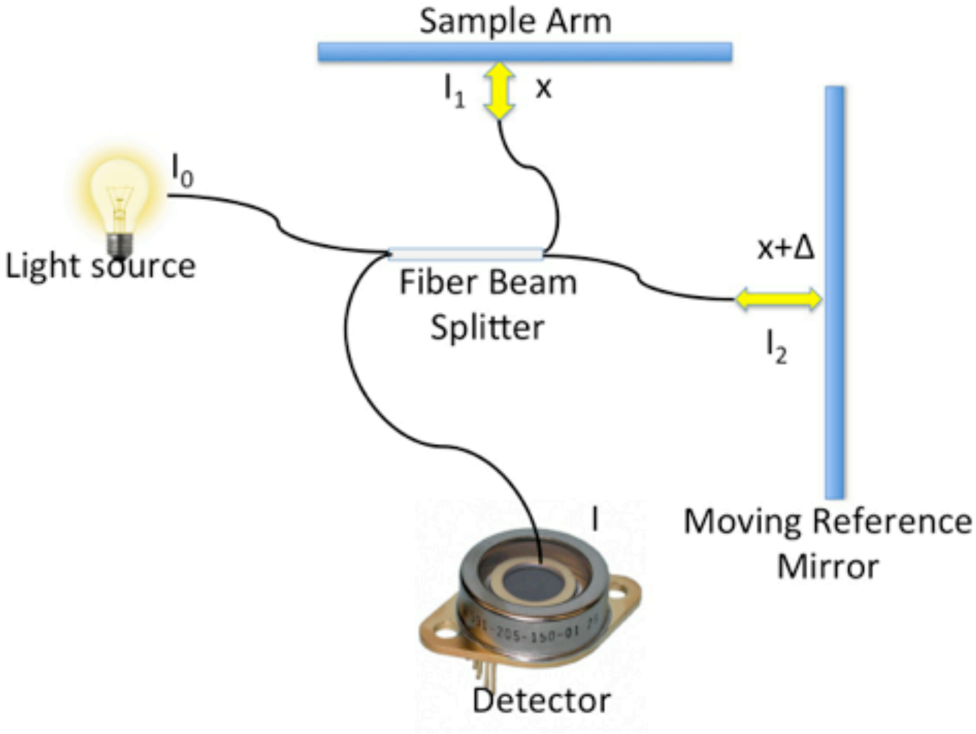

Figure 4. Interferometer with unbalanced beam splitter

Accounting for differences in the optical path lengths (Δ), imbalance in the beam splitter (k_1 = % in path 1, and k_2 = % path 2), output intensity becomes:

Equation 3. Broad spectrum light in an unbalanced interferometer

$$\boldsymbol{I = k_1 I_1 + k_2 I_2 + \sqrt{k_1 I_1 \cdot k_2 I_2} \cdot \cos(\tau \Delta),}$$

with τ = wavenumber (2π/λ).[92] Recall, in the case of time domain OCT with a broadband source, a signal is only present at $\Delta \cong 0$. Output intensity is a function of the intensities backscattered from the two optical paths in time domain OCT.

2.3 SPECTRAL DOMAIN OPTICAL COHERENCE TOMOGRAPHY

If the bandwidth of the light were infinitely wide, intensity at the detector would be exactly zero at all locations of Δ except at $\Delta = 0$. Finite width light sources produce a peak detector intensity at $\Delta = 0$, with fall-off intensities still detectable near $\Delta=0$.[93] The relationship between light source bandwidth and detector intensity as a function of bandwidth ($\Delta\lambda$) is the same as that of the relationship between the width of a rect function and its Fourier transform, the sinc function.[93] Specifically, coherence length (full width half maximum, axial resolution, all the same) of a wide-bandwidth source is

Equation 4. Axial resolution as a function of wavelength and bandwidth.

$$\textbf{axial resolution} = \frac{2\ln(2)}{\pi} \cdot \frac{\lambda_0^2}{\Delta\lambda}\ .$$

SDOCT differs from time domain OCT in the configuration of the detector, and the reference mirror (Figure 5).

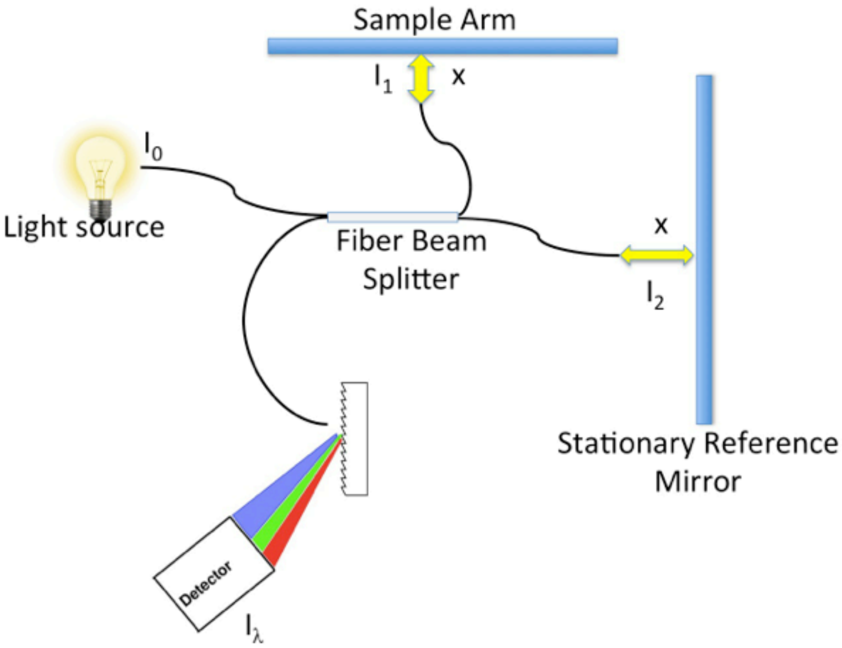

Figure 5. SD-OCT has a stationary reference mirror, and spectrometer

The interference pattern detected by SD-OCT is described by the same relationship as that of time domain (Equation 3).[92] However, in the case of SD-OCT, the location of reflective sources is encoded in the wavenumber (τ).

2.4 OCT SIGNAL PROCESSING

The signal reaching the detector in a time domain OCT scanner consists of a brief pulse of light modulating in intensity (Figure 6).[94] A broadband pulse of light (approximate envelope shown in Figure 6 as broadband spectrum) passes through reflective surfaces. As the reference mirror (Figure 4) is moved through the positions incidental to the locations of the reflective sources, the detector signal displays two modulating fluctuations in intensity. The only processing required to recover reflectivity data needed to assemble an axial scan (A-scan) is demodulation of the detector signal. The intensity of pulses in the demodulated signal is proportional to the reflectivity of the surfaces, and the location of the pulses is set to the position of the reference mirror when the pulses were detected.

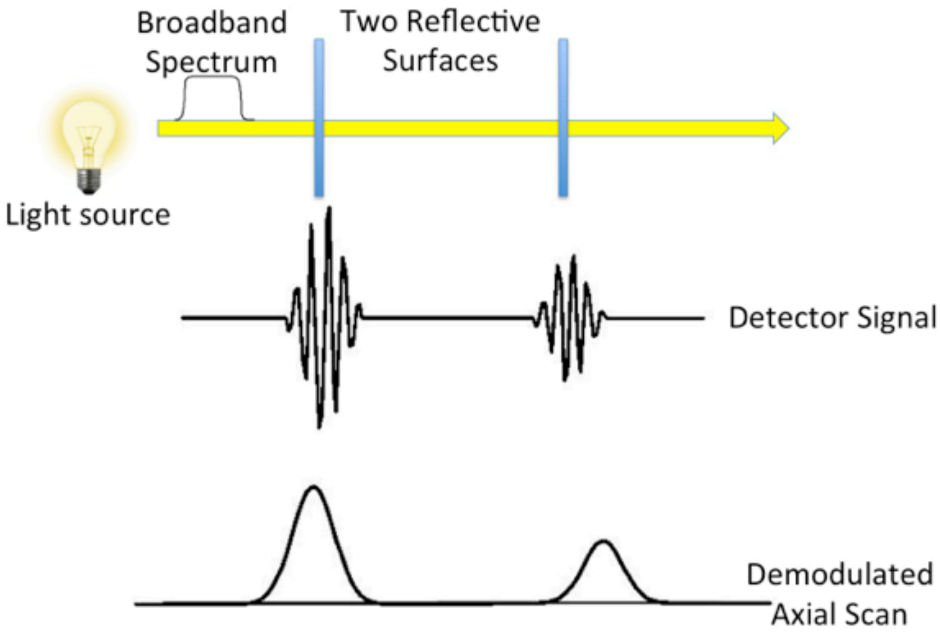

Figure 6. Time domain OCT from source to A-scan

SDOCT acquires an entire A-scan in a single read of the spectrographic detector (Figure 5).[94,95] Specifically, power spectrum of the of the interference pattern contains reflectance data for all points within the a-scan.[94,95] A linear array camera records the fringe pattern produced by interference of back-reflected light from the reference and sample paths (Figures 5 and 7). When the light of a broadband light source (approximate envelope labeled as broadband spectrum in Figure 7) interferes with the light of a stable reference mirror, and the resultant fringe pattern is observed on a spectrographic detector, the majority of the signal consisting of the original envelope with a small high frequency fringe added (Figure 7).

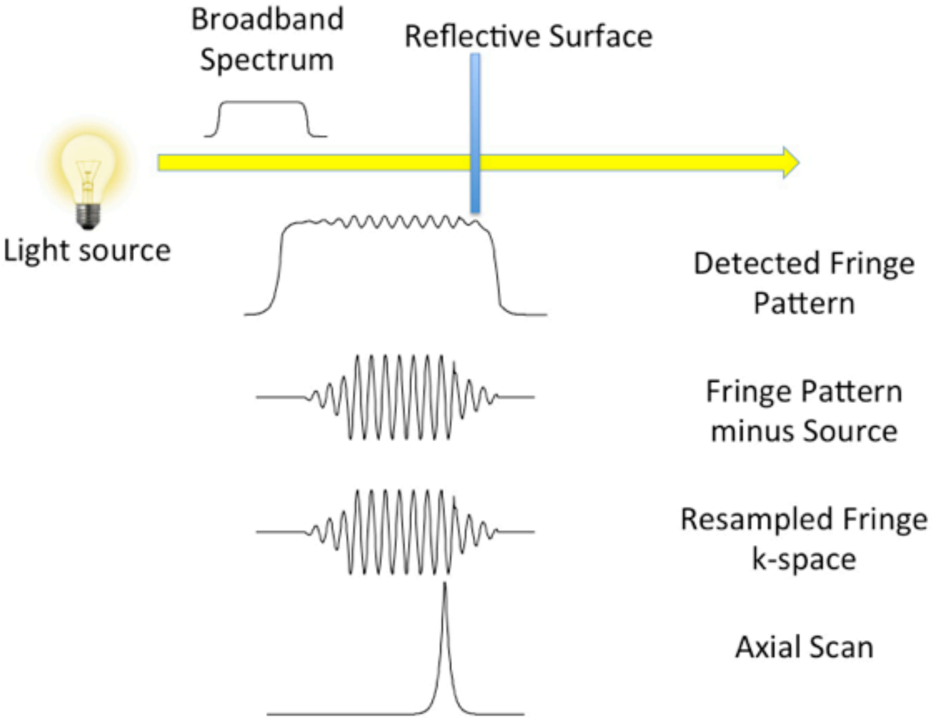

Figure 7. SD-OCT from source to scan

To process the signal, the envelope of the source is subtracted from the detector signal to isolate the fringe. This signal is a function of λ. The signal is resampled to provide equal spacing by wavenumber (τ, equation 3); i.e. k-space. The real portion (power spectrum) of the inverse Fourier transform of the fringe pattern in k-space produces the A-scan in its entirety.[94,95]

2.5 OCT IN OPHTHALMOLOGY

Optical coherence tomography for imaging of the layers of the human retina was first described in 1991.[91] Huang's prototype device acquired A-scans at a rate of 2 per second, providing great logistical challenges in the acquisition of line scans in the retina due to eye movements, and negating the possibility of volumetric scans. Subsequent time domain devices increased scanning rates, and the advent of spectral domain techniques (including swept source, which is beyond the scope of this work) exponentially increased the rate at which A-scans were made (Table 1).[91,96-111] The majority of the development work in OCT hardware has been conducted in the Jim Fujimoto's Lincoln Laboratory at the Massachusetts Institute of Technology (MIT), or by graduates of MIT working at Massachusetts General Hospital (MGH), and the Ludwig Maximilians University (LMU) in Munich. The exceptions are the work of Wojtkowski at the Institute of Physics, Nicolaus Copernicus University (NCU) and Rollins at Case Western.

Table 1. Progress in A-scan acquisition rates with the development of OCT technology

Light Source	Processing	Year	Author	Lab	A-Scan Speed
Broadband	Time Domain	1991	Huang	MIT	2 Hz
Broadband	Time Domain	1993	Swanson	MIT	150 Hz
Broadband	Time Domain	1996	Tearney	MIT	600 Hz
Broadband	Time Domain	1998	Rollins	Case Western	4 kHz
Broadband	Spectral Domain	2003	Wojtkowski	NCU	15 kHz
Broadband	Spectral Domain	2003	Yun	MGH	18 kHz
Broadband	Spectral Domain	2004	Nassif	MGH	30 kHz
Broadband	Spectral Domain	2008	Potsaid	MIT	310 kHz
Swept	Spectral Domain	1997	Goubovic	MIT	2 kHz
Swept	Spectral Domain	2003	Yun	MGH	15 kHz
Swept	Spectral Domain	2005	Huber	MIT	20 kHz
Swept	Spectral Domain	2006	Huber	MIT	230 kHz
Swept	Spectral Domain	2006	Huber	LMU	370 kHz
Swept	Spectral Domain	2011	Klein	LMU	1.37 MHz

While useful for visualization of retinal pathologies such as macular holes,[112-115] drusen,[116-119] and epiretinal membranes,[115,120-123] assessment of RNFL thickness by OCT has become a standard clinical procedure in the management of glaucoma.[4,112,113,124-131] OCT imaging of the anterior segment has been used to assess the angle;[132-140] however despite having the advantage of being a non-invasive procedure, OCT does not have the ability to produce imagery of the ciliary body, an exam left to a more invasive procedure, ultrasound biomicroscopy.[134,141,142] OCT imaging of the cornea has been shown to be useful in the visualization of pathologies, injuries, and for the purpose of central corneal thickness measurements.[143-146]

Recently OCT imaging has been used to assess the structures of the aqueous humor outflow system.[141,147-150] While the visualization of internal bleb (see section 1.3.3.3) structure may be useful in determining the reason for IOP elevation after trabeculectomy, visualization of the aqueous humor outflow system in its entirety, from SC to scleral veins, may be possible, and would provide the glaucoma specialist a wealth of new information (see Chapter 1). In the next chapter, evidence suggesting that specific portions of the aqueous humor outflow system can indeed be imaged by OCT is presented.

3.0 IDENTIFICATION AND ASSESSMENT OF SCHLEMM'S CANAL BY SD-OCT

3.1 INTRODUCTION: WHAT DO WE REALLY SEE? CAN IT BE MEASURED?

To demonstrate the ability to map the aqueous humor outflow system, identification of its components within SD-OCT imagery of the anterior segment is required. In this chapter, evidence of the identification SC, collector channels, and aqueous vessels within 3D SD-OCT scans of the anterior segment is provided. Reproducibility of measurements of those structures from two independent observers analyzing a single dataset is also presented. Finally, initial anatomical insights gleaned from the ability to measure the living and functioning SC are presented.

Glaucoma is the second leading cause of blindness worldwide[48], and the most important risk factor of glaucoma is elevated IOP.[51,151] IOP in the human eye is regulated, in part, by aqueous outflow through the TM draining into SC and then to the collector channels (CC) which empty into scleral veins.[5] Previous studies suggest that eyes of subjects with glaucoma have smaller SC's than those of healthy individuals.[152] Reduced SC size may be associated with elevated IOP because the size of SC is related to outflow facility.[152] Past observations of reduced SC size and the correlation of SC size and outflow facility were obtained in cadaver eyes.

Non-invasive measurement of aqueous outflow and aqueous outflow structures including SC, CC, and the SC at CC ostia (SC/CC) in the human eye would provide a powerful tool for both clinical and basic research, and the clinical management of glaucoma. The purpose of the present study was to non-invasively measure SC in living human eyes, determine the reproducibility of morphometric measurements within SC at collector channel ostia, and to compare SC area in different regions of the eye.

3.2 METHODS

3.2.1 Ethics Considerations

The study was conducted in accordance to the tenets of the declaration of Helsinki, and the Health Insurance Portability and Accountability Act. The institutional review board of the University of Pittsburgh approved the study. All subjects gave written informed consent prior to participation in the study.

3.2.2 Subjects

Healthy volunteers were recruited from the staff and faculty of the University of Pittsburgh Medical Center (UPMC) Eye Center. Glaucoma subjects were recruited from patients seen on the glaucoma service of the UPMC Eye Center. Schlemm's canal and active collector channels were imaged by SD-OCT.

3.2.3 Imaging of Schlemm's Canal

We have developed techniques combining structural and functional SD-OCT imaging to accurately identify SC, to assess Doppler signals from aqueous outflow in SC, collector channels and scleral veins, and to make structural measurements throughout.[153] SD-OCT Doppler measurements have been described in detail previously, and validated in an *in vivo* model.[154] Since successful SD-OCT imaging of SC and CC has not been accomplished previously, Doppler images were used in combination with structural images to confirm the location and identity of SC and CCs in SD-OCT limbus images in the first 5 subjects (Figure 8 A, B). Radial scans of the limbus and Schlemm's canal were obtained. (Figure 8A) Reflectance and Doppler images appear side-by-side (Figure 8B). Doppler shifts are graphed (Figure 8B and 8C right) along the red vertical line, with the blue horizontal line used to locate the measurement site within the structural, Doppler, and velocity graphs (Figures 8B and 8C). The strong Doppler shift against the stable background (Figure 8B, center) contains laminar flow within a scleral vein (parabolic velocity distribution, Figure 8B right) and collector channel (smaller parabolic velocity distribution, Figure 8C right). The identity of Schlemm's canal was made by virtue of its connection to scleral veins via tortuous collector channels. This connection was confirmed by tracing collector channels from superficial veins into the depths of the limbus to the slit-like structure.

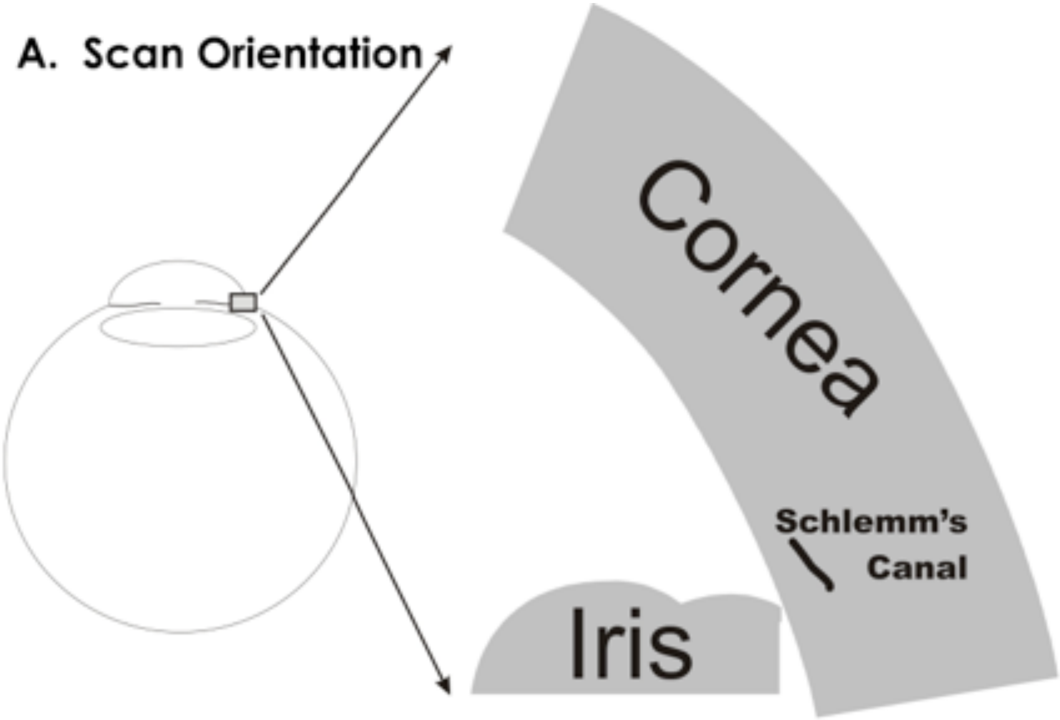
A. Scan Orientation
Cornea
Schlemm's
Canal
Iris

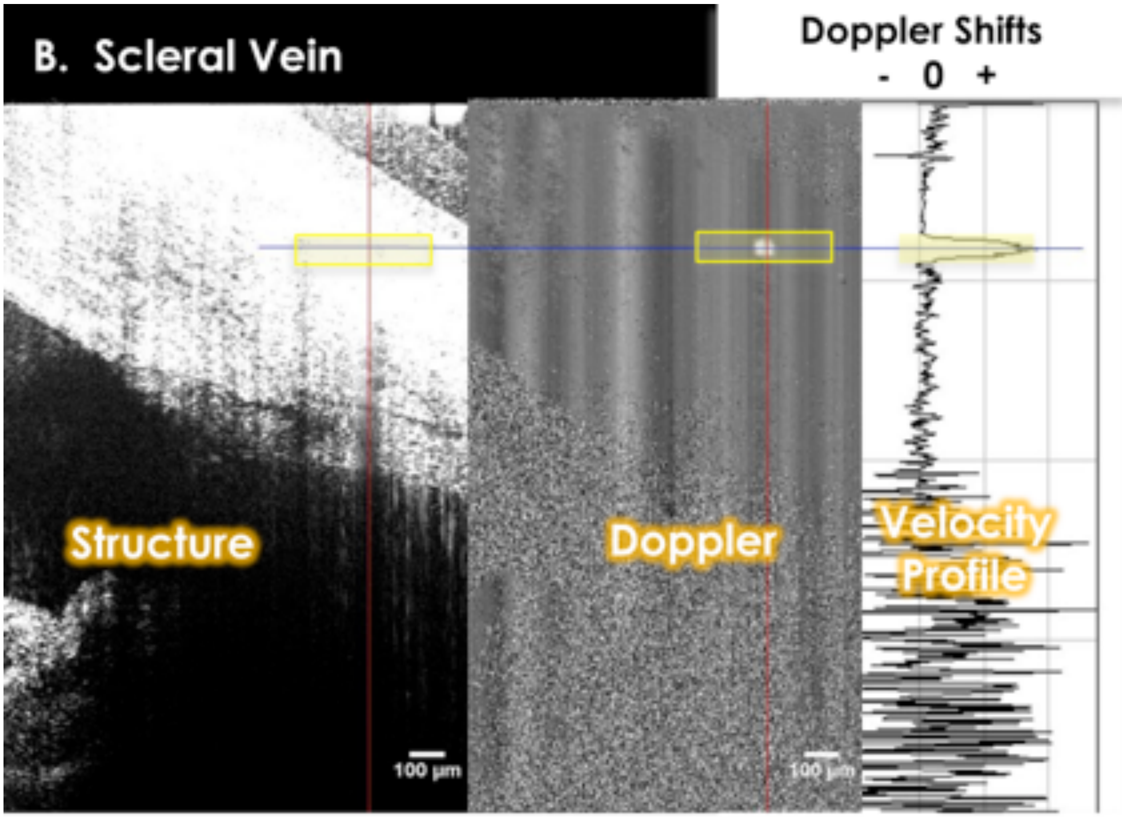
B. Scleral Vein
Doppler Shifts
- 0 +
Structure
Doppler
Velocity
Profile
100 µm
100 µm

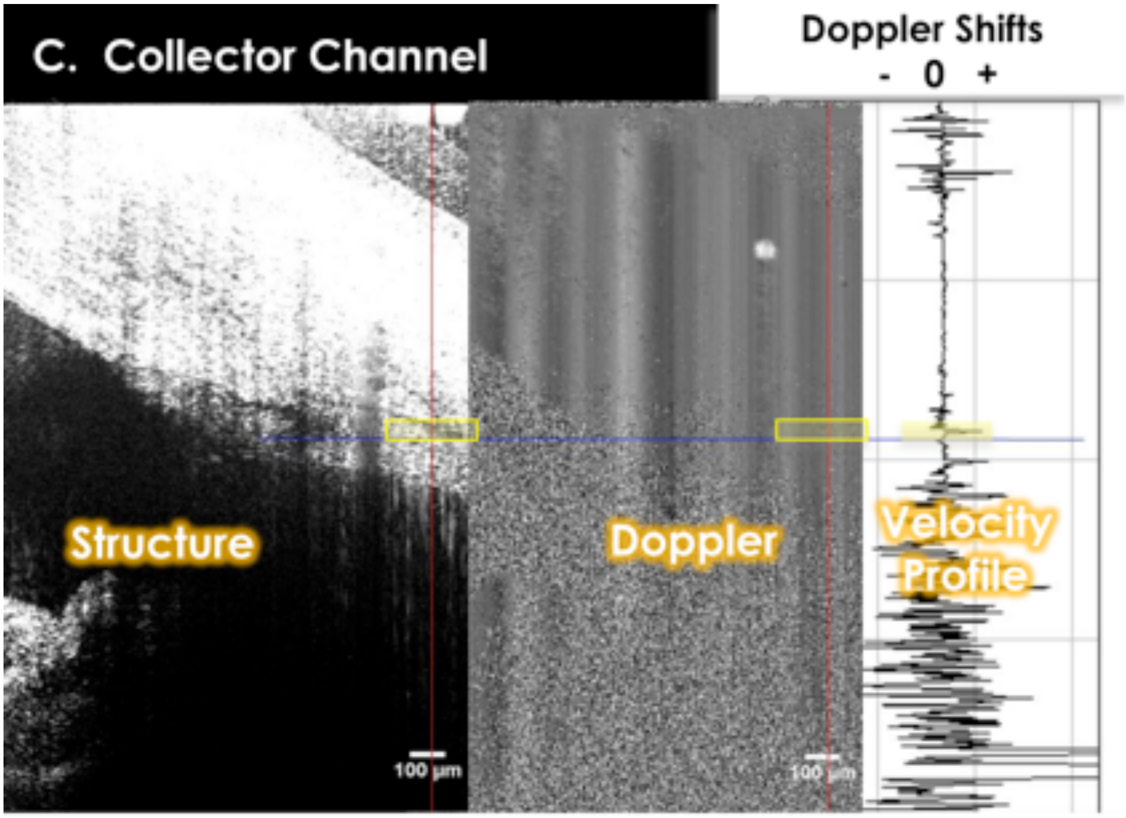

Figure 8. SD-OCT scan location and side-by-side structure and Doppler

CC's appeared in the images as dark structures following tortuous paths from superficial veins to a deep slit-like structure (Figure 9).

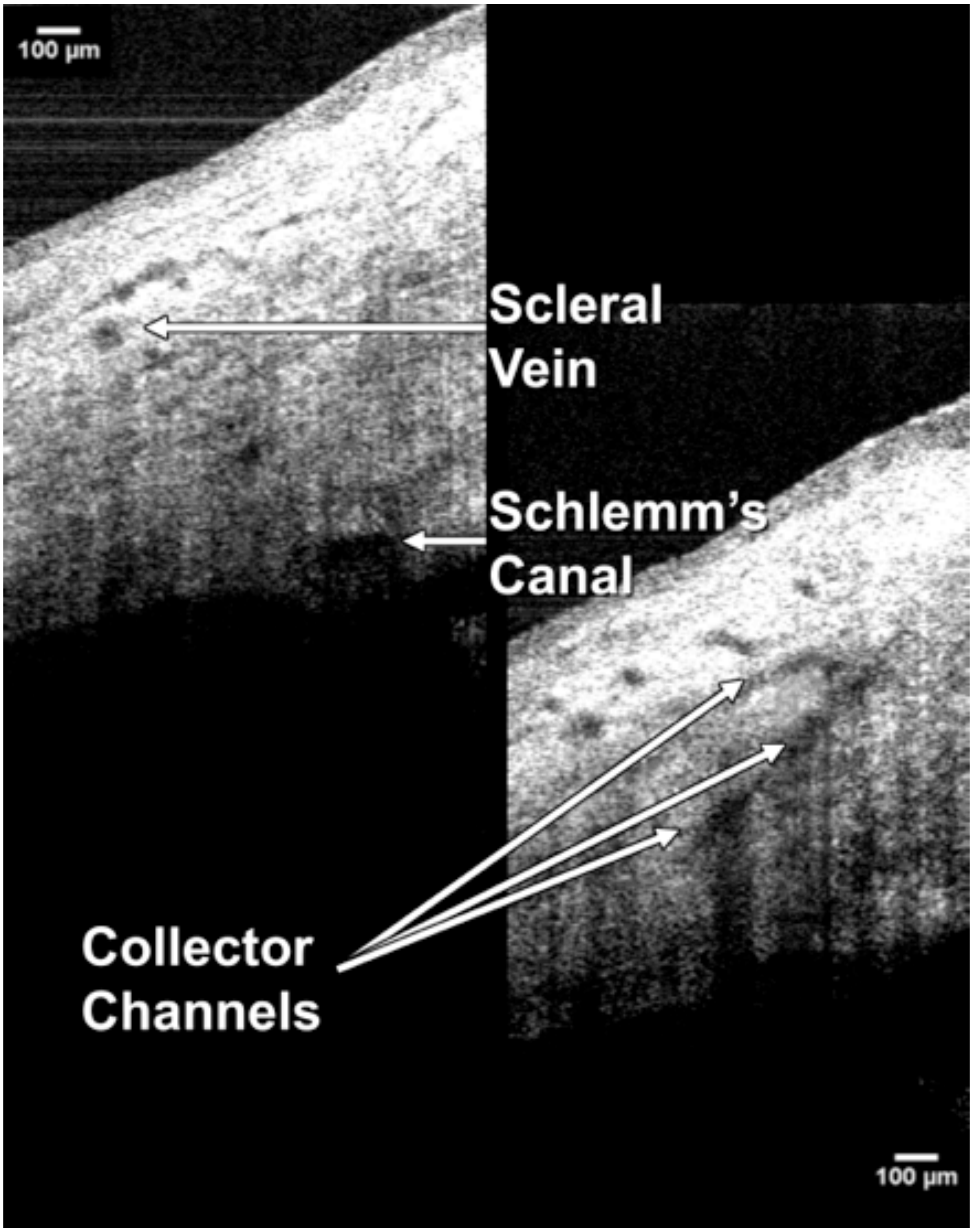

Figure 9. Schlemm's canal, the scleral vein into which it drains, and a collector channel

The Doppler signature of the vein confirmed its identity as a structure containing laminar flow (Figure 8A). CC's were tracked from the vein to Schlemm's canal, using the Doppler signature within the CC to confirm it as a structure containing laminar flow (Figure 8B).

A commercially available SD-OCT optics engine (Bioptigen, Research Triangle, North Carolina, USA) permitted the use of a wide-bandwidth superluminescent diode array, specifically a quad diode coupled source with an 870nm center wavelength and a 200nm bandwidth (Q870, Superlum Ltd, Dublin, Ireland). This light source had a theoretical axial resolution of 1.3μm in tissue; however, tissue water absorption results in a somewhat reduced true axial resolution in the eye. The non-isotropic raster scan consisted of 700x10 axial scans (A-scans) sampling a 1.3mm x 0.6mm slice of tissue 2mm thick. The raster scan was centered on a SC/CC, so that raster volumes contained both a SC/CC and adjacent areas of SC with no visible junction (Figure 9). In order to reduce background noise, each of the 700x10 A-scans was calculated by averaging 18 sequential raw A-scans. Raw A-scans were acquired at a rate of 28,000 per second. A bite bar was used to minimize fore and aft head motions during the 4.5 second scan. In healthy subjects, SC was imaged in both eyes nasally and temporally. In glaucoma subjects, SC was imaged on the nasal side of the glaucomatous eye.

3.2.4 Image Processing

Each of the 10 B-scans (consisting of 700 averaged A-scans) was resampled to a 1:1 aspect ratio, and measurements were obtained using ImageJ (ImageJ 1.40g, http://rsb.info.nih.gov/ij/). Contrast and magnification were subjectively adjusted to maximize visualization of SC, which was manually traced using the “freehand selection tool”. (Figure 10)

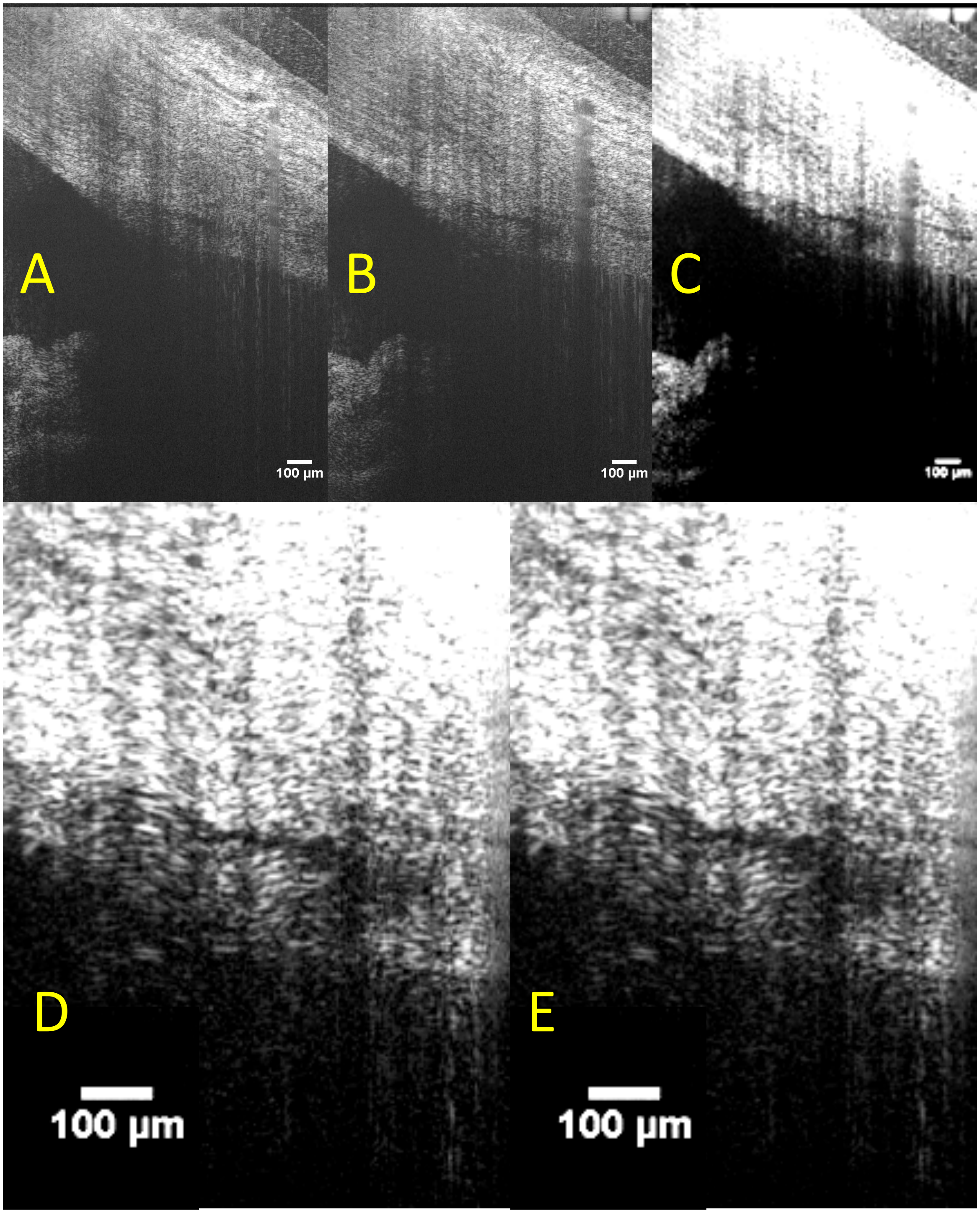

Figure 10. Schlemm's canal is visible adjacent to a collector channel ostium (A) and at the ostium (B). Measurements were made in both locations by increasing contrast (C) and magnification (D). Schlemm's canal was then outlined using the freehand tool in ImageJ (E). When outlined, ImageJ automatically measured the enclosed area, presenting results in square micrometers in calibrated images.

3.2.5 Reproducibility of Morphometric Measurements of Schlemm's Canal

In a subset of healthy subjects, 1 volumetric scan of SC was measured 3 times by two independent observers. Observers were instructed to locate the SC/CC junction within the raster scan, and select a cross-sectional image of SC within a few frames of the junction, no more than 3 frames (180 μm) from the SC/CC. To estimate bias (relative systematic difference) and imprecision (random difference) between two observers, a latent variable measurement error model was fitted to the six repeated measurements (3 from each observer). This model included parameters of observer, and measurement number (measurement 1, 2, and 3).

3.2.6 Comparison of Schlemm's Canal Area in Different Regions of the Eye

The effects of scan location within the eye (temporal versus nasal) and scan location within SC (on versus off SC/CC) were analyzed by a linear mixed effects model. SC cross-sectional areas were compared between healthy and glaucoma subjects by Mann-Whitney Rank U-test. A p value less than 0.05 was considered statistically significant.

3.3 RESULTS

3.3.1 Imaging of Schlemm's Canal in Living Human Eyes

SC was successfully identified and imaged in every normal healthy subject in whom imaging was attempted. Specifically, SC was located nasally and temporally in both eyes in 17 female and 4 male healthy subjects (34 ± 9 years, range 24 - 49). Three glaucoma subjects were imaged (57 ± 6 years, range 52 - 63). SC and collector channels were successfully located in two of the glaucoma subjects. SC and collector channels were not found in the third subject, who had an implanted glaucoma drainage device.

3.3.2 Reproducibility of Morphometric Measurements of Schlemm's Canal

A randomly selected subset of 12 healthy subjects was included in the reproducibility and location comparison studies. Each observer made three measurements of Schlemm's canal cross-sectional area on and adjacent to a collector channel ostia. The latent variable model produced calibration equations relating the measurements of the two observers. No bias between repeats within observers was observed. A model without bias was fitted. A coefficient of variability (CoV) of 11.4% was calculated from quantification of imprecision.

3.3.3 Comparison of Schlemm's Canal Area in Different Regions of the Eye

Schlemm's canal cross-sectional area (Table 2, mean (standard deviation)) was measured at visible collector channel junctions, and adjacent to those junctions by two independent observers. Average measurements from the subjects included in the reproducibility study are listed in Table 2.

Table 2. Schlemm's Canal area measurements in healthy eyes (μm^2)

		Schlemm's Canal at Collector Channel Ostium*			**Schlemm's Canal near Collector Channel Ostium**		
		Nasal	**Temporal**	**Combined**	**Nasal**	**Temporal**	**Combined**
OD	**Observer 1**	13,797 (6,770)	10,390 (4,846)	12,605 (6,261)	7,998 (3,207)	4,964 (1,503)	7,027 (3,099)
	Observer 2	12,280 (2,894)	11,236 (2,510)	11,915 (2,746)	7,446 (1,658)	6,080 (914)	7,009 (1,580)
	Combined	13,039 (5,160)	10,813 (3,744)	12,260 (4,785)	7,722 (2,529)	5,523 (1,333)	7,018 (2,345)
OS	**Observer 1**	13,738 (4,177)	12,485 (5,176)	13,768 (5,512)	8,739 (3,068)	6,411 (3,676)	7,721 (3,481)
	Observer 2	11,785 (1,939)	12,073 (2,153)	12,033 (2,427)	7,706 (2,190)	7,028 (1,719)	7,385 (1,958)
	Combined	12,762 (3,342)	12,279 (3,815)	12,593 (3,474)	8,276 (2,679)	6,720 (2,802)	7,557 (3,255)
Combined	**Observer 1**	13,768 (5,512)	11,438 (4,946)	12,592 (5,376)	8,310 (3,121)	5,730 (2,881)	7,336 (3,255)
	Observer 2	12,033 (2,472)	11,654 (2,288)	11,900 (2,356)	7,542 (1,835)	6,582 (1,443)	7,171 (1,742)
	Combined	12,900 (4,306)	11,546 (3,782)	12,426 (4,158)	7,933 (2,577)	6,156 (2,285)	7,254 (2,605)

*Mean (SD)

Nasal SC areas were significantly larger than temporal SC areas (p = 0.009). Cross-sectional SC areas were significantly greater at junction sites than adjacent to those sites, 12,426 ± 4,158μm^2 versus 7,254 ± 2,605μm^2 respectively (mean ± SD; $p < 0.0001$). In the two glaucomatous eyes, cross-sectional SC areas on and off collector channel junctions were 6,025 ± 1,909μm^2 and 3,725 ± 742μm^2 respectively. SC areas were statistically significantly smaller in glaucoma patients than in normal subjects, whether pooled (p=0.006), or grouped by measurements on SC/CC (p=0.039) or off SC/CC (p=0.031).

3.4 DISCUSSION

3.4.1 Summary of Findings

We found that a combination of signal averaging and high axial resolution enables the location of superficial vessels in the limbus and the collector channels that drain into them, which can be traced, either in live acquisition mode or in 3D data blocks, to locate SC. When located, the cross-sectional area of SC can be reproducibly measured. The cross-sectional area of SC was larger at junctions with active collector channels; determination of activity was based on the presence of a Doppler signal within. SC was significantly smaller in the two patients with glaucoma compared to the healthy subjects. In one patient with a glaucoma drainage device, SC and CC could not be located.

3.4.2 Reproducibility

A latent variable model using measurements from two observers computed imprecision associated with the measurement process. Each observer measured a single set of images 3 times. Since variability changed with level, data were log transformed, and SD estimated in log-space. In order to account for the change in SD with level, SD was normalized to level, and the resulting CoV was 11.4%. This value estimates measurement imprecision, and is needed when calculating statistical power during the design of clinical experiments.

3.4.3 In-Vivo Versus In-Vitro Analysis of Schlemm's Canal

SC areas have been measured after fixation in several histological studies. Hulzen et al examined the effect of perfusion pressure on SC area, measuring immersion fixed versus perfusion fixed at 15 mmHg.[155] Wild et al. compared viscoelastic substances in viscocanalostomy procedures, and their study included a control group.[156] In the Wild study, SC area was measured at the location of a deep flap penetrating to SC, and 6m away from the flap. Using their published data, we calculated the overall mean and standard deviation of the data as presented, and used those values to calculate the 95% confidence interval, which was calculated as mean ± 1.96*standard deviation. Histological values then increased to account for 15% tissue shrinkage associated with fixation.[157] (Table 3)

Table 3. Published values of Schlemm's canal area

	Published Values		**Adjusted Values**	
Author: Condition	**Lower Limit**	**Upper Limit**	**Lower Limit**	**Upper Limit**
Johnson: IM-Fixed	825	8,138	971	9,574
Johnson: PP-Fixed	176	5,715	207	6,724
Wild: at flap	858	7,762	1,009	9,132
Wild: 6mm from flap	1,202	7,310	1,414	8,600

Considering SC area measurements away from CC ostia, all temporal data fell within the 95% confidence interval for all normative data adjusted for shrinkage, except for observer 2's OS and combined measurements. All nasal and temporal SC area measurements off of CC ostia fell within immersion fixed 95% confidence intervals, with the lone exception of observer 1's OS nasal measurement. None of the measurements obtained at CC ostia were within the 95%

confidence intervals regardless of fixation method. Overall, the magnitudes of SC area measurements in the present study are in good agreement with published values, after adjusting for shrinkage, though tended to be toward the high end of the 95% confidence interval. This suggests the possibility that some statistically insignificant difference between the present in-vivo measurements and published histological measurements exists. Such a systematic difference could result from an underestimation of the effects of tissue shrinkage, some systematic difference between study populations in this and the published work, or some small error in the calibration of the SD-OCT images.

3.4.4 Ostia Versus Adjacent Regions of Schlemm's Canal

If measurements are made exclusively on ostia, they are statistically significantly larger than published values since they are not contained within the adjusted 95% confidence intervals. The broadness of the confidence intervals for published data suggests that histological assessment was performed on a wide range of SC presentations. It is unknown whether histological measurements obtained exclusively at ostia would agree with data in the present study.

After ongoing validation studies are complete, this non-invasive measurement of aqueous outflow may find a number of immediate applications. The most obvious is basic research of the physiology of aqueous outflow and the pathophysiology of aqueous outflow in glaucoma. The present findings in two glaucoma subjects showed that the structures involved in aqueous outflow are narrow in vivo, in agreement with prior histological findings.[152] Other applications will include investigations of the impact of glaucoma medications and treatments on the modulation of aqueous outflow in both healthy and glaucomatous eyes. Eventually, aqueous outflow measurements may also be useful in pre-surgical planning. The utility of aqueous outflow imaging for pre-surgical planning may vary with procedure. If a procedure is designed to facilitate aqueous outflow from the TM into SC, then it is suggested (but remains to be demonstrated) that optimal outcomes will occur when flow from the TM is increased in a region adjacent to a large and active SC ostium

3.4.5 Nasal Versus Temporal Schlemm's Canal Areas

SC was found to be statistically significantly larger on the nasal side compared to the temporal. This finding was consistent whether on or off of a SC/CC. This may suggest preferential nasal drainage in the normal healthy eye, and may suggest that interventions designed to enhance outflow on the nasal side may be preferred. Further study is required.

In the patient with a glaucoma drainage device, neither CCs nor SC were visualized. It is possible that the natural outflow system collapsed beyond the limits of resolution employed after being replaced by an alternate outflow pathway.

3.4.6 Limitations of the Present Study

There are several limitations to the present study. First, and foremost, a single scan was obtained from each area and measured repeatedly. The coefficient of variability of 11% only represents the variability of the measurement process, and provides no information on the actual variability of SC. Without a knowledge of SC cross-sectional area variability within SC and over time, the findings in this study cannot be generalized beyond the constraints of this study design; specifically, SC cross-sectional area at an ostium is larger than the cross-sectional area of SC immediately adjacent to the ostium. The measurement technique functions with adequate reproducibility, allowing further studies of the reproducibility of SC size in repeated measurements.

Samples of SC away from SC/CC were limited to locations within 180 μm (3 adjacent frames) of a visible junction. As a result, only a small sample of SC was imaged and analyzed in this study. Future work must include a comprehensive 360° survey of SC. Such a survey will be difficult to accomplish in humans for several reasons. First, each scan volume was acquired in 4.5 seconds; each individual frame requiring 0.45 seconds. Eye movements may be minimized with the use of a bite bar; however, movements between scans make it extremely difficult to obtain a series of adjacent raster scans at known locations. With each scan volume traversing only 0.6 mm of SC in 4.5 seconds, under ideal conditions, imaging of the SC all around the eye would require 279 seconds (4.65 minutes) of scan time. Second, despite being located in all eyes without shunts, each eye had many regions in which shadowing from superficial blood vessels obscured SC and the CC's (Figure 11).

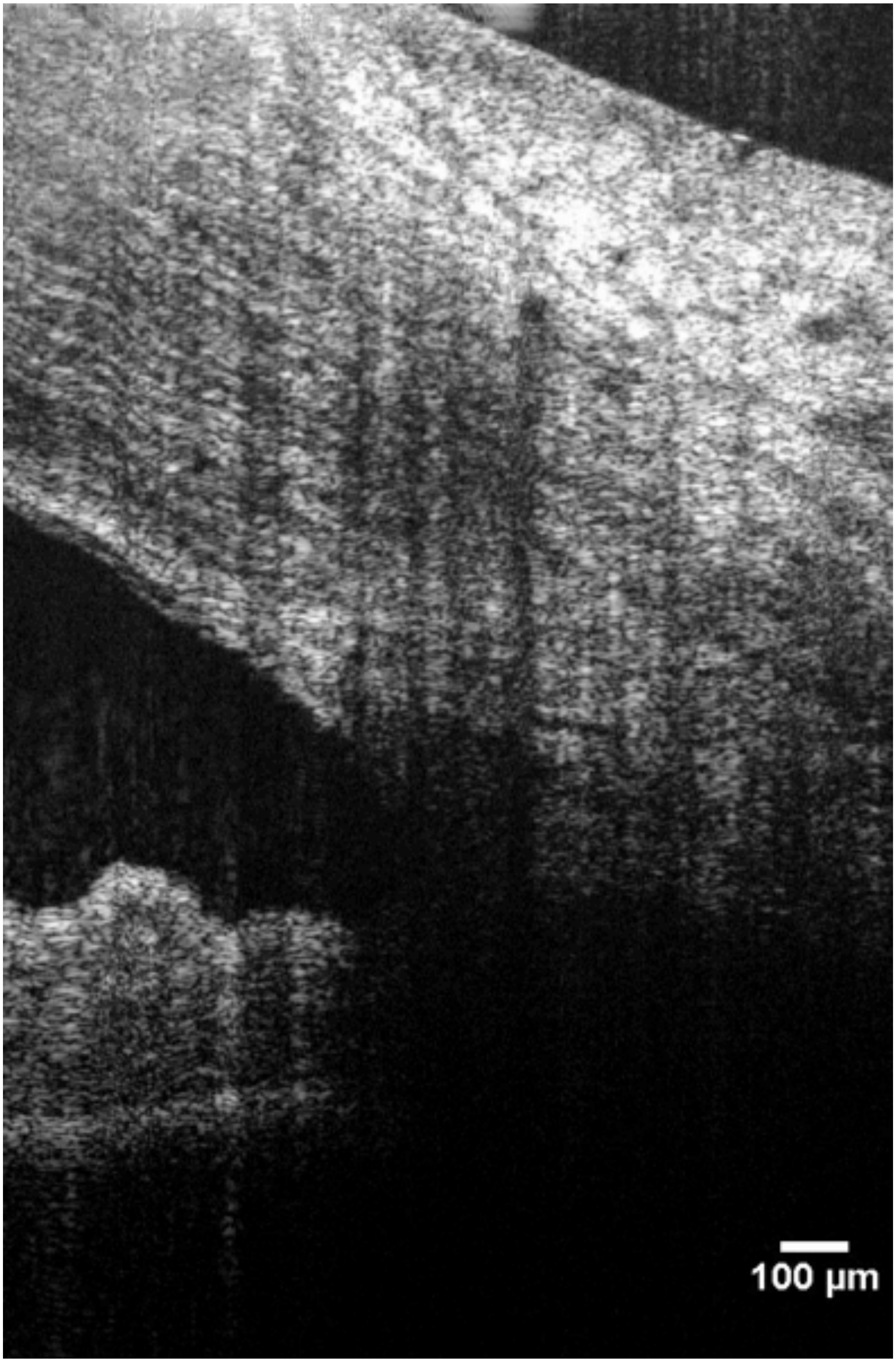

Figure 11. Shadows from superficial blood vessels often obscure part or all of Schlemm's canal.

Shadowing did not prevent the identification and measurement of SC/CC junctions, as locations with sufficiently few shadows were present in all eyes (usually the 3 or 9 o'clock nasal location). However; the combination of blood vessel shadowing and scan time makes the completion of a comprehensive map of all collector channel junctions and all of SC unlikely. It is possible that longer wavelength systems may be more robust to shadow artifact, but it is unknown whether longer wavelengths will have sufficient axial resolution to image SC, nor would such a system address the limitation of scan time. Axial resolution is inversely proportional to center wavelength, and as longer wavelengths are used, resolution suffers. The optimal wavelength for SC imaging and measurement may differ, and is yet to be determined. Another limitation of the study is the small number of glaucoma subjects. Caution should be used in interpretation of results drawn from the small sample, however the observed differences are of interest, and our pilot results emphasize the need for further investigation.

In the present study, a simple subjective method of quality control was used to detect eye movements. Since the scan set consisted of 10 B-scans obtained approximately in a single location, it was simple to page rapidly between B-scans and compare the appearance of the anterior corneal surface. Scans containing apparent eye movements were not used for analysis. Generally speaking, no technological advance can be trusted to completely eliminate eye movement artifacts from OCT or any other scanning ophthalmic imaging technique. Some method of quality control or image validation will always be needed. That being said, it is possible that reduced scan times in future OCT systems will lessen the deleterious effects of eye movements. Swept-source technology has increased the A-scan rate to 1.37 MHz in a prototype system.[95] Applied to the scan protocol used in the present study, a 1.37 MHz scan rate would reduce the B-scan acquisition time from 0.45 to only 0.01 seconds. Visual inspection for eye movements between slices will always be necessary when images are being used to characterize morphology, but increased scan speeds will likely reduce the number of frames discarded due to eye movements.

3.4.7 Conclusions

SC and the aqueous outflow system can be non-invasively imaged and Doppler shifts quantified in the living human eye. These measurements will be useful in physiological studies of aqueous outflow, and clinically useful for the determination of the impact of glaucoma therapies on IOP as well as in pre-surgical planning.

4.0 VARIABILITY OF SCHLEMM'S CANAL CROSS-SECTIONAL AREA ALONG ITS CIRCUMFERENCE

4.1 INTRODUCTION: SUBJECTIVE OBSERVATIONS AND CONVENTION

In the previous chapter, the ability to reproducibly measure SC cross-sectional area was established. In that study, two independent observers measured two slices from a single 3D scan repeatedly. Further, a definite landmark (a collector channel ostium) was used to ensure that both observers measured the same location. These data do not address the spatial variability characteristic of SC along its circumferential length. In February 2011, while reviewing SD-OCT volumetric scans and SC histology slides side by side together with Dr. Haiyan Gong, she noted that she has observed large variations in SC size, shape, and location in sequential histology sections. While informally known and accepted in the research community, that characteristic of SC variability has not been reported in the literature. The advent of volumetric scanning of the outflow system with SD-OCT allows quantification of SC cross-sectional area in sequential scans, and more importantly, allows the quantification of *change* in area along its length. The purpose of this study was to quantify changes in SC cross-sectional area in sequential SD-OCT scans.

4.2 METHODS

4.2.1 Ethical Considerations

The study was conducted in accordance with the tenets of the Declaration of Helsinki and the Health Insurance Portability and Accountability Act. The institutional review board of the University of Pittsburgh approved the study. All subjects before participation gave written informed consent.

4.2.2 Study Design

Six healthy volunteers were recruited from the staff and faculty of the UPMC Eye Center. SD-OCT images of the limbus were obtained from the nasal and temporal quadrants. Images were 4x4mm, with a slab thickness of 2mm. SC was located within the images. Of the 4mm length of SC contained in 128 b-scans, a 1mm sequence of 32 sequential scans in which SC was clearly visible without shadow or other artifacts was identified. Slice to slice differences in SC cross-sectional area in a 1mm sample length were measured.

4.2.3 Imaging of SC

SD-OCT (Cirrus HD-OCT; Carl Zeiss Meditec, Inc., Dublin, CA) was used to image SC. 512 x 1024 x 128 samples were acquired in a 4 x 2 x 4 mm volume of the limbus. The acquisition rate was 27,000 A-scans per second. Moving chin and forehead rests were used to center the eye in the image frame, and then verbal commands were used to position the desired region of the limbus in the image. B-scans (or slices) were separated by 31.25μm. Scan time was 2 seconds.

4.2.4 Image Processing and SC Visualization

Images were pre-processed with a 3x3x3 kernel-size averaging filter using software of our own design (Listed in Appendix A). Images were then blurred and contrast enhanced using an automatic local contrast enhancement by adaptive histogram filter, and then subjectively by manual contrast and brightness adjustment in Fiji (ImageJ 1.45q, NIH, http:imagej.nih.gov/ij). SC was manually circled as in the previous chapter, and area was measured. A second independent observer reviewed the images with and without outlines to confirm accuracy.

Individual slices were excluded when SC was not visible for any of the following reasons: 1) SC was present and visible but closed, 2) SC was not in the imaged field of view, or 3) SC was obstructed by poor image quality or shadowing. The quadrant was excluded if all 32 consecutive slice sequences contained 12 or more excluded slices.

4.2.5 Statistics

The absolute difference between sequential slices was calculated. If a slice was excluded, the gap was not included in any difference calculation.

4.3 RESULTS

4.3.1 Subjects

Six healthy eyes (3 right (OD), 3 left (OS)) from six volunteer subjects (4 male, 2 female; age range: 25-53 years) were recruited for the study.

4.3.2 Imaging of SC

For each of the 6 eyes, both nasal and temporal quadrant image series were taken, giving 12 total image series. Of the 12 image series, 10 presented as complete and containing visible SC throughout the entire 1mm (32 slices) sample length. Of the 2 series with incomplete quadrants, 1 (Subject 2, temporal) was missing 5 slices (remaining 27 of 32 slices used), while the second (Subject 5, nasal) was excluded based upon the stack exclusion criteria.

4.3.3 SC Variability

The average cross-sectional area and standard deviation using all eleven stacks was 10546.96μm^2 and 4200.95μm^2, respectively. The average slice-to-slice change in SC cross-sectional area across all stacks was 2875.54μm^2 ± 2019.65 μm^2 (mean ± standard deviation). This represents an average change of SC cross-sectional area of 27.27% in within a 31.25μm distance along its circumference, or a spatial rate of change in SC cross-sectional area of ± 93$\mu m^2/\mu m$. Projecting these results to a histological series of 5μm sections, each section would be expected to differ in SC cross-sectional area by a difference of 465μm^2. Table 4 shows the average and standard deviation of slice-to-slice cross-sectional area change for each stack.

Table 4. Slice to slice variation in Schlemm's Canal cross-sectional area (CSA)

Subject	Region	Average CSA (std. deviation) [μm^2]	CoVariance [%]	Slice-to-Slice CSAChange (std. deviation) [μm^2]
1	temporal	6566.05 (1764.99)	27.09	1660.75 (1294.87)
1	nasal	4438.40 (1836.26)	41.70	1143.92 (884.16)
2	temporal	3162.53 (1209.65)	38.60	752.38 (854.01)
2	nasal	9948.73 (4450.19)	45.08	3161.03 (3086.15)
3	temporal	16195.30 (5567.89)	34.65	3573.51 (2315.94)
3	nasal	14074.33 (4922.24)	35.25	2899.17 (1895.58)
4	temporal	13256.07 (5553.59)	42.22	2955.28 (2591.00)
4	nasal	21056.18 (8259.66)	39.53	6002.12 (4463.55)
5	temporal	9962.08 (4430.76)	44.82	2875.54 (2019.65)
6	temporal	10055.54 (5107.41)	51.19	2978.91 (3379.81)
6	nasal	7301.33 (3107.83)	42.90	2264.21 (1779.77)
Average		10546.96 (4200.95)	40.74 (6.40)	2751.53 (2233.14)

Figure 12 provides a sample of 10 sequential frames of SC (radial sections, bottom) in a typical region of nasal limbus (coronal section, top). SC is nearly closed in frame 5, open at two locations in frame 6, slit-like in frames 4, 6, and 7, open in frames 10 and 1, at an ostium in frames 2 and 3, and all of this occurring within 281µm SC's circumferential length.

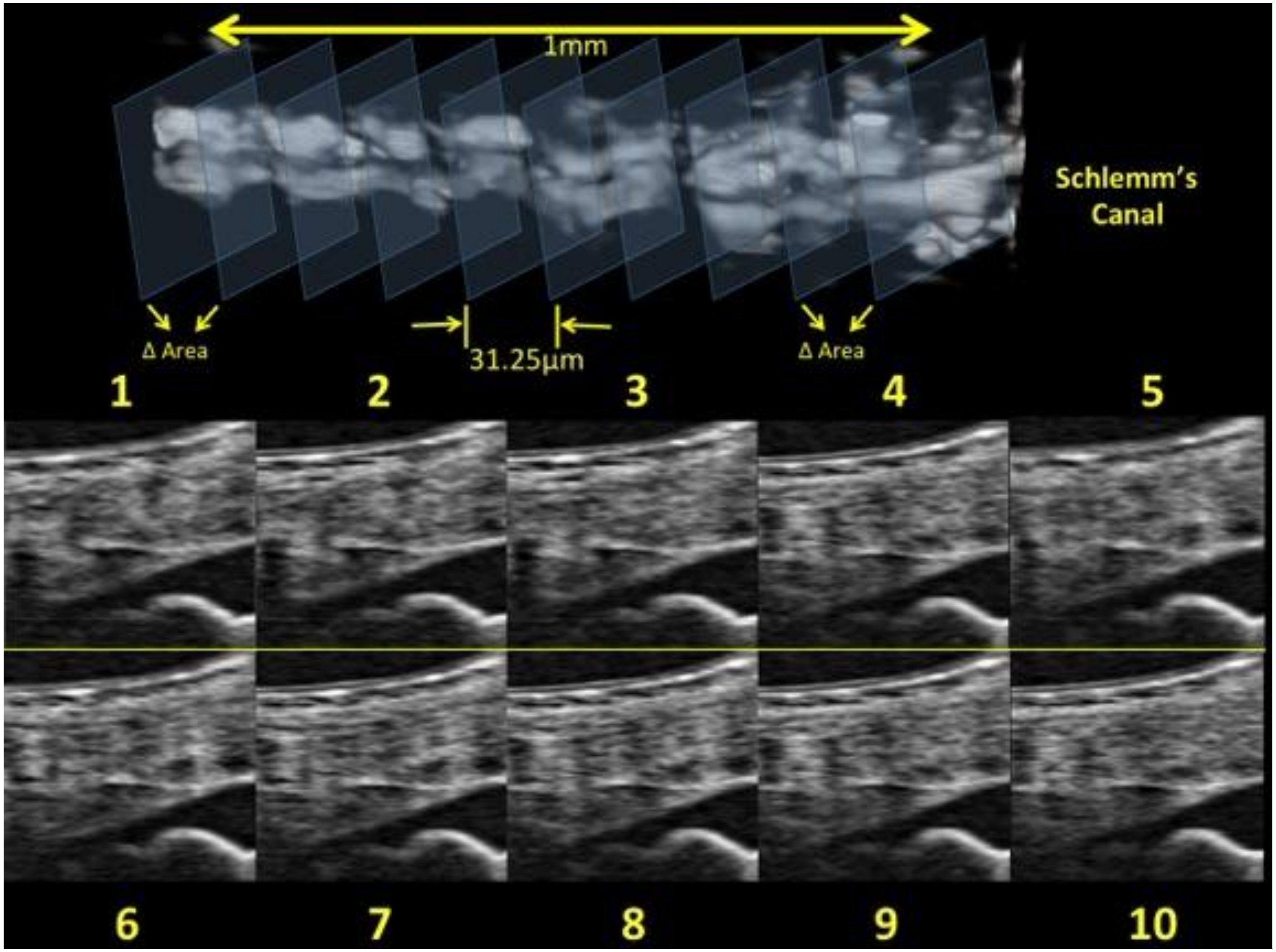

Figure 12. Ten sequential cross-sectional b-scans of Schlemm's canal along its length

4.4 DISCUSSION

4.4.1 Summary of Findings

In the present study, we found that the average change in SC cross-sectional area in sequential slices separated by 31.25μm was 2,876μm^2. With an observed average cross-sectional area of 10,547μm^2, the coefficient of variance for SC cross-sectional area slice to slice measurement is over 40%.

4.4.2 The Impact of Variability on SC Characterization

Given the mean coefficient of variation to 40.74%, a sample of 500 slices would be needed to estimate the average SC cross-sectional area within a 3% margin of error at a 90% power. For perspective, assuming a 12mm limbus diameter, sectioning SC in 1μm slices would yield approximately 37,700 samples. The SD-OCT scanning protocol used in this study acquires 128 B-scans in a 4mm length. Assuming the ability to rotate the scans (the current generation of scanner cannot rotate scans), this protocol would yield 1,206 B-scans. Nearly half of the scans in the OCT protocol would be required to accurately assess SC cross-sectional area. An alternative technique is required.

4.4.3 A Possible Solution

Faced with a similar situation in blood flow measurements, the distribution of flow values was used to describe a flow field in lieu of a single mean value.[158] We found that a single average used to describe non-normally distributed data reduced sensitivity to differences, whereas using quartile and 10 and 90 percent values in the histogram (a rank-order approach) of all measurements allowed discernment between health and disease.[158]

In the previous chapter, a single measurement was used to compare two distinct locations on SC within a single scan; specifically, the cross-sectional area at an ostium and immediately adjacent to one. In this context, single measurements were meaningful, since no attempt to characterize SC as a whole was being made. The challenge here is to create a technique to characterize the size of SC in cross-sectional sections. Beyond the need for accuracy, there is also a need to determine those parameters characterizing SC size and morphology that are best related to aqueous humor outflow. It is possible that the entire need of cross-sectional measurements may be circumvented if total SC volume is found to be more pertinent for the characterization of aqueous humor outflow. Future studies examining the relationship between SC volume and descriptions of cross-sectional area and are needed.

4.4.4 Conclusion

In conclusion, cross-sectional area fluctuates greatly within short circumferential lengths of SC. Because of this, single or small numbers of measurements of cross-sectional area may provide a limited characterization of SC. An alternative method may be required to describe the size of SC.

5.0 REPRODUCIBILITY OF SCHLEM'S CANAL CROSS-SECTIONAL AREA ASSESSMENT IN REPEATED SCANS

5.1 INTRODUCTION: CAN IT BE DONE AT ALL?

In Chapter 3, the variability of a SC measurement technique was demonstrated to be approximately 11%; however, the in previous chapter, application of that same measurement technique to a sequence of radial scans of the limbus found that SC cross-sectional area within a single volumetric scan changes radically. SC scans separated by only 31.25μm have an average change in cross-sectional area of 2875.54μm^2. The large changes in SC cross-sectional area that occur within small changes in location call into question whether it is physically possible to return repeatedly to the same location of SC with sufficient precision for stable and reproducible measurements of cross-sectional area. The purpose of the present study was to quantify the variability of repeated measurement of SC cross-sectional area and measurement technique in a series of SD-OCT volumetric scans.

5.2 METHODS

5.2.1 Ethical Considerations

The study was conducted in accordance with the tenets of the Declaration of Helsinki and the Health Insurance Portability and Accountability Act. The institutional review board of the University of Pittsburgh approved the study. All subjects before participation gave written informed consent.

5.2.2 Study Design

Ten healthy volunteers were recruited from the staff and faculty of the UPMC Eye Center. Three SD-OCT scans of the limbus were obtained from the nasal quadrant of the right eye at a single visit. Images were 4x4mm, with a slab thickness of 2mm. The analysis comprised two parts: 1: SC was identified and, using surrounding collector channels and vascular landmarks, a single location was identified and measured by two observers in each of the three scans. SC cross-sectional area was measured independently at that location by the same two observers. Observers each subjectively manually adjusted contrast to optimize visualization of SC and made cross-sectional measurements as described in Chapter 3. Images were then closed without saving and re-opened, and an automated processing routine performed to adjust contrast. SC was then re-measured with the automatically processed images (code provided in Appendix 2). 2: A single observer measured all 31 sequential B-scans centered on the previously identified B-scan. Measurements were performed after automatic contrast enhancement.

5.2.3 Imaging of SC

SD-OCT (Cirrus HD-OCT; Carl Zeiss Meditec, Inc., Dublin, CA) was used to image SC. 512 x 1024 x 128 samples were acquired in a 4 x 2 x 4 mm volume of the limbus. The acquisition rate was 27,000 A-scans per second. Moving chin and forehead rests were used to center the eye in the image frame, and then verbal commands were used to position the desired region of the limbus in the image. Scan time was 2 seconds.

5.2.4 Image Processing and SC Visualization

Images were pre-processed with a 3x3x3 kernel-size averaging filter using software of our own design. For part 1 (subjective contrast enhancement), contrast and brightness were manually adjusted to optimize visualization of SC. Pre-processed images were then re-opened, and an automatic processing routine (provided in Appendix B) in which images were blurred and contrast enhanced using by local contrast enhancement by adaptive histogram filtering Fiji (ImageJ 1.45q, NIH, http:imagej.nih.gov/ij). A final manual adjustment of contrast and brightness was permitted. SC was manually circled as in the previous chapters, and area was measured.

5.2.5 Statistics

In part 1 (one measurement manually and automatically processed, analyzed by two observers), differences in area measurements between observers and automation were compared by analysis of variance (ANOVA). The coefficient of variability was calculated for each subject's set of 3 scans for each observer for both manual and automated image processing. In part 2, the coefficient of variation for the mean was calculated for each subject. Since each scan produced 32 area measurements, the quartiles for each scan were recorded, and coefficients of variability calculated for the quartiles.

5.3 RESULTS

5.3.1 Part 1: Observers and Automation

When contrast was adjusted manually, there was a statistically significant difference between SC cross-sectional area measurements between observers 1 and 2 (9,387±3,597μm^2 and 13,739±8,781μm^2 respectively; mean±SD, p=0.017). When contrast was adjusted automatically, the difference between SC cross-sectional area measurements was eliminated (9,296±3,908μm^2 and 9,845±4,333μm^2; p=0.615). Post-hoc analysis revealed that there was a significant difference in pooled SC cross-sectional area between manually and automated adjustment (p=0.0136), but when separated by observer, only observer 2 presented with a difference in cross-sectional area measurements between manually and automated processing (p=0.0017) while there was no difference between the two for observer 1 (p=0.8856). Interestingly, the coefficient of variability actually increased for both observers with automated contrast enhancement compared to manual adjustment (Table 5).

Table 5. Automated contrast enhancement increases measurement variability

	Manual Adjustment	**Automated Adjustment**
Observer 1	13.5%	17.6%
Observer 2	15.5%	19.5%

5.3.2 Part 2: 31 Samples per Image

When 31 samples of SC cross-sectional area were taken from each image (representing 1mm of circumferential arc length in SC) overall mean SC cross-sectional area was 4046±1055μm^2. The average coefficient of variability for the estimate of mean cross-sectional area across all subjects was 26.0%. The 25th, 50th, and 75th percentile measurements of SC cross-sectional area were 2911±965, 3901±1100, and 5048±1207μm^2 respectively. The coefficients of variability for the 25th, 50th, and 75th percentile measurements of SC cross-sectional area were 34.6%, 28.1%, and 24.0% respectively.

5.4 DISCUSSION

The data in the present study strongly suggest that the subjective identification of a location for measurement of SC cross-sectional area is highly biased toward unrepresentatively high values. The mean±SD and median±SD SC cross-sectional area measurements were 4046±1055μm^2 and 3901±1100 μm^2 respectively when a 1mm circumferential arc length of SC was sampled. When the observers identified an area for measurement from the slices within the 3D dataset based on the ability to locate the same position in each of the three scans within a subject, the means±SD for the two observers of those measurements were 9387±3597μm^2 and 13,739±8781μm^2 for manually adjusted contrast, and 9296±3908μm^2 and 9845±4333μm^2 with automated contrast adjustment. These estimates of cross-sectional area are ***more than two times larger*** than the either the mean or median estimates of SC size. Indeed, they are approximately twice as large as the 75th percentile value of 5048±1207μm^2! It appears that, despite the effort to locate a "representative" image of SC, observers will choose a region that represents an outlier with respect to actual SC cross-sectional area. This means that if the purpose of a study is to honestly estimate SC area, a 3D scan containing numerous samplings is necessary to avoid bias toward unrepresentatively high values.

Interestingly, the coefficients of variability in measurements of area decreased steadily as size increased. Note steady decline of coefficient of variability as quartiles increase with values of 34.6%, 28.1%, and 24.0%, respectively. Also, the coefficient of variability for the mean was 26.0%; similar to that of the median. This may be due to increasing ease of measurement of progressively larger and larger structures. The coefficient of variability of the subjectively located behemoth region of SC with an area twice that of the average had a scan to scan coefficient of variability of 13.5% and 15.5% for the two observers; scarcely larger than the 11.4% found for the measurement of identical images in Chapter 3. Indeed, these data support the ability to return to a single location of SC for non-invasive longitudinal quantification of cross-sectional area based on the subjective appearance and measurement agreement between three sequential scans; however, values for cross-sectional area for an average size of SC have an associated coefficient of variability of 26%, while measurements in regions that are unrepresentatively large have inherent variability of a more acceptable level. This creates a conundrum. If serial sections within a 3D scan volume are analyzed, the experiment will have greater sensitivity to the detection of change using measurements of larger cross-sectional areas;

perhaps using the 75th percentile value. However, these values may not be representative of SC overall. If an investigator anticipates that only the smallest regions of SC will be changed by an experimental perturbation, then the 25th percentile value may be the best parameter to use, but that change may be more difficult to detect since the 25th percentile value had an associated coefficient of variability of nearly 35%. If detection of ANY change is desired, regardless of location, then a single measurement at a user selected region is sufficient, as this will be most sensitive to detectable change by virtue of the much lower associated measurement variability of ~14%. These data are vital in the planning of an experiment, and an educated guess as to the location where change is expected is needed if anticipated measurement variability of less than 35% is desired.

It was also interesting that automation, while reducing differences between observers, increased measurement variability for both. It appears that subjective control of the appearance of the image improves performance as suggested by lower measurement variability. This brings into question the effects of various levels of image processing on SC cross-sectional area measurements. In Figure 13, a single histological image of SC from a human cadaveric eye is processed in two ways; the top emphasizing the difference between the tissue types near SC and the surrounding regions, and the bottom emphasizing the open spaces within the region of SC. The yellow outline demonstrates two different interpretations of SC cross-sectional area that could be made from this single histological slice.

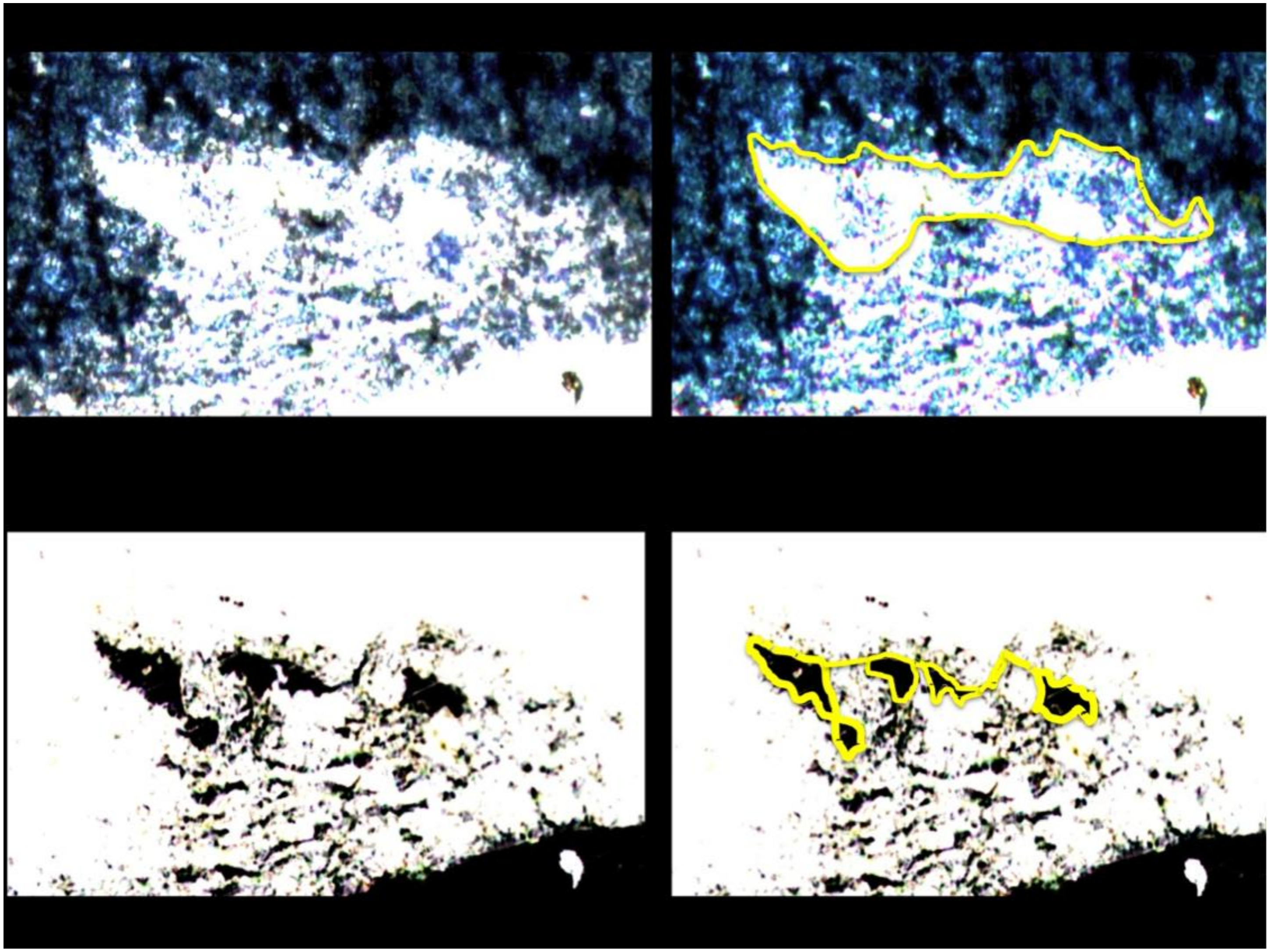

Figure 13. Processing of contrast alters the appearance of SC in a histological section

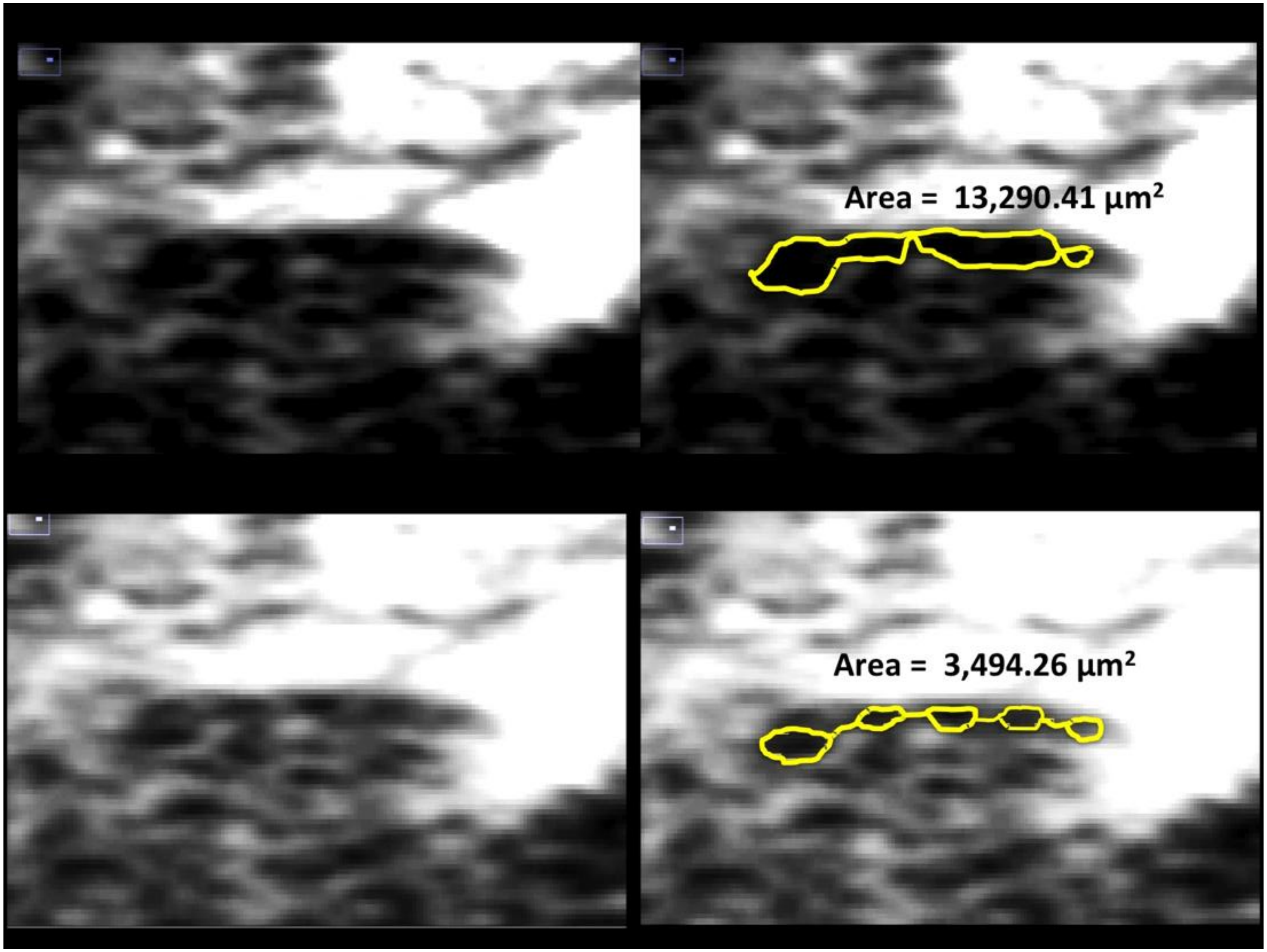

Figure 14. Processing of contrast alters the appearance of SC in a SD-OCT image

Similarly, the processing of OCT images can result in similar alternative interpretations. A single OCT image (Figure 14) has been processed in two ways; the upper emphasizing the region of SC, and the lower showing the open regions among the septa within SC. Note that the difference in processing results in an enormous difference in measured SC area; a difference of over 10,000 μm^2! As with the identification of measurement location discussed previously, defining the purpose of the measurement is necessary before designating an imaging strategy. If the purpose is to quantify the available empty space for the passage of aqueous humor, then the processing strategy on the bottom is appropriate. If the purpose is to assess the region of SC regardless of internal septa, the top processing strategy is appropriate. Based on previously published values of SC cross-sectional area, either the upper strategy has been employed previously, or the bias discussed above also plays a roll in histological studies.[155,149,156]

5.4.1 Conclusion

In conclusion, the best processing and analysis strategy for the measurement of SC cross-sectional area depends on goal of the investigation. The best strategy for a measurement with the lowest variability is a single assessment at a user-identified location, with the understanding that the result will be an area measurement that grossly over-estimates actual SC size. The most representative measurement is obtained by measuring a sequence of samples through a circumferential arc of SC, with the understanding that the variability will be twice that of the single measurement.

6.0 ELEVATED IOP REDUCES THE CROSS-SECTIONAL AREA OF SC IN HUMAN EYES

6.1 INTRODUCTION: CLINICAL USE OF SD-OCT SC IMAGES IN 2D

Glaucoma is the second leading cause of irreversible blindness worldwide.[159] The greatest risk factor for the presence and progression of glaucoma is elevated IOP.[50,51,57,160,161] The balance between aqueous humor production and outflow regulates IOP,[162-165] though the relationship between IOP and the morphology of the primary aqueous humor outflow pathways remains unclear.

It is known that that herniation of the inner wall of SC occurs with IOP elevation in a bovine eye perfusion model.[166,167] The precise effect of IOP elevation in the human eye on SC morphology remains unknown, though the animal model predicts that the inner wall will move into the SC space as IOP increases. In the previous chapter, the ability to assess SC cross-sectional area with sufficiently low measurement variability was demonstrated. The purpose of the present study was to observe SC morphology non-invasively in a human cadaveric eye perfusion model at two different levels of IOP.

6.2 METHODS

6.2.1 Ethical Consideration

Two human cadaver eyes with no history of eye disease, trauma or ocular surgery other than cataract were obtained from the Center for Organ Recovery and Education (Pittsburgh, PA). The Committee for Oversight of Research Involving the Dead of the University of Pittsburgh approved the study. Consent for the use of all tissues for research was obtained by the individual agency responsible for harvesting and supplying the tissue.

6.2.2 Tissue

The perfusion model and imaging technique have been described in detail previously.[150] Briefly, warmed eyes were placed in a custom-made fixation mount. Eyes were irrigated with 40°C saline to prevent dehydration and to minimize cooling during imaging. A 27-gauge needle was inserted into the peripheral cornea, with the needle tip passing through the pupil and positioned posterior to the iris and anterior to the lens. Barany's mock aqueous humor[165] was used to perfuse the eyes. After 20 minutes of perfusion for stabilization, the rate of perfusion was determined by recording the weight of the mock aqueous humor in a reservoir in real time. Immediately after completion of the perfusion experiments, the eyes were perfusion fixed with 10% formalin buffered solution before further processing for histological evaluation.

Eyes were perfused at 2 and 17 mmHg. Assuming a normal episcleral venous pressure of 8 mmHg in living eyes,[168] these perfusion pressures represent physiological IOP levels of 10 and 25 mmHg, representing the very low and high ends of the physiological range.[169-172]

6.2.3 SD-OCT Imaging

An SD-OCT optics engine (Bioptigen, Research Triangle, NC) was coupled with a high bandwidth superluminescent diode array (870nm center wavelength, 200nm bandwidth; model Q870, Superlum Ltd, Dublin, Ireland). This configuration provided a theoretical axial resolution of 1.3µm in tissue. The optics engine allows the user to specify any number of A-scans per frame, and any number of frames, limited only by system memory. It also allows the user to specify any number of sequential A-scans to be acquired in a single location during a raster scan for the purpose of averaging and Doppler assessment; also limited only by system memory. Each eye was scanned twice at the limbus, first at low perfusion pressure then at elevated perfusion pressure. Each set of images was comprised of 36 individual radial scan sets; three at each centered at each clock hour, and offset to the left and right. The angle of each set of clock hour scans was set so that the center clock hour scan was on a radial line from the center of the pupil (i.e. the 9 o'clock scan was at 0^o, the 10 o'clock scan at 30^o, the 11 o'clock scan at 60^o, etc.). The protocol consisted of 700 x 20 A-scans probing a 2x3mm area of tissue with 2mm slab depth. Each A-scan was repeated 18 times, and the average of those 18 scans recorded.

6.2.4 Image Processing

No pre-processing was necessary, as 12 sequential A-scans from each transverse location were averaged and the averaged data stored at the time of acquisition. Images were resampled to provide a 1:1 pixel aspect ratio in each frame; from 700 x 1024 to 1024 x 1024. The "Set Scale" tool was then used to set 1024 pixels to 2mm, allowing spatial measurements directly from the image. Contrast was adjusted to maximize visualization of SC. SC was traced by hand with the “freehand selection tool” and its area measured (Chapter 3, Figure 10). The line tool was used to measure SC length and height (Figure 15). Measurements were compared by paired t-test within each eye, with a p value of 0.05 or less considered significant.

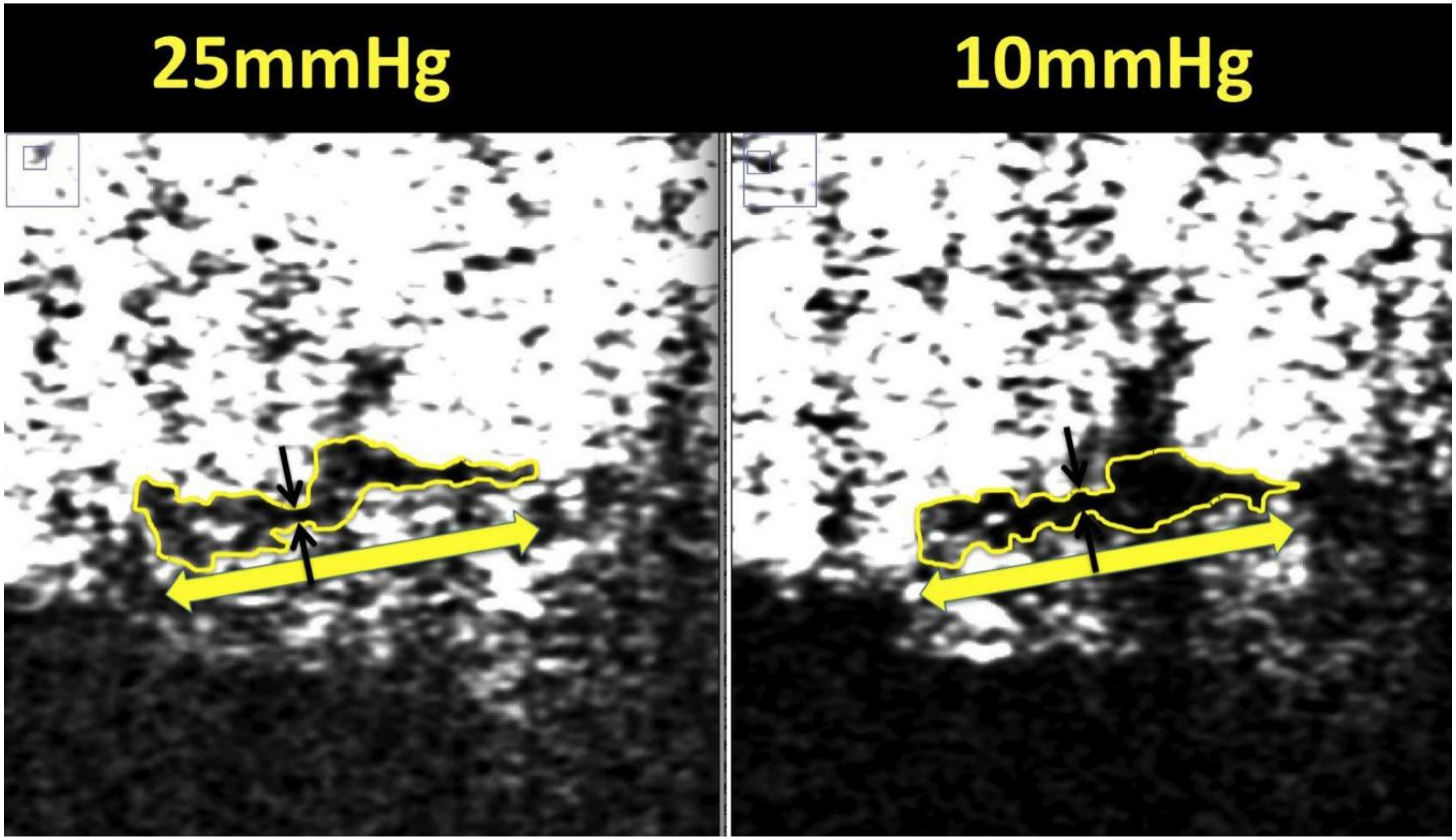

Figure 15 Schlemm's at 2 IOP levels and sample measurement locations

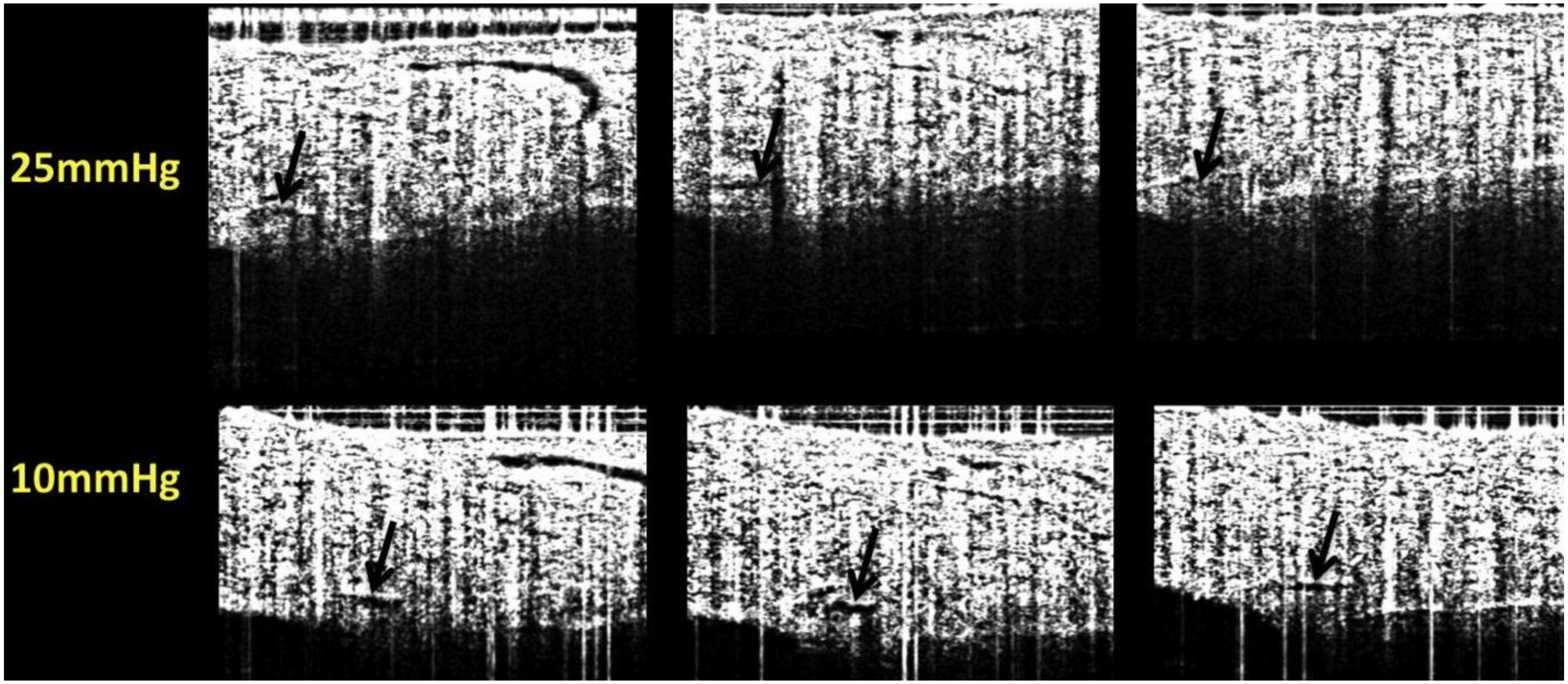

Figure 16. Three sequential frames at 2 IOP levels. Black arrow shows Schlemm’s canal

6.3 RESULTS

The right and left eyes (OD and OS respectively) had outflow rates of 1.76 and 0.16 µl/min at a perfusion pressure of 2 mmHg respectively. At 17 mmHg, right and left eye flow rates were 3.42 and 0.7 µl/min respectively (Table 6).

Fifteen paired locations were identified, 4 OD (10 o'clock) and 14 OS (at 4, 8, 9 and 10 o'clock). There was no significant change in the length of SC in either eye when measured at high and low perfusion pressures. SC height was statistically significantly reduced in the high perfusion pressure compared to the low perfusion pressure in both right and left eyes (p = 0.041 and 0.0014 respectively; Figures 15, 16). SC cross-sectional area was statistically significantly reduced in the higher perfusion pressure in the left eye (p = 0.0003) and reduced in the right eye (p = not significant). Measurements are provided in Table 6.

Table 6. Schlemm's canal height, length, and cross-sectional area at 2 IOP levels

Eye	Perfusion Pressure (mmHg)	Outflow Rate (µl/min)	Height Mean (SD) (µm)	Length Mean (SD) (µm)	Area Mean (SD) (μm^2)
OS	2	0.17	43.95 (13.95)	345.82 (67.91)	17291.82 (5456.87)
OS	17	0.6	27.96 (9.92)	344.51 (89.12)	14070.91 (4348.32)
OD	2	1.76	21.75 (7.73)	329.75 (70.01)	9266.50 (3809.60)
OD	17	3.42	14.75 (7.54)	323.00 (94.52)	5627.25 (891.82)

6.4 DISCUSSION

6.4.1 Summary of Findings

In this study, we found that IOP elevation decreases SC cross-sectional area and height. The thickness and cross-sectional area of SC were reduced with no change in SC length. Subjectively, IOP elevation was observed to displace the inner wall of SC anteriorly. These changes were readily observable in sequential slices (Figure 18). In the third panel of Figure 18, the IOP elevation pushes SC to near collapse. The impact of these morphological changes on outflow facility remains unknown.

6.4.2 Limitations

Under normal physiological conditions, there is approximately 8mmHg venous pressure. This may provide resistance to the IOP induced movement of the inner wall of SC that is not present in the cadaver flow model. It is possible that these findings may not be applied to living eyes. Imaging of SC in living eyes at baseline and increased IOP is ongoing.

In the present study, a representative location was subjectively identified and used for a measurement of SC height. The amorphous morphology of SC presented difficulties in determining a representative value for its thickness. In future studies, as automated analysis techniques are developed, it may be possible and beneficial to measure all SC thicknesses in sequential A-scans and use their mean as the representative thickness. In this study, the primary objective in selecting a measurement location was to use visible landmarks in SC to ensure that the same location was used at both pressure levels (Figures 15 and 16).

6.4.3 Conclusions

In conclusion, SC inner wall collapses with elevated IOP in human cadaveric eyes. These morphometric changes can be observed by SD-OCT. Volumetric scans are required to locate image pairs at single locations. These findings agree with the findings in the bovine perfusion model, and may describe the physiologic consequence of IOP elevation on outflow structure morphology.

7.0 THREE DIMENSIONAL VISUALIZATION OF AQUEOUS OUTFLOW SYSTEM MACROSTRUCTURES

7.1 INTRODUCTION: WHAT DO THE SMALL MOVING DOTS BETWEEN SD-OCT FRAMES REALLY REPRESENT?

Having established the abilities of SD-OCT to measure Doppler shifts, and to image outflow structures in cross-section, the next step toward clinical implementation of flow measurements is the establishing the morphology of the outflow structures. In Chapter 3, the connectivity between SC and the outflow vasculature in two-dimensional (2D) slices was introduced, but the 3D morphology of the vasculature distal to Schlemm's canal has yet to be demonstrated. In this chapter, advanced image processing is used to assemble 3D morphometric virtual castings from the 2D image stacks.

SD-OCT and ultrasound imaging of the anterior segment have produced cross-sectional images of the drainage system (Figure 17), but these do not yield sufficient visualization to ascertain the condition or density of the complex 3D structures of the aqueous humor outflow system.[149,173,174] In Figure 17, the anterior chamber angle is scanned by SD-OCT. Scans contain portions of the iris, cornea, and limbus (Figure 17A). Within the scan (Figure 17B) Schlemm's canal and aqueous veins, and the intrascleral venous plexus (ISVP) are seen.

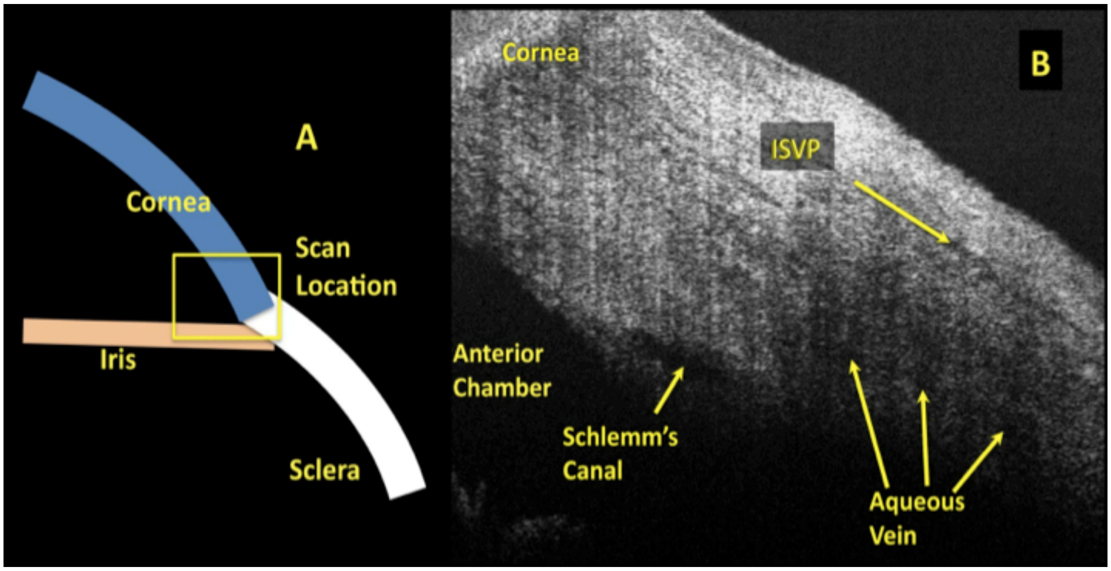

Figure 17. Scan orientation and structure identification in SD-OCT anterior segment scans

SD-OCT rapidly quantifies tissue reflectance in 3D cubes.[100,175] Coupling the high scanning speed with ultrahigh resolution, it is possible to visualize the individual components of the aqueous humor outflow system from the anterior chamber throughout the system of aqueous veins in the living human eye. [149] However, shadows from superficial structures may obscure the deeper structures.[149] Superficial outflow structures, specifically the ISVP and episcleral veins, are readily visualized by SD-OCT. The purpose of the present work was to develop a method for visualizing the 3D structures of the conventional aqueous humor outflow system in human cadaver eyes during perfusion with SD-OCT. After imaging, these same eyes were processed and examined by light microscopy for correlative histology.

7.2 METHODS

7.2.1 Ethics Considerations

Human cadaver eyes with no history of eye disease, trauma or ocular surgery other than cataract were obtained from the Florida Eye Bank (Miami, FL), and the Center for Organ Recovery and Education (Pittsburgh, PA). The Committee for Oversight of Research Involving the Dead of the University of Pittsburgh approved the study. Consent for the use of all tissues for research was obtained by the individual agency responsible for harvesting and supplying the tissue.

7.2.2 Tissue Preparation and Perfusion

To prepare for perfusion, seven eyes (Table 7) were wrapped in saline-soaked gauze, submerged in normal saline, and warmed to 34^0C.

Table 7. Perfusion conditions in cadaveric eyes

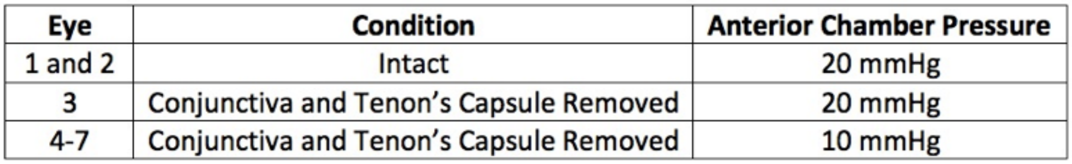

Eye	Condition	Anterior Chamber Pressure
1 and 2	Intact	20 mmHg
3	Conjunctiva and Tenon's Capsule Removed	20 mmHg
4-7	Conjunctiva and Tenon's Capsule Removed	10 mmHg

Eyes were then placed in front of the SD-OCT scanner in a custom-made fixation mount. Throughout the experiment, the eye was irrigated with 40^0C saline to prevent dehydration and to minimize cooling. A 27-gauge needle was inserted into the peripheral cornea, with the needle tip passing through the pupil and positioned posterior to the iris and anterior to the lens. This positioning prevented artificial deepening of the anterior chamber during perfusion and artifactual increases in outflow facility.[176] Barany's mock aqueous humor [165] was used to perfuse the eyes. The initial 20 minutes of perfusion was used to establish baseline outflow. The rate of perfusion was determined by recording the weight of the aqueous humor in the reservoir in real time, 20 measurements per second. Measurements were recorded by a 4-channel 10-bit digital acquisition system (DATAQ Instruments, Akron, OH). Immediately after completion of the perfusion experiments, the eyes were perfusion fixed with 10% formalin buffered solution before further processing for histological evaluation.

Perfusion pressure is the hydrostatic force between the anterior chamber pressure and the pressure within the vessels receiving aqueous humor outflow. In this study, a normal episcleral venous pressure of 8 mmHg in living eyes was assumed.[168] The first two intact eyes were perfused with an anterior chamber pressure of 20 mmHg. Since the episcleral venous pressure in a cadaver eye is approximately 0 mmHg, an anterior chamber pressure of 20 mmHg produced a perfusion pressure equivalent to an IOP of 28 mmHg in a living eye. An anterior chamber pressure of 10 mmHg yielded a perfusion pressure equivalent to an IOP of 18 mmHg in a living eye.

We previously established the ability to image the structures of the aqueous humor outflow system throughout.[149] In the cadaver model, there is no active circulatory system present to remove aqueous humor expelled from the outflow system. We found that fluid gradually accumulates in the conjunctiva and Tenon's capsule when that tissue was left intact on the globe (Figure 20), causing shadows obscuring visualization of outflow structures. Figure 20 shows the cross-sectional scan of the region of the limbus in a perfused eye reveals that the conjunctiva and Tenon's capsule engorge with mock aqueous humor. A section of the limbus is seen after being perfused for 5 minutes (Figure 18 left) and 60 minutes (Figure 18 right) showing thickening of the superficial tissue layers (black arrows).

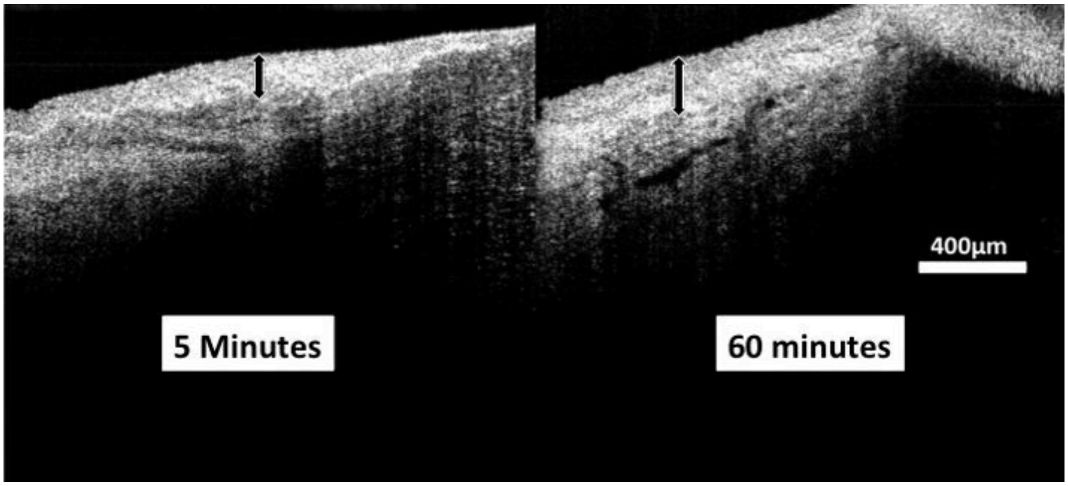

Figure 18. Mock aqueous thickens superficial tissue layers

Therefore, we found that cadaver eyes require the removal of these layers prior to perfusion to produce images of equal quality to those obtained in unperturbed living eyes. The conjunctiva and Tenon's capsule were dissected in all but the first set of eyes.

Four eyes were perfused and imaged at 10 mmHg, and then perfusion fixed at 10 mmHg for histology. One of these eyes was first imaged at a perfusion pressure of 0 mmHg. One eye was perfused and imaged at 20 mmHg. After imaging, it was perfusion fixed at 20 mmHg.

7.2.3 SD-OCT Imaging

An SD-OCT optics engine (Bioptigen, Research Triangle, NC) was coupled with a high bandwidth superluminescent diode array (870nm center wavelength, 200nm bandwidth; model Q870, Superlum Ltd, Dublin, Ireland). This configuration provided a theoretical axial resolution of 1.3µm in tissue. The optics engine allows the user to specify any number of A-scans per frame, and any number of frames, limited only by system memory. It also allows the user to specify any number of sequential a-scans to be acquired in a single location during a raster scan for the purpose of averaging and Doppler assessment; also limited only by system memory. Two scan protocols were created; one optimized for the acquisition of 3D data (the "volume" protocol) and one optimized for visualization of individual frames (the "2D slice" protocol). Each eye was scanned twice at the limbus, first with a protocol optimized for 3D volumes, and the second with a protocol optimized for visualization of 2D slices. Each set of images was comprised of 36 individual radial scan sets; each clock hour imaged at its center, and offset to the left and right. The angle of each set of clock hour scans was set so that the center clock hour scan was on a radial line from the center of the pupil (i.e. the 9 o'clock scan was at 0^0, the 10 o'clock scan at 30^0, the 11 o'clock scan at 60^0, etc.). The 3D volume scan protocol was limited by system memory, and consisted of 512x512 A-scans probing a 2x3 mm area of tissue (Figure 19 C and D). This scan protocol only moved the 20μm diameter SD-OCT beam 9μm between A-scans, thus including a single tissue volume in multiple adjacent samples (oversampling). Acquiring oversampled SD-OCT data allowed post-process averaging. The 2D slice protocol consisted of 700 x 20 A-scans probing a 2x3mm area of tissue. Each A-scan of the 2D slice imaging protocol was repeated 18 times, and the average of those 18 scans recorded (Figure 19 A and B). This method was previously described in detail.[177] Spectral domain optical coherence tomography images would normally be displayed with a low level of brightness (Figure 19A). In the case of highly averaged image data (700 A-scans in this frame; each A-scan the average of 18 sequentially acquired A-scans), brightness can be increased (Figure 19B) allowing visualization of deep low signal structures such as the iris, angle, trabecular meshwork, and endothelial /Descemet's complex without compromising due to visible noise. SD-OCT images obtained without averaging (512 A-scans, each presented without averaging) and displayed with a low level of brightness (Figure 19C) have an appearance similar to those obtained with averaging at the same noise suppression level. But, increasing brightness reveals the noise masking the deep layers where the signal is low (Figure 19D).

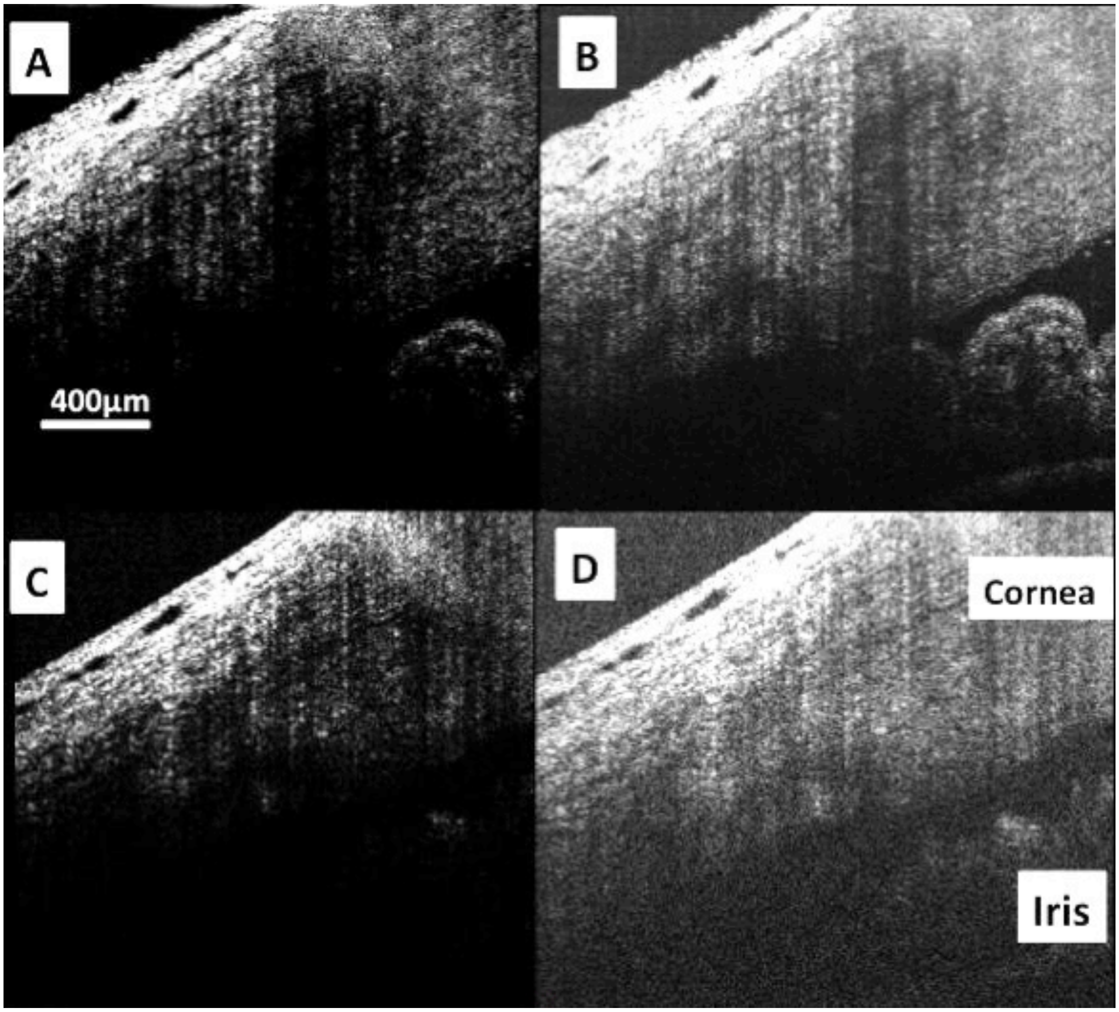

Figure 19. Contrast adjustment to improve visualization of outflow structures

7.2.4 Correlative Light Microscopy Imaging

After imaging using SD-OCT, two eyes were perfusion-fixed at 10 mmHg and one eye was perfusion fixed at 20mmHg. Following perfusion fixation, the three eyes were placed in 10% formalin buffered solution overnight and then transferred to PBS. The anterior chamber of each eye was cut radially into 12 pieces (1 clock hour each) and processed for light microscopic examination. The sections were post-fixed with 2% osmium tetroxide (Electron Microscopy Sciences, Hatfield, PA) in 1.5% potassium ferrocyanide (Fisher Scientific, NJ) for 2 hours, dehydrated in a graded series of ethanols, and embedded in Epon-Araldite (Electron Microscopy Sciences, Hatfield, PA). 3 µm sections were cut (4 blocks each eye at 3, 6, 9 and 12 o'clock) and stained with 1% Toluidine Blue (Fisher Scientific, NJ). Light micrographs were taken at an original magnification of 4X and 10X. The histological images were compared with SDOCT images from the same locations.

7.2.5 SD-OCT Image Processing

Raw SD-OCT scan data are analyzed by histogram. The 75% of SD-OCT data with the lowest reflectance values are set to 0 when displayed.[178] This approach is effective for the subjective improvement of visualization of highly reflective structures, but if the structures are in a region of low signal strength, they will not be displayed. In the slice image set, averaging during image acquisition improved visualization of structures with low reflectance. Increasing image brightness in highly averaged image data further improves visualization of the deep outflow structures (Figure 19). However, in the volume image data set, raw data acquired from deep outflow structures were difficult to visualize. Increasing image brightness increases visualization of deep low-reflectance structures, but also increases the appearance of speckle noise, obscuring structure details (Figure 19). This can be overcome by post-processing averaging. The volume image protocol spatially oversamples the tissue, allowing averaging with minimal loss of structural information. A floating 5x5 pixel transverse kernel, consisting of 5 pixels in each of 5 adjacent frames, was used to produce an average dataset, using customized software of our own design (Appendix A, Figure 20). Visualization of deep layers within the post-processing averaged volume dataset was comparable to that of the slice data (Figures 20 and 19B).

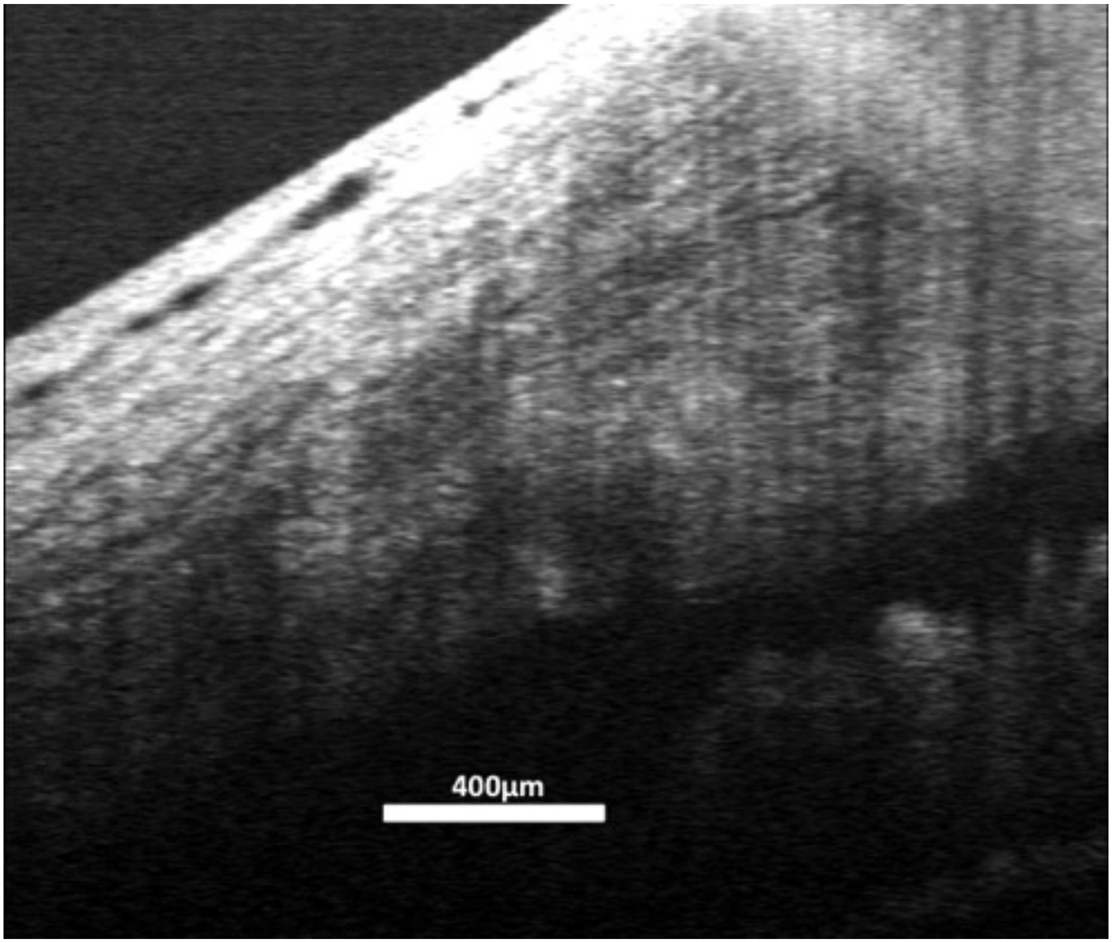

Figure 20, Averaging the 3D volume increases visualization

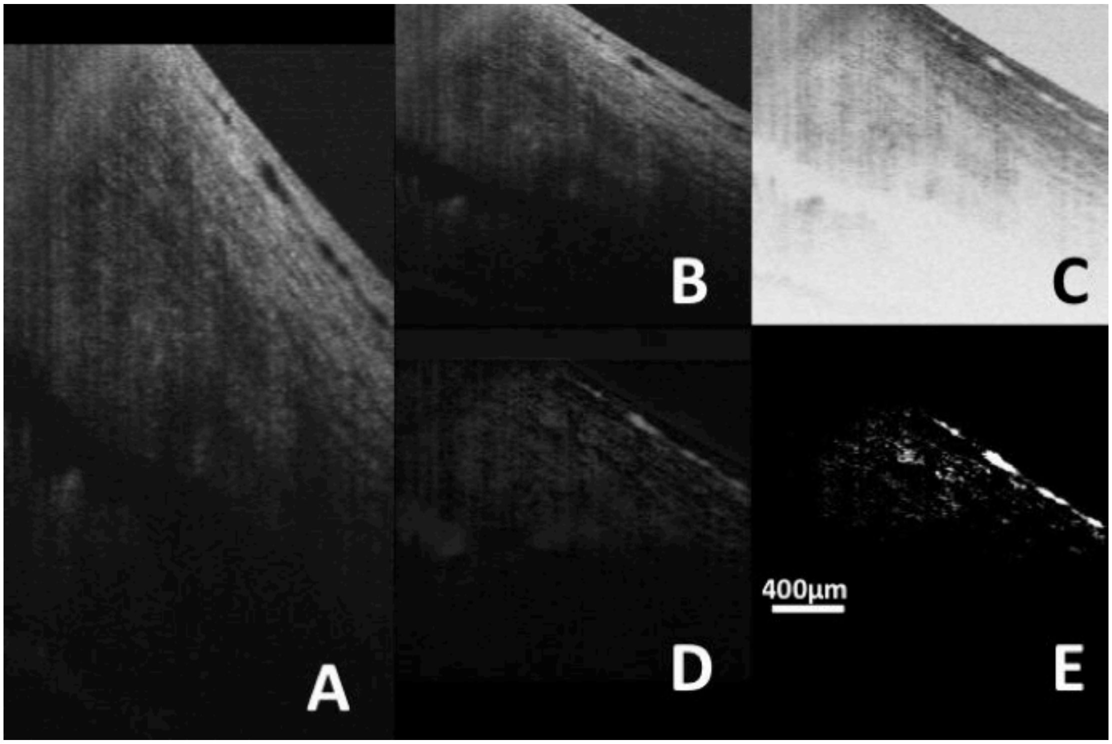

Figure 21. Image processing steps to isolate the ISVP

Further image processing was performed using ImageJ 64 (ImageJ 1.40g, http://rsb.info.nih.gov/ij/). Images were resampled to provide a 1:1:1 voxel aspect ratio in three dimensions; from 512 x 512 x 1024 (Figure 21A) to 342 x 512 x 342 (Figure 21B) for each 2x3x2mm volume. Images were then inverted so that the black collector channels appeared as white structures (Figure 21C). The ImageJ "subtract background" filter was applied with a 30 pixel kernel and without further averaging (Figure 21D). Contrast was then adjusted to isolate the collector channels (Figure 21E), and the volumes rendered using the ImageJ 64 3D viewer plug-in (Figure 22). The isolated intrascleral venous plexus image data was rendered in 3D to visualize the ISVP during active outflow. Figure 22 shows one of 36 circumferential scans of the limbus, featuring a portion of the venous network. The red marker on the right indicates the X, Y, and Z axes of the 3D space, with the interrogating SD-OCT beam projecting down the Z-axis, and raster scanning the X-Y plane.

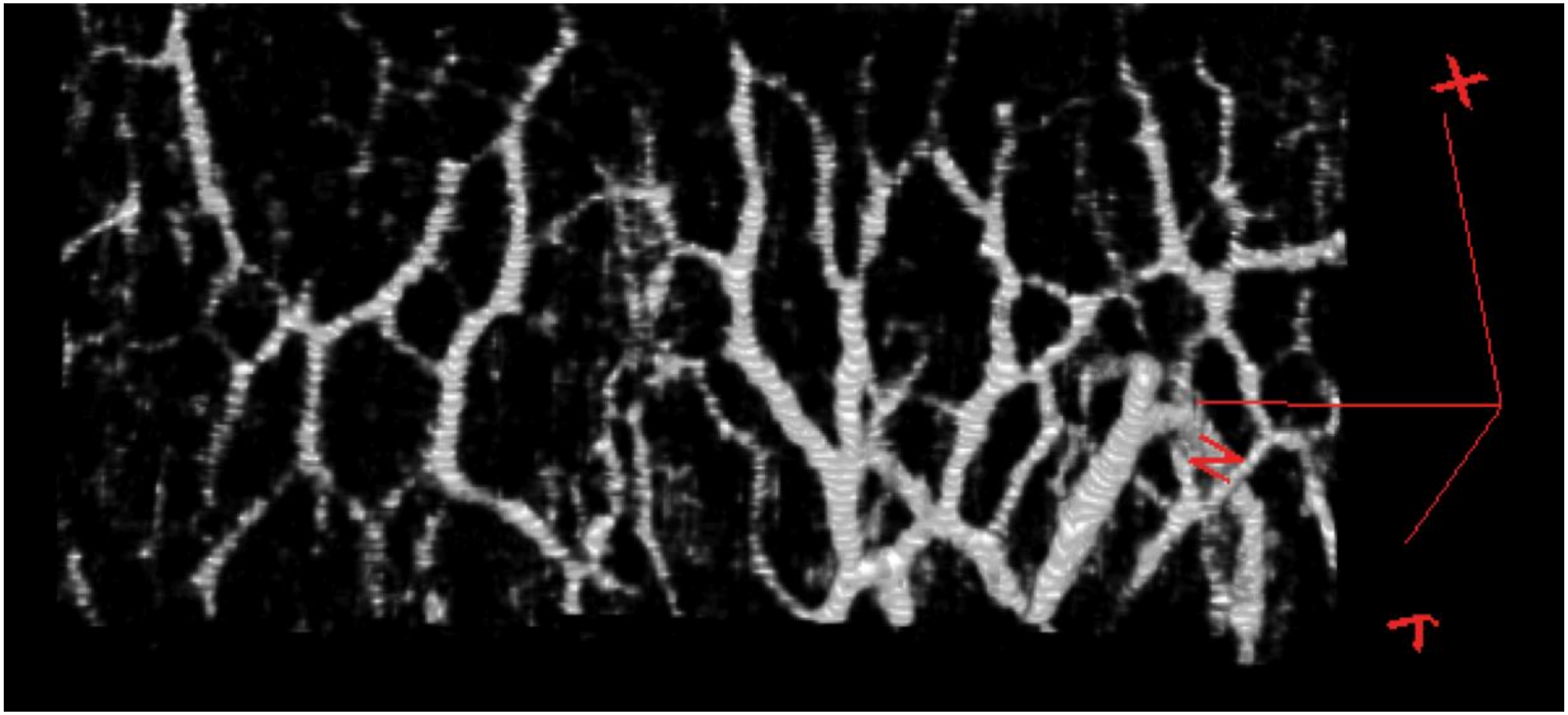

Figure 22. The ISVP rendered in 3D

Individual stacks were opened in Amira 4.1 (Visage Imaging Inc., San Diego, CA) and rendered in 3D space with the Voltex module (2D texture, rendering down sample 3,3,3). Stacks were manually assembled in 3D space by overlaying aqueous veins and structures visible in adjacent scans. The volume scan protocol provided a large degree of overlap; most individual aqueous veins were contained in two images, and occasionally in three.

7.3 RESULTS

7.3.1 Subjective Observations

Outflow structures from the TM through the CC could be visualized throughout the limbus. The slice imaging protocol provided better visualization of outflow structures in cross-section, likely due to the combined effects of spatial oversampling (700 A-scans per frame) and aggressive averaging (18 sequentially acquired A-scans averaged to produce each displayed A-scan; Figure 19B). Unfortunately, scanner memory restrictions limit the number of frames that can be acquired using this protocol. The low number of frames makes the slice protocol unsuitable for enface imaging or 3D reconstructions. The volume imaging protocol provides excellent enface images, and post-processing averaging allows the recovery of detail within deep structures (Figure 20). The sampling density of the volume protocol also allows high-resolution 3D reconstruction of the outflow system within individual scans (Figure 22).

7.3.2 Effect of Pressure

It has been shown that exposure to elevated IOP may lead to closure of SC as the TM pushes and compresses the inner wall towards the outer wall.[166] At 20 mmHg perfusion pressure, SD-OCT revealed very few locations with a visible patent SC. This finding was confirmed by histology. Figure 23 shows a histological section from the 6:00 position in an eye perfused at 20 mmHg, which presents with an open ostium (Figure 23A-1) despite the anterior surface of the trabecular meshwork compressing SC (Figure 23A-2). Vessels of the ISVP are visible (Figure 23A-3). The same eye at the 9:00 position also presents with a compressed SC, but no visible ISVP vasculature (Figure 23B). A different eye perfused at only 10 mmHg presents with a large open SC at the 9:00 position (Figure 23C-4). At the 12:00 position, SC ISVP vessels are present (Figure 23D-5), as are SC and open ostia (Figure 23D-6).

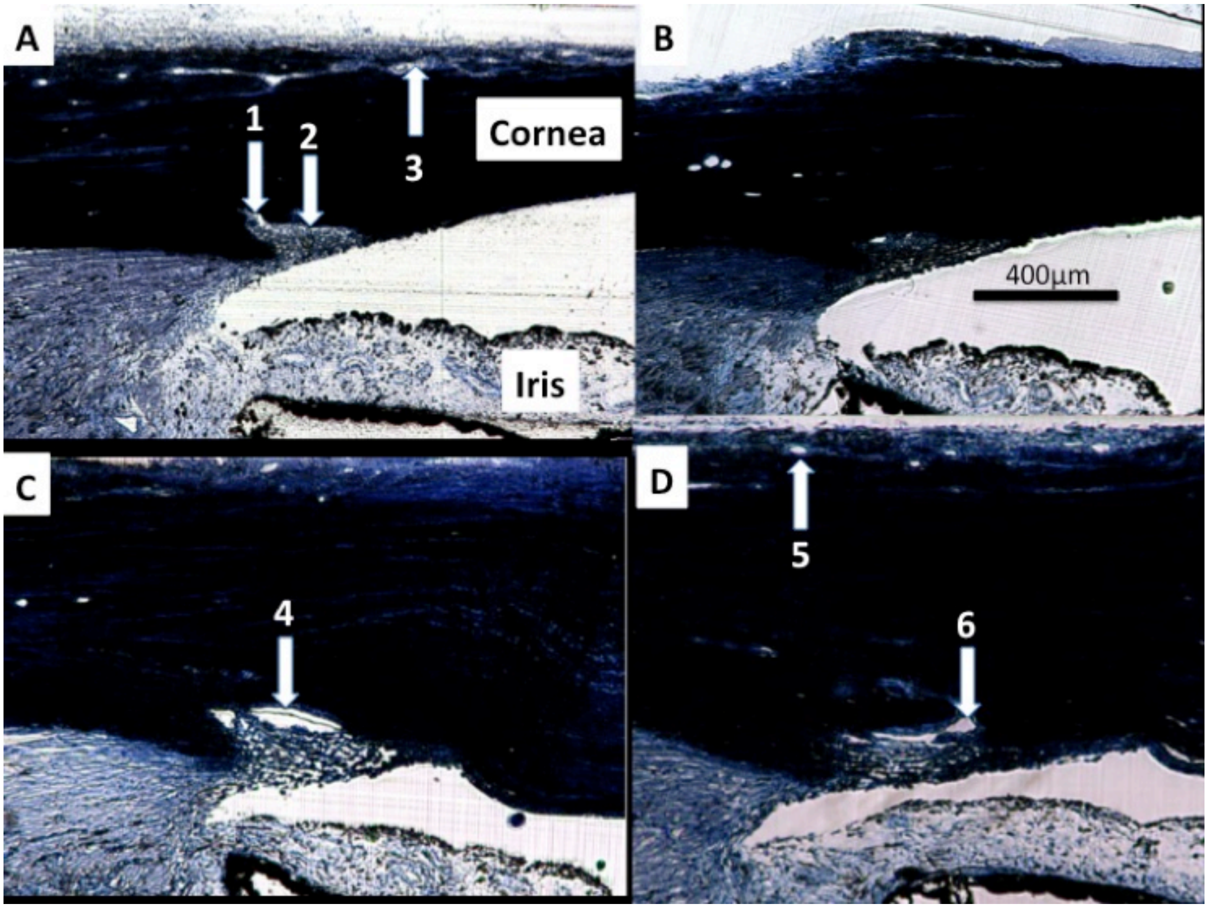

Figure 23. Effects of pressure on SC morphology

Collector channel ostia and patent aqueous venous structures were observed by SDOCT and confirmed by histology (Figure 23). At 10 mmHg, SC was not compressed (Figure 23). Smaller scleral veins running from the ISVP down toward the deep scleral venous plexus were frequently observed in individual frames of the 3D datasets, but seldom achieved sufficient contrast, relative to background tissue, to be observed in the 3D reconstructions. Occasionally, a large aqueous vein could be observed, but only when isolated from other branches of the ISVP. Figure 24A shows the front and side views of a scan obtained from one eye. Note the vessels that penetrate perpendicular to the ISVP. A histological section from the 6:00 position in an eye perfused at 20 mmHg can be rotated (Figure 24B) to expose the posterior surface (Figure 24C) revealing two aqueous veins. (white arrows)

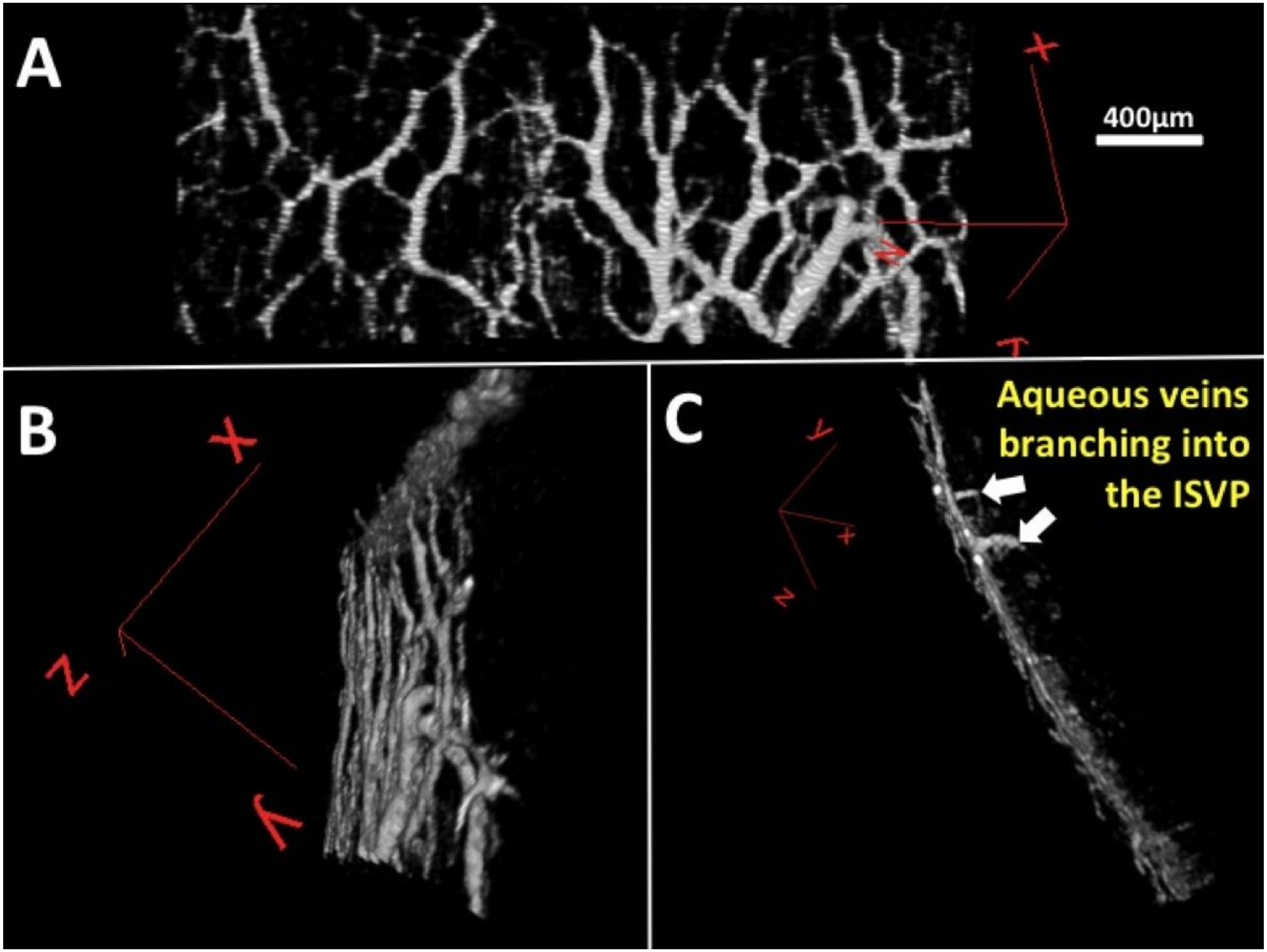

Figure 24. ISVP feeder vessels

7.3.3 Composite 3D Casting of the Outflow System

After individually processing the 36 scans of the limbus of the structural imaging protocol a composite casting of the collector channels of the aqueous humor outflow system was rendered (Figure 27). The densest arrays of aqueous veins within the ISVP were observed near the 6 and 12 o'clock positions. In Figure 27, 36 circumferential limbal scans were processed and assembled manually in 3D space to yield a full casting of the episcleral and intrascleral venous plexus throughout the limbus in-situ during active perfusion.

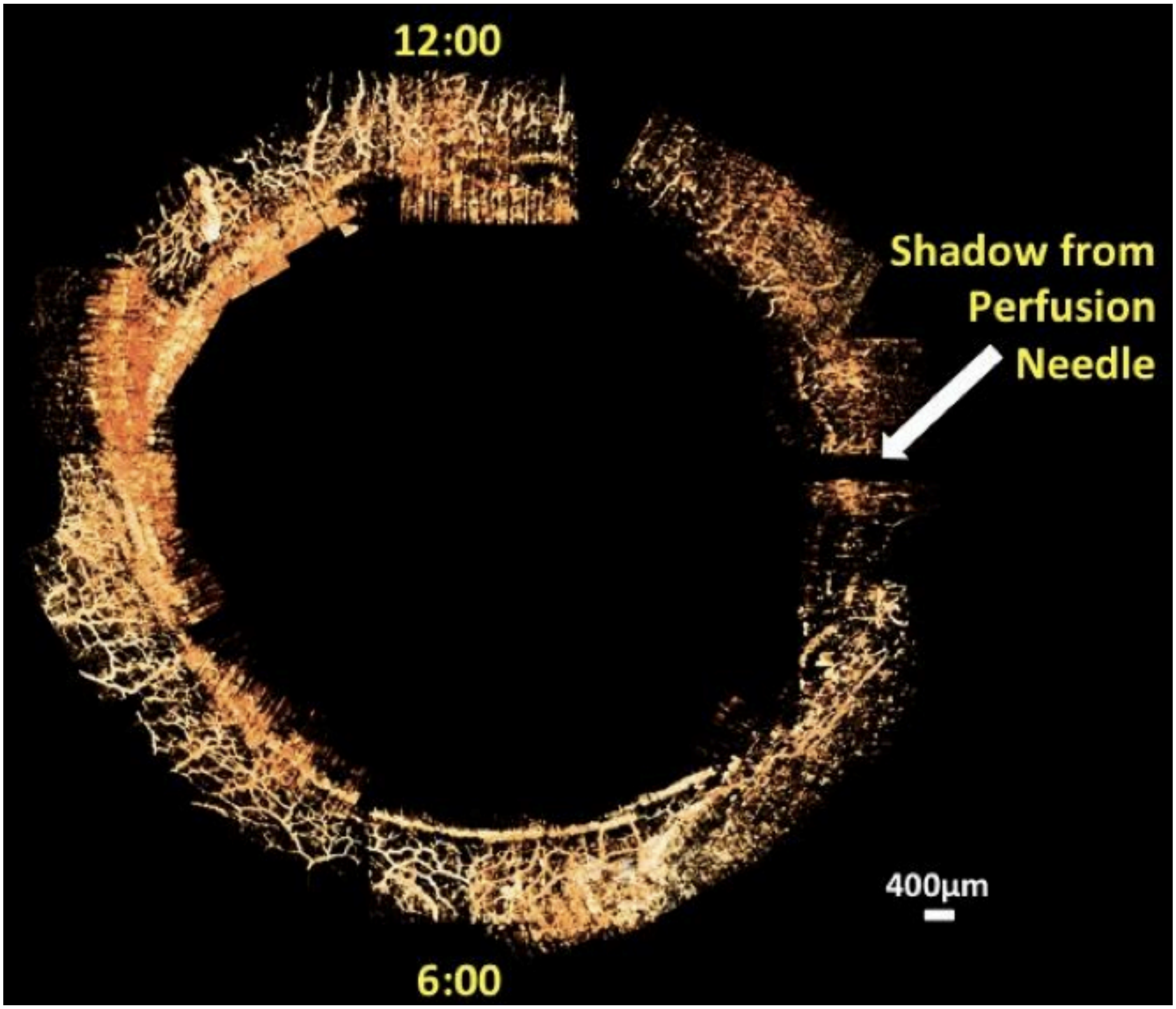

Figure 25. Circumferential virtual casting of the outflow system

7.4 DISCUSSION

7.4.1 Summary of Findings

We present the first virtual casting of superficial venous plexus of aqueous humor outflow system. The imaging process is completely non-contact and requiring no dyes or contrast agents. In living human eyes, the imaging process is completely non-invasive. In the cadaver model, the conjunctiva and Tenon's capsule must be removed to produce images of similar quality as those produced in living eyes. Virtual casting was made possible by the high degree of contrast between the superficial venous plexus of aqueous humor outflow system (including aqueous veins) and surrounding tissues achieved by aggressive post-processing averaging.

There was good agreement between features observed in the SD-OCT 2D scans and the corresponding histological sections (Figure 23). This included the appearance of SC under different perfusion pressure conditions as well as the presence or absence of the open superficial vessels comprising the ISVP.

7.4.2 Differences between In-Vitro and In-Vivo Conditions

A cadaver eye, as used in this experiment, differs from a living eye. Specifically, the cadaver eye lacks circulatory-related pulsations in IOP and blinking which each may contribute force to outflow.[179] The change from a pulsatile to non-pulsatile environment may alter the conditions dictating the preferential location of outflow within the eye. There is also a lack of pulsatility in the vessels receiving aqueous humor. In the living eye, scleral veins receive aqueous humor in an environment of transient pressure waves. In the cadaver eye, aqueous humor arrived in vessels with no backpressure. During perfusion, the vessels were observed to fill with aqueous humor, resulting in some small constant backpressure. Combined with gravity, it is possible that the preferential outflow path in a cadaver model differs significantly from that of a living eye. But, if gravity were the only influence, we would have expected full aqueous vessels in the inferior with a gradual diminution of the casting until it appeared empty in the superior. The present study found the fullest ISVP castings in the superior and inferior quadrants. Previously, we reported that in living human eyes, SC near CC ostia appeared to be larger in the nasal quadrant of the limbus, thought only the lateral quadrants were measured in that study.[149]

Our initial data indicated that the conjunctiva and Tenon's capsule needed to be removed before perfusion in order to image the deep layers of the limbus with quality equal to that obtained in living human eyes and avoid distention of the outer tissue layers as they filled with aqueous humor. It is likely that the superficial-most vessels of the outflow system were also removed. In the remaining tissues, it is impossible to determine what percentage, if any, of the virtual casting consisted of ISVP or the midlimbal intrascleral plexus, or some combination therein. Interconnectivity was observed within the vascular network. The lack of blood flow supports the contention that the casting is of active aqueous humor outflow, though the identity of the actual observed vessels, whether aqueous vessels or venules, can only be inferred by their location and connectivity. We are confident that some portion of the castings consisted of aqueous veins, as those portions were observed to penetrate into the limbus (Figure 26) and could be seen in individual frames extending directly to SC ostia. Nevertheless, since there was no active cardiac circulation in the imaged tissues, all passages captured in the casting were open and connected because they were carrying mock aqueous humor as part of the outflow process.

It would be desirable to have a complete casting of the outflow system, down to SC. A recent study produced virtual castings of the outflow system at the level of SC in sections of a stained eye using micro CT.[180] In the present method, only the superficial venous plexus or occasional large penetrating aqueous veins could be optically isolated from surrounding tissues, though this was accomplished non-invasively and without introduction of any contrast agents. It is possible that a more sophisticated image processing technique could include more structures in the casting. Specifically, imposing a connectivity requirement for inclusion in the casting might reduce the use of contrast for isolation and allow the smaller structures to be included despite weak signal levels.

As we continue to develop the ability to image aqueous humor outflow as it occurs, our goals is to be able to detect deficits associated with disease, and determine the effects of glaucoma medications and surgical interventions on outflow and the associated structures. Currently the two largest impediments to clinical implementation are penetration and eye movements. The structural and functional scan protocols used in this study required approximately 10 seconds each, with a data acquisition rate of 28,000 A-scans per second. This is far too slow to obtain useful data in human eyes, as eye movement artifacts are readily visible in the typical ~2 second scans obtained with commercially available SD-OCT's. However, "cutting edge" SD-OCT systems have achieved a scan rate of 1.37 million A-scans per second, which would reduce the scan time to 0.1 seconds.[175] Longer wavelength systems may overcome current limitations in penetration, but despite the limits of the 870nm centered system, using aggressive averaging we are able to resolve the structures of the angle and conventional outflow system (Figures 19 and 20).

Clinical and research use will require the development of meaningful parameters that quantify outflow structures. The outflow structures are too numerous and dense, and with marked regional variation, to arbitrarily choose individual CC's to represent outflow. Assessment of the outflow venous network will involve an automated quantification of aqueous vein density and the distribution of vein sizes. Quantification of the number of branch points may also have some clinical meaning. Ultimate utility will depend on determination of how each of these potential parameters is affected by the presence of glaucoma.

7.4.3 Conclusions

In conclusion, we present the first virtual casting of aqueous humor outflow structures obtained non-invasively in-situ ex-vivo. Continued development of this technique may lead to clinically useful direct assessment of outflow in patients with glaucoma.

8.0 REPRODUCIBILITY OF 3D VIRTUAL CASTING OF THE AQUEOUS HUMOR OUTFLOW SYSTEM IN THE LIVING HUMAN EYE

8.1 INTRODUCTION

In chapter 7, the ability to create virtual castings of the outflow system was demonstrated in cadaveric eyes. This suggests that enhanced processing of structure images may be useful in the living human eye for the mapping and study of outflow structures, and the possible measurement of Doppler signals within. But, the utility of these measurements requires that they identify and display structures in a consistent and reproducible manner.

There is a SD-OCT scanner in clinical use equipped for anterior segment scanning, including an FDA approved protocol for volumetric scans of the limbus. Transition of this technology to clinical use will be accelerated if it can be accomplished with existing clinical equipment. The purpose of the present study was to determine if the same structures can be cast in sequential volumetric scans of the human limbus with a clinically used SD-OCT platform.

8.2 METHODS

8.2.1 Ethical Considerations

The study was conducted in accordance with the tenets of the Declaration of Helsinki and the Health Insurance Portability and Accountability Act. The institutional review board of the University of Pittsburgh approved the study. All subjects before participation gave written informed consent.

8.2.2 Study Design

Ten healthy volunteers were recruited from the staff and faculty of the UPMC Eye Center. SD-OCT images of the limbus were obtained from the nasal quadrant of the right eye in three sequential scans at a single visit. In the previous chapter, unobstructed visualization of outflow vessels was limited in the lateral quadrants, however constraints of the scanner limit scans to the nasal and temporal quadrants. It was likely that vessel isolation would not be possible in all subjects. Images were 4x4mm, with a slab thickness of 2mm. Two independent observers created 3D virtual casts of visible outflow structures. Structural features were subjectively compared, specifically to determine if the same features could be identified in multiple scans of the same region.

8.2.3 Imaging of SC

SD-OCT (Cirrus HD-OCT; Carl Zeiss Meditec, Inc., Dublin, CA) was used image SC. 512 x 1024 x 128 samples were acquired in a 4 x 2 x 4 mm volume of the limbus. The acquisition rate was 27,000 A-scans per second. Moving chin and forehead rests were used to center the eye in the image frame, and then verbal commands were used to position the desired region of the limbus in the image. Scan time was 2 seconds.

8.2.4 Image Processing and SC Visualization

Images were pre-processed with a 3x3x3 kernel-size averaging filter using software of our own design (Appendix A). Pre-processed images filtered with an automatic processing routine in which images were blurred and contrast enhanced using by local contrast enhancement by adaptive histogram filtering, and then background was subtracted; all in Fiji (ImageJ 1.45q, NIH, http:imagej.nih.gov/ij). A final manual adjustment of contrast and brightness was made to isolate outflow structures and minimize noise.

8.2.5 Statistics

The image data created in this study did not produce numerical data. 3D casts were subjectively examined to determine if the same structures could be identified in all casts. The frequency of success is reported.

8.3 RESULTS

Two observers produced the virtual outflow vascular casts in the 10 Figures below. The top rows are all casts from the first observer, and the bottom row those of the second observer. Each row features three casts from each of the three sequential scan volumes obtained. The differences observed in texture result from personal differences in the observer's technique regarding the best way to manually adjust the contrast in the final step. Figure 28 demonstrates the various levels of vessel visibility achieved with varying levels of noise reduction via contrast enhancement. While the upper left panel of Figure 28 most cleanly isolated the observable vasculature, the lower center panel presents a casting containing a wider range of gray scale, producing a more textured casting with more complete vasculature network. In all Figures except 30 and 32, arrows mark identifiable vascular structures that are both consistently visible throughout the three castings of the subject, and found by two independent observers. As discussed in the previous chapter and methods, the nasal and temporal quadrants tend to present with more noise and obscured visualization of the vessels. In this cohort, two of the subjects, shown in Figures 30 and 32, failed to present with prominent vasculature.

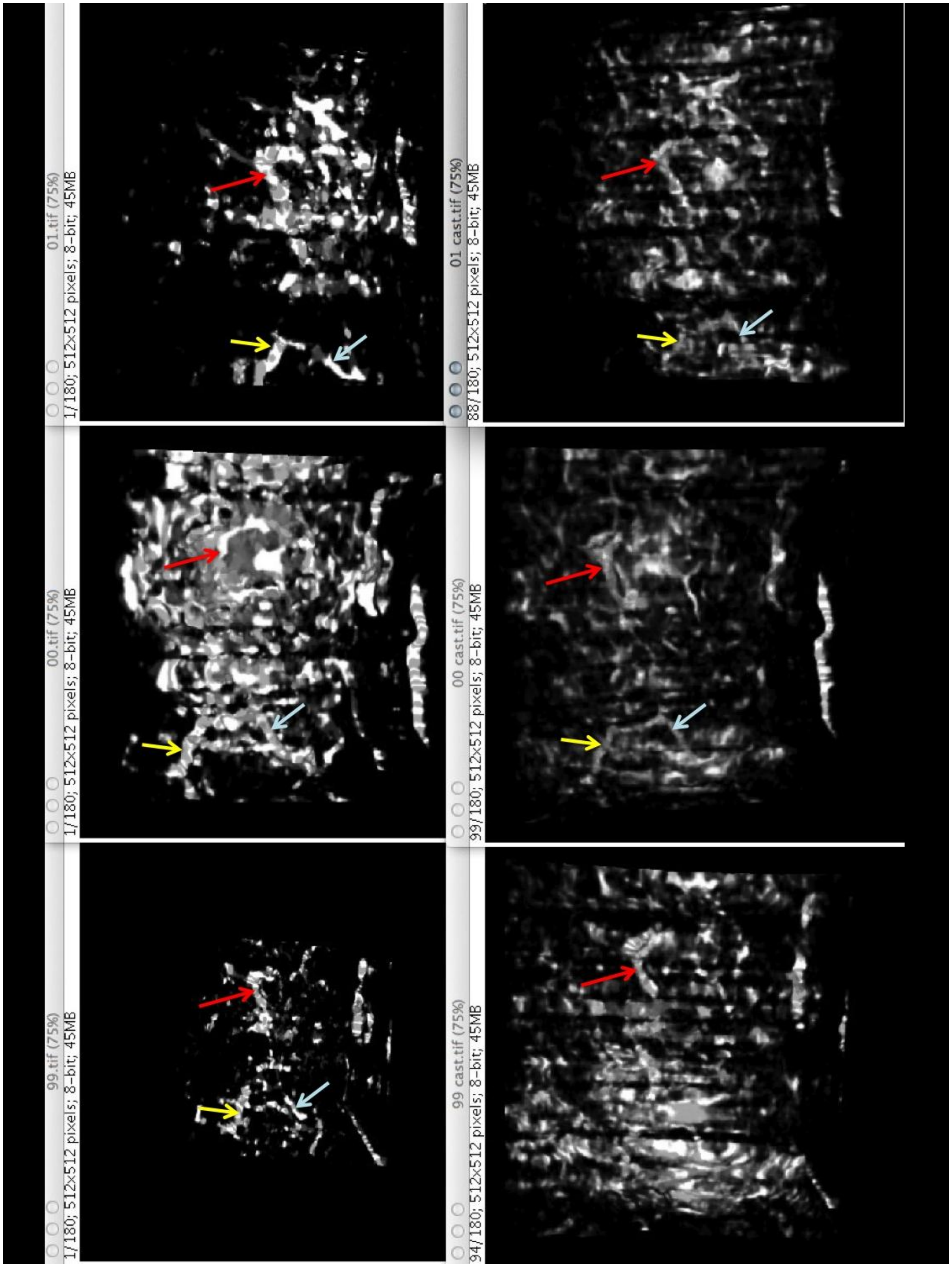

Figure 26. Reproducibility subject 1

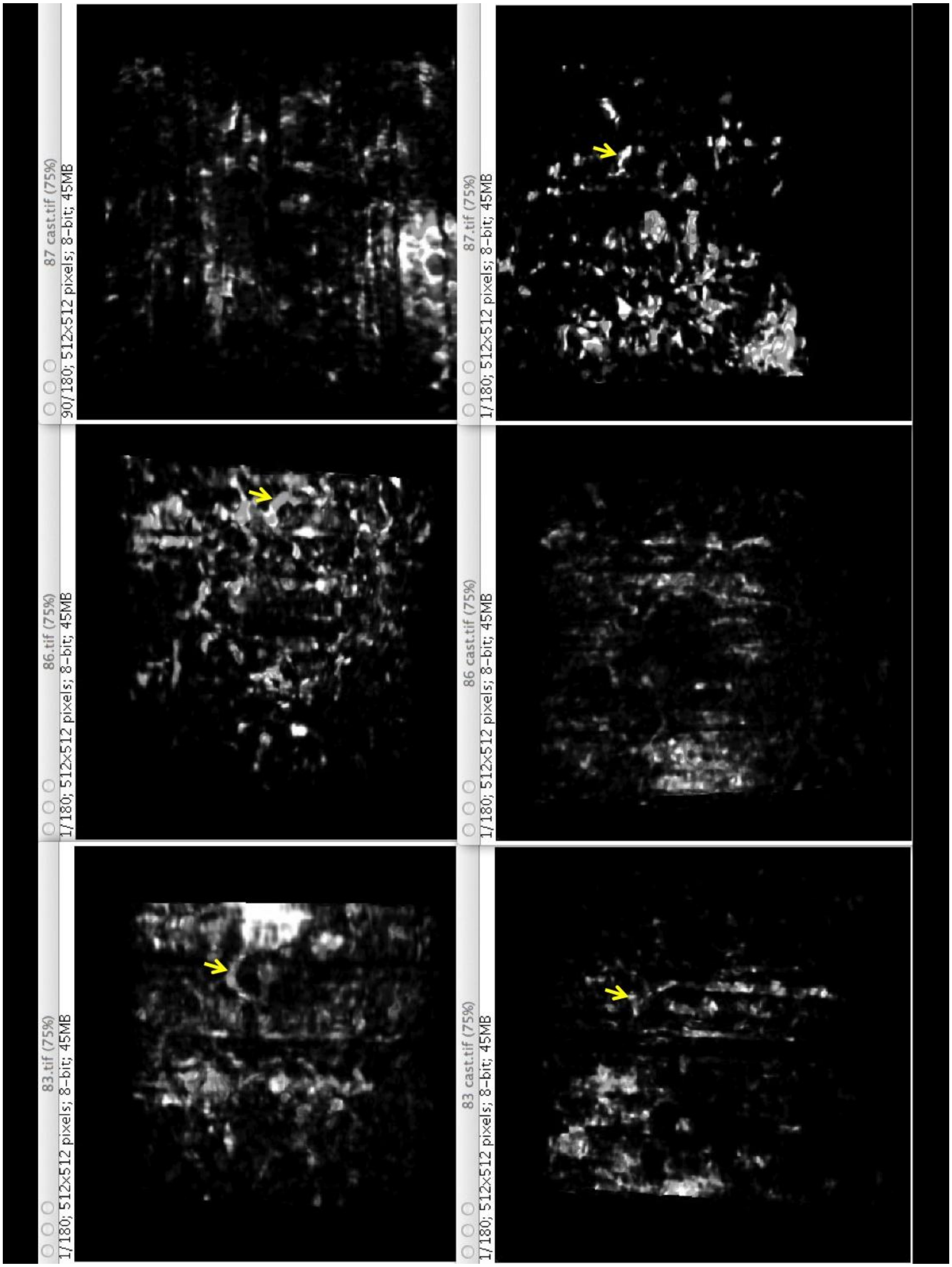

Figure 27. Reproducibility subject 2

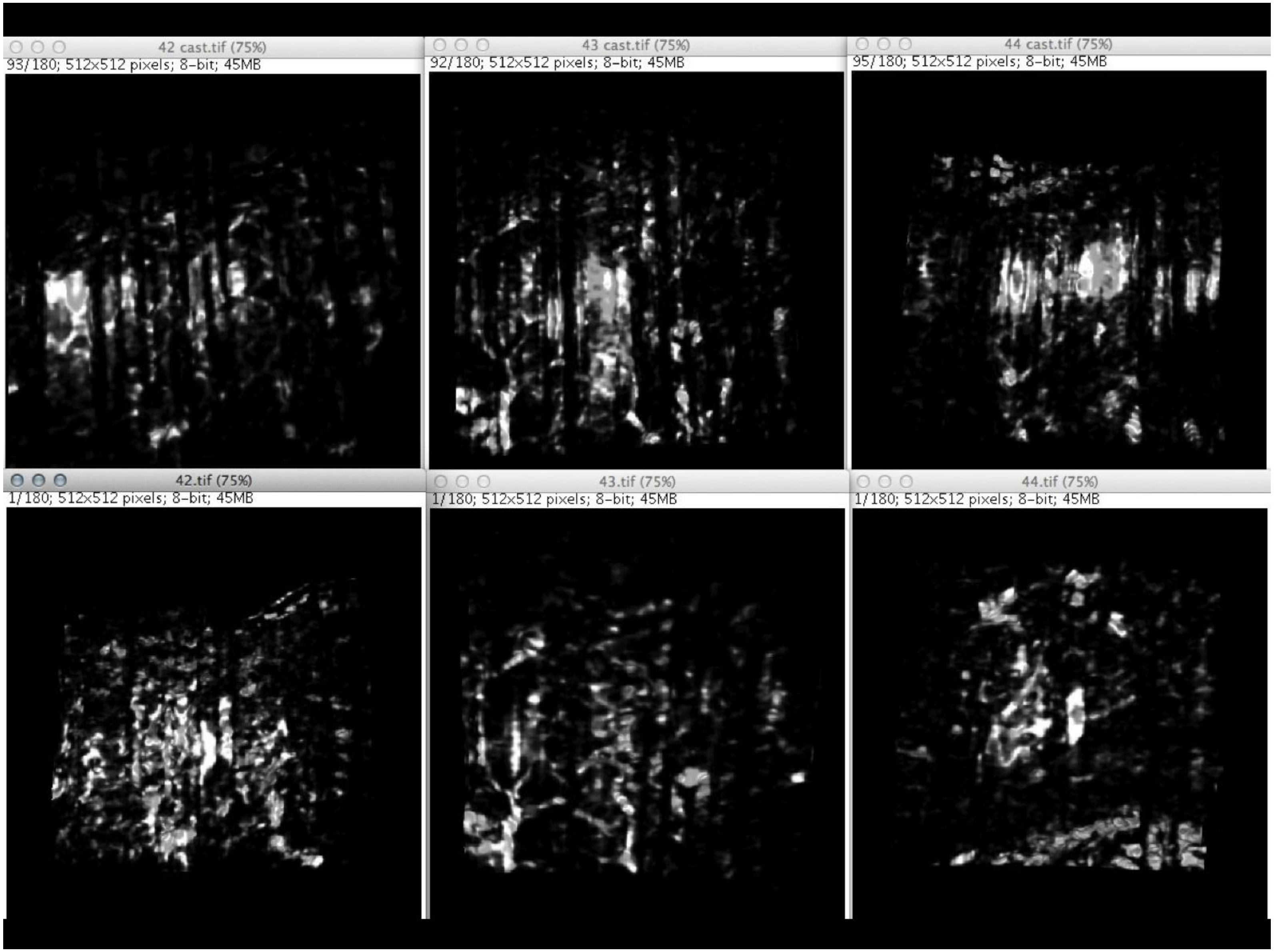

Figure 28. Reproducibility subject 3

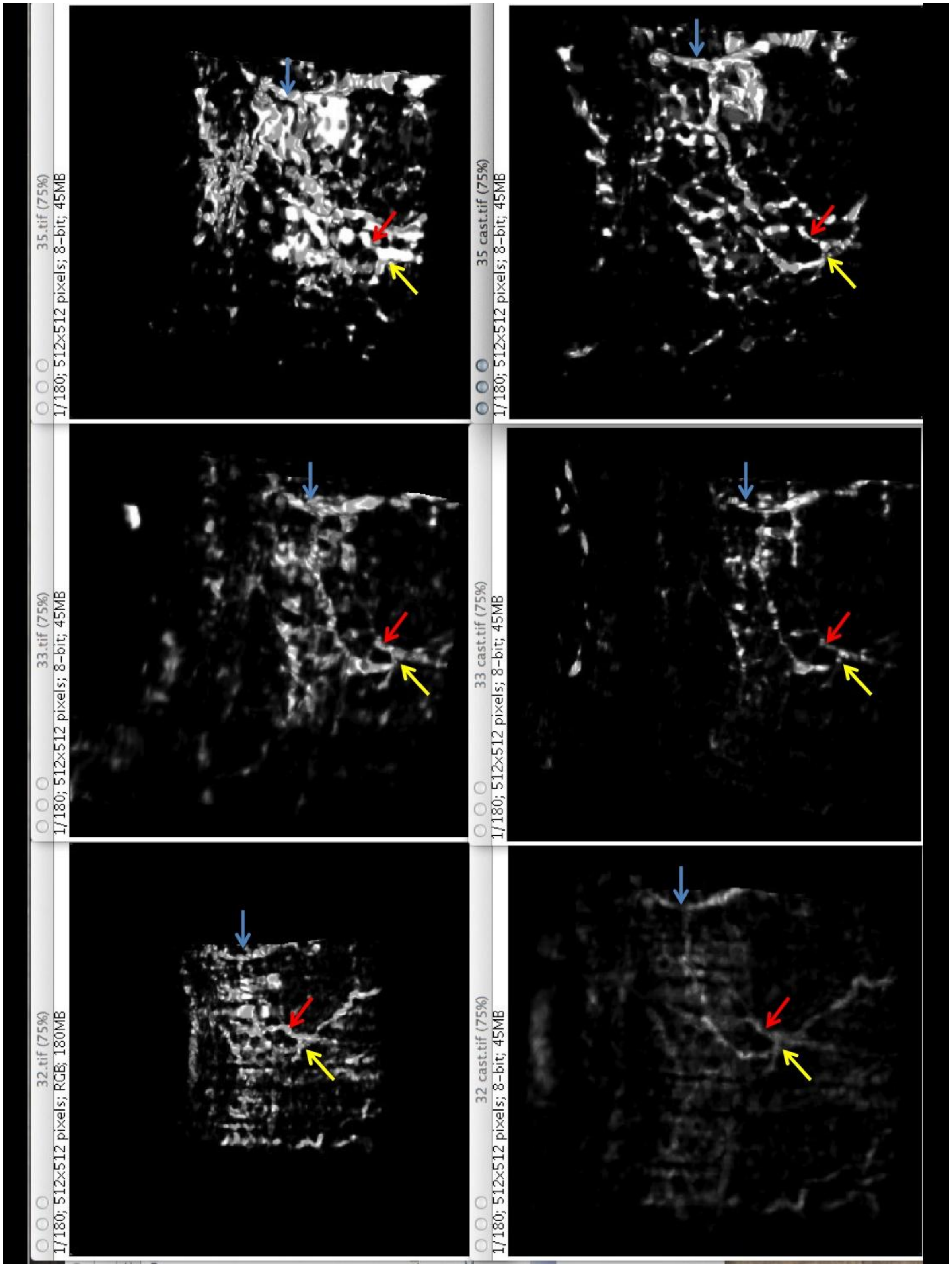

Figure 29. Reproducibility subject 4

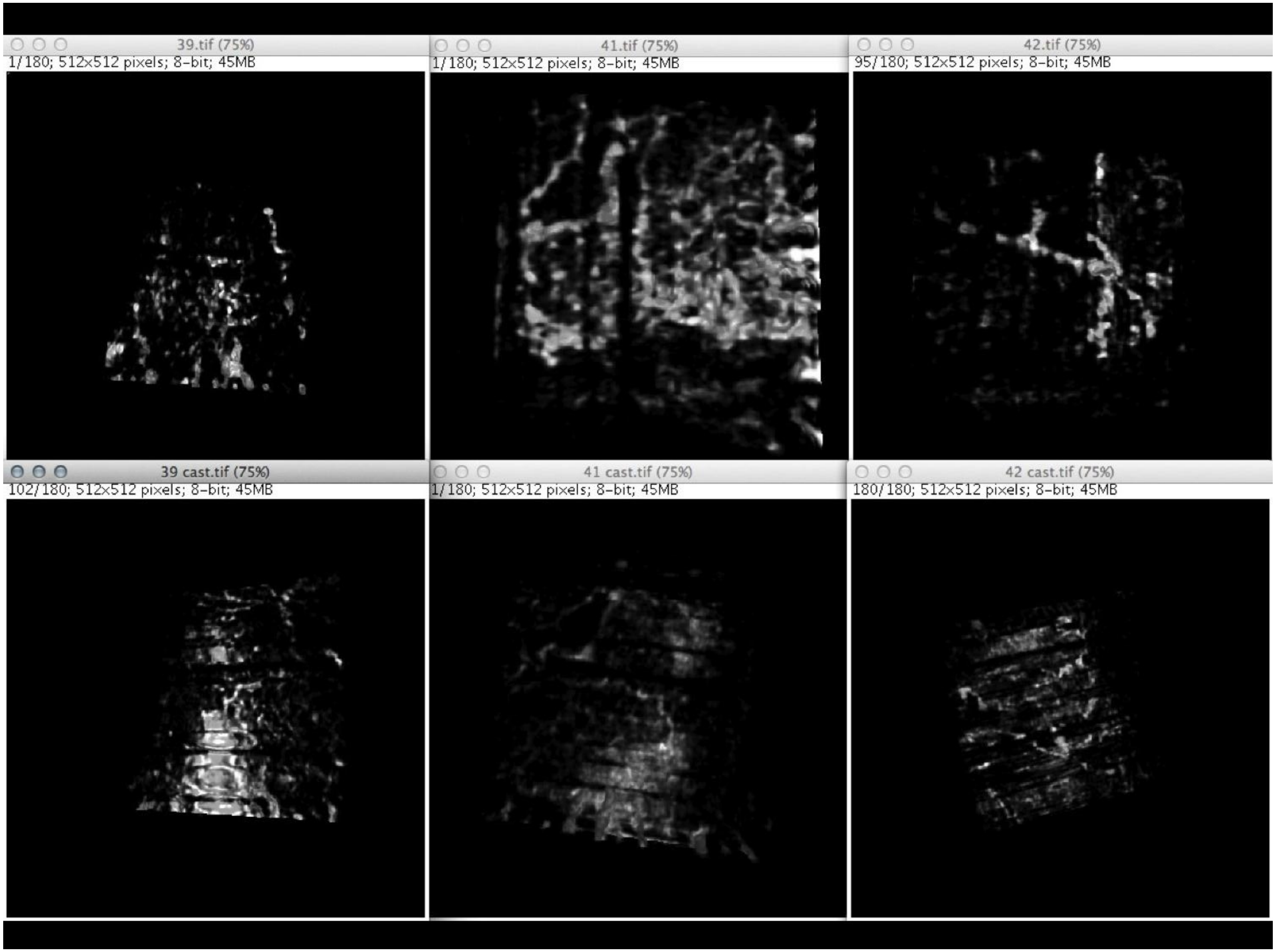

Figure 30. Reproducibility subject 5

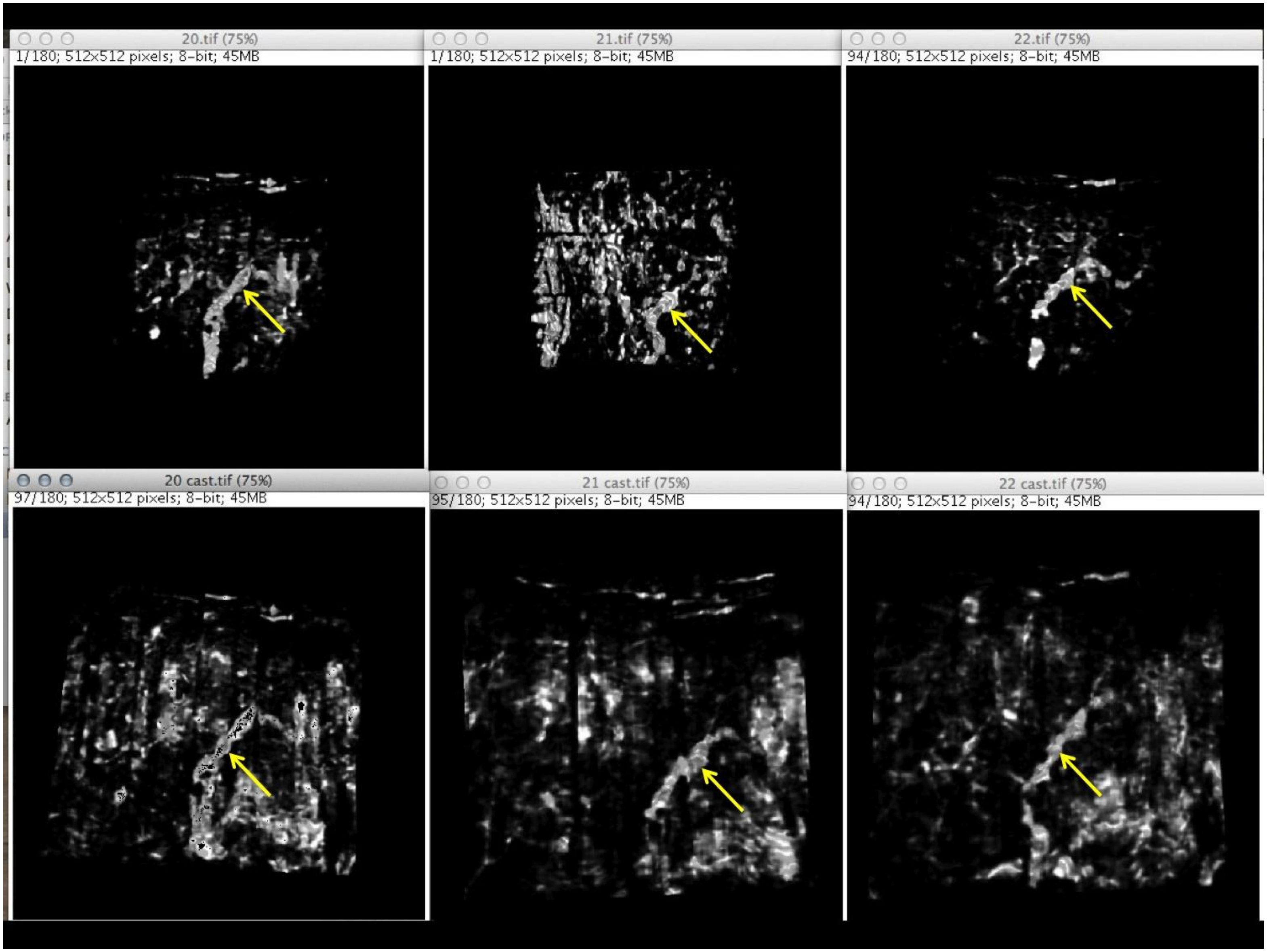

Figure 31. Reproducibility subject 6

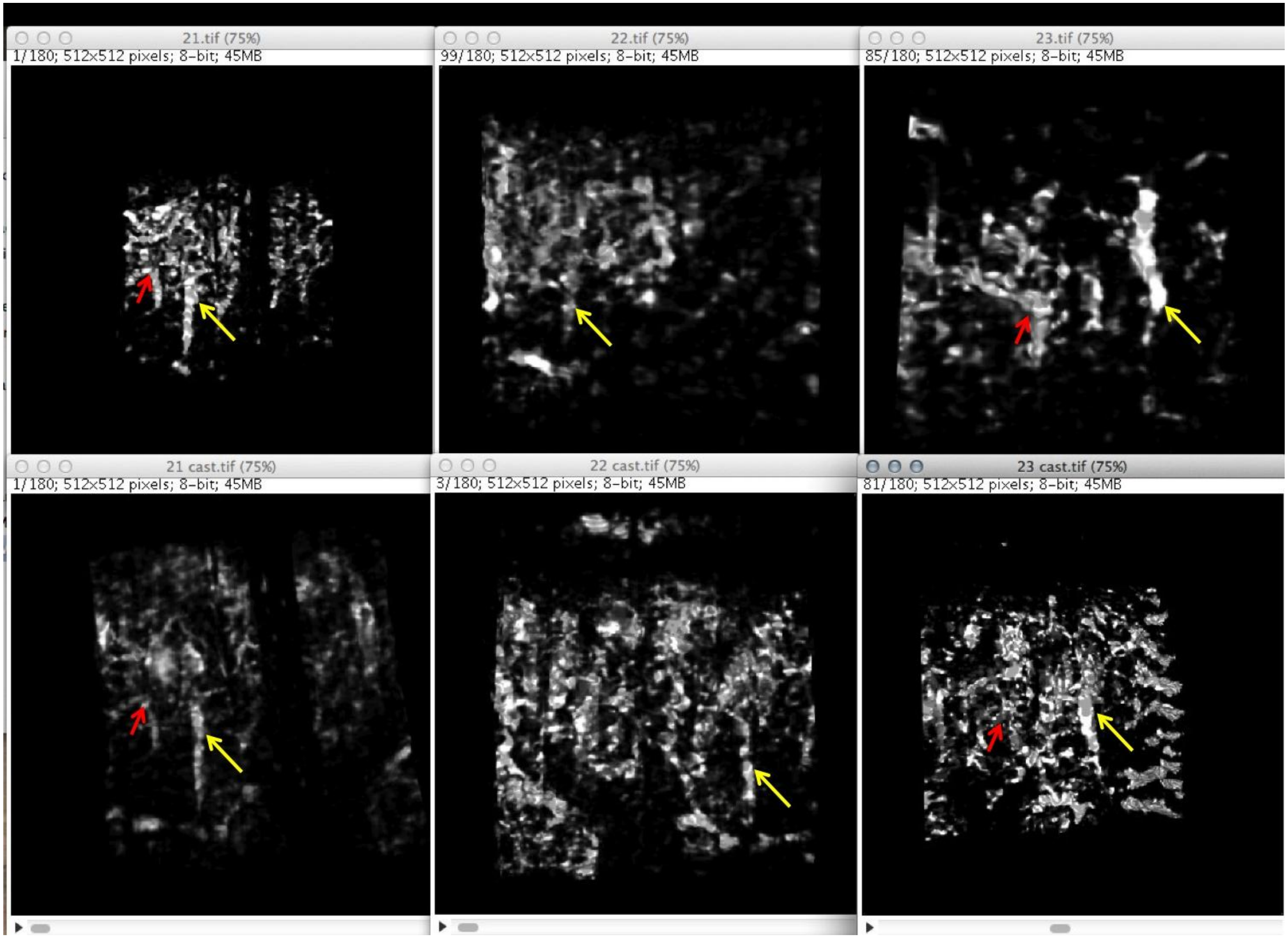

Figure 32. Reproducibility subject 7

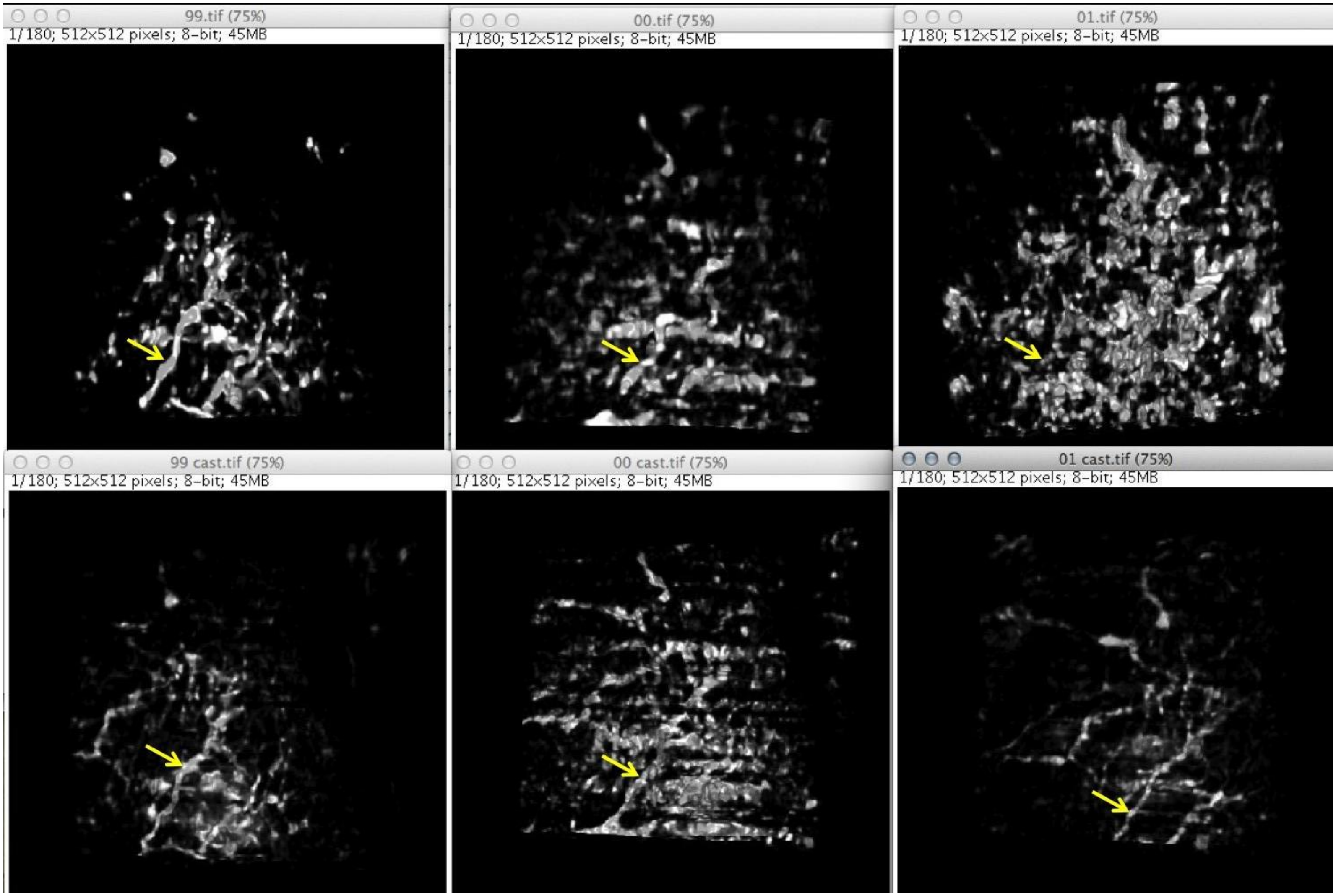

Figure 33. Reproducibility subject 8

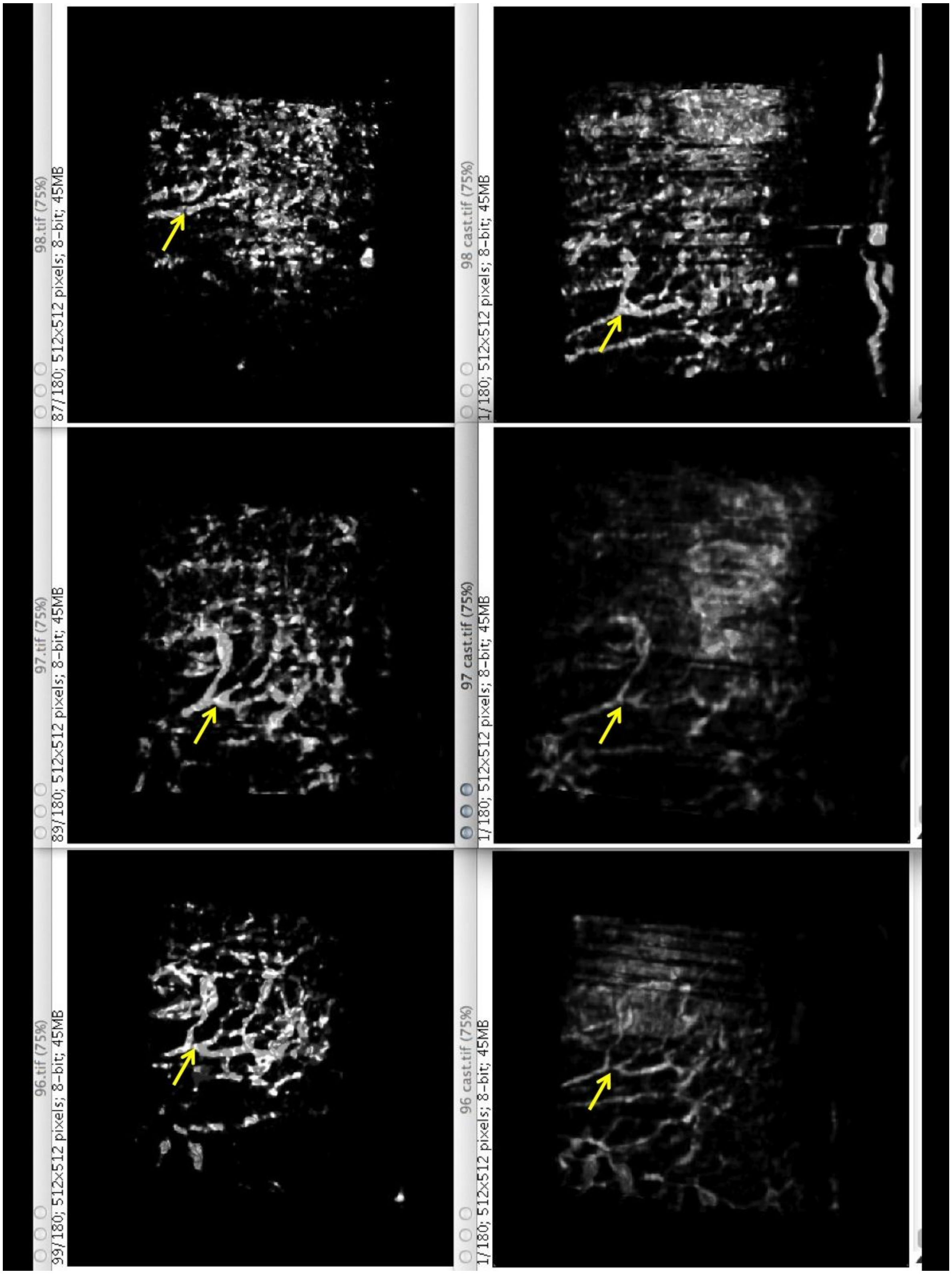

Figure 34. Reproducibility subject 9

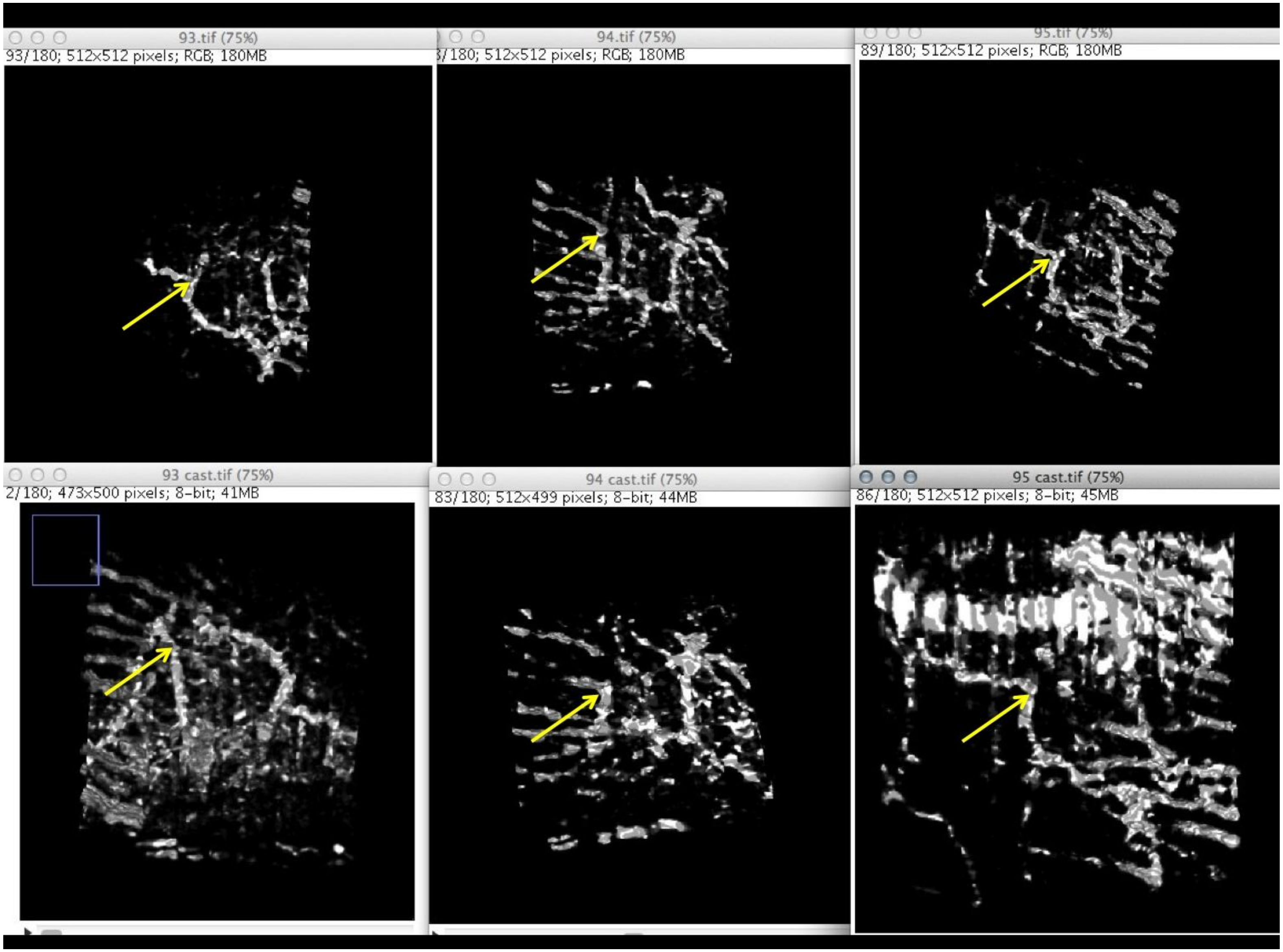

Figure 35 Reproducibility subject 10

8.4 DISCUSSION

Sequential scans of the limbus consistently produced reproducible visualization of vascular structures with identifiable morphologies in 8 of 10 subjects. In the two subjects in whom no clear vessels were seen, the consistent presence of noise, as opposed to the appearance and disappearance of vessels, is equally supportive of the reproducibility of the technique. This consistency of vascular appearance or absence was present between two independent observers. In the series of castings, textural differences were present as the result of each observer's technique in the manual adjustment of contrast. The completeness of the vascular network varied with the level of contrast enhancement, and was greater in "softer" images, or those in which a larger range of gray values was present. When the contrast enhancement pushed the images toward binary, the remaining noise was more prominent and effectively masked otherwise viewable vascular networks. In order to reduce this noise effect; larger portions of the signal content were reduced along with the noise resulting in the loss of visualized vessels (See Figure 28 upper left versus Figure 28 lower center).

Recall from the previous chapter that, in the cadaveric eyes, the nasal and temporal quadrants presented with the least distinct castings of outflow vasculature. In the present study, the findings in living eyes are consistent with those of the cadaveric eyes; specifically, there were only a small number of vessels that could be identified by casting. It is possible that these regions contain a similar vascular content, but also contain more sources of noise that obscure present vessels. Ultimately, concordance with actual physiological content will required a comparison with true physical castings of these vessels for side-by-side comparison with the virtual casts. This will be impossible in living human eyes, and an animal model may ultimately be necessary for comparison of castings of living eyes versus actual physical castings of the outflow system.

In conclusion, the vascular casting technique presented in the previous chapter in cadaveric eyes can be performed with data obtained from living eyes using off-the-shelf clinical scanners. These castings are reproducible, showing either vascular structure consistently from multiple scans of a single area, or the lack thereof with equal consistence. Independent observers analyzing the same set of scans produce virtual castings displaying vascular networks with the same morphology (or noise) depending on the scan content.

9.0 THREE DIMENSIONAL VISUALIZATION OF AQUEOUS OUTFLOW SYSTEM MACROSTRUCTURES: SCHLEMM'S CANAL AND COLLECTOR CHANNELS

9.1 INTRODUCTION: 2D IS COOL, BUT CAN YOU SEE SCHLEMM'S CANAL IN 3D?

We previously demonstrated the ability to visualize SC non-invasively in living human eyes in two dimensions (2D), and more distal structures in a cadaver eye outflow model in three dimensions (3D).[149,181] Those images were acquired with a SD-OCT device in an experimental configuration. The purpose of this study was to demonstrate 3D visualization of the aqueous outflow system in living human eyes using commercially available SD-OCT systems.

9.2 METHODS

9.2.1 Ethics Considerations

The study was conducted in accordance to the tenets of the declaration of Helsinki and the Health Insurance Portability and Accountability Act. The institutional review board of the

University of Pittsburgh approved the study. All subjects gave written informed consent prior to participation in the study.

9.2.2 Imaging of Schlemm's Canal in Human Eyes

Six healthy volunteers were recruited from the staff and faculty of the University of Pittsburgh Medical Center (UPMC) Eye Center. SC and aqueous veins were imaged using two commercially available SD-OCT devices: Cirrus HD-OCT (Carl Zeiss Meditec, Dublin, CA) and a modified Bioptigen SDOIS (Bioptigen, Research Triangle, NC). The Cirrus light source has a 50nm bandwidth centered at 840nm, resulting in a 5µm coherence length in tissue. The Bioptigen optics engine was coupled with a quad diode light source with an 870nm center wavelength and a 200nm bandwidth (Q870, Superlum Ltd., Dublin, Ireland). The light source had a coherence length of 1.3µm in tissue.

Two scan protocols were used; one optimized for the acquisition of 3D data (the "volume" protocol, 512x512 A-scans with no averaging, ~9.4 second acquisition time) and one optimized for visualization of individual frames (the "2D slice" protocol, 700x40 A-scans, each averaged 8 times at acquisition, ~8 second acquisition time). Each protocol imaged a 4x4 mm transverse area of the limbus with a 2mm A-scan length at the 3, 6, and 12 o'clock positions. Sequential scans in the volume protocol had a center-to-center spacing of 7.8µm. With a lateral resolution of 20µm, there was a high level of overlap (resampling) of tissue with any single point within the scan volume being sampled by 5 axial scans (center plus nearest neighbors in the x-y plane). Sequential scans in the 2D slice protocol were separated by 100µm. All scans were oriented so that the scan cube was tangential to limbus and the center scan was radial to the limbus.

The commercially available Cirrus HD-OCT had two FDA approved anterior segment scan protocols. The 512 x 128 A-scan "cube" protocol (~2.5 second scan time) was used, covering a 4x4 mm area of the limbus at 3, 6, and 12 o'clock. Unlike the Bioptigen, which was capable of orienting the B-scans at any arbitrary angle, only the 3 and 6 o'clock Cirrus B-scans had a radial orientation relative to the limbus while the 12 o'clock scan had a tangential orientation. Sequential frames in the Cirrus scans had a 31µm center-to-center separation. Raw OCT signal data were exported from both devices.

9.2.3 Image Processing

Scans were pre-processed with a custom-written OCT browser of our own design (Appendix A),[182-184] and then visualized in 3D using ImageJ Fiji (ImageJ 1.45k java, http://rsb.info.nih.gov/ij/). Cirrus scans were pre-processed with a 3x3x3-averaging kernel. Specifically, each voxel in the dataset was replaced by the average of 27 voxels in surrounding 3x3x3 3D space. Bioptigen volume images were pre-processed with a flat 5x5 averaging kernel. Each voxel was replaced with the average of the surrounding 5x5 voxel 2D plane. Averaging protocols were selected subjectively based on the appearance of the outcome. Processing time for averaging was approximately 1 minute per image for both Bioptigen and Cirrus.

The Fiji "enhance local contrast" filter was used to improve visualization of structure throughout. To create virtual castings, images were inverted so that the black collector channels appeared as white structures. The "subtract background" filter was applied with a 30-pixel kernel. Images were resampled to provide a 1:1:1 voxel aspect ratio in 3D. Contrast was adjusted to isolate the collector channels, and the volumes rendered using the 3D viewer plug-in. The total time to produce a 3D visualization was approximately 20 minutes, though multiple attempts to maximize visualization of structures were frequent. Varying levels of noise sources surrounding structures of interest necessitated flexibility in degree to which noise was suppressed in order to minimize noise content with minimal loss of image content.

Two distinct layers of aqueous venous plexuses were subjectively identified in the 2D visualizations (Figure 38, white block arrows). The Cirrus image of the limbus (Figure 36 left) clearly reveals Schlemm's canal (yellow arrows), as well as a distinctive "fallen Y" aqueous vein. The characteristics of this structure can be used to locate the same cross-sectional image within the Bioptigen image data (Figure 36 right). Two distinct layers of aqueous venous plexuses are visible (white block arrows right), at two depths within the limbus (white block arrows, left). Unlike blood vessels (Figure 38 stars), which cast vertical shadows into the scan (X's), aqueous veins do not create shadowing artifacts in the image.

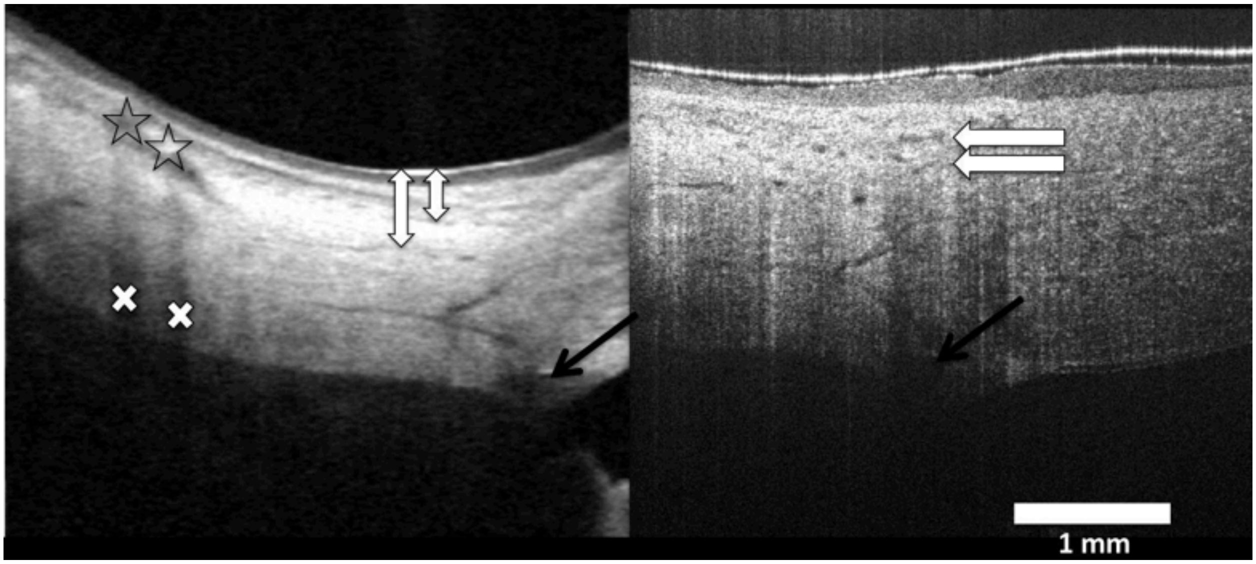

Figure 36. Cirrus and Bioptigen images of the same tissue location.

The distance from the surface of the limbus to each aqueous venous plexus was measured in the 2D slices in nasal, inferior, temporal, and superior quadrants. The diameters of aqueous veins in each layer of aqueous venous plexus were measured in each quadrant. No fewer than 6 of the 40 frames of the "2D" scan protocol were included for each location when venous plexus depth and aqueous vein diameter were assessed.

9.3 RESULTS

9.3.1 Subjective Observations

Four males and 2 females (average age 38.5 and 29 years respectively) were imaged on two different days. Outflow pathways were readily visible in both Cirrus and Bioptigen images from all eyes (Figure 37). 2D slices reveal both outflow and vascular structures. Blood vessels cast vertical shadows in OCT images[185] (Figure 36, x's). Shadows can be used to identify blood vessels (Figure 36, stars). Tracing their pathway to Schlemm's canal can identify aqueous veins, and their identity as aqueous veins is confirmed by the lack of shadows (Figure 36, block arrows). The average depth of the superficial and deep aqueous venous plexuses and the average aqueous vein diameters are presented in Table 8. The distance between the surface of the limbus and each of the two layers of aqueous venous plexuses was measured in each quadrant. The diameter of aqueous veins within those plexuses was also measured (Table 8).

Table 8. Aqueous venous plexus characteristics

Location	Mean (St. Dev.) Distance from Surface to Aqueous Venous Plexus (µm)	Mean (St. Dev.) Aqueous Vein Diameter (µm)
Nasal Superficial	133.17 (23.93)	38.28 (7.22)
Inferior Superficial	95.49 (12.44)	33.03 (8.72)
Temporal Superficial	115.30 (14.08)	32.88 (9.23)
Superior Superficial	99.50 (52.71)	18.07 (8.58)
Nasal Deep	295.61 (59.72)	48.53 (9.05)
Inferior Deep	318.35 (68.81)	74.42 (20.56)
Temporal Deep	258.58 (51.77)	39.46 (6.13)
Superior Deep	270.55 (132.67)	34.22 (16.49)

Acquisition of 3D volumetric samples enabled identification of the same location within the limbus in both scan sets, based on subjective observation of outflow pathway morphology (Figure 36). Speckle noise obscured visualization of SC and aqueous veins within the raw Cirrus scans, but 3x3x3 averaging reduced speckle and allowed clear visualization. Figure 38 shows a contrast-enhanced image sequence obtained with the Bioptigen in which the pathway (underlined in orange) from SC (underlined in yellow) is traced to the midlimbal intrascleral plexus. These images are from a sequence of 40 axial slices of the limbus acquired in 8 seconds. The center-to-center spacing of the slices in image 33 is 100µm.

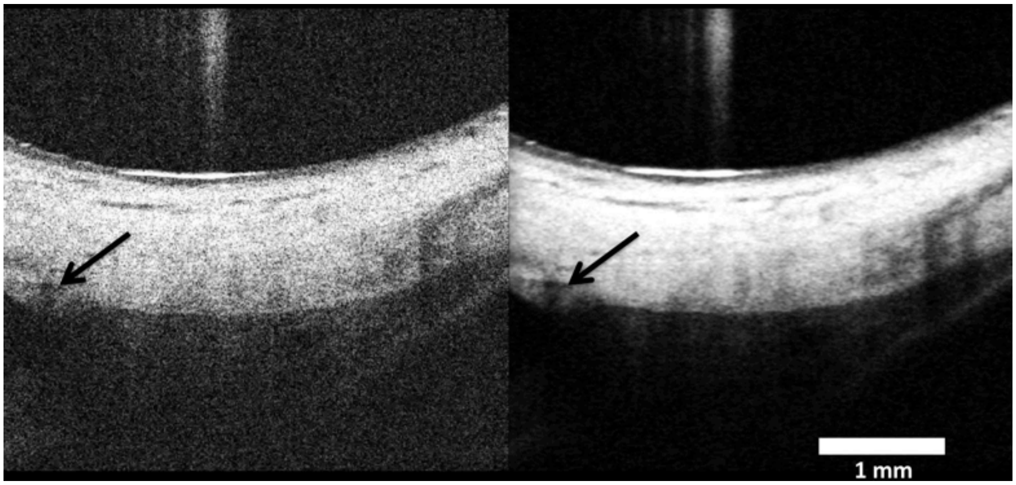

Figure 37. Cirrus before and after averaging

Utilizing adjacent frames, the pathway from SC to the mid-limbal intrascleral plexus could be traced (Figure 38).

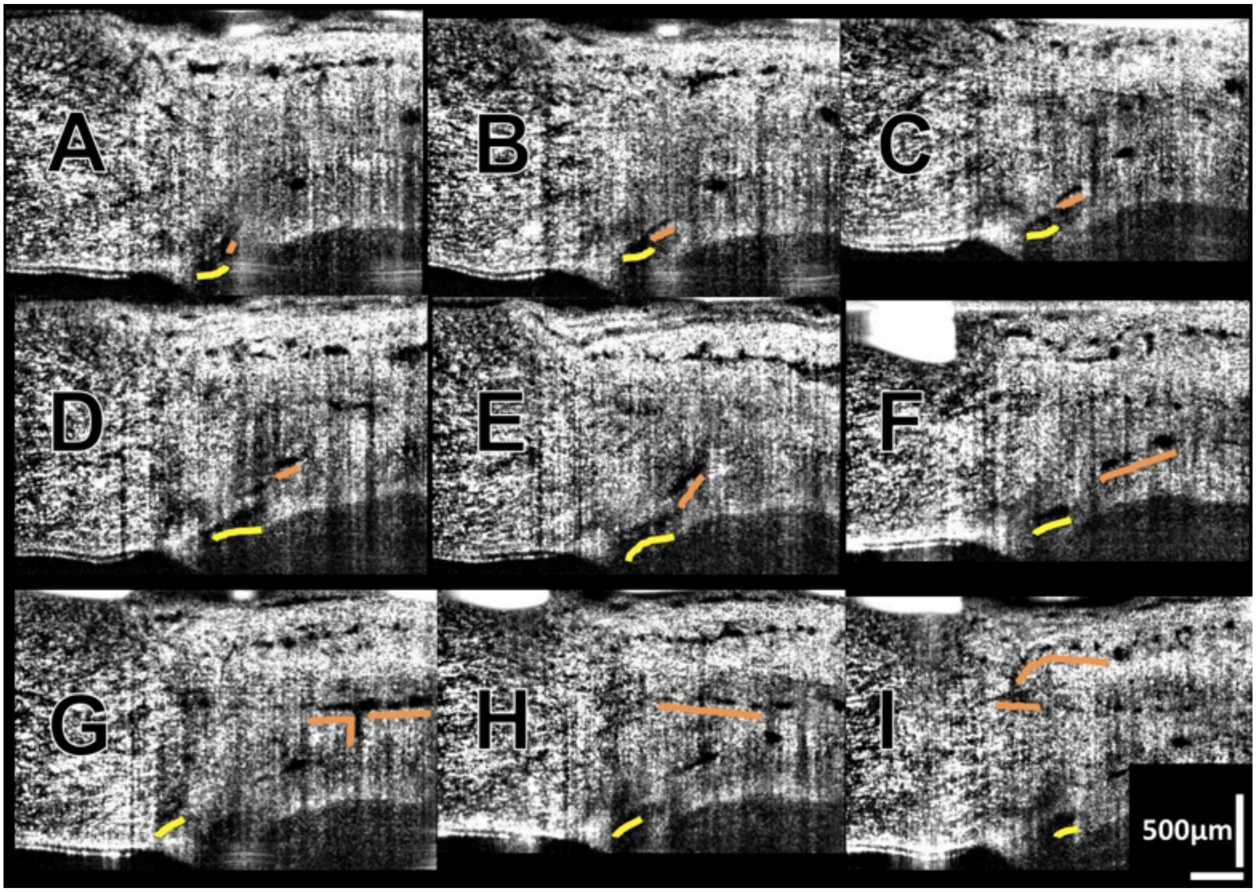

Figure 38. 2D visualization of the outflow pathway from SC to the ISVP

Virtual casting of the aqueous humor outflow structures between SC and the episcleral vasculature, as well as surrounding blood vessels, whose identity is suggested by their relatively large size, was feasible with the data produced on each system. Inclusion of more noise (Figure 39 right, Bioptigen) allows a more complete virtual casting of the aqueous humor outflow pathway (yellow arrows), compared to a casting with heavily suppressed noise (Figure 39 left, Cirrus), which washes out many of the outflow structures (yellow arrows) leaving, for the most part, large blood vessels (red arrows).

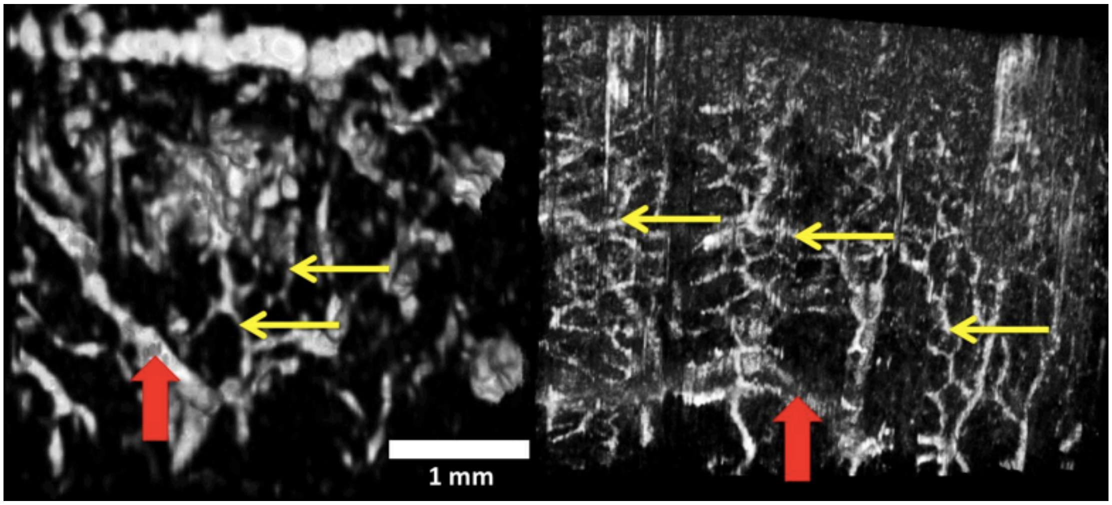

Figure 39. Cirrus and Bioptigen castings of the living human ISVP

The degree to which noise was suppressed altered image content. Leaving more noise (Figure 39 Bioptigen casting right) allowed visualization of aqueous outflow microvasculature with a "fishnet" appearance. Removal of more noise (Figure 39 Cirrus casting left) eliminated visualization of the aqueous humor microvasculature, leaving only large blood vessels in the casting.

Figure 40 presents the first virtual castings of SC (asterisks) in the living human eye. Several collector channels (arrows) and aqueous veins extending from SC were observed within the 4mm section of SC.

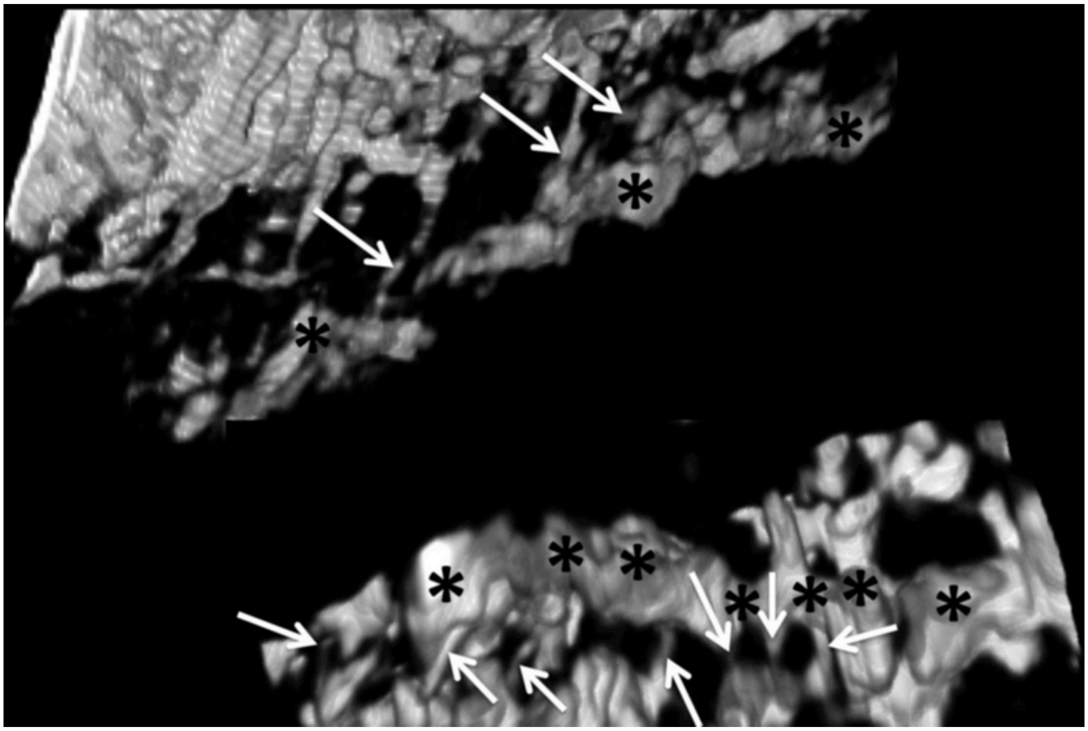

Figure 40. The living human Schlemm's canal *in-situ*

When the 2D image stack that produced these castings was reviewed, the presence of 4 aqueous vein branch points were not evident. SC could be cast from all Cirrus scans at both nasal and temporal quadrants (Figure 41, SC marked by asterisks). When the castings were rotated in 3D space, collector channels emanating from SC could be observed in 9 of the 12 castings.

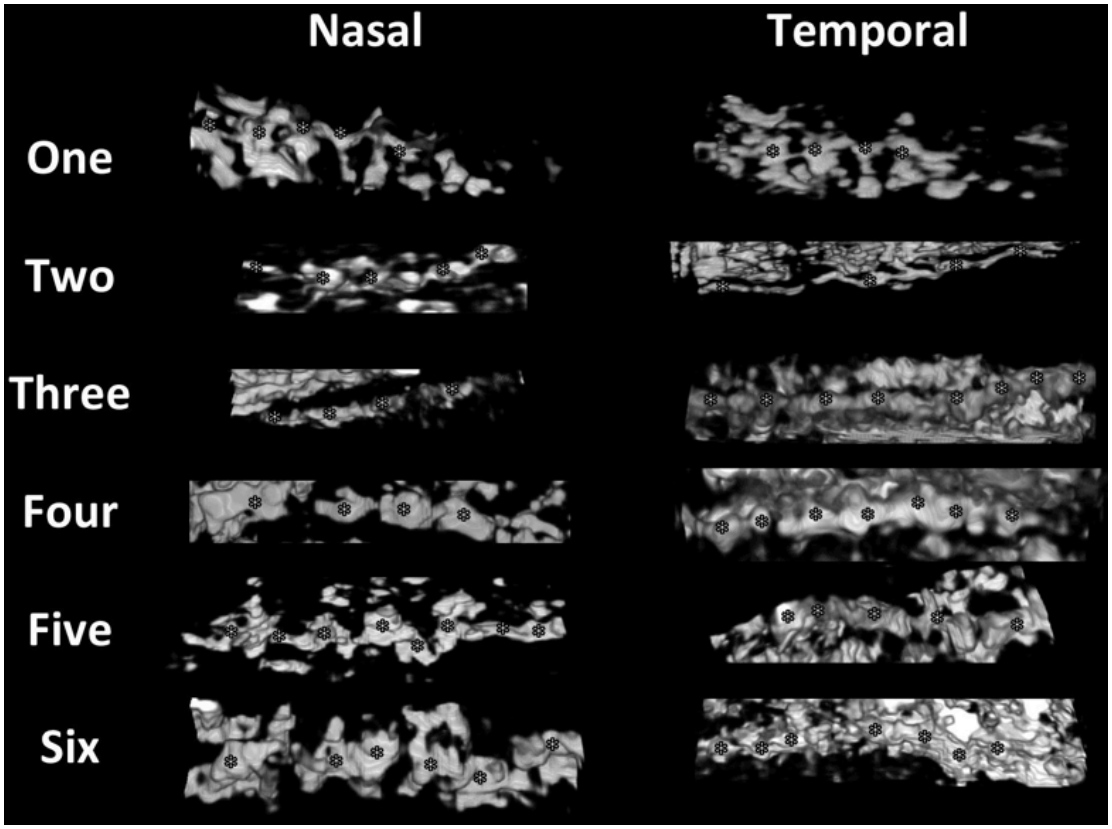

Figure 41. Schlemm's canal castings from all nasal and temporal Cirrus scans

9.4 DISCUSSION

9.4.1 Summary of Findings

In the present study we demonstrate the ability of SD-OCT to acquire volumetric scans of the limbus, from which the outflow pathway can be tracked from SC to the superficial vascular plexuses in 2D image sequences, and from which virtual castings of those same outflow structures can be produced. We also found that averaging the raw scan data improved visualization of the outflow pathway. We present the first 3D castings of outflow structures in the living human eye.

9.4.2 2D Versus 3D Analysis of Ostia

The ability to visualize SC and surrounding aqueous veins in 3D increases the ability to detect detailed information of the outflow pathway, such as the branch points, in comparison with the 2D images. We have previously described a number of instances in which 3D visualization of a structure within a raster scan set reveals its identity.[186] In the present study, the observation of small vessels adjacent to and emanating from SC allowed their identification as collector channels despite their weak and hidden appearance when observed in 2D.

9.4.3 Importance of 3D Imaging of Ostia in Glaucoma

The ability to cast SC in 3D could improve the management and treatment of glaucoma. Visualization of SC and collector channels could give guidance to the glaucoma surgeon wishing to improve aqueous outflow through the conventional pathways. The TM and inner wall of SC could be removed specifically in the region of collector channels and their ostia as well as aqueous veins to maximize the impact of that surgery on outflow facility and reduction of intraocular pressure. The same is true for devices that would reside in SC and bypass the TM and inner wall of SC – placement at the sites in proximity of collector channel ostia would potentially maximize their effectiveness in IOP reduction, since aqueous would not have to traverse long distances in SC prior to exiting through the collector channels. Conversely, it is possible that leaving currently active regions of aqueous humor outflow undisturbed and using implanted devices to enhance outflow by positioning them in regions devoid of observable aqueous vein/SC branch points would maximize outflow. This casting technique may be useful in elucidating the optimal implant placement strategy. This hypothesis could be tested in the perfused cadaver eye model.

The findings in the present study also include the first virtual castings of the distal outflow vasculature in a living eye, similar to the castings of cadaver eyes published in a previous study.[181] Unlike the previous study, the casting in the living eye includes patent blood vessels (Figure 36). It is likely that, based on their relative size, the large vessels more prominent in the Cirrus casting in Figure 39 are blood vessels. The small aqueous humor vessels visible in the Bioptigen casting in Figure 39 features a distinct network of straight segments sharing branch points. Some evidence of this same microvasculature exists in the Cirrus casting, but the extent to which it pervades the morphology of the aqueous humor outflow vasculature cannot be appreciated. Unfortunately, visualization of the smaller vessels cannot be accomplished without the inclusion of substantial image noise. A study focusing on the morphology of small aqueous vessels is currently underway.

9.4.4 Conclusions

3D virtual casting of the aqueous outflow vasculature is possible in living human eyes with existing off the shelf general purpose SD-OCT technology. The outflow pathways from SC to the superficial vasculature can be identified and tracked, and SC can be cast in 3D from these scans. Post-processing is required to maximize the visualization of the content within.

10.0 THREE DIMENSIONAL VISUALIZATION OF AQUEOUS OUTFLOW SYSTEM MACROSTRUCTURES: AQUEOUS VENOUS PLEXUSES

10.1 INTRODUCTION: THERE WERE SMALL HINTS OF VASCULAR MESHWORKS IN THE PREVIOUS CHAPTER. WHAT DO THEY REALLY LOOK LIKE?

The earliest imaging studies intended to elucidate the normal structure of limbal outflow vasculature utilized biomicroscopic examination *in-situ* or in whole enucleated eyes with or without the use of contrast.[187,188] These early studies established that aqueous humor flowed from the anterior chamber (AC) to SC and reached the superficial limbal vasculature via connecting vessels. Further studies have shown the majority of aqueous humor leaves the eye through limbal structures that comprise the conventional pathway (TM, Schlemm's canal, collector channels, aqueous venous plexus and episcleral veins). The aqueous venous plexus is a complex network that includes the deep, midlimbal and perilimbal scleral plexuses leading to scleral veins or Ascher's aqueous veins which bypass this tortuous pathway and connect directly from SC to the episcleral veins.[26,27,29,189,190]

SD-OCT and ultrasound imaging of the anterior segment have produced cross-sectional images of the drainage system, but these do not yield sufficient visualization to ascertain the condition or density of the complex 3D structures of the aqueous humor outflow system.[149,173,174]

SD-OCT rapidly quantifies tissue reflectance in 3D cubes at speeds up to 1.37 million axial scans (A-scans) per second.[95,100,191] Coupling the high scanning speed with ultrahigh resolution, it is possible to visualize the individual components of the aqueous humor outflow system from the anterior chamber throughout the system of aqueous veins in the living human eye.[149] In an earlier study visualizing the gross morphology of the aqueous humor outflow channels, a not previously described fine meshwork structure was observed in the aqueous humor capillary networks.[150] The purpose of the present study was to create 3D visualizations of the aqueous humor outflow vasculature to reveal morphometric details of microvasculature visible with an improved SD-OCT processing schema and to compare microvascular morphologies to those found in corrosion casting studies.

10.2 METHODS

10.2.1 Ethics Considerations

Human cadaver eyes with no history of eye disease, trauma or ocular surgery other than cataract were obtained from the Florida Eye Bank (Miami, FL) and the Center for Organ Recovery and Education (Pittsburgh, PA). The Committee for Oversight of Research Involving the Dead of the University of Pittsburgh approved the study. Consent for the use of all tissues for research was obtained by the individual agency responsible for harvesting and supplying the tissue. In addition, *in-vivo* healthy eyes were imaged recruited from the staff of the University of Pittsburgh. The living subject portion of the study was conducted in accordance with the tenets of the declaration of Helsinki and the Health Insurance Portability and Accountability Act. The institutional review board of the University of Pittsburgh approved the study. All subjects gave written informed consent prior to participation in the study.

10.2.2 Tissue Preparation and Perfusion

Seven cadavers and three living eyes were imaged (Table 9). Perfusion pressures are provided in the Table. The time window between death and fixation was less than 24 hours. To prepare for perfusion, *ex-vivo* eyes were wrapped in saline-soaked gauze, submerged in normal saline and warmed to 34°C. Eyes were then placed in front of the SD-OCT scanner in a custom-made fixation mount. Throughout the experiment, the eye was irrigated with 40°C saline to prevent dehydration and to minimize cooling.

Table 9. Perfusion Pressures

Eye	Condition	Anterior Chamber Pressure
1, 2	Intact	20 mmHg
3	Conjunctiva and Tenon's Capsule Removed	20 mmHg
4-7	Conjunctiva and Tenon's Capsule Removed	10 mmHg
8-10	Healthy *In-vivo*	n/a

A 27-gauge needle was inserted into the peripheral cornea, with the needle tip passing through the pupil and positioned posterior to the iris and anterior to the lens. This positioning prevented artificial deepening of the anterior chamber during perfusion and artificial increases in outflow facility.[176] Barany's mock aqueous humor was used to perfuse the eyes.[165] The initial 20 min of perfusion was used to establish baseline outflow. The rate of perfusion was determined by recording the weight of the aqueous humor in the reservoir in real time at 20 measurements per second. Measurements were recorded by a 4-channel 10-bit digital acquisition system (DATAQ

Instruments, Akron, OH). Immediately after completion of the perfusion experiments, the eyes were perfusion-fixed with 10% formalin buffered solution. Perfusion pressure is the hydrostatic force between the anterior chamber pressure and the pressure within the vessels receiving aqueous humor outflow. In this study, a normal episcleral venous pressure of 8 mmHg in living eyes was assumed.[168] The first two intact eyes were perfused with an anterior chamber pressure of 20 mmHg. Since the episcleral venous pressure in a cadaver eye is approximately 0 mmHg, an anterior chamber pressure of 20 mmHg produced a perfusion pressure equivalent to an IOP of 28 mmHg in a living eye. An anterior chamber pressure of 10 mmHg yielded a perfusion pressure equivalent to an IOP of 18 mmHg in a living eye.

In the cadaver model, there is no active circulatory system present to remove aqueous humor expelled from the outflow system. We found that fluid gradually accumulates in the conjunctiva and Tenon’s capsule when that tissue was left intact on the globe, causing shadows obscuring visualization of outflow structures. Therefore, we found that cadaver eyes require the removal of these layers prior to perfusion to produce images of equal quality to those obtained in unperturbed living eyes.[150] The conjunctiva and Tenon’s capsule were dissected in all but the first pair of eyes. Four eyes were perfused and imaged at 10 mmHg, and then perfusion fixed at 10 mmHg. One of these eyes was first imaged at a perfusion pressure of 0 mmHg. One eye was perfused and imaged at 20 mmHg. After imaging, it was perfusion fixed at 20 mmHg.

To validate our SD-OCT images, additional eyes (N=3) from ostensibly non-glaucomatous donors were obtained from the National Disease Research Interchange. Eyes were perfused with mock aqueous humor containing fluorescent tracer microspheres (Invitrogen Inc., Molecular Probes, Eugene OR; 0.2 µm; 0.002% volume-to-volume) at 7 or 15 mmHg. Each eye was perfusion-fixed with 4% paraformaldehyde and sectioned into quadrants. The tracer labeling pattern within the episcleral vessels was imaged in each quadrant using an epifluorescent microscope (Nikon TE-2000E) outfitted with a 1x objective.

10.2.3 SD-OCT Imaging

An SD-OCT optics engine (Bioptigen, Research Triangle, Durham, NC) was coupled with a wide-bandwidth super luminescent diode array (870 nm center wavelength, 200 nm bandwidth; model Q870, Superlum Ltd., Dublin, Ireland). This light source has a coherence length of 1.3 µm in tissue. The optics engine allows the user to specify any number of A-scans per frame, as well as any number of frames, limited only by system memory. It also allows the user to specify any number of sequential A-scans to be acquired in a single location during a raster scan for the purpose of averaging and Doppler assessment; also limited only by system memory. One living eye was scanned using Doppler so that velocity could be used to distinguish large blood vessels from large aqueous humor outflow vessels. Subsequently, two scan protocols were created: one optimized for the acquisition of 3D data (the "volume" protocol) and one optimized for visualization of individual frames (the "2D slice" protocol). Each eye was scanned twice at the limbus, first with a protocol optimized for 3D volumes, and the second with a protocol optimized for visualization of 2D slices. For each eye a set of 36 individual radial scan sets were acquired: each clock hour imaged at its center, and offset to the left and right. The angle of each set of clock hour scans was set so that the center clock hour scan was on a radial ray from the center of the pupil (i.e. the 9 o'clock scan was at 0°, the 10 o'clock scan at 30°, the 11 o'clock scan at 60°, etc.). The density of the 3D volume scan protocol was limited by system memory, and consisted of 512 x 512 A-scans probing a 2 x 3 mm (radial x transverse) area of tissue. This scan protocol only moved the 20 µm diameter SD-OCT beam 9 µm between A-scans, thus including a single tissue volume in multiple adjacent samples (oversampling). Acquiring oversampled SD-OCT data allowed post processing averaging. The 2D slice protocol consisted of 700 x 20 A-scans probing the same sized (2 x 3 mm) area of tissue. Each A-scan of the 2D slice imaging protocol was repeated 18 times, and the average of those 18 scans recorded. The final 2 x 3 area of tissue image was converted to a uniform 4 x 4 mm image. This method was previously described in detail.[149,177]

10.2.4 Image Processing

Raw SD-OCT's were averaged with a floating 5 x 5 pixel transverse kernel, consisting of 5 pixels in each of 5 adjacent frames, were used to produce an average dataset, using customized software of our own design (Listed in Appendix C). Further image processing was performed using Fiji (Fiji 1.44, http://fiji.sc/wiki/index.php/Fiji). Images were imported in raw .bog file format after the 5x5x5 "rolling average" function was completed. A "Gaussian blur" filter was then applied before converting the image to 8-bit format. Images were resampled to provide a 1:1:1 voxel aspect ratio in three dimensions; from 512 x 512 x 1024 to 342 x 512 x 342 for each 2 x 3 x 2 mm volume. Images were then inverted so that the black collector channels appeared as white structures and the Fiji "subtract background" filter was applied.

Contrast enhancement was applied to both SD-OCT and microsphere fluorescence images. An "Enhance Local Contrast" filter was applied followed by introduction of a Gaussian blur. Contrast was repeatedly adjusted to isolate small vessels. The "subtract background" filter was used to isolate the vessels of interest. Contrast was manually adjusted in both SD-OCT and fluorescence images to suppress remaining noise. The SD-OCT 3D volumes were rendered using the Fiji 3D viewer plug-in.

10.3 RESULTS

10.3.1 Subjective Observations

Direct observations of the SD-OCT images revealed components of the superficial ISVP, connecting aqueous veins, and SC in all eyes. Confirmation of location was obtained by matching vascular patterns seen in the 3D virtual corrosion cast with corresponding B-scan cross-sectional images (Figure 42a-d). The superficial venous plexus visualized was composed of a series of small, interconnected venules between 25 – 100 μm in diameter with many interconnecting branch points forming a dense vascular hexagonal meshwork (Figure 42A). Red arrows indicate a vessel seen on the virtual casting (Figure 42A) and its corresponding location in B-scan (Figure 42B). Blue arrows indicate a suspected aqueous vein (Figure 42C) descending from the superficial ISVP to the midlimbal ISVP and its corresponding location in B-scan (Figure 42D). Yellow arrows indicate two suspected aqueous veins seen in this 180 degree rotated virtual casting image (Figure 42E).

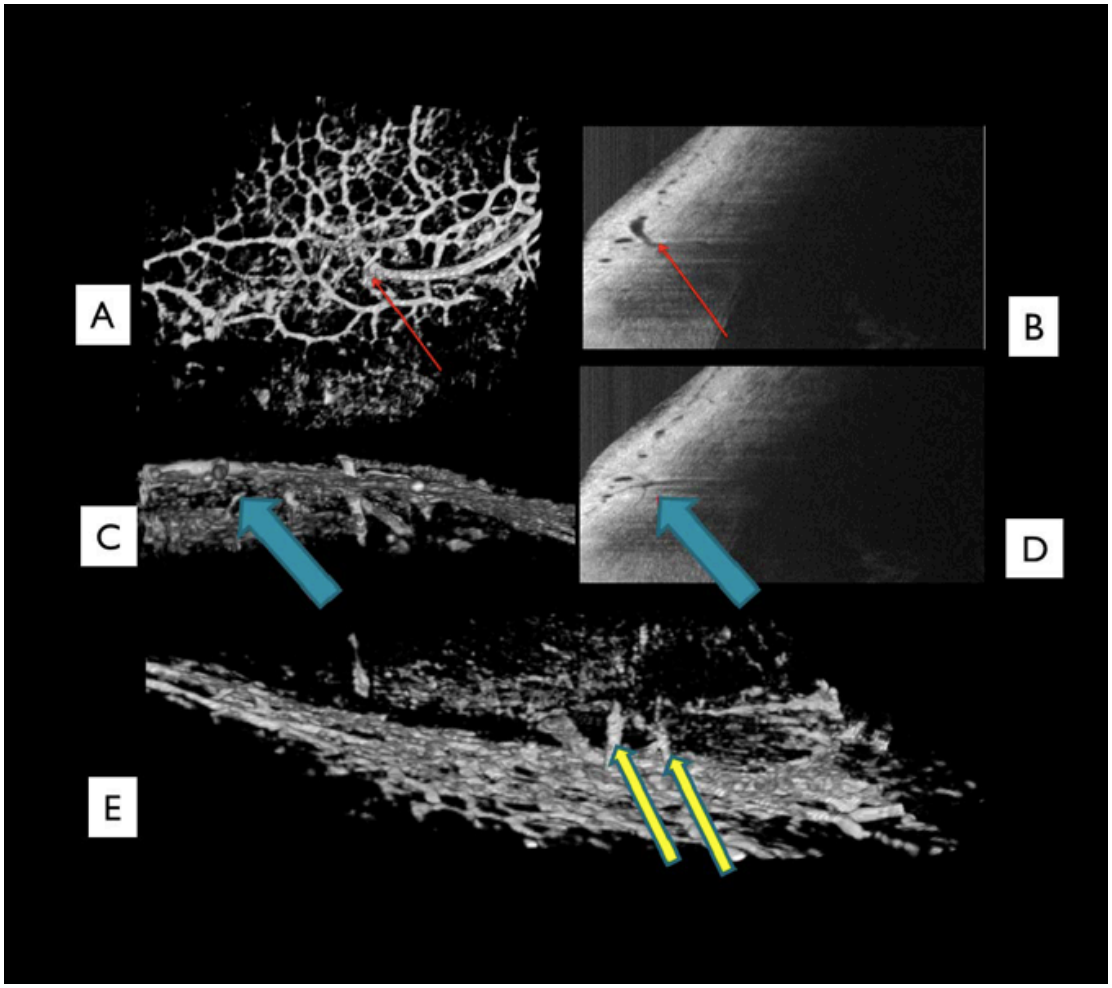

Figure 42. ISVP in 3D and its feeder vessels

10.3.2 Vessel Size

The superficial venous plexus visualized was composed of a series of small-interconnected venules 10 – 50 μm in diameter with many interconnecting branch points forming a dense vascular hexagonal meshwork (Figure 44A). Vessels approaching the size of capillaries (<10 μm) were assumed to be present, but were not visualized. Vessel diameters were measured in the 4 x 4 mm scan according to estimation of pixel number/image volume and compared to known measurements from previous physical corrosion casting studies of the eye (Figure 45).

Vessel type and diameter was estimated based on the pixel count and image volume and compared to known measurements from previous corrosion casting studies of the eye. The yellow arrow shows a vessel between 75-100 µm draining into a larger vessel approximately 200 µm in diameter (Figure 45). Red arrow points to a small connecting vessel between approximately 25 µm in diameter.

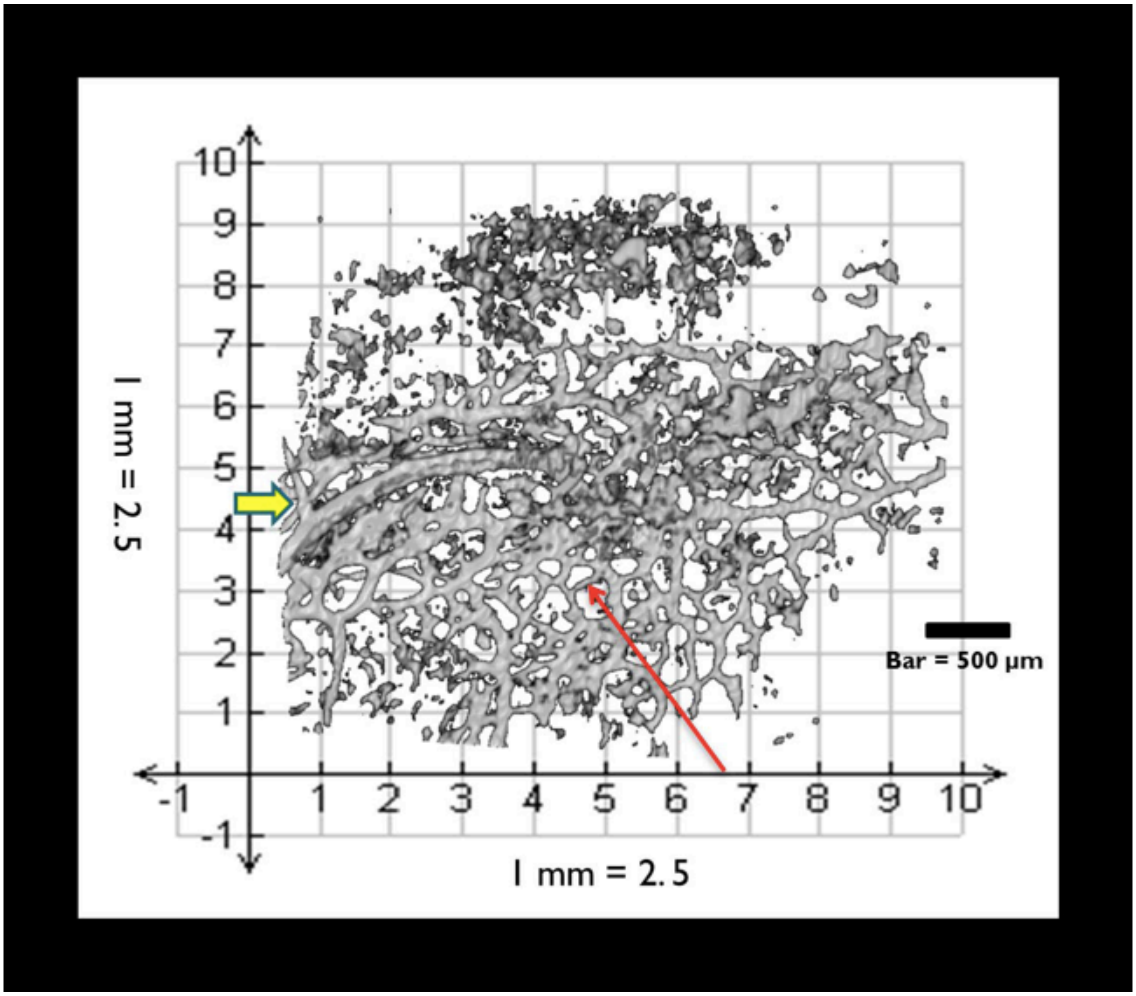

Figure 43. ISVP size

For example, in the x direction, each pixel corresponds to a width of 4mm/342. When viewed along the long horizontal axis, venous structures are seen to descend into the deeper limbus and form branches into midlimbal venous plexus structures, which are also visible in B-scan cross-sections (Figure 42c-d).

10.3.3 Outflow Network Morphology

The venous plexus was drained posteriorly by several larger veins forming a series of radial arcades. These vessels are 50 - 100 µm in diameter and progressively converge into larger vessels moving posteriorly away from the image margin and SC (Figure 44, yellow arrows).

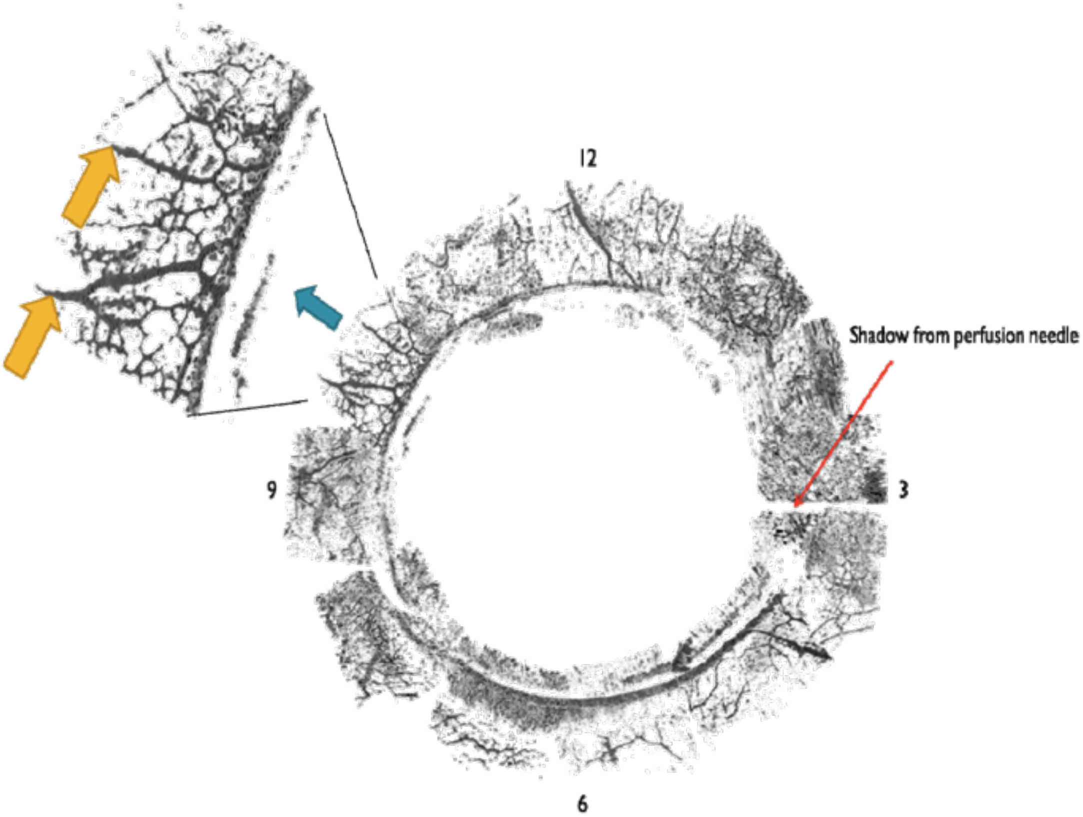

Figure 44. A 360-degree virtual casting of a cadaver eye

The blue arrow in Figure 44 points to an enlarged section with several straight radial arcades draining vessels perpendicularly to the limbal margin. Note the dense array of vasculature located superiorly, nasally, and temporally with sparser vasculature seen inferiorly. The red arrow indicates where the perfusion needle penetrated the cornea (Figure 44). These vessels converge with larger more tortuous vessels, which were rarely observed. These tortuous vessels ranged from 200 - 400 µm in diameter (Figure 45, yellow arrow).

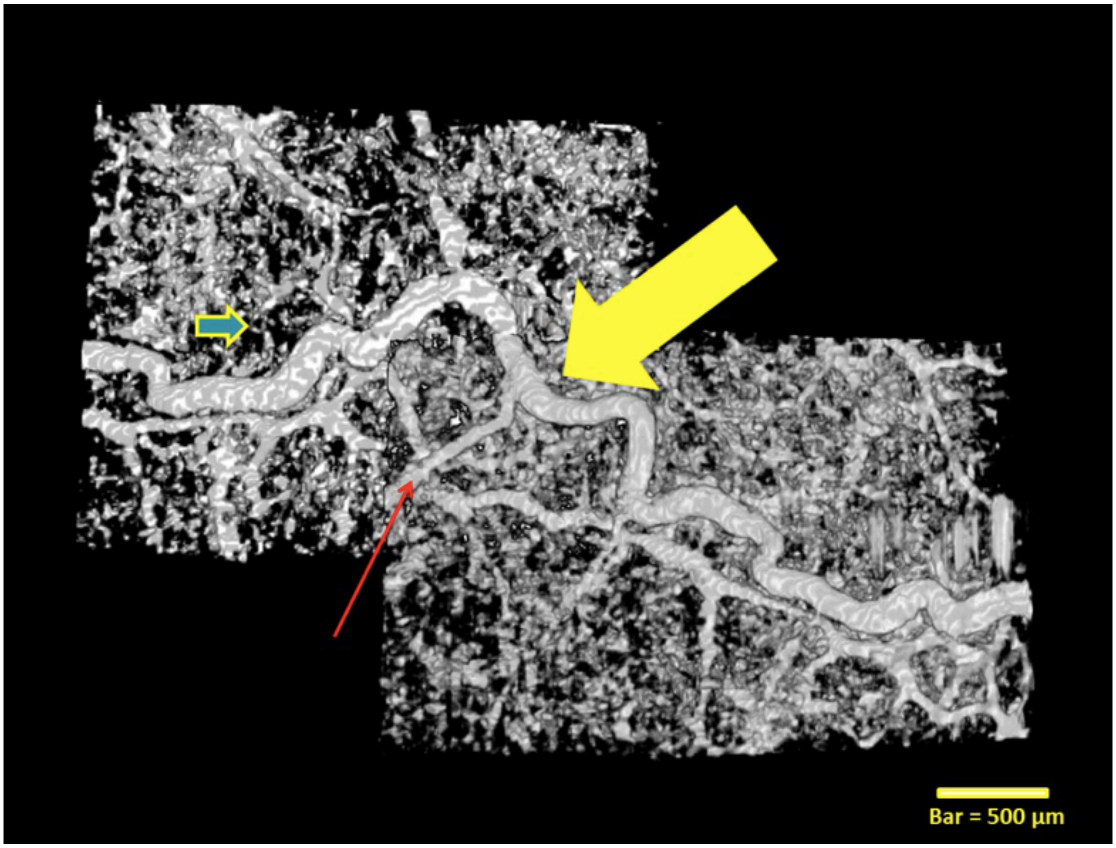

Figure 45. A large tortuous vessel

A large tortuous vein, with characteristic striations (seen after image contrast enhancement) is shown in Figure 45 (yellow arrow). A smaller venous structure is shown draining into the larger tortuous vein (Figure 45 red arrow). The smallest visualized structures form a dense vasculature mesh surrounding the large drainage vessels (blue arrow). Unlike the radial arcades, large tortuous veins do not travel in a consistent direction in relation to the image margin. It is unclear, from these visualizations, where these large tortuous vessels terminate or converge.

A similar vascular pattern was observed in tracer-perfused eyes (Figure 46),

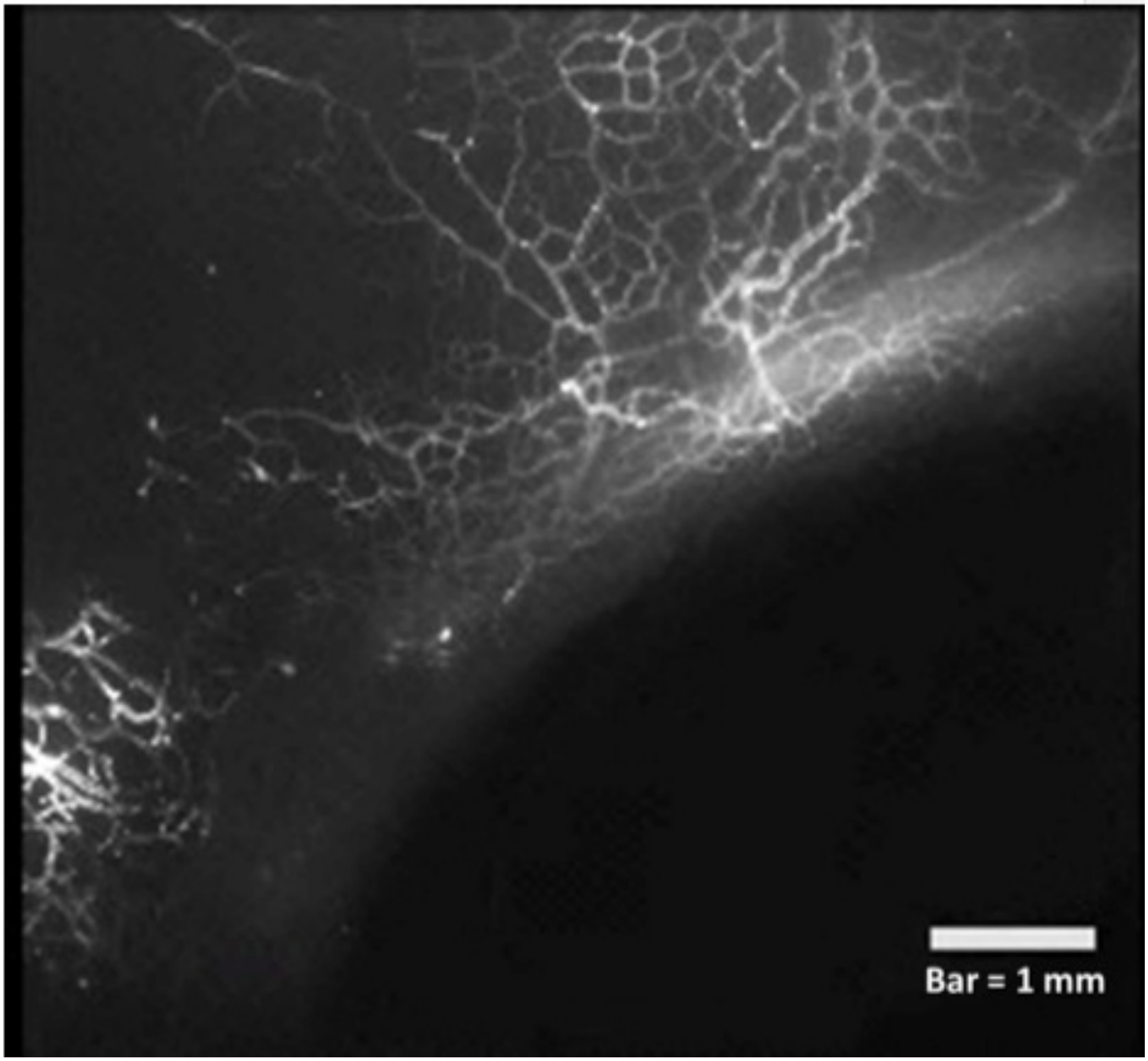

Figure 46. Fluorescent microsphere labeled outflow system

where tracer was found to decorate several larger vessels (50 – 100 μm) extending posteriorly from the limbus in both raw (Figure 46) and contrast enhanced (Figure 47) fluorescence images. Fluorescent microspheres (diameter = 0.02 μm) revealed a meshwork-like network of aqueous humor outflow veins. Figure 47 shows a microsphere labeled outflow system after local histogram equalization and background subtraction filters were applied, revealing visualization of a meshwork of outflow vasculature extending into the outflow vascular tree down to Schlemm's canal. (Figure 47)

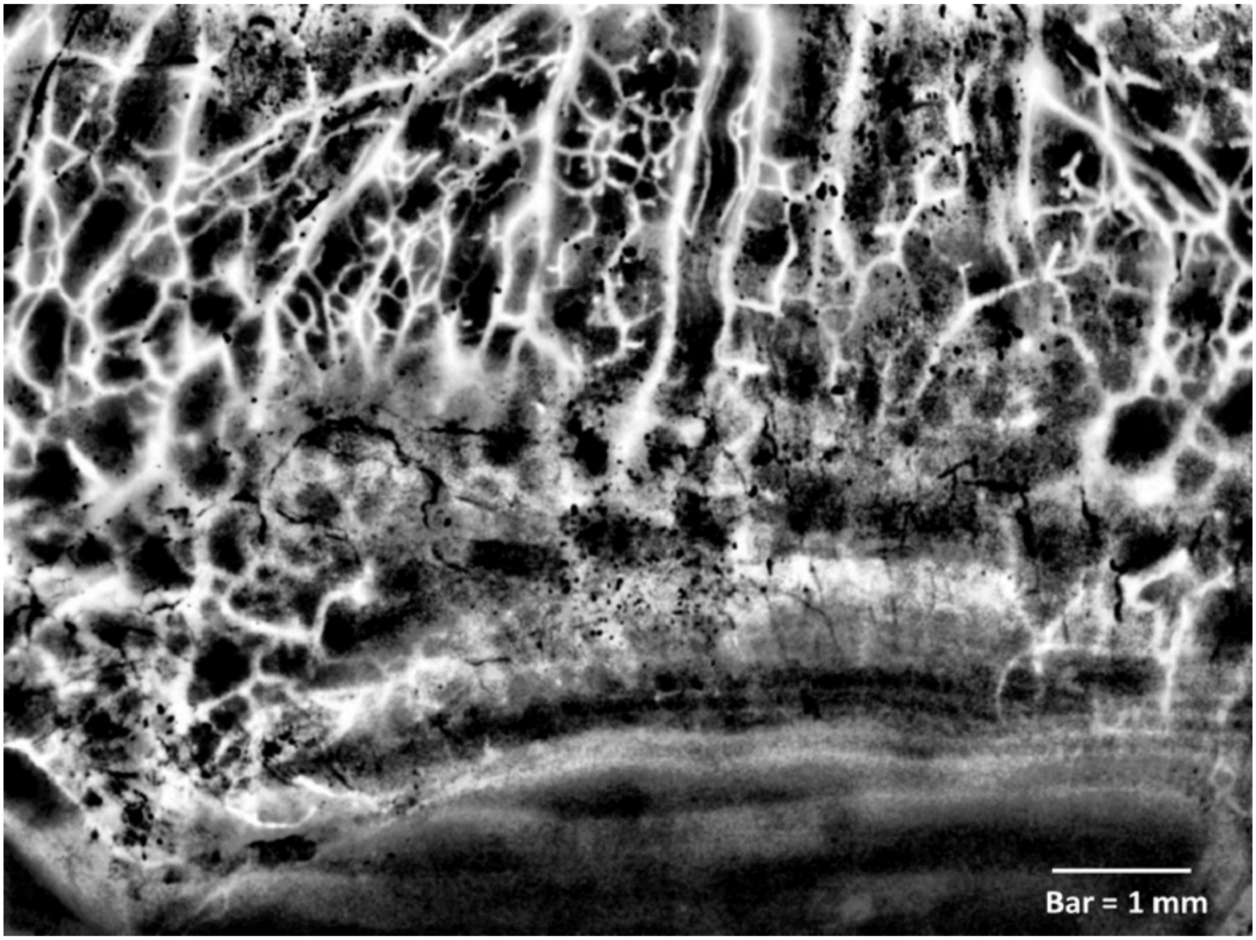

Figure 47. Enhanced visualization of the outflow vasculature down to Schlemm's canal.

Smaller tracer-labeled vessels (30 – 40 µm) were often seen branching between the larger vessels, occasionally exhibiting a hexagonal network pattern (Figure 47). There was significant variability in tracer labeling around the episcleral limbus, with intense labeling observed in some quadrants while other quadrants of the same eye exhibited very little label.

Nasal and temporal *in-vivo* scans in three eyes confirmed the vessel morphology observed in cadaver eyes. All three previously described vascular structures (venules, radial veins, and large tortuous veins) were visualized *in-vivo*. Few significant differences were observed between *in-vivo* and *ex-vivo* virtual castings. Structures *in-vivo* appeared less consistent in diameter than *ex-vivo* (Figure 48) Direct observations did not show marked differences in-vivo (Figure 48A) vs. ex-vivo (Figure 48B), except that in-vivo castings appeared to have a smaller average vessel diameter, perhaps due to engorgement of vessels during perfusion ex-vivo. In-vivo castings are expected to also include arterial blood vessels, which are not active in the cadaver eye.

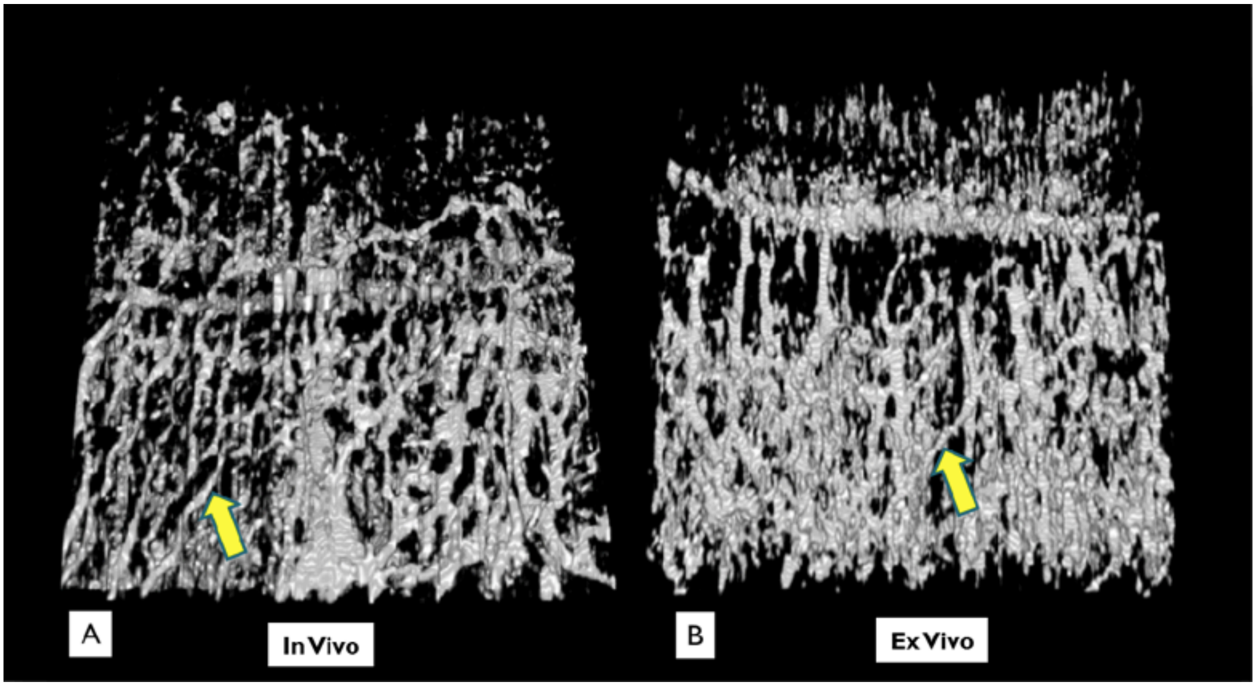

Figure 48. Living versus cadaveric virtual casting

Doppler studies were performed on one eye *in-vivo* to confirm flow through a large tortuous venous structure (Figure 49). A large tortuous vein (yellow arrow) casts shadows towards the anterior chamber (Figure 49A). Several aqueous venous shadows can be seen (brown arrows). A contact lens worn during this study is seen (red arrow). The vessel can be seen to have a characteristic laminar flow pattern, with slower flow near the edges of the vessel and more uniform flow near its center (Figure 49B blue arrow). Slow blood flow increases reflectance and mimics stationary tissue. Color Doppler flow patterns are indicated and overlaid on top of a structural scan (Figure 49C). Both blue and red flow patterns are seen in the same vessel due to the variable course of the vessel in relation to the OCT scanner resulting in blood flowing towards and away from the probe at different areas.

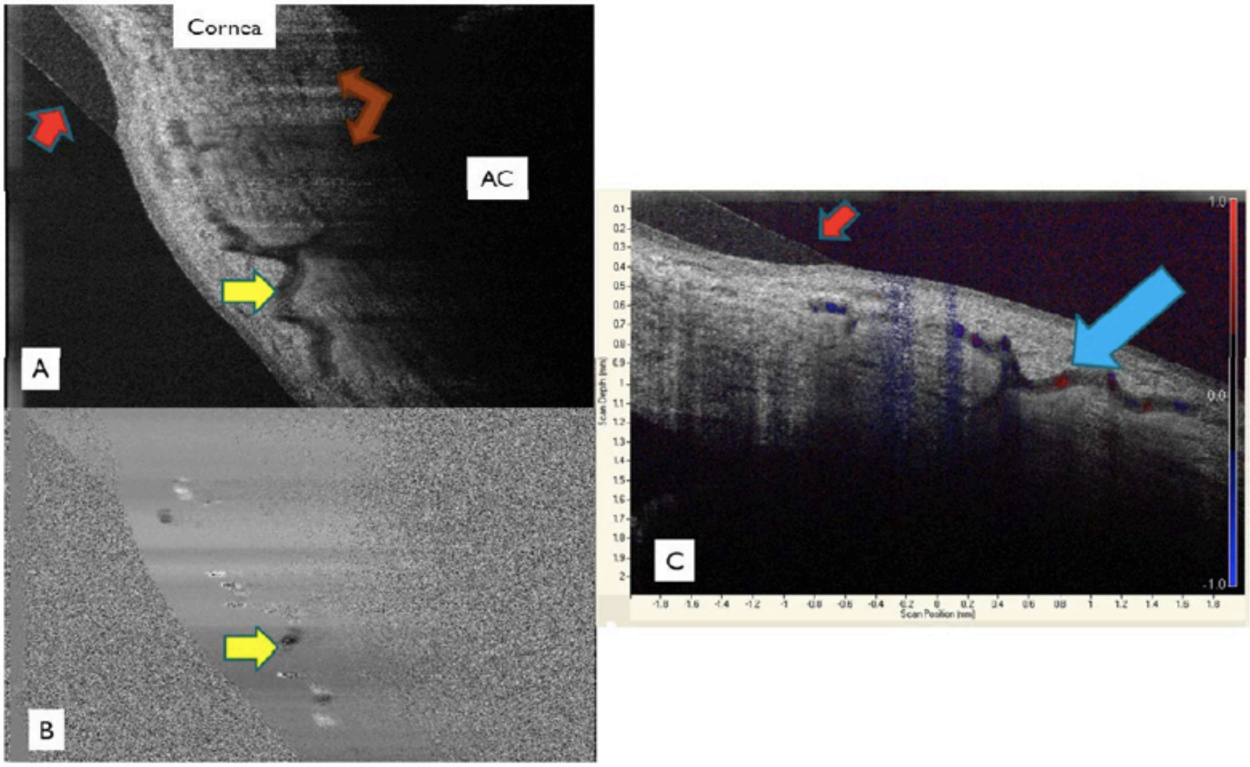

Figure 49. Doppler observed in a living human eye

The high velocity signature of this vessel, compared to the low velocities within aqueous humor outflow vasculature, suggest that this was a blood vessel.

Qualitative assessment of vasculature density showed dense concentrations of vasculature in the nasal and temporal position in all eyes, forming branching arcades that drained into progressively larger vessels at increasing distances from the limbus. Similarities were observed between 360-degree virtual castings and previous studies using colored silicone casting agents in monkey eyes.

10.4 DISCUSSION

10.4.1 Summary of Findings

We present the first SD-OCT 360 degree virtual casting of outflow microvasculature comprising the ISVP, connecting aqueous veins, and components of SC. Our methodology, in contrast to physical corrosion casting, is completely non-invasive and may be performed in living human eyes. Previous methods used to image the limbal vessels include serial sections with or without dye, ultrathin sections, microvascular perfusion with plastics, rubber or silicone and corrosion casting, x-ray microcomputed tomography, fluorescein angiography and vascular endothelial labeling techniques.[190] Of these, only SD-OCT images allows for non-invasive structural identification without contrast media, chemicals or ionizing radiation. Further, without the need for corrosion, our method allows localization of the various components of the casting relative to the surrounding tissue by referring to the corresponding structures within the 2D image stack (Figure 44).

There was excellent agreement between structures visualized with SD-OCT and previous casting studies. Vascular morphological structures observed in this study (Figures 52, 53) were compared to micro-corrosion vascular castings in the published literature using either Microphil or neoprene studies in humans,[26-28] methyl methacrylate polymer resin studies with or without Mercox injected into blood vessels,[192-197] or colored silicone.[42,198] In the present study, perfusion with fluorescent microspheres was used for further confirmation that the virtual castings created with OCT indeed isolate outflow microvasculature (Figures 48 and 49). As with castings in the literature, there was excellent agreement between the microvasculature visualized in SD-OCT castings and that labeled by the microspheres.

A characteristic radial striation was observed in our 3D virtual castings as a series of light and dark stripes after contrast enhancement on larger vessels. This correspond with striations of similar morphology on venous structures observed in corrosion casts of the eye under high power in rabbits[199] and rats[193,197] and in vessels of the GI tract,[200] bladder,[201] and cerebral cortex[202] in humans and biliary tract[203] in rat models and were present both *in-vivo* and *ex-vivo* (Figure 48). Although these striations in micro-corrosion castings may be accounted for by leakage of the casting resin to the subendothelial space in corrosion castings,[194] we feel it is unlikely these are artifact due to the consistent radial pattern along vascular structures often moving in different directions relative to the image plane and their presence in multiple previous studies.

Our SD-OCT hardware has a theoretical axial resolution of 1.3 μm, however no vessels less than 10 μm were observed which raised a question as to whether structures smaller than venules were present in our findings. Nevertheless, we were able to track the vascular sources of the cast structures back to SC, suggesting that vessels of the smallest magnitude in the outflow vascular tree were visualized and included in the casting. Vessels smaller than those present in our study, if present and connected to SC, may have collapsed post-mortem and were not reopened during perfusion due to the higher surface tension within.

In-vivo vasculature appeared smaller and less distinct than *ex-vivo* (Figure 50). Ex-vivo vasculature may also be artificially larger due to engorgement as part of the perfusion process or small eye movement *in-vivo* may be a factor. Further mathematical schema and image software are needed to better determine vasculature size, diameter, and corresponding function.

10.4.2 Vessel Identification

We are confident that at least some structures we observed were venous vasculature comprising aqueous humor veins. By tracing vessels in the 2D stack, we could confirm the smallest vessels connected directly to SC and we have surrounding tissue in the slice to place the actual location of the vessels that we cast. The perfusion process allows enhancement of venous structures over arteries due to the preferential outflow through the conventional outflow system to the episcleral vasculature which is principally a venous network.[204] Previous corrosion casting studies utilizing the conventional outflow system also confirm the outflow vasculature is venous, not arterial, and no anastomoses could be located between veins and arteries after filling in these studies.[42,198] Finally, although the superficial limbus contains lymphatic vessels which share some morphological similarities to venous networks, visualization of lymphatic vessels generally requires separate perfusion in the lymphatic system.[190]

Doppler studies were performed on one eye *in-vivo* to provide further evidence of venous outflow (Figure 51). The large Doppler signal visible in this vessel, compared to smaller signals in surrounding vasculature, suggest that this vessel is likely part of the blood flow system, possibly a terminal drainage vein in the aqueous outflow vascular tree. The vessel can be seen to have a characteristic laminar flow pattern, with slower flow near the edges of the vessel and more uniform flow near its center. Slow blood flow increases reflectance and mimics stationary tissue.

A 360-degree virtual casting is compared to a casting using silicone[198] and shares many similarities (Figure 52). Vascular density appears highest temporally, superiorly and nasally in the virtual casting with less dense arcades noted inferiorly. The authors concede that, at present, there is no universally accepted method of quantifying vasculature structures in 3D SD-OCT virtual castings so we cannot comment with absolute certainty that all vessels are being observed. Further methods of quantifying our findings, including using corrosion casting techniques or histological sectioning are needed to confirm whether preferential outflow based on density of vasculature exists in the human eye *ex-vivo*. Ultimately, application of virtual castings will depend on determination of how each of these potential parameters is affected by the presence of glaucoma.

10.4.3 Study Limitations

Limitations of the study included the lack of direct comparison between virtual castings and histological castings currently in progress. Additionally, although we created a custom mount to limit eye movements *in vivo*, we could not completely eliminate these from our *in vivo* castings. Finally, non-isotropic pixel aspect ratio refers to the fact that our pixels may not be exactly square in "real" space. We estimated vessel size based on the pixel count knowing that in the x direction, each pixel corresponds to a width of 4mm/342. Development of an algorithm to measure pixels with a standardized pixel size from the anterior eye may give us more specific estimates of vessel size.

10.4.4 Conclusions

We present the first detailed morphometric analysis of small aqueous humor outflow structures obtained non-invasively in-situ using SD-OCT. Continued development of this technique may lead to clinically useful direct assessment of outflow in subjects with glaucoma.

11.0 VALIDATION OF DOPPLER MEASUREMENTS IN-VITRO

11.1 INTRODUCTION: ARE SD-OCT MEASUREMENTS OF DOPPLER ACCURATE?

In Chapter 4, the presence of Doppler within vessels observed to emanate from Schlemm's canal was one piece of evidence identifying those vessels as collector channels. Specifically, the direction of flow within the vessels demonstrated flow out of Schlemm's canal. The detection of Doppler introduces the potential to go beyond mapping the outflow system, but with the combination of structural (mapping) and functional (Doppler) imaging, to use SD-OCT 3D imagery to calculate volumetric outflow. Before using Doppler measurements in flow calculations, Doppler measurements obtained by SD-OCT must be validated. In this chapter, an in-vitro model utilizing a glass tube and turbid liquid is used to validate SD-OCT's ability to accurately measure flow at known rates. Limitations of the device are also revealed and discussed.

OCT is a ranging technique based on low coherence interferometry which has been applied to structural imaging of the eye.[91] SD-OCT utilizes advances in broadband low coherence light sources and high speed linear array detector technologies, acquiring complete 1024 pixel A-scans in a single spectrometer measurement.[95,205] Reflectance intensities are frequency encoded in the raw SD-OCT fringe pattern. Fourier analysis of SD-OCT yields more than just reflectance data. Doppler signals from all points within the reflectance data set are also produced, and have recently been used to measure retinal blood flow.[206,207] The real (or power) component of the Fourier transform of SD-OCT data produces an A-scan, and Doppler measurements are contained in the imaginary (or phase) component.[206-208] But, the dynamic range of SD-OCT Doppler measurements is limited to low velocities by spectrometer limitations.

High velocities produce large Doppler shifts that physically manifest as rapid translation of the associated carrier frequency across the face of the spectrometer. Because of this, both structural measurements of moving back scattering sources and SD-OCT Doppler measurements are limited by the A-scan rate, which limits the CCD's ability to capture moving carrier waves without blur.[207] The purpose of the present study was to validate SD-OCT Doppler velocity measurements under well-controlled conditions in an *in vitro* laminar flow model.

11.2 METHODS

11.2.1 Experimental Setup

A 30cc syringe was filled with skim milk and inserted into a syringe pump (Perfusor® basic, B. Braun Medical Inc., Bethlehem, PA). Flow rates were set in terms of the amount of time to empty the syringe. The slowest available settings were used in this experiment, keeping them within a range relevant to measurements in retinal vessels. The pump used flow settings of minutes per 30 cc's. Based on the volume of the capillary tube, pump settings produced the flow and velocity rates listed in Table 10.

Table 10. Flow pump settings, velocity, and flow rates

Pump Setting (min)	Flow Rate (ml/min)	Mean Velocity in Tube (mm/sec)	Peak Velocity in Tube
55	0.55	35.0	70.0
50	0.6	38.5	77.0
45	0.67	42.8	85.6
40	0.75	48.1	96.2
35	0.86	55.0	110.0

Intravenous (IV) tubing connected the syringe within the pump to a glass capillary tube (internal diameter = 0.579mm; Yankee 20λ disposable micropipette, Becton Dickinson and Co, Parsippany, NJ) shallowly embedded in agarose gel. IV tubing then carried the milk to a collection reservoir (Figure 50). Skim milk was pumped at controlled rates from a 30cc syringe pump, through a glass capillary tube embedded in a shallow bed of agarose gel (Figure 50 top). The capillary tube was oriented at approximately 83° to the scanning beam. The 3D scan volume contained a series of axial slices acquired along the length of the capillary tube.

The orientation of the milk column within the 3D scan data was used to determine the Doppler angle relative to the interrogating SD-OCT beam. All measurements were performed with the capillary tube in a single location and the Doppler angle remained constant throughout the experiment.

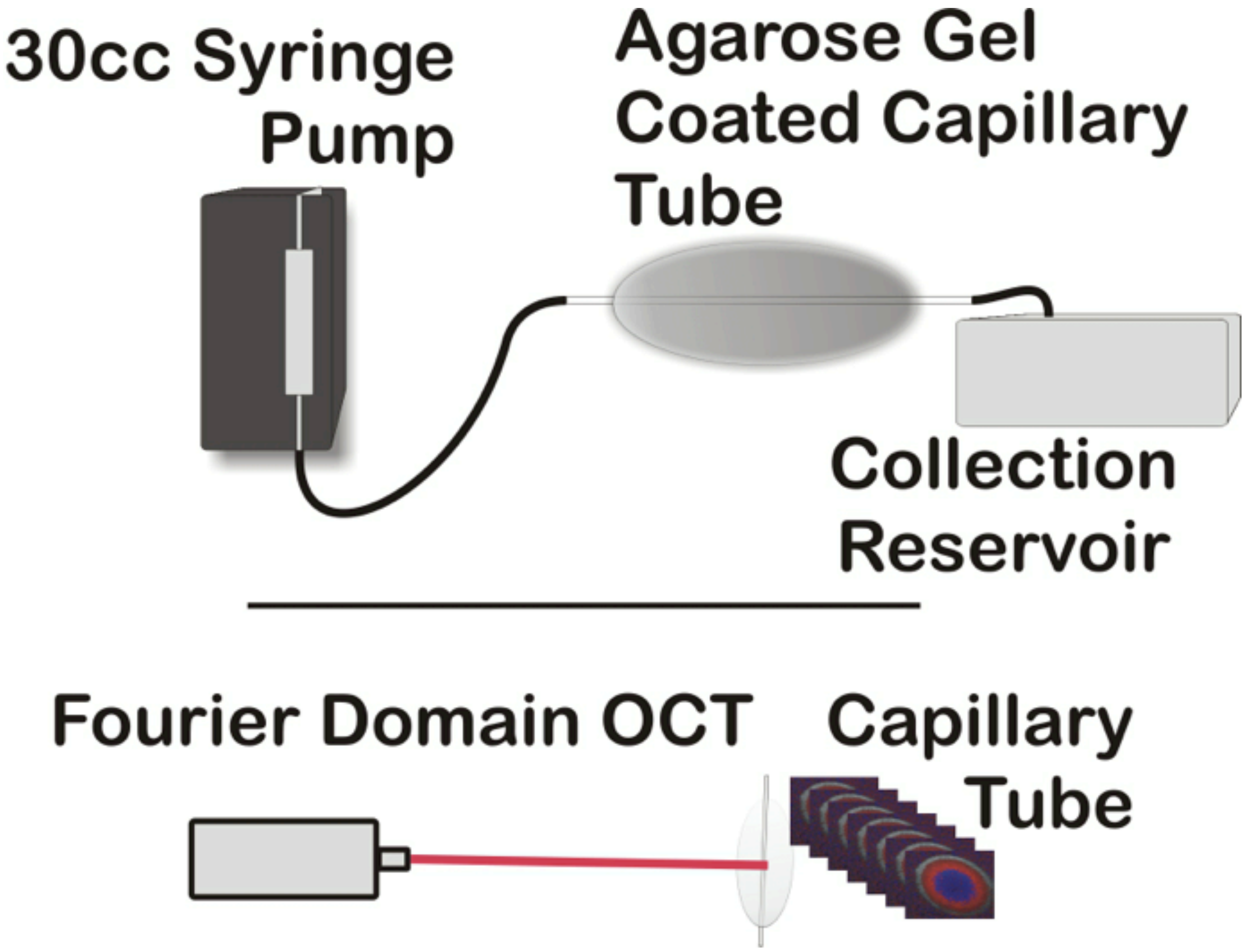

Figure 50. *In-vivo* Doppler model setup

11.2.2 Imaging

All imaging was performed using a customized SD-OCT consisting of an anterior segment eye scanner and optics engine (Bioptigen Inc., Research Triangle Park, NC) coupled with a 3-diode 100nm bandwidth broadband superluminescent diode (T-840, Superlum, Co. Cork, Ireland). This configuration yields a theoretical axial scan resolution of 3.5μm in medium. CCD integration time was set at 35 microseconds, yielding an A-scan frequency of 28,571 Hz and a Nyquist limit of 14,285 Hz for Doppler shifts. The velocity associated with this limit is a function of the center wavelength of the SD-OCT light source, the medium in which flow occurs, and the angle of the velocity vector relative to the SD-OCT beam,[206] and is calculated as shown in equation 5.

Equation 5. SD-OCT Velocity Equation from Doppler Shift

$$\text{Velocity} = \frac{\text{Doppler Frequency} \times \text{Center Wavelength}}{2 \times \text{Refractive Index} \times \text{Cos(Doppler Angle)}}$$

In water (refractive index = 1.33), and with velocity oriented perpendicular into the beam (angle = 0, cosine (0) = 1), an 870nm centered light source sampled at 28,000 Hz has a Doppler velocity Nyquist limit of 4.58 mm/sec.[206] Doppler shift measurements were recorded on a 16-bit scale. The center of the scale (32,767) represents a Doppler shift of zero. Negative Doppler shifts are evenly distributed from 32,766 to zero, with zero being the negative Doppler Nyquist velocity. Positive Doppler shifts are evenly distributed from 32,768 to 65,535, with 65,535 being the positive Nyquist Doppler limit. Thus, Figures 51 and 52 display Doppler samples with background noise fluctuating around 32,767 (0 Doppler). Doppler images were processed using ImageJ (ImageJ 1.38X, National Institutes of Health, USA). In Figure 51, velocity profiles at the location of Nyquist velocity (A) and through the center of the flow image (B) are shown. Note the random appearance of Doppler signals within the phase-wrapped and fringe washout center velocities (Figure 51B). The yellow line marks the location of velocity profile, and the red line marks the level of 0 Doppler shift.

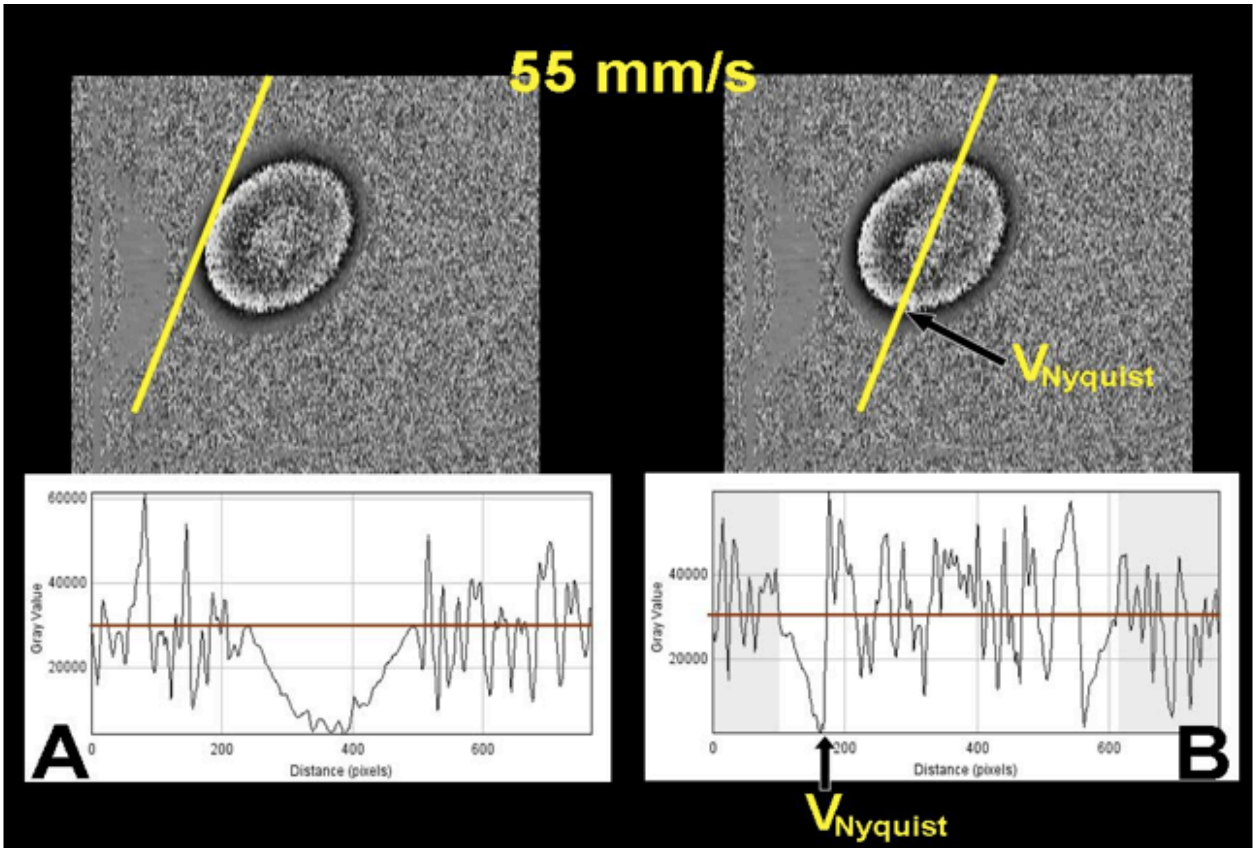

Figure 51. Doppler shift and velocity profile maps.

Examination of the Doppler signal (Figure 52A) suggests that phase wrapped twice in this measurement, i.e. the maximum center velocity is greater than two times the Nyquist velocity. Smoothing failed to produce a velocity profile (Figure 52B) that could accurately be measured. The red line (Figure 52) marks the level of 0 Doppler shift. The region in Figure 52 highlighted in blue is the background noise, consisting of random Doppler signals from the stationary glass tube, and the region highlighted in red is the Doppler flow under and up to the Nyquist limit. The region fading from green to white is the flow signature beginning at a measureable level of phase wrapping, but fading to noise due to fringe washout. The appearance of the light center (Figure 52) suggests that a second Nyquist limit may have been passed, however the noise observed in the velocity profile suggests that the signal has degraded beyond a useful level.

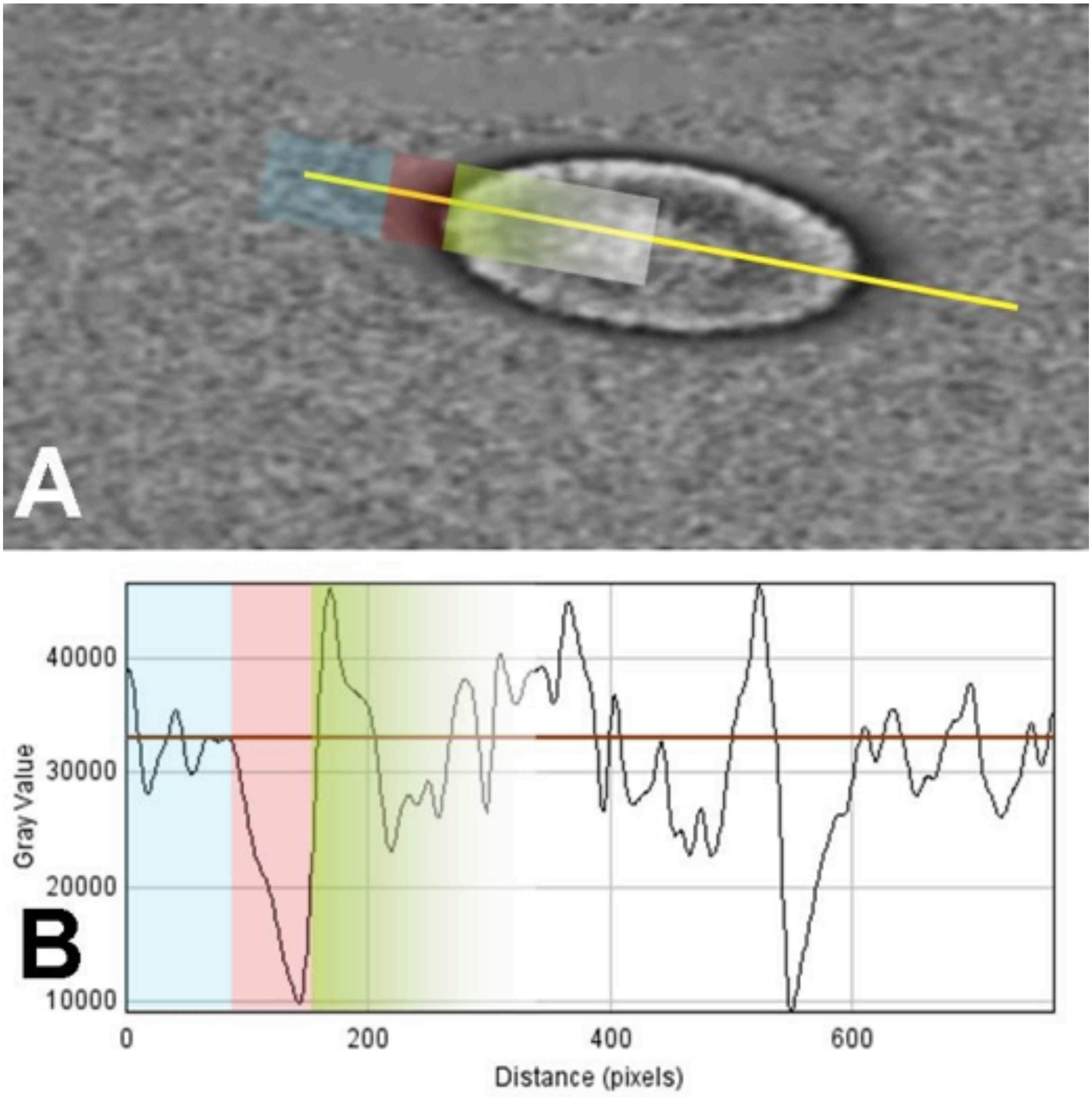

Figure 52. Doppler shift noise versus signal

A-scan density of 128 x 128 A-scans was spread over a 4 x 4 mm area, and each A-scan was 2 mm in length. Fifteen sequential stationary A-scans were obtained at each of the 128 x 128 positions, and Doppler shifts calculated from temporal changes in phase.

11.2.3 Measurement Validation

The model produced laminar flow at well-controlled rates. This means that the velocity throughout the tube was known because of the parabolic velocity distribution. With this knowledge, it was possible to determine exactly where the velocity would surpass the upper limit of the measurement device. This location was calculated for each flow rate used in the experiment. The known and measured location of the Nyquist limit velocity within the flow profile was compared. Specifically, expected and observed proportions of usable signal at each flow level were compared by Wilcoxon signed-rank comparison. Expected values were regressed against known values created by the model. $P < 0.05$ was considered statistically significant.

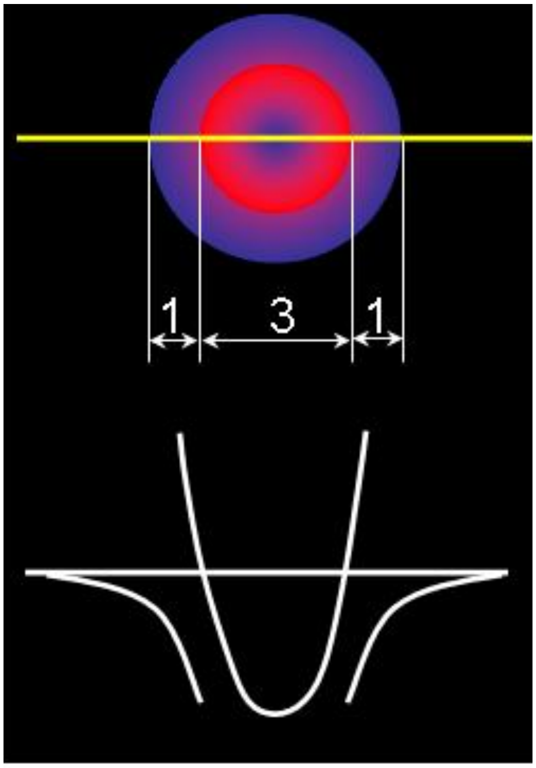

Figure 53. Presentation of phase-wrapping without fringe washout

11.2.4 Subjective Observations

In all reflectance and Doppler images, a clear laminar flow pattern was observed, with maximum velocity appearing in the center of the flow column, and an apparent parabolic velocity distribution observed in the "bull's-eye" pattern of the Doppler image, and the non-phase-wrapped portions of the cross-sectional velocity profiles (Figure 53). Phase wrapping was observed (Figure 53). In Figure 53, the outer circle represents flow below the Nyquist limit, and the portion of the velocity profile below Nyquist has a length of 2 (1+1), out of a total length of 5 (1+3+1). Thus, 40% of the velocity profile occurs below the Nyquist limit. The predicted percentage of flow below Nyquist was used as the outcome parameter. The velocity profile (Figure 53 bottom) is obtained at the yellow line.

11.2.5 Doppler Imaging and Flow Orientation

Clear, well focused 3D reflectance and Doppler domain image sets were successfully recorded at mean flow speeds of 35.0, 38.5, 42.8, 48.1, and 55.0 mm/sec. The position of the fluid column relative to the scanning beam was determined by locating two points on the column in space: x_1, y_1, z_1, and x_2, y_2, z_2. Specifically, these points were identified on two different slices (x1 and x2, Figure 54) widely spaced within the 3D data set. The length of the tangential component (Figure 54) was calculated as

Equation 6. Tangential magnitude from Cartesian coordinates

$$Tangential = \sqrt{(x_2 - x_1)^2 + (y_2 - y_1)^2}$$

and the measured component as z_2-z_1. The angle between the beam and flow vector was equal to

Equation 7. Doppler angle

$$\tan^{-1}\left(\frac{Tangential}{measured}\right)$$

The orientation of the tube velocity vector relative to the illuminating laser was computed, yielding a Doppler angle of 83.24º (Figure 54).

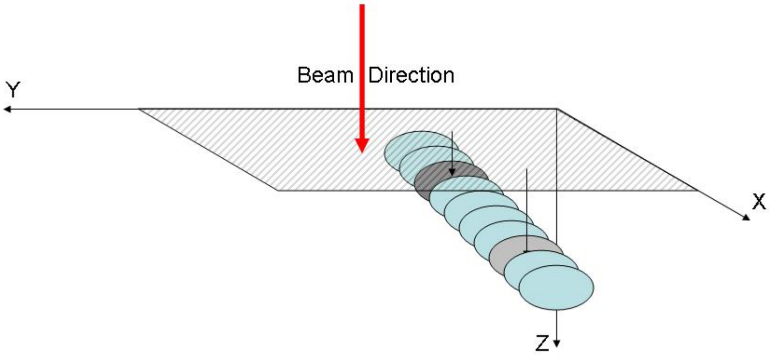

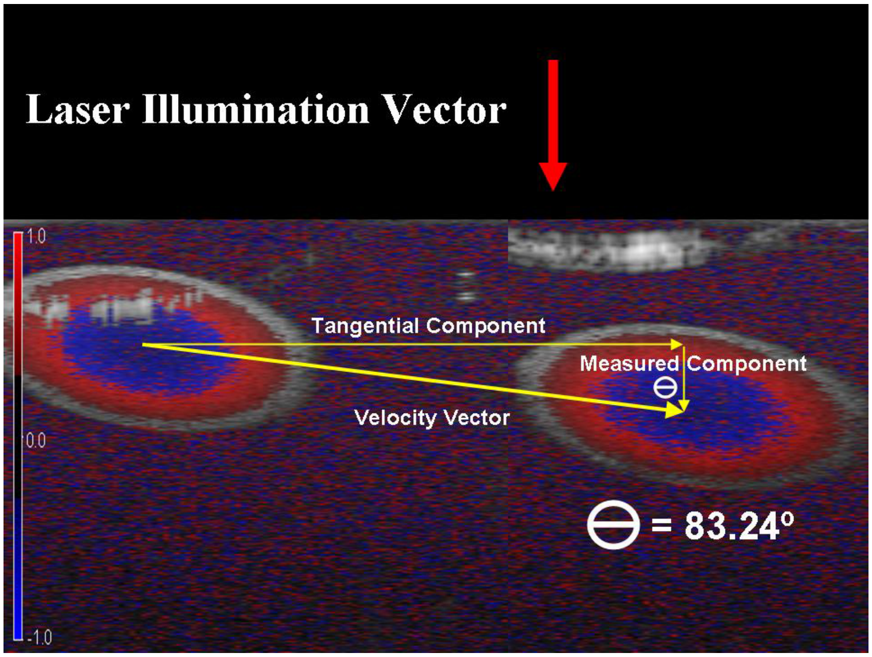

Figure 54. The position of the fluid column from two frames

Because the measured component of the flow vector was oriented away from the illuminating laser beam, Doppler shifts were negative. Reflectance within the flow column decreased with increasing velocity (Figure 55). Fringe washout occurred in the experimental setup, resulting in the loss of signal from milk moving at velocities similar to those known to exist in the large vessels of the eye (Figure 55 bottom).

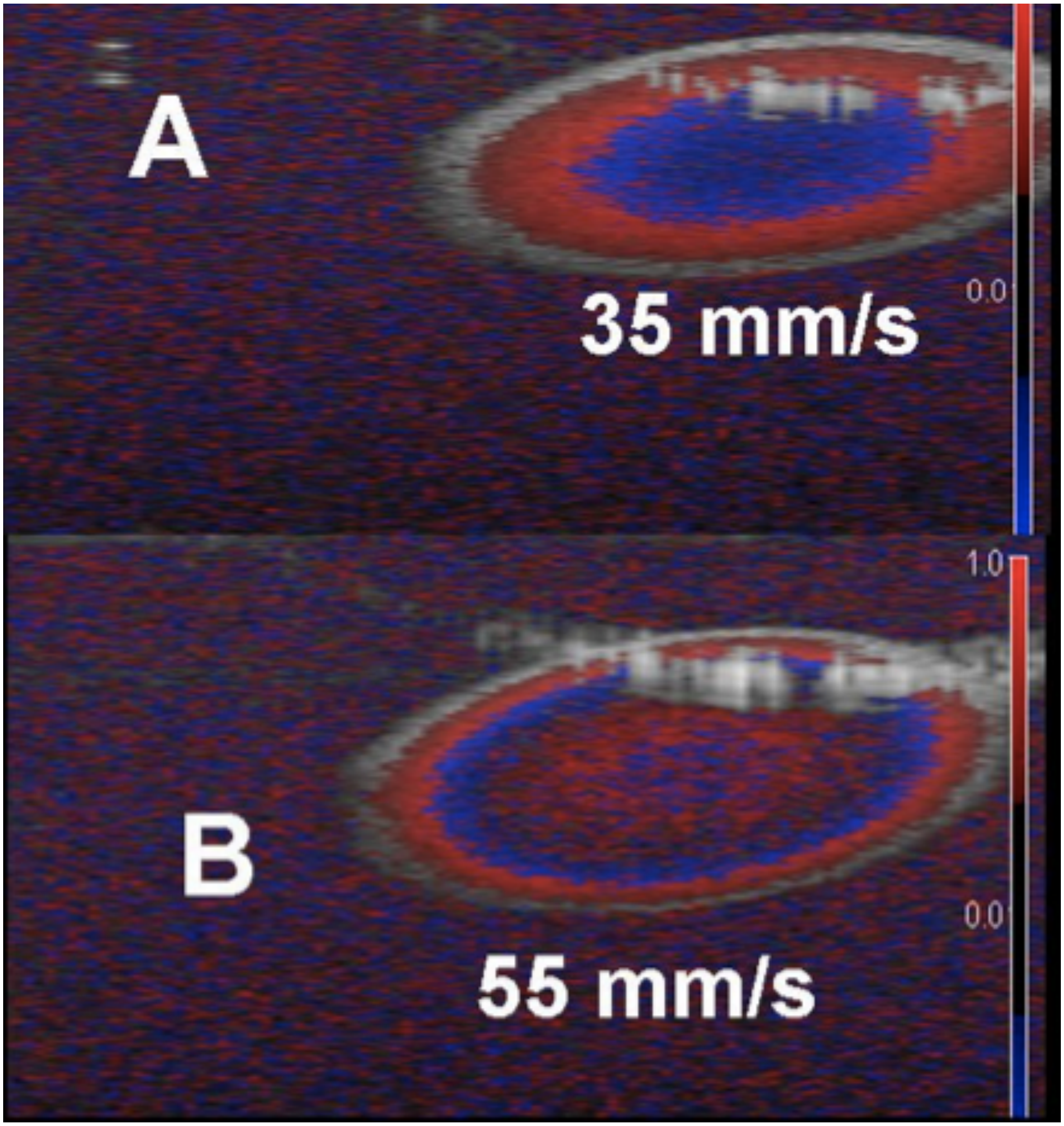

Figure 55. Examples of fringe washout

11.2.6 Phase Wrapping

Phase wrapping was observed at all measured flow velocities. The Nyquist velocity, or location of phase wrap, was observed at the point where black Doppler velocity signal becomes white abruptly (Figure 51). Velocity profiles were created at the Nyquist frequency (Figure 51A), and through the center of the Doppler image (Figure 51B). Smoothing (3x3 averaging kernel) of the Doppler image (Figure 52) failed to produce a recognizable phase-wrap signal as presented in the theoretical Figure 56. Under ideal conditions, Doppler signals would be below the Nyquist limit (Figure 56A). If the Doppler signals exceed the Nyquist limit (Figure 56, arrows), phase wrapping will occur, and a velocity pattern similar to (Figure 56B) is expected. The red line in Figure 56 marks the level of 0 Doppler shift.

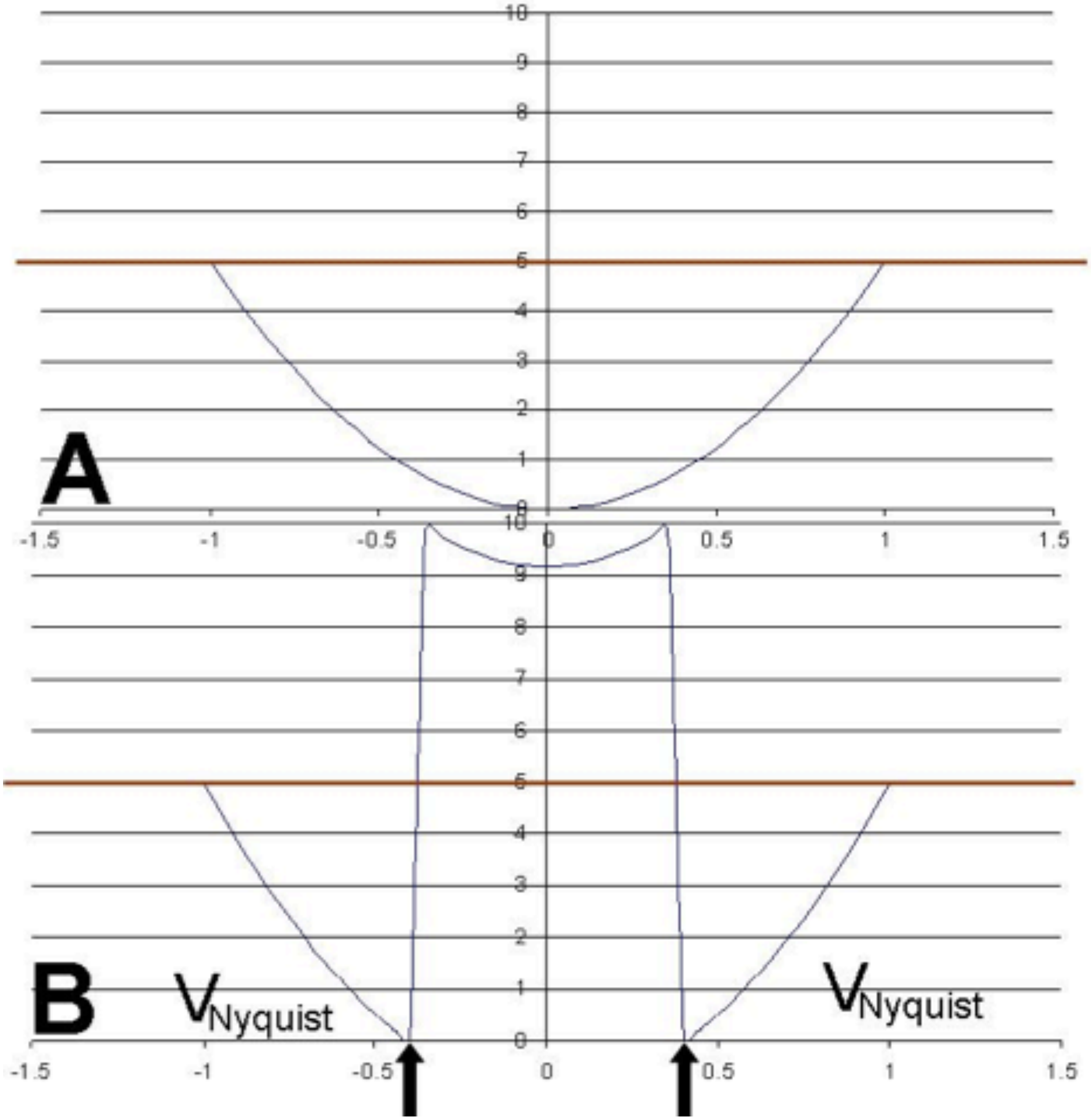

Figure 56. Appearance of velocity profile in ideal phase wrapping

11.2.7 Doppler Validation Below Nyquist

There was no statistically significant difference between predicted and observed percentage of signal below Nyquist. The observed percentages of the velocity profile at or below Nyquist frequency was highly correlated with the predicted percentages ($R^2=0.934$, p=0.007; Table 11).

Table 11. Predicted and observed Nyquist location

Mean Velocity (mm/sec)	Predicted Percentage Below Nyquist	Observed Percentage Below Nyquist
35.0	47.86%	44.28%
38.5	41.86%	40.27%
42.8	36.40%	37.80%
48.1	31.43%	31.68%
55.0	26.75%	23.59%

11.3 DISCUSSION

11.3.1 Summary of Findings

In the present study, we found that Doppler measurements, when performed within the measurement limits imposed by optical and scan parameters, was in excellent agreement with known values. However, as velocities increased above the Nyquist limit and phase wrapping was *observed*, fringe washout reduced both reflectance and Doppler signals resulting in the degradation of Doppler signal to noise. It is possible to limit assessment to locations where flow is below Nyquist (Figure 51A). Reflectance images display phase wrapped flow as regions without observable reflective sources; thus blood vessels typically present as black spaces in OCT images. Doppler images display phase wrapped flow fields as areas containing stark black to white (or red to blue in color images) circles of transition surrounding a salt and pepper appearing area of pure noise (Figures 52 and 55).

11.3.2 Phase Wrap and Fringe Washout

SD-OCT is capable of measuring Doppler shifts throughout each A-scan, but large Doppler shifts induce phase wrapping (Figure 55).[207] Given laminar flow in the present study, it might appear that phase unwrapping techniques could recover the actual velocity profile at velocities above the Nyquist limit.[209] However, progressive signal degradation after phase wrapping may prevent recovery of the true velocity signal. Within the fringe pattern, Doppler shifts physically manifest as a lateral drift across the CCD within the spectrometer. Faster velocities produce larger Doppler shifts resulting in faster drift. These drifts only occur within the frequency components associated with the location of the source of the Doppler shift, leaving other frequencies for the most part unaffected. If this drift is fast enough, fringe washout occurs.[210] Specifically, several peaks and troughs move across individual CCD pixels within the integration time of the camera, resulting in destructive interference and signal loss. This is the reason that large blood vessels appear to be black within the center. The phase unwrapping techniques referenced previously may be useful in situations where Nyquist limit violations result in strong but erroneous signals, however in the case of SD-OCT Doppler measurements, excessively high Doppler shifts result in signal drop-out, leaving only noise in the measurement.

It might also be thought that given valid velocity measurements in the low velocity edge of the flow column, the actual flow distribution might be recovered by modeling the available accurate measurements to a parabolic flow distribution. This technique was employed in the present study to predict the location in the flow column at which phase wrapping would occur. This technique is only applicable to biological systems if laminar flow is known to exist. When flow is laminar, the mean velocity is equal to half of the maximum velocity; the mean velocity in a turbulent flow system is equal to the mean. Studies of blood flow in glass tubes with diameters similar to those of retinal vasculature suggest that velocity was 1.6 times greater than the mean,[211] suggesting that flow in the retinal vasculature is neither purely laminar nor turbulent. Fitting measurements to a parabolic distribution would be invalid in either type of vessel.

The findings in the present study suggest that the current setting of SD-OCT is of limited use in biological systems. The Nyquist limit of 4.58 mm/sec of the system used in this study is typical for SD-OCT configurations using currently available linear array camera technologies. This limit is far less than the peak arterial blood velocity in retinal arteries.[212] In order for arterial velocity to be scaled down by geometry, specifically the cosine term in the Doppler velocity equation, to be measurable by SD-OCT, the flow vector (i.e. the artery) would need to be oriented within approximately 4° of perpendicular to the beam. However, the present system's setting is appropriate and useful for the measurement of very small velocities such as that in the retinal capillaries, or in the aqueous drainage vasculature.

11.3.3 Conclusions

SD-OCT provides objective Doppler measurements of laminar fluid flow in an *in vitro* flow system in a range up to the Nyquist limit. Efforts to obtain velocity measurements above the Nyquist limit may be impeded by the severe loss of data quality in the phase-wrapped range of velocities. These limits exclude measurements in large retinal vessels, but allow accurate assessment of slow velocity systems such as retinal or anterior segment capillaries or the aqueous drainage system.

12.0 VALIDATION OF DOPPLER IN IN-VITRO SD-OCT SCANS OF THE AQUEOUS HUMOR OUTFLOW SYSTEM

12.1 INTRODUCTION

Measuring flow has a number of medical, research and industrial applications. The use of Doppler ultrasound[213] and laser flowmetry[214] has changed the way medicine is practiced and our understanding of physiology[215]. However, low velocity flow fields are often not visible. It would be advantageous if these flow fields could be made visible, facilitating measurement, without perturbation. In the previous chapter, the ability of SD-OCT to measure Doppler, as well as its limitations, were demonstrated. Here, Doppler measurements are applied to aqueous humor outflow cadaver model eyes.

SD-OCT is conventionally used as an imaging technique for high-resolution structural scans of optically turbid tissues[91,216]. Recent increases in acquisition time makes OCT a promising device for detecting microscale flows[217]. Previous work demonstrated OCT's ability to detect blood flow in the human retina[218], skin[219] and the heart.[220]

Only fluids containing scattering media at the wavelength of the OCT light source will show a Doppler shift. A number of physiologically relevant flows, such as that of the aqueous humor, lymphatics, synovial fluids and cerebrospinal fluid may not show a distinct Doppler signal. Aqueous humor is of particular relevance to glaucoma because the balance between its production and outflow controls intraocular pressure. Elevated intraocular pressure is the primary risk factor for the presence and progression of glaucoma, an optic neuropathy that is the second leading cause of blindness worldwide[48]. Improving our understanding and measuring aqueous outflow is an important process in understanding glaucoma.

Nanoparticles have increasingly been used in areas of medicine as well as industry. Magnetic nanoparticles have been used as an MRI contrast agent and anti-cancer heating agent[221]. Nahrendorf et al[222] demonstrated the use nanoparticles to enhance contrast on macrophages in atherosclerotic plaques. Oldenburg et al[223] established the use of gold nanorods as a structural contrast agent for OCT. OCT Doppler imaging has been previously used to detect movement of magnetic nanoparticles[224].

Despite the use of nanoparticles as structural contrast, the use of nanoparticles as functional contrast to increase visibility of a physiological process has not been reported. This chapter describes the use of plasmon resonant gold nanorods as a functional contrast agent for OCT and demonstrates an application by imaging *ex-vivo* the anterior outflow pathway of porcine and human eyes.

12.2 METHODS

12.2.1 Titration

A concentrated polyelectrolyte sodium salt coated plasmon resonant GNRs (60nm length 12nm radius, nanorods LLC) was titrated with deionized water to different concentrations. The concentrations scanned were: 0.3, 0.4, 0.5, 0.7 and 1 x 10^{12} GNRs/mL. Concentrations were increased until a subjectively strong Doppler signal was observed throughout the entire flow field.

Doppler scans (2mm x 3mm x 2mm, 700 x 20 x 1024) were acquired using SD-OCT (Bioptigen, Durham, NC) while the fluid was stationary within a capillary tube with a radius of 0.32mm. 12 Doppler frames were acquired for analysis with an acquisition rate of 28kHz, resulting in a Nyquist limit of 4.62mm/s normal to the scanning beam. Doppler and structural scans were analyzed to determine the concentration at which it was possible to scan through the volume of the tube while maintaining Doppler signal.

12.2.2 Validation

A 0.7×10^{12} GNRs/mL solution mixed with deionized water was passed through a glass tube with radius 0.32mm. The glass tube was suspended 45 degrees to the direction of the OCT scanning beam. The angle to the scanning beam was independently confirmed on the structural scans in SD-OCT.

The GNR solution was pumped at a volumetric rate of 0.335mL/min with a constant pressure perfusion system. Flow rate was measured by changes in the weight of solution remaining in a reservoir. Doppler scans (2mm x 0.4mm x 2mm, 700 x 20 x 1024) were acquired using SD-OCT (Bioptigen).

12.2.3 *Ex-Vivo* Porcine Outflow Model

Three cohorts porcine eyes were warmed to 40 degrees Celsius then perfused in the anterior chamber with a) mock aqueous alone (control, n = 6) and b) 1×10^{12} GNRs/mL solution with mock aqueous (n = 3). The eyes scanned within 16 hours of death. A DATAQ acquisition unit recorded rate of perfusion in the constant pressure perfusion system. Of the three eyes perfused with GNRs, the aqueous humor within the anterior chamber was replaced with GNR solution at the start of perfusion in the final 2 eyes.

A 27-gauge perfusion needle was inserted through the cornea, between the lens and the iris. The tip of the needle was placed near the ciliary muscle, the physiological site of aqueous production. The needle was inserted into the nasal side for all eyes. Before imaging GNR solutions flowed under constant pressure for 20 minutes to allow outflow to stabilize. Doppler scans (700 x 20 x 1024) were taken over a 4mm x 4mm x 2mm area with 12 repeated scans using OCT. Samples of the mock aqueous and GNR solutions used in these perfusion experiments were scanned using a spectrophotometer to determine exact optical density (used to confirm concentrations).

Flow rates were calculated by identifying all observed Doppler signals within the 360° SD-OCT scans, calculating the velocity in that position, measuring cross-sectional outflow vessel area in the associated structural image at that location, and calculating flow. Total volumetric flow was calculated as the sum of observed flow in the limbus. Paired flow and structural images are described in the previous chapter.

12.2.4 *Ex-Vivo* Human Outflow Model

The same model described above for the porcine eye was used for the human eye. As with the second two porcine eyes, the aqueous humor in the anterior chamber of the human eye was replaced with GNR solution via a second needle paracentesis. The GNR concentration was increased to a 3:10 GNR/mock aqueous solution concentration.

12.3 RESULTS

12.3.1 Titration

GNRs created a visible Doppler signal across a range of concentrations: 0.3, 0.4, 0.5, 0.7 and 1 x 10^{12} GNRs/mL. The optimal concentration of GNRs for enhanced Doppler signal without the creation of obstructive shadows in the structural image was 0.7 x 10^{12} GNRs/ml. All Doppler scans of different titrations are shown in Figure 57.

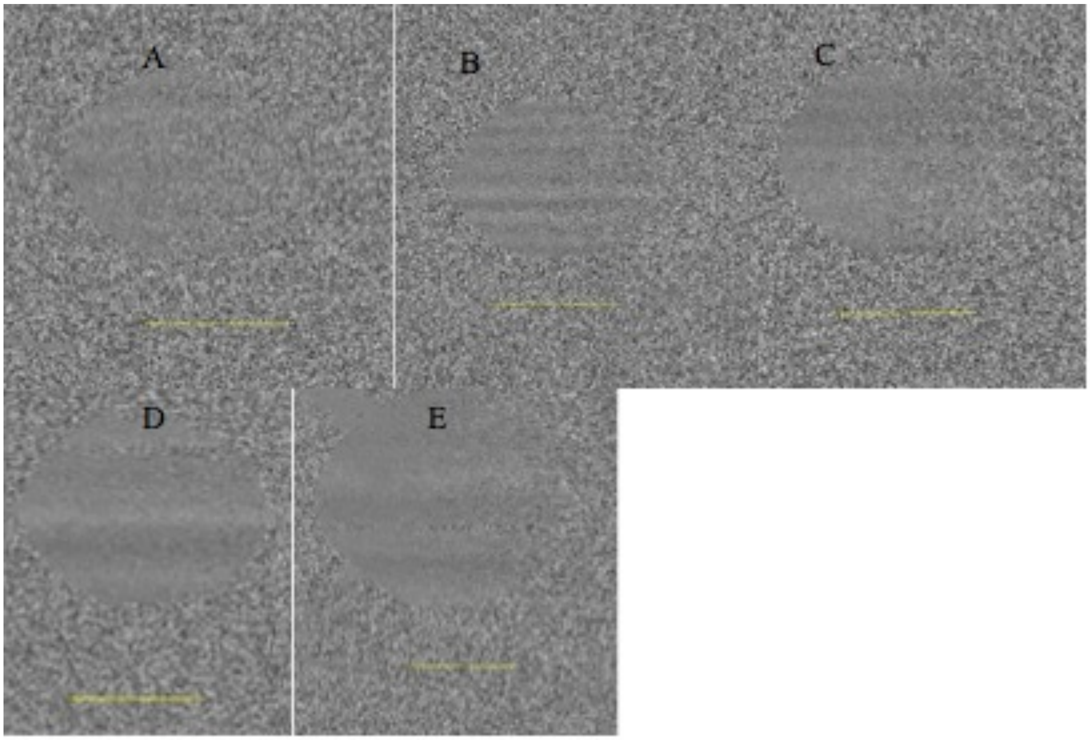

Figure 57. Doppler scans of non-flowing nanorods at a) 0.3, b) 0.4, c) 0.5, d) 0.7 and e) 1x1012 GNRs/mL

12.3.2 Validation

The OCT Doppler cross-sectional scan through the 0.7 x 1012 GNRs/mL solution is shown on Figure 58. A theoretical velocity profile was calculated based upon the flow measured by the perfusion system and superimposed on the Doppler velocity profile in Figure 59. The difference between predicted and observed velocities is presented in Figure 60.

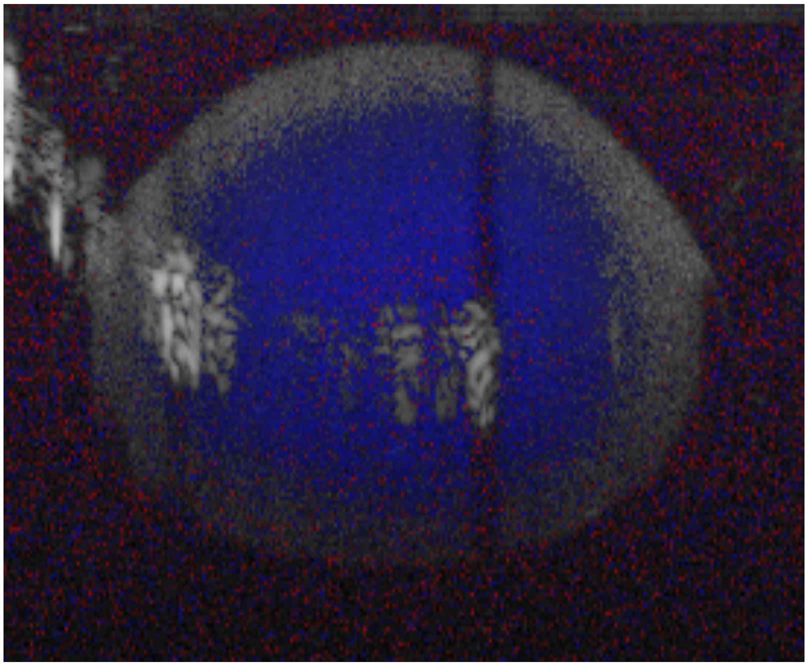

Figure 58. Doppler image of GNR solution flow field (0.7 x 1012 GNRs/mL)

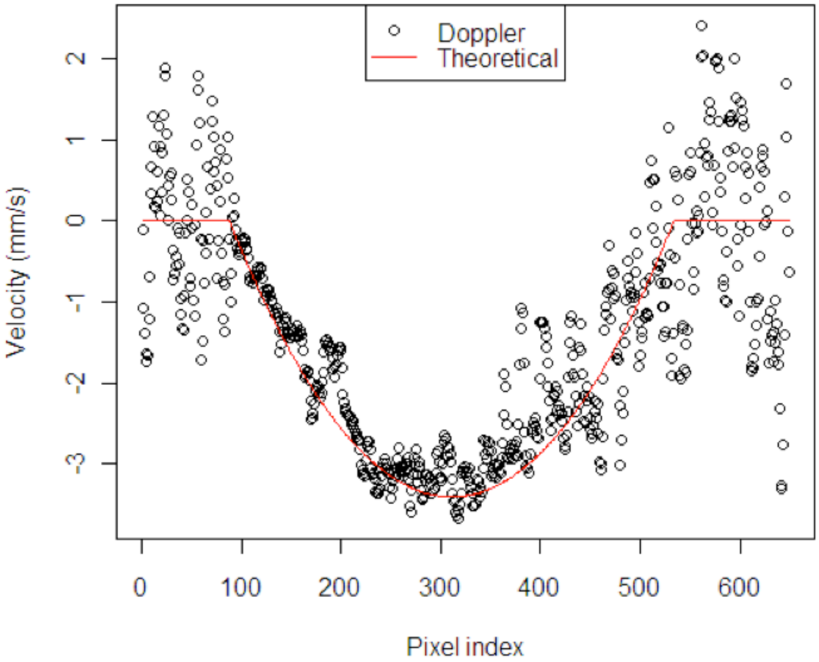

Figure 59. Theoretical versus actual velocities

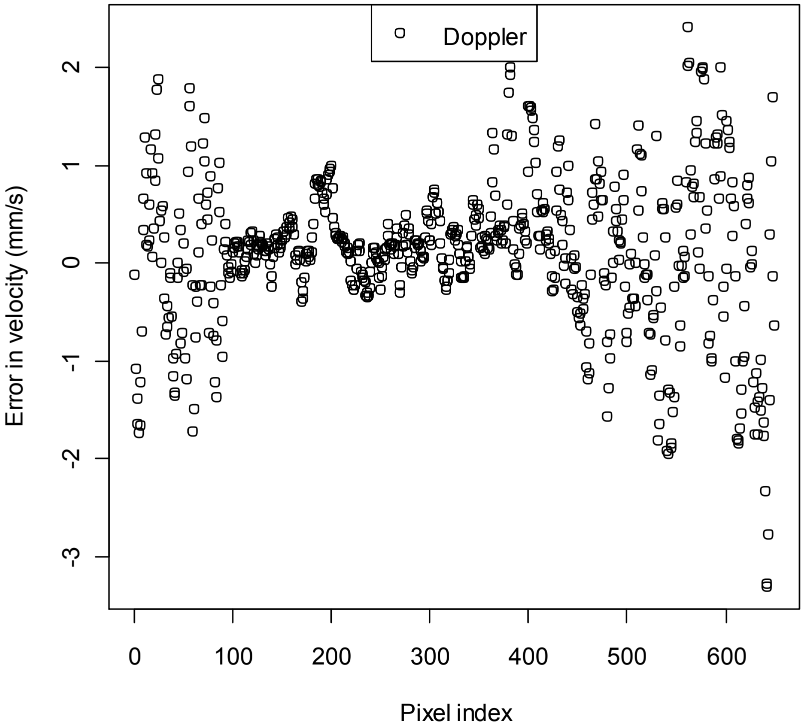

Figure 60. Difference between predicted and observed velocities

12.3.3 *Ex-Vivo* Porcine Eye Model

With mock aqueous alone, the Doppler signal in the pig anterior chamber (Figure 61) was weak. The addition of GNRs increased the contrast within vessels and showed clear Doppler signals in Figure 61. The velocity profile of the Doppler scan, in Figure 62, shows laminar flow within the vessels.

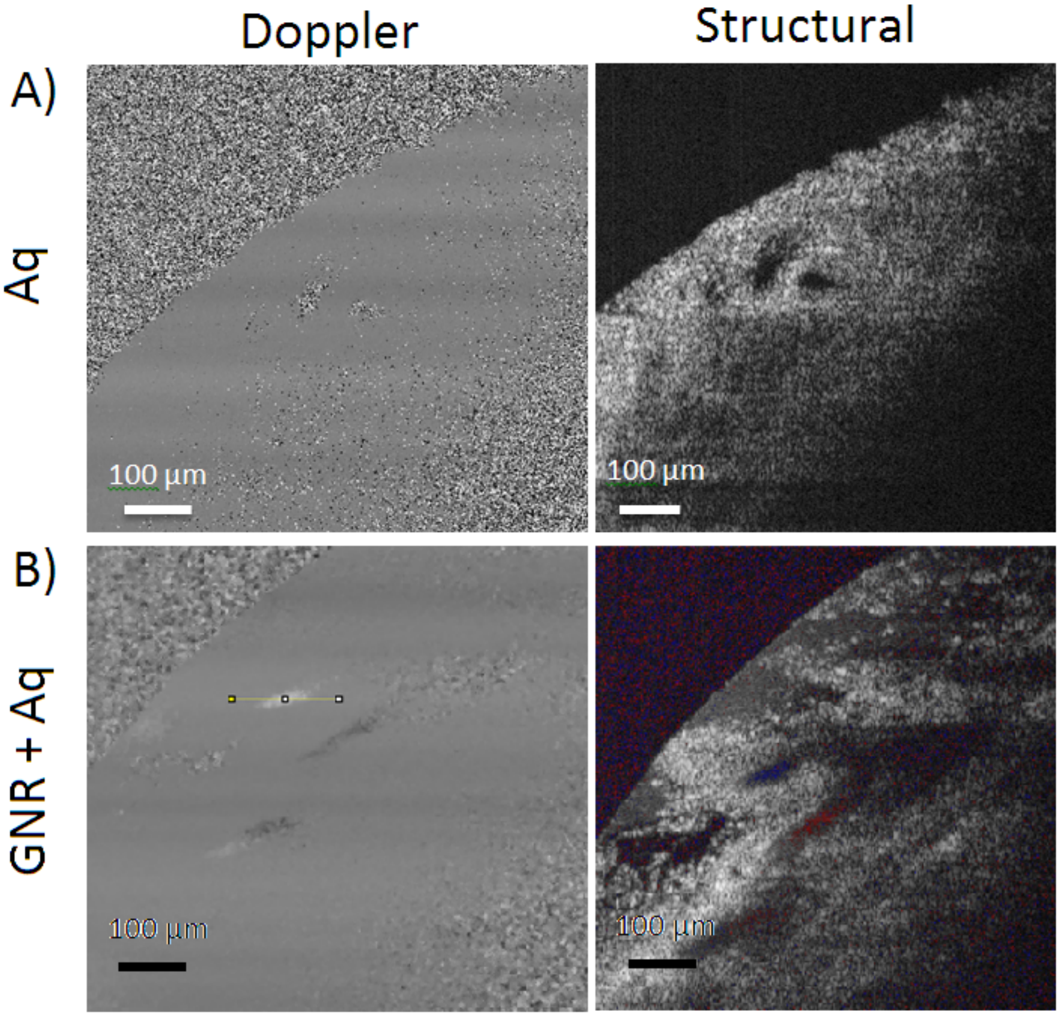

Figure 61. Doppler and structural OCT of the outflow drainage system in porcine eyes perfused with a) mock aqueous and b) 1 x 10^{12} GNRs/mL with mock aqueous.

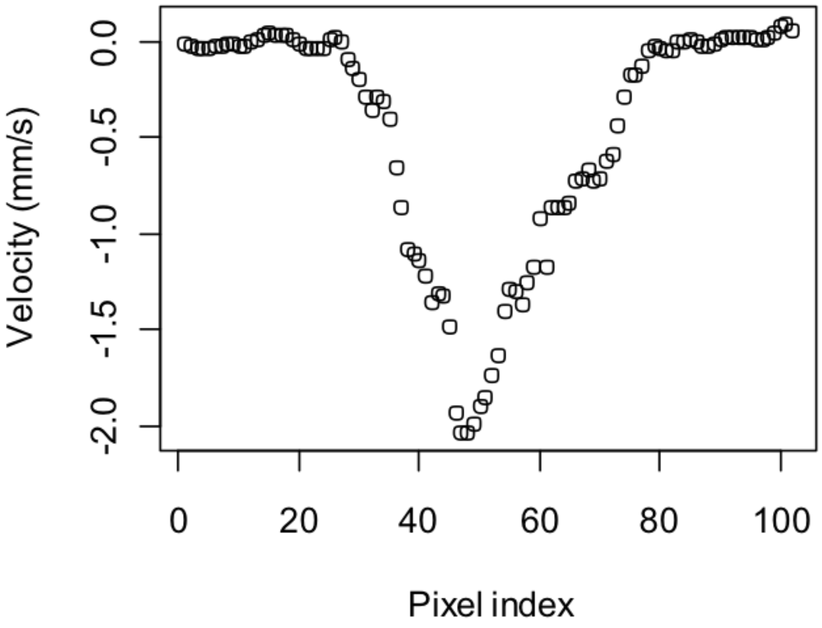

Figure 62. Velocity profile of the GNR enhanced Doppler scan in a porcine eye

Doppler scans of the first of the three GNR porcine eyes produced no discernable Doppler signal. The known flow rate based on the change of reservoir weight over time was 3.42 µl/min. Integrating observed Doppler signals over the limbus of the second porcine eye yielded a calculated flow rate of 4.41 µl/min in the Doppler SD-OCT scans for eye 2. The known flow rate for the second eye based on the change in reservoir weight over time was 6.25 µl/min. The third eye and had a SD-OCT measured flow rate of 7.31 µl/min and known flow rate of 7.02 µl/min.

12.3.4 *Ex-Vivo* Human Eye

Observed Doppler signals in the human eye did not yield sufficient Doppler signals to produce a measurement. Figure 68 shows a large deep vessel (yellow arrows). Since this is a cadaver eye, it is likely that the vessel is open due to the pressure of the mock aqueous GNR solution within the anterior chamber and outflow system. Despite the likely presence of GNR solution, the Doppler signature in this region is characteristic of pure noise (Figure 63, yellow arrow right). Some small traces of consistent Doppler signal were observed. Figure 64 shows the structural and Doppler images with a small region featuring a consistently small white path in the region of an aqueous vein (yellow arrows). Figure 65 shows a magnified view of the same region. Note that the Doppler signals within the region correspond to the visibly open portions of the aqueous vein. It was previously shown (Figure 16, chapter 5) that the SD-OCT slice may either contain both septa and internal open spaces, or in this case, may only intersect with portions of a tortuous vessel. Figure 66 shows the velocity profile of a line extending throughout the limbus, and intersecting a portion of the white Doppler signal. Note the scale of the graph. In 16-bit space, positive Doppler shifts are encoded with values between 32,768 and 65,535 (at the Nyquist limit). With a surrounding Doppler shift level of approximately 32,700, the peak shift in this sample is only 38,000, representing a velocity of 0.74mm/sec; assuming that the velocity is vertical in the image at the point of measurement. Figures 67 and 68 show another location where consistent Doppler shifts were observed, but with much smaller intensities and corresponding velocities. Figure 69 shows what appears to be a large measurable velocity profile in a large superficial vessel. Note that the velocity is largest at the center, and trails off at the edges, suggesting laminar flow. However; examination of the region of active Doppler as a whole shows the salt and pepper pattern characteristic of noise. It is difficult to determine if the observed consistent area of positive Doppler signals truly represent a true signal, or just a fortunate gathering of noise. The presence of and scattered locations of negative Doppler signals within a field of positive shift suggests that this is noise, and that numerous velocity profiles must be made and examined before allowing this vessel to be included in a flow measurement.

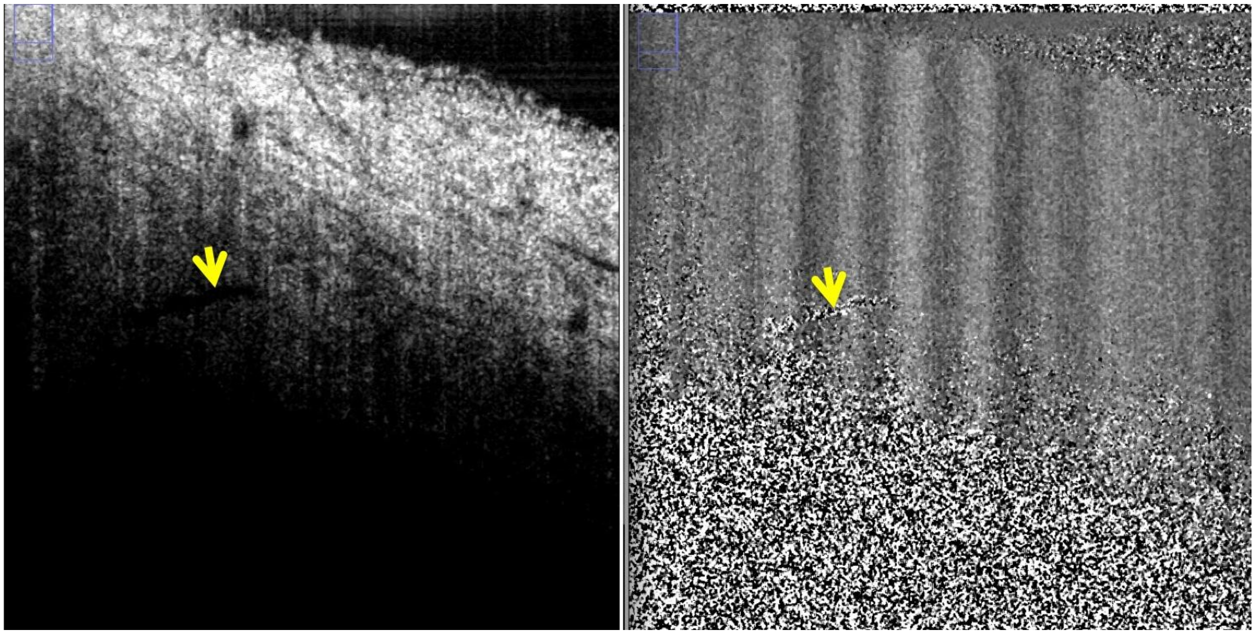

Figure 63. Large vessels had a Doppler signature of noise (see porcine Figure 61 A above)

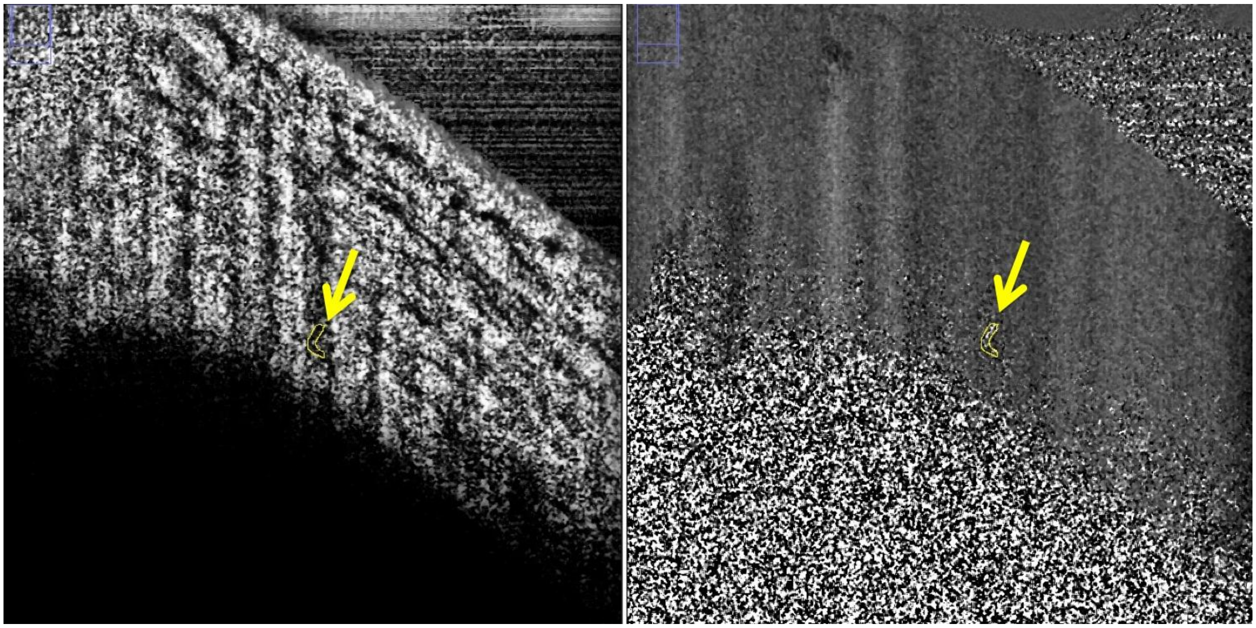

Figure 64. Some small regions presented with consistent Doppler signal, but in very small areas.

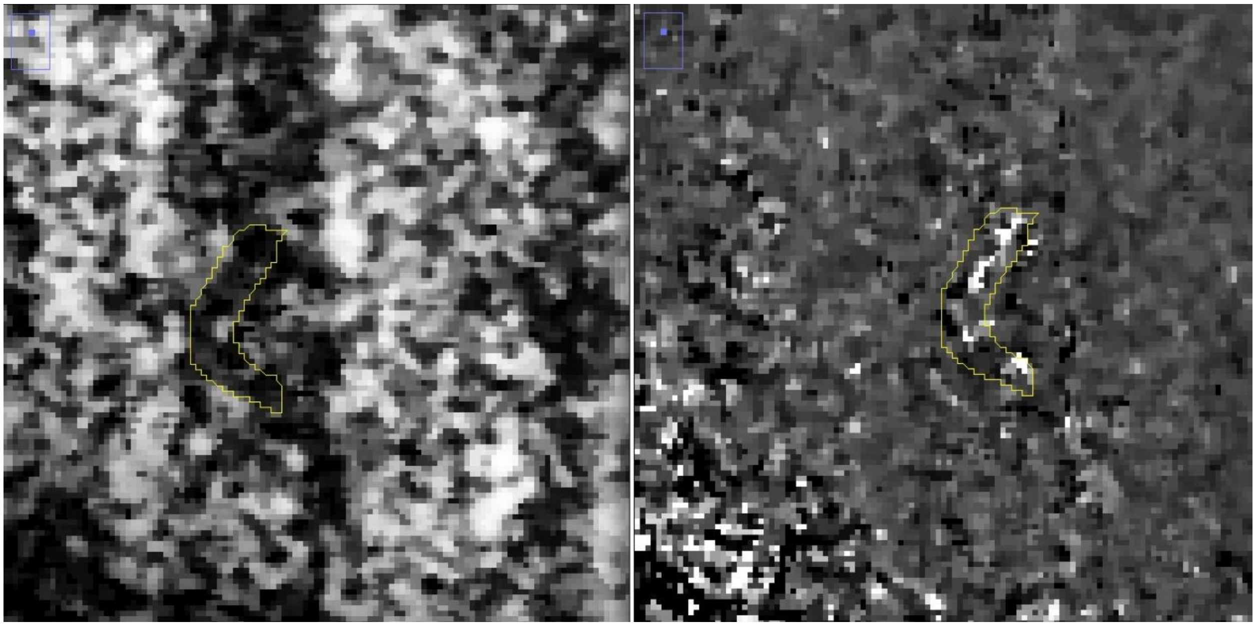

Figure 65. A magnified view shows that the regions of white Doppler signal correspond to the dark open spaces within the outflow vessel.

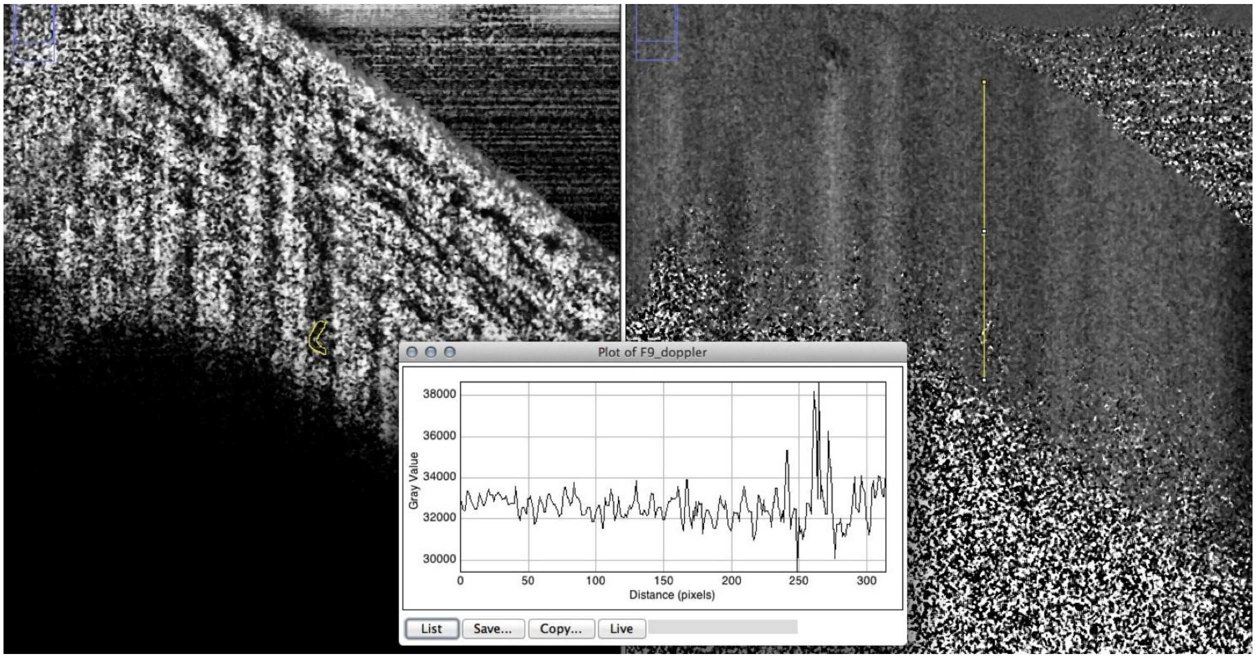

Figure 66. The Doppler signal within the small vessel is minimal but detectable and larger than background scatter.

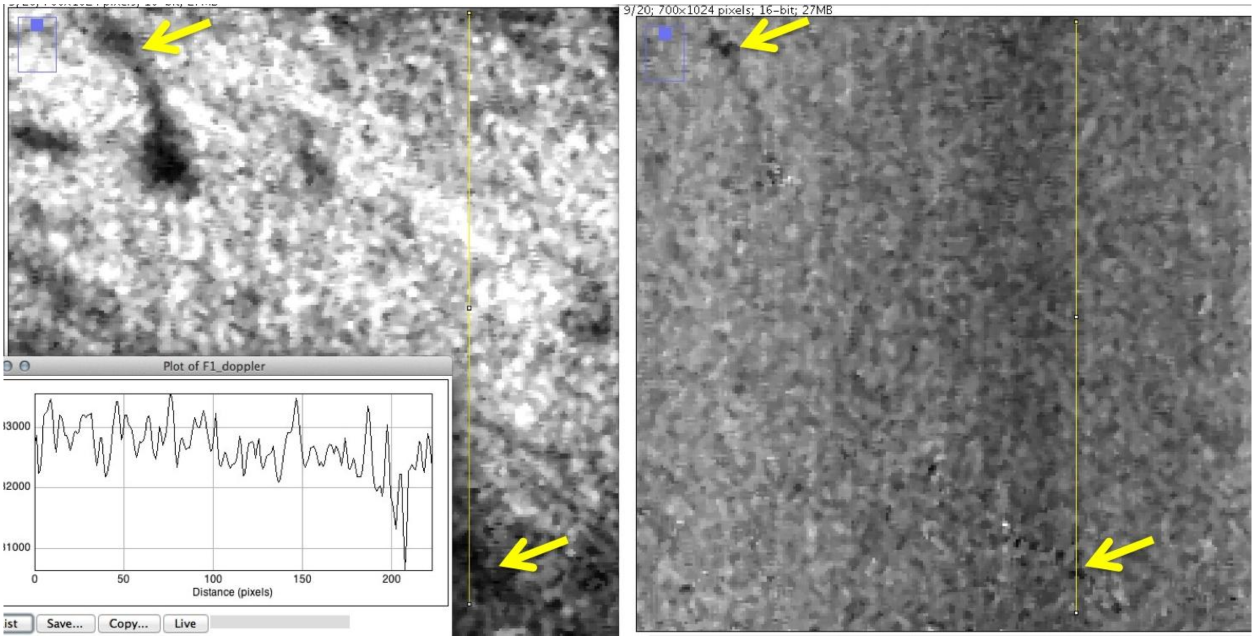

Figure 67. Another slice displayed two regions of small negative Doppler with signals of a similarly small magnitude.

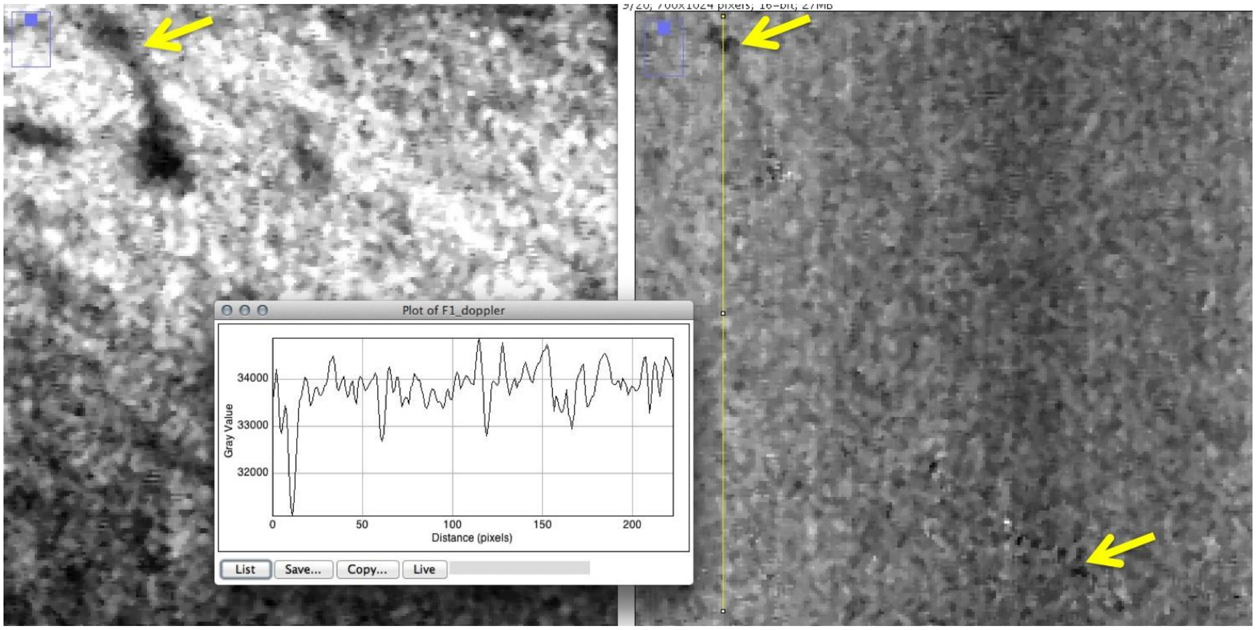

Figure 68. The second Doppler region signal

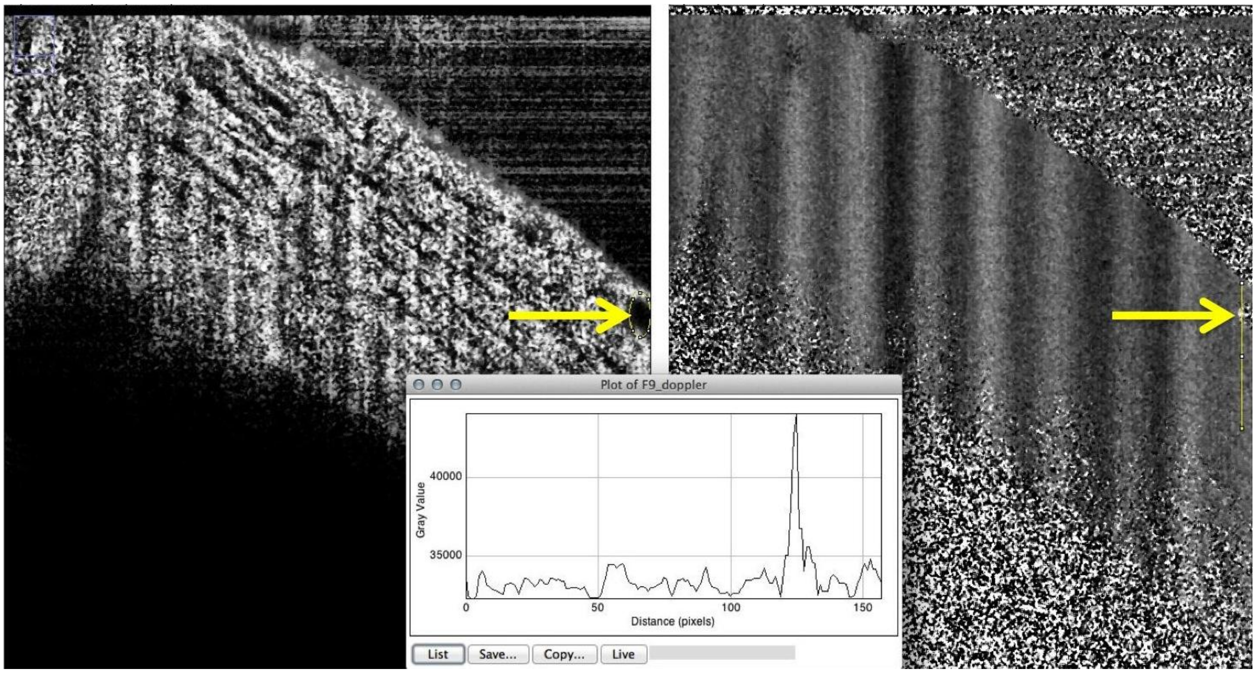

Figure 69. Despite containing a large measureable Doppler signal, this region ***may*** be noise as suggested by the salt/pepper Doppler pattern.

12.4 DISCUSSION

12.4.1 Summary of Findings

This study demonstrates the first use of gold GNRs for the purpose of enhancing a functional signal with OCT. An optimal concentration of GNRs was identified to maximize penetration without losing signal. The use of GNR to enhance Doppler OCT was validated in an experiment with known flow parameters. Finally, the use of GNRs and Doppler OCT was demonstrated ex-vivo in porcine eyes, providing the first Doppler OCT scans of anterior chamber outflow. The result was an accurate measurement of aqueous humor outflow with SD-OCT in the porcine eye.

While GNRs successfully infiltrated the porcine outflow system, they failed to flow through the human outflow system in sufficient concentration to produce a measureable Doppler signal.

The tradeoff between signal strength and depth of penetration plays an important factor in the optimal GNR concentration. As seen in Figure 62, the Doppler signal was strong at $0.7x10^{12}$ GNRs/mL while maintaining the ability to scan through the entire tube. However, once concentration increases to $1x10^{12}$ GNRs/mL, there is an increase in Doppler noise as the A-scan penetrates the solution.

As the OCT scanning beam traverses the solution, scattering and absorption reduces the signal-to-noise ratio of the system. Increasing GNR concentration will increase the quality of Doppler signal. However, the OCT system will experience lower depth of penetration. Due to the small size of vessels present in the anterior chamber, a $1x10^{12}$ GNRs/mL solution was used to perfuse the ex-vivo porcine eye for two reasons. First, the solution will mix with aqueous humor already present in the anterior chamber, reducing its concentration. Second, higher GNR concentrations should not cause a large signal loss because typical vessel size in the anterior chamber is approximately an order of magnitude smaller than the glass tube. Therefore, depth of penetration is less of an issue in the ex-vivo porcine experiments.

A comparison between theoretical and actual flow measurements validates the use of GNR to enhanced Doppler signals. Figure 59 demonstrates GNR's ability to measure Doppler signal. As expected, noise level increased as the scanning beam penetrates a single line scan due to increased absorption and scattering as the light passes through the solution. A comparison of error with respect to a theoretical in Figure 58 demonstrates that the measured velocity profile is representative of the theoretical with a center at 0.192±0.498mm/s. Figure 60 shows that in the histogram, the distribution of the error is relatively normal. However, the histogram has a left skew. This systematic error may result from slight vibrations during the scanning procedure, resulting in an alternating pattern on the Doppler scans.

GNRs' potential to enhance Doppler signals is demonstrated in the ex-vivo porcine model. Prior to scanning, a mix of GNR and mock aqueous was tested to insure that it does not alter the functional properties of the nanorods. Figure 66 shows that the Doppler signal was weak in the porcine eye perfused with mock aqueous alone. All vessels perfused with mock aqueous appear dark on the structural scan, showing little reflectivity. Doppler scans of the same region show pure noise. Adding GNRs substantially improved the contrast in the Doppler scans (Figure 61). The flow profile (Figure 62) appears to be laminar, with maximum fluid velocity occurring near the center. This suggests that the Doppler signal within the area is not just an imaging artifact. Further, the agreement between the measured and known flow rates in the porcine eye support validity of the Doppler signals within the SD-OCT scans.

Doppler signals were not visible in the human eye despite high perfusion pressure and high concentration. Previous experience in mouse eyes with the same batch of GNRs suggests that they are prone to sticking to tissue and to each other. It is possible that the GNRs used in this experiment failed to pass through the trabecular meshwork of the human eye. Since the present study was performed, triple coated GNRs have been injected in the mouse model, and no longer appear to stick to internal structures. Triple coated GNRs will be used in future trials in human eyes with hopes of improving penetration into the distal outflow structures.

There are several limitations to the present study. Although the scanning process is non-invasive, current methods of inserting GNRs into the eye are invasive. A non-invasive delivery vehicle would help make GNRs more clinically relevant. Theoretically, GNRs can pass through the cornea. However, GNR eye drops would limit our ability to control the concentration within the eye. In its current form, GNRs are still useful as a research tool.

Addition of GNRs had the side effect of decreasing the structural contrast. Normally (Figure 61) outflow vessels have little reflectivity. This is in stark contrast to the tissue, which has varying degrees of reflectivity depending on the tissue type. GNRs have the unintended side effect of reducing structural contrast in the OCT image. While it is possible to distinguish vessels from tissue, the boundaries were less defined.

12.4.2 Future directions

For research purposes, this paper presents a method for non-invasively imaging flow at a microscale using OCT in fluids with little reflectivity. For the applicability of GNRs and OCT, other physiologically relevant flows with low Doppler signal must be identified. GNR may be useful for enhancing current understanding of lymph, CSF or synovial fluid exchange. There may also be potential industrial applications with measuring velocities of microfluids without disturbing the system.

12.4.3 Conclusion

This paper demonstrates the ability to measure Doppler signals using GNR enhanced Optical Coherence Tomography. The optimal concentration of GNRs for Doppler enhancement without shadowing is approximately 0.7×10^{12} particles/ml. The technique allows us to visualize aqueous humor outflow in a constant pressure porcine model, which may lead to increased understanding of glaucoma pathogenesis. This technique enables the first successful measurement of volumetric aqueous humor outflow by SD-OCT Doppler scans in the pig eye model. Combining OCT with GNRs may provide a useful tool for looking at flow at a microscale in experimental medical and industrial applications.

13.0 SUMMARY AND FUTURE WORK

When the work contained herein began in 2007, the aqueous humor outflow system had never been visualized with OCT, SC measurements were only feasible in histological sections, and 3D visualization of the distal outflow system was only possible with physical corrosion castings in cadaveric eyes. Beyond demonstrating the feasibility of these measurements non-invasively in the living human eye, their reproducibility has also been documented. Non-invasive mapping of the human aqueous humor outflow system promises to be an important new implement in the armamentarium of the glaucoma specialist.

In order to move forward with the combined use of Doppler and mapping for aqueous humor outflow volumetric measurements, a usable cadaver eye model must first be established for validation and calibration of the technique. Results from the porcine eye are promising, which was the reason for moving forward with human eye flow models with GNRs. However, it is likely that the differences between the porcine and human outflow anatomies resulted of the failure of previous generation of GNRs to reach the distal outflow structures and provide a Doppler signal. Studies with an improved GNR are ongoing. Should those fail, it may be necessary to perfuse the GNR solution directly into SC in order to observe its passage through the distal outflow vasculature at known rates. In either event, validation will precede applications in living human eyes.

Future studies will include examining the effect of the most common implant devices and glaucoma surgeries on the aqueous outflow system. The reason that a question as simple as “what happens to the outflow system when this tube is implanted?” remains unanswered is because it could never before be measured. The ability to finally see SC and the distal outflow vessels has opened an entirely new field of ophthalmic research. To that end, the basic clinical questions such as differences associated with disease, the effects of medications, or just a description of the normal healthy system across a range of ages all remain to be studied.

One of the most exciting and promising findings was the fact that differences in IOP could be directly observed in the morphology of SC. This introduces the possibility of not only a series of studies on the normal and glaucomatous outflow system response to IOP elevation and reduction, but also a potential test useful in the management of the disease. In the living human eye, brief elevation and release of IOP produce a pressure lower than the initial baseline. Scanning SC and the outflow system before and immediately after IOP elevation should allow its examination at two pressure levels at a single visit in the clinical setting. This has never before been done, and may provide important information concerning the outflow system’s ability to compensate for changes in pressure, as well as demonstrating the expected morphological response to medicinal IOP reduction apriori. This study is ongoing in normal eyes.

In conclusion, the aqueous humor outflow system remains beyond the view of the glaucoma specialist. Laser procedures are performed with no knowledge of the condition of the outflow pathway distal to the locations of laser injury. It is possible that a foreknowledge of locations of patent collector channel ostia within SC would allow the surgeon more precise placement of laser treatments, increasing the efficacy of the procedures. Similarly, penetrating procedures currently remove portions of the outflow system with no knowledge of the prominent outflow pathways in individual eyes. If the locations of the prominent outflow pathways were known before surgery, it might be possible to augment and not destroy existing ostia and large collector channels.

APPENDIX A

VOLUMETRIC AVERAGING CODE

This code is a routine to perform 3D averaging of a volumetric image. It is a modification of a sequential frame averaging routine written and owned by Dr. Hiroshi Ishikawa (Ishikawah@upme.edu). It was implemented in Dr. Ishikawa's OCT image browser software written in XCode for Macintosh.

```
- (NSString*)VoxelAverageRaster
{
      if (numFrames > 5) {
        int size = pixelsX*pixelsY;                                        // size is the number
of pixels in a frame; 1024 x a-scan count
        int totalsize = size*numFrames;                                    // totalsize is the
number of pixels in the raster scan
        int sourceIndex, destIndex, lineIndexS, lineIndexD, enfaceIndex;
        int *workI = malloc(size*sizeof(int));              //Single frame.
        int i, j, k, x, y;
        // Prepare dataBuffer
        UInt16 *dataBuffer = malloc(totalsize*sizeof(UInt16));
        for (i = 1; i < numFrames*size; i++)
               dataBuffer[i] = 0;                                                 //initiate
dataBuffer array (contains the entire averaged raster scan dataset)
        // Rolling average
        for (i = 1; i < numFrames-1; i++) {                         // i counts frames
               destIndex = i*size;                                                // Index
located to start of the current frame
               for (k = 0; k < size; k++)                                  // k counts locations
within a frame
                      workI[k] = 0;                                               // resets the
working frame to 0's
               for (j = -1; j <= 1; j++) {                                 // j counts plus or
minus 1 to work between three frames
                      sourceIndex = (i+j)*size;                            // index to the start
of the immediate frame (i.e. 1, 2, or 3 of the current 3 frame average).
                      lineIndexS = sourceIndex;
                      lineIndexD = destIndex;
                      for (x = 0; x < pixelsX; x++) {                      // x is the x location
```

```
counter; covers all the a-scans along a single frame
                                for (y = 0; y < pixelsY; y++) {            // y is the y location
counter; covers 1024 points along each a-scan

                                        lineIndexS++;
                                        workI[x*pixelsY+y] +=
(rawData[lineIndexS]+rawData[lineIndexS-pixelsY]+rawData[lineIndexS-pixelsY-
1]+rawData[lineIndexS-pixelsY+1]+rawData[lineIndexS+pixelsY]+rawData[lineIndexS+pixelsY-
1]+rawData[lineIndexS+pixelsY+1]+rawData[lineIndexS-1]+rawData[lineIndexS+1]);
                                }
                        }
                }
                for (x = 0; x < pixelsX; x++)
                        for (y = 0; y < pixelsY; y++)
                                dataBuffer[destIndex++] = (UInt16)(workI[x*pixelsY+y] / 27);
        }
        // Handle the first and last frame
        destIndex = 0;
        for (x = 0; x < pixelsX; x++) {
                for (y = 0; y < pixelsY; y++) {
                        dataBuffer[destIndex] = rawData[destIndex++];
                }
        }
        destIndex = (numFrames-1)*size;
        for (x = 0; x < pixelsX; x++) {
                for (y = 0; y < pixelsY; y++) {
                        dataBuffer[destIndex] = rawData[destIndex++];
                }
        }
        free(workI);

        // Prepare file path for exporting
        NSString *averagePath = [[sourceFile stringByDeletingPathExtension]
stringByAppendingString:@" VoxAvg.bog"];

        // Save averaged OCT data
        if ([[NSFileManager defaultManager] fileExistsAtPath:averagePath]) { // If file already
exists delete it
                [[NSFileManager defaultManager] removeFileAtPath:averagePath handler:nil];
        }
        [[NSFileManager defaultManager] createFileAtPath:averagePath contents:nil
attributes:nil];
        // Setup exporting data file
        NSFileHandle *exportFile = [NSFileHandle fileHandleForWritingAtPath:averagePath];
        // Write file header
        int step = 1;
        if (evenlySampled)
                step = 2;
        BioptigenDataFileHeader exportHeader;
        exportHeader.lineCount = CFSwapInt32HostToLittle(pixelsX/step);
        exportHeader.lineLength = CFSwapInt32HostToLittle(pixelsY*2);
        exportHeader.frameCount = CFSwapInt32HostToLittle(numFrames);
        exportHeader.xMin = myBogHeader.xMin;
        exportHeader.xMax = myBogHeader.xMax;
        exportHeader.yMin = myBogHeader.yMin;
        exportHeader.yMax = myBogHeader.yMax;
        exportHeader.scanDepth = myBogHeader.scanDepth;
        exportHeader.scanLength = myBogHeader.scanLength;
        exportHeader.azScanLength = myBogHeader.azScanLength;
        exportHeader.elScanLength = myBogHeader.elScanLength;
        exportHeader.objectDistance = myBogHeader.objectDistance;
        exportHeader.scanAngle = myBogHeader.scanAngle;
        [exportFile writeData:[NSData dataWithBytesNoCopy:&exportHeader
length:sizeof(BioptigenDataFileHeader) freeWhenDone:NO]];

        // Write raw data (swap if necessary)
        UInt16 *exportBuffer = malloc(pixelsX/step*pixelsY*numFrames*sizeof(UInt16));
        destIndex = 0;
        int srcIndex;
```

```
        for (i = 0; i < numFrames; i++) {
                srcIndex = pixelsX*pixelsY*i;
                for (x = 0; x < pixelsX/step; x++)
                        for (y = 0; y < pixelsY; y++)
                                exportBuffer[destIndex++] = 
CFSwapInt16HostToLittle(dataBuffer[srcIndex+x*step*pixelsY+y]);
        }
        [exportFile writeData:[NSData dataWithBytesNoCopy:exportBuffer 
length:pixelsX/step*pixelsY*numFrames*sizeof(UInt16) freeWhenDone:NO]];
        free(exportBuffer);

        // Finalize exporting
        [exportFile closeFile];

        free(dataBuffer);

        return averagePath;
      }
      else
        return nil;
}
```

APPENDIX B

IMAGEJ FIJI MACROS

A number of utility macros were written for ImageJ Fiji. These macros allowed single keystroke execution of single or a sequence of existing routines. The “process” routine at the top was used to prepare 3D image stacks for virtual casting. The “size” routine resizes Cirrus OCT scans to a 1:1 aspect ratio and scales them for direct measurement. The various “enhance” macros allow experimentation with a number of enhancement strategies.

```
macro "Process [P] "{

  run("Gaussian Blur...", "sigma=1.50 stack");
  n=nSlices;
   for (i=1; i<n; i++) {
      setSlice(i);
         run("Enhance Local Contrast (CLAHE)", "blocksize=31 histogram=256 maximum=4
mask=*None* fast_(less_accurate)");
      }
    setSlice(n);
    run("Enhance Local Contrast (CLAHE)", "blocksize=31 histogram=256 maximum=4
mask=*None* fast_(less_accurate)");
run("Gaussian Blur...", "sigma=1.5 stack");
run("Invert", "stack");
run("Subtract Background...", "rolling=30 disable stack");
run("Size...", "width=400 height=200 depth=400 interpolation=Bilinear");
}


macro "Size [S] "{
```

```
   run("Flip Vertically", "stack");
   n = nSlices;
   setSlice(n);
   run("Delete Slice");
   setSlice(1);
   run("Delete Slice");
   run("Size...", "width=1024 height=512 depth=126 average interpolation=Bilinear");
   run("Set Scale...", "distance=1024 known=4000 pixel=1 unit=Micrometer");

}



macro "Import Raw Image [R]"{
run("Raw...");
}



macro "Enhance Fast [E] "{
  n = nSlices;
    for (i=1; i<n; i++) {
        setSlice(i);
            run("Enhance Local Contrast (CLAHE)", "blocksize=63 histogram=256 maximum=5
mask=*None* fast_(less_accurate)");
        }
     setSlice(n);
     run("Enhance Local Contrast (CLAHE)", "blocksize=63 histogram=256 maximum=5
mask=*None* fast_(less_accurate)");
}

macro "Enhance Fast 31 3 fast "{
  n = nSlices;
    for (i=1; i<n; i++) {
        setSlice(i);
            run("Enhance Local Contrast (CLAHE)", "blocksize=31 histogram=256 maximum=3
mask=*None* fast_(less_accurate)");
        }
     setSlice(n);
     run("Enhance Local Contrast (CLAHE)", "blocksize=31 histogram=256 maximum=3
mask=*None* fast_(less_accurate)");
}

macro "Last Minute Rush [L]" {
run("Set Scale...", "distance=512 known=1 pixel=2.926 unit=mm");
run("Gaussian Blur...", "sigma=1.5 stack");
 n = nSlices;
    for (i=1; i<n; i++) {
        setSlice(i);
```

```
        run("Enhance Local Contrast (CLAHE)", "blocksize=31 histogram=256 maximum=3
mask=*None* fast_(less_accurate)");
      }
   setSlice(n);
   run("Enhance Local Contrast (CLAHE)", "blocksize=31 histogram=256 maximum=3
mask=*None* fast_(less_accurate)");
run("Gaussian Blur...", "sigma=2 stack");
run("8-bit");
run("Brightness/Contrast...");
}


macro "Enhance HiRes 2 [2] "{
 n = nSlices;
   for (i=1; i<n; i++) {
      setSlice(i);
        run("Enhance Local Contrast (CLAHE)", "blocksize=63 histogram=256 maximum=2
mask=*None*");
      }
   setSlice(n);
   run("Enhance Local Contrast (CLAHE)", "blocksize=63 histogram=256 maximum=2
mask=*None*");
}



macro "Enhance Fast 31 4 fast "{
 n = nSlices;
   for (i=1; i<n; i++) {
      setSlice(i);
        run("Enhance Local Contrast (CLAHE)", "blocksize=31 histogram=256 maximum=4
mask=*None* fast_(less_accurate)");
      }
   setSlice(n);
   run("Enhance Local Contrast (CLAHE)", "blocksize=31 histogram=256 maximum=4
mask=*None* fast_(less_accurate)");
}



macro "Enhance Fast 31 5 fast "{
 n = nSlices;
   for (i=1; i<n; i++) {
      setSlice(i);
        run("Enhance Local Contrast (CLAHE)", "blocksize=31 histogram=256 maximum=5
mask=*None* fast_(less_accurate)");
      }
   setSlice(n);
   run("Enhance Local Contrast (CLAHE)", "blocksize=31 histogram=256 maximum=5
mask=*None* fast_(less_accurate)");
}
```

```
macro "Enhance Fast 31 6 fast "{
 n = nSlices;
  for (i=1; i<n; i++) {
    setSlice(i);
      run("Enhance Local Contrast (CLAHE)", "blocksize=31 histogram=256 maximum=6 mask=*None* fast_(less_accurate)");
    }
   setSlice(n);
   run("Enhance Local Contrast (CLAHE)", "blocksize=31 histogram=256 maximum=6 mask=*None* fast_(less_accurate)");
}
```

```
macro "Enhance HiRes 2 [2] "{
 n = nSlices;
  for (i=1; i<n; i++) {
    setSlice(i);
      run("Enhance Local Contrast (CLAHE)", "blocksize=63 histogram=256 maximum=2 mask=*None*");
    }
   setSlice(n);
   run("Enhance Local Contrast (CLAHE)", "blocksize=63 histogram=256 maximum=2 mask=*None*");
}
```

```
macro "Enhance HiRes 3 [3] "{
 n = nSlices;
  for (i=1; i<n; i++) {
    setSlice(i);
      run("Enhance Local Contrast (CLAHE)", "blocksize=63 histogram=256 maximum=3 mask=*None*");
    }
   setSlice(n);
   run("Enhance Local Contrast (CLAHE)", "blocksize=63 histogram=256 maximum=3 mask=*None*");
}

macro "Enhance HiRes 4 [4] "{
 n = nSlices;
  for (i=1; i<n; i++) {
    setSlice(i);
```

```
      run("Enhance Local Contrast (CLAHE)", "blocksize=63 histogram=256 maximum=4
mask=*None*");
    }
   setSlice(n);
   run("Enhance Local Contrast (CLAHE)", "blocksize=63 histogram=256 maximum=4
mask=*None*");
}


macro "Enhance HiRes 5 [5] "{
 n = nSlices;
  for (i=1; i<n; i++) {
    setSlice(i);
      run("Enhance Local Contrast (CLAHE)", "blocksize=63 histogram=256 maximum=5
mask=*None*");
    }
   setSlice(n);
   run("Enhance Local Contrast (CLAHE)", "blocksize=63 histogram=256 maximum=5
mask=*None*");
}


macro "Enhance HiRes 6 [6] "{
 n = nSlices;
  for (i=1; i<n; i++) {
    setSlice(i);
      run("Enhance Local Contrast (CLAHE)", "blocksize=63 histogram=256 maximum=6
mask=*None*");
    }
   setSlice(n);
   run("Enhance Local Contrast (CLAHE)", "blocksize=63 histogram=256 maximum=6
mask=*None*");
}


macro "Delete Slice [D]" {
   run("Delete Slice");
 }

macro "Setup TIF File"{
run("Size...", "width=1024 height=1024 depth=20 average interpolation=Bilinear");
run("Set Scale...", "distance=1024 known=2 pixel=1 unit=Micrometer");
makeRectangle(644, 842, 254, 28);
run("Fill", "stack");
run("Set Scale...", "distance=512 known=1000 pixel=1 unit=Micrometer");
}

macro "Doppler Processing " {
run("Rotate 90 Degrees Right");
run("Minimum...", "radius=3 stack");
run("Gaussian Blur...", "sigma=6 stack");
```

```
run("Subtract Background...", "rolling=20 light disable stack");
run("8-bit");
run("Brightness/Contrast...");
}

macro "Doppler Processing " {
run("Size...", "width=1024 height=1024 interpolation=Bilinear");
run("Make Binary", "calculate");
run("Analyze Particles...", "size=250-Infinity circularity=0.00-1.00 show=Nothing exclude clear
add stack");
setOption("Show All",false);
}

macro "Jump to Slice [J]" {
Slic=getNumber('Jump to slice #?',1);
setSlice(Slic);
}


macro "SET TO 8 BIT [8]" {
run("8-bit");
}
```

APPENDIX C

5X5 PLANAR AVERAGING

This code is a routine to perform averaging of a volumetric image using a flat 5x5 averaging kernel. It is a modification of a sequential frame averaging routine written and owned by Dr. Hiroshi Ishikawa (Ishikawah@upme.edu). It was implemented in Dr. Ishikawa's OCT image browser software written in XCode for Macintosh.

```
- (NSString*)TwentyfiveAverageRaster
{
      if (numFrames > 5) {
       int size = pixelsX*pixelsY;
       int sourceIndex, destIndex, lineIndexS, lineIndexD, enfaceIndex;
       UInt32 *workI = malloc(pixelsX*pixelsY*sizeof(UInt32));
       int i, j, k, x, y;
       // Prepare dataBuffer
       UInt16 *dataBuffer = malloc(size*numFrames*sizeof(UInt16));
       for (i = 1; i < numFrames*size; i++)
               dataBuffer[i] = 0;
       // Rolling average
       for (i = 2; i < numFrames-2; i++) {                         //changed the 2's from1 1's.
               destIndex = i*size;
               for (k = 0; k < pixelsX*pixelsY; k++)
                      workI[k] = 0;
               for (j = -2; j <= 2; j++) {                                //changed the 2's
from1 1's.
                      sourceIndex = (i+j)*size;
                      lineIndexS = sourceIndex;
                      lineIndexD = destIndex;
                      for (x = 0; x < pixelsX; x++) {
                              for (y = 0; y < pixelsY; y++) {


                                     if(x == 0){
                                      lineIndexS++;
                                      workI[x*pixelsY+y] +=
(rawData[lineIndexS]+rawData[lineIndexS]+rawData[lineIndexS]+rawData[lineIndexS+pixelsY]+rawData[
```

```
lineIndexS+pixelsY+pixelsY]);
                                       }
                                       if(x == 1){
                                       lineIndexS++;
                                       workI[x*pixelsY+y] += (rawData[lineIndexS-
pixelsY]+rawData[lineIndexS]+rawData[lineIndexS]+rawData[lineIndexS+pixelsY]+rawData[lineIndexS+p
ixelsY+pixelsY]);
                                       }

                                       if (x > 1 && x < pixelsX-2) {
                                       lineIndexS++;
                                       workI[x*pixelsY+y] +=
(rawData[lineIndexS]+rawData[lineIndexS-pixelsY]+rawData[lineIndexS+pixelsY]+rawData[lineIndexS-
pixelsY-pixelsY]+rawData[lineIndexS+pixelsY+pixelsY]);
                                       }

                                       if(x == pixelsX-2) {
                                       lineIndexS++;
                                       workI[x*pixelsY+y] +=
(rawData[lineIndexS]+rawData[lineIndexS-pixelsY]+rawData[lineIndexS-pixelsY-
pixelsY]+rawData[lineIndexS]+rawData[lineIndexS+pixelsY]);
                                       }
                                       if(x == pixelsX-1) {
                                       lineIndexS++;
                                       workI[x*pixelsY+y] +=
(rawData[lineIndexS]+rawData[lineIndexS-pixelsY]+rawData[lineIndexS-pixelsY-
pixelsY]+rawData[lineIndexS]+rawData[lineIndexS]);




/*                                    if(x == 0){
                                             lineIndexS++;
                                             workI[x*pixelsY+y] +=
(rawData[lineIndexS]+rawData[lineIndexS]+rawData[lineIndexS]+rawData[lineIndexS+pixelsY]+rawData[
lineIndexS+pixelsY+pixelsY]);
                                      }
                                      if(x == 1){
                                             lineIndexS++;
                                             workI[x*pixelsY+y] += (rawData[lineIndexS-
pixelsY]+rawData[lineIndexS]+rawData[lineIndexS]+rawData[lineIndexS+pixelsY]+rawData[lineIndexS+p
ixelsY+pixelsY]);
                                      }

                                      if (x > 1 && x < pixelsX-2) {
                                             lineIndexS++;
                                             workI[x*pixelsY+y] +=
(rawData[lineIndexS]+rawData[lineIndexS-pixelsY]+rawData[lineIndexS+pixelsY]+rawData[lineIndexS-
pixelsY-pixelsY]+rawData[lineIndexS+pixelsY+pixelsY]);
                                      }

                                      if(x == pixelsX-2) {
                                             lineIndexS++;
                                             workI[x*pixelsY+y] +=
(rawData[lineIndexS]+rawData[lineIndexS-pixelsY]+rawData[lineIndexS-pixelsY-
pixelsY]+rawData[lineIndexS]+rawData[lineIndexS+pixelsY]);
                                      }
                                      if(x == pixelsX-1) {
                                             lineIndexS++;
                                             workI[x*pixelsY+y] +=
(rawData[lineIndexS]+rawData[lineIndexS-pixelsY]+rawData[lineIndexS-pixelsY-
pixelsY]+rawData[lineIndexS]+rawData[lineIndexS]); */
                                      }
                              }
                       }
               }
               for (x = 0; x < pixelsX; x++)
                       for (y = 0; y < pixelsY; y++)
                              dataBuffer[destIndex++] = workI[x*pixelsY+y] / 4;   //THIS NEEDS TO
```

```
BE / 25 WHEN PUT BACK TO 5X5!!!!!!
        }
        // Handle the first and last frame
        destIndex = 0;
        for (x = 0; x < pixelsX; x++) {                                    //Write one frame
                for (y = 0; y < pixelsY; y++) {
                        dataBuffer[destIndex] = rawData[destIndex++];
                }
        }
        for (x = 0; x < pixelsX; x++) {                                    // Write another frame
                for (y = 0; y < pixelsY; y++) {
                        dataBuffer[destIndex] = rawData[destIndex++];
                }
        }


        destIndex = (numFrames-2)*size;
        for (x = 0; x < pixelsX; x++) {                                    // Write second to
last frame frame
                for (y = 0; y < pixelsY; y++) {
                        dataBuffer[destIndex] = rawData[destIndex++];
                }
        }
        for (x = 0; x < pixelsX; x++) {                                    // Write the last one
                for (y = 0; y < pixelsY; y++) {
                        dataBuffer[destIndex] = rawData[destIndex++];
                }
        }

        free(workI);

        // Prepare file path for exporting
        NSString *averagePath = [[sourceFile stringByDeletingPathExtension]
stringByAppendingString:@"_Flat25.bog"];

        // Save averaged OCT data
        if ([[NSFileManager defaultManager] fileExistsAtPath:averagePath]) { // If file already
exists delete it
                [[NSFileManager defaultManager] removeFileAtPath:averagePath handler:nil];
        }
        [[NSFileManager defaultManager] createFileAtPath:averagePath contents:nil
attributes:nil];
        // Setup exporting data file
        NSFileHandle *exportFile = [NSFileHandle fileHandleForWritingAtPath:averagePath];
        // Write file header
        int step = 1;
        if (evenlySampled)
                step = 2;
        BioptigenDataFileHeader exportHeader;
        exportHeader.lineCount = CFSwapInt32HostToLittle(pixelsX/step);
        exportHeader.lineLength = CFSwapInt32HostToLittle(pixelsY*2);
        exportHeader.frameCount = CFSwapInt32HostToLittle(numFrames);
        exportHeader.xMin = myBogHeader.xMin;
        exportHeader.xMax = myBogHeader.xMax;
        exportHeader.yMin = myBogHeader.yMin;
        exportHeader.yMax = myBogHeader.yMax;
        exportHeader.scanDepth = myBogHeader.scanDepth;
        exportHeader.scanLength = myBogHeader.scanLength;
        exportHeader.azScanLength = myBogHeader.azScanLength;
        exportHeader.elScanLength = myBogHeader.elScanLength;
        exportHeader.objectDistance = myBogHeader.objectDistance;
        exportHeader.scanAngle = myBogHeader.scanAngle;
        [exportFile writeData:[NSData dataWithBytesNoCopy:&exportHeader
length:sizeof(BioptigenDataFileHeader) freeWhenDone:NO]];

        // Write raw data (swap if necessary)
        UInt16 *exportBuffer = malloc(pixelsX/step*pixelsY*numFrames*sizeof(UInt16));
        destIndex = 0;
        int srcIndex;
```

```
        for (i = 0; i < numFrames; i++) {
                srcIndex = pixelsX*pixelsY*i;
                for (x = 0; x < pixelsX/step; x++)
                        for (y = 0; y < pixelsY; y++)
                                exportBuffer[destIndex++] =
CFSwapInt16HostToLittle(dataBuffer[srcIndex+x*step*pixelsY+y]);
        }
        [exportFile writeData:[NSData dataWithBytesNoCopy:exportBuffer
length:pixelsX/step*pixelsY*numFrames*sizeof(UInt16) freeWhenDone:NO]];
        free(exportBuffer);

        // Finalize exporting
        [exportFile closeFile];

        free(dataBuffer);

        return averagePath;
      }
      else
        return nil;
}
```

BIBLIOGRAPHY

1. Glasser A, Kaufman PL. Accommodation and Presbyopia. In: Kaufman PL, Alm A, eds. *Adler's Physiology of the Eye*. 10 ed. St. Louis: Mosby; 2003:197-233.

2. Matsubara JA. Central Visual Pathways. In: Kaufman PL, Alm A, eds. *Adler's Physiology of the Eye*. 10 ed. St. Louis: Mosby; 2003:348-357.

3. Gabelt B, Kaufman PL. Aqueous Humor Hydrodynamics. In: Kaufman PL, ed. *Adler's Physiology of the Eye*. St. Louis: Mosby; 2003 237-289.

4. American Academy of Ophthalmology Glaucoma Panel. Preferred Practice Pattern® Guidelines. Primary Open-Angle Glaucoma. San Francisco CAAoO.

5. Grant WM. Clinical measurements of aqueous outflow. *Am J Ophthalmol.* Nov 1951;34(11):1603-1605.

6. Lucas B. Mr. Lucas on the Origin of the Aqueous Humour. *Prov Med Surg J (1840).* Dec 5 1840;1(10):174.

7. Krause U, Raunio V. Proteins of the normal human aqueous humour. *Ophthalmologica.* 1969;159(1):178-185.

8. Dernouchamps JP. The proteins of the aqueous humour. *Doc Ophthalmol.* Nov 1 1982;53(3):193-248.

9. Krupin T, Civan MM. The physiological basis of aqueous humor formation. In: Ritch R, Shields MB, Krupin T, eds. *The Glaucomas*. St. Louis: Mosby; 1996:251-280.

10. Osborne WA. A contribution to the physiology of the aqueous humour. *J Physiol.* Mar 25 1919;52(5):347-350.

11. Bill A. The role of ciliary blood flow and ultrafiltration in aqueous humor formation. *Exp Eye Res.* Aug 10 1973;16(4):287-298.

12. Reitsamer HA, Kiel JW. Relationship between ciliary blood flow and aqueous production in rabbits. *Invest Ophthalmol Vis Sci.* Sep 2003;44(9):3967-3971.

13. Cole DF. Effects of some metabolic inhibitors upon the formation of the aqueous humour in rabbits. *Br J Ophthalmol.* Dec 1960;44:739-750.

14. Sires B. Orbital and Ocular Anatomy. In: Wright E, ed. *Textbook of Ophthalmology*. Baltimore, MD: Williams and Wilkins; 1997.

15. Toris C. Aqueous Humor Dynamics I; Measurement Methods and Animal Studies. In: Civan MM, ed. *The Eye's Aqueous Humor.* Vol 62. 2 ed. San Diego: Elsevier; 2008:193-229.

16. Civan MM, Macknight AD. The ins and outs of aqueous humour secretion. *Exp Eye Res.* Mar 2004;78(3):625-631.

17. Brubaker RF. Flow of aqueous humor in humans [The Friedenwald Lecture]. *Invest Ophthalmol Vis Sci.* Dec 1991;32(13):3145-3166.

18. Heys JJ, Barocas VH. A boussinesq model of natural convection in the human eye and the formation of Krukenberg's spindle. *Ann Biomed Eng.* Mar 2002;30(3):392-401.

19. Pletneva NA, Sakhieva SM, Kapustina EV. [Aqueous humor outflow]. *Vestn Oftalmol.* Jul-Aug 1955;34(4):14-17.

20. Cohan BE. Aqueous humor outflow: an experimental study using radiopaque materials. I. Paracentesis technique, response evoked, and demonstration of pathway of outflow. *AMA Arch Ophthalmol.* Jun 1956;55(6):792-799.

21. Cohan BE. Radiography of aqueous humor outflow. *AMA Arch Ophthalmol.* Jul 1958;60(1):110-115.

22. Bill A, Barany EH. Gross facility, facility of conventional routes, and pseudofacility of aqueous humor outflow in the cynomolgus monkey. The reduction in aqueous humor formation rate caused by moderate increments in intraocular pressure. *Arch Ophthalmol.* May 1966;75(5):665-673.

23. Marre E. [Aqueous humor outflow of the primate eye--a model]. *Albrecht Von Graefes Arch Klin Exp Ophthalmol.* 1968;174(3):212-216.

24. McMaster PR, Macri FJ. Secondary aqueous humor outflow pathways in the rabbit, cat, and monkey. *Arch Ophthalmol.* Mar 1968;79(3):297-303.

25. Fritz A. [Normal parameters for aqueous humor outflow]. *Bull Soc Belge Ophtalmol.* 1970;156:666-678.

26. Ashton N. Anatomical study of Schlemm's canal and aqueous veins by means of neoprene casts. Part I. Aqueous veins. *Br J Ophthalmol.* May 1951;35(5):291-303.

27. Ashton N. Anatomical study of Schlemm's canal and aqueous veins by means of neoprene casts. II. Aqueous veins. *Br J Ophthalmol.* May 1952;36(5):265-267; contd.

28. Ashton N, Smith R. Anatomical study of Schlemm's canal and aqueous veins by means of neoprene casts. III. Arterial relations of Schlemm's canal. *Br J Ophthalmol.* Oct 1953;37(10):577-586.

29. Ashton N, Brini A, Smith R. Anatomical studies of the trabecular meshwork of the normal human eye. *Br J Ophthalmol.* May 1956;40(5):257-282.

30. Brubaker RF. Determination of episcleral venous pressure in the eye. A comparison of three methods. *Arch Ophthalmol.* Jan 1967;77(1):110-114.

31. Phelps CD, Armaly MF. Measurement of episcleral venous pressure. *Am J Ophthalmol.* Jan 1978;85(1):35-42.

32. Krupin T. Pressure-dependent Outflow. In: Ritch R, Shields MB, Krupin T, eds. *The Glaucomas*. St. Louis: Mosby; 1996:307-333.

33. Klein BE, Klein R, Linton KL. Intraocular pressure in an American community. The Beaver Dam Eye Study. *Invest Ophthalmol Vis Sci.* Jun 1992;33(7):2224-2228.

34. Klein BE, Klein R, Sponsel WE, et al. Prevalence of glaucoma. The Beaver Dam Eye Study. *Ophthalmology.* Oct 1992;99(10):1499-1504.

35. Leske MC, Connell AM, Schachat AP, Hyman L. The Barbados Eye Study. Prevalence of open angle glaucoma. *Arch Ophthalmol.* Jun 1994;112(6):821-829.

36. Leske MC, Connell AM, Wu SY, Hyman LG, Schachat AP. Risk factors for open-angle glaucoma. The Barbados Eye Study. *Arch Ophthalmol.* Jul 1995;113(7):918-924.

37. Grant WM. Further studies on facility of flow through the trabecular meshwork. *AMA Arch Ophthalmol.* Oct 1958;60(4 Part 1):523-533.

38. Kass MA, Hart WM, Jr., Gordon M, Miller JP. Risk factors favoring the development of glaucomatous visual field loss in ocular hypertension. *Surv Ophthalmol.* Nov-Dec 1980;25(3):155-162.

39. Bill A. Conventional and uveo-scleral drainage of aqueous humour in the cynomolgus monkey (Macaca irus) at normal and high intraocular pressures. *Exp Eye Res.* Jan 1966;5(1):45-54.

40. Fritz MA. [Aqueous outflow and uveal circulation, determinate factors in primary glaucoma]. *Bull Soc Belge Ophtalmol.* 1966;143:701-714.

41. Zimmerman LE. The outflow problem in normal and pathologic eyes. *Trans Am Acad Ophthalmol Otolaryngol.* Sep-Oct 1966;70(5):767-776.

42. Jocson VL, Sears ML. Channels of aqueous outflow and related blood vessels. II. Cercopithecus ethiops (Ethiopian green or green vervet). *Arch Ophthalmol.* Feb 1969;81(2):244-253.

43. Bill A, Phillips CI. Uveoscleral drainage of aqueous humour in human eyes. *Exp Eye Res.* Nov 1971;12(3):275-281.

44. Inomata H, Bill A, Smelser GK. Aqueous humor pathways through the trabecular meshwork and into Schlemm's canal in the cynomolgus monkey (Macaca irus). An electron microscopic study. *Am J Ophthalmol.* May 1972;73(5):760-789.

45. Gabelt BT, Kaufman PL. Changes in aqueous humor dynamics with age and glaucoma. *Prog Retin Eye Res.* Sep 2005;24(5):612-637.

46. Goel M, Picciani RG, Lee RK, Bhattacharya SK. Aqueous humor dynamics: a review. *Open Ophthalmol J.* 2010;4:52-59.

47. Rylander NR, Vold SD. Cost analysis of glaucoma medications. *Am J Ophthalmol.* Jan 2008;145(1):106-113.

48. Quigley HA, Broman AT. The number of people with glaucoma worldwide in 2010 and 2020. *Br J Ophthalmol.* Mar 2006;90(3):262-267.

49. Friedman DS, Wolfs RC, O'Colmain BJ, et al. Prevalence of open-angle glaucoma among adults in the United States. *Arch Ophthalmol.* Apr 2004;122(4):532-538.

50. Sommer A, Tielsch JM. Risk factors for open-angle glaucoma: the Barbados Eye Study. *Arch Ophthalmol.* Feb 1996;114(2):235.

51. Sommer A, Tielsch JM, Katz J, et al. Relationship between intraocular pressure and primary open angle glaucoma among white and black Americans. The Baltimore Eye Survey. *Arch Ophthalmol.* Aug 1991;109(8):1090-1095.

52. Sommer A, Tielsch JM, Katz J, et al. Racial differences in the cause-specific prevalence of blindness in east Baltimore. *N Engl J Med.* Nov 14 1991;325(20):1412-1417.

53. Leske MC, Connell AM, Wu SY, Hyman L, Schachat AP. Distribution of intraocular pressure. The Barbados Eye Study. *Arch Ophthalmol.* Aug 1997;115(8):1051-1057.

54. Leske MC, Wu SY, Hennis A, Honkanen R, Nemesure B. Risk factors for incident open-angle glaucoma: the Barbados Eye Studies. *Ophthalmology.* Jan 2008;115(1):85-93.

55. Mitchell P, Lee AJ, Rochtchina E, Wang JJ. Open-angle glaucoma and systemic hypertension: the blue mountains eye study. *J Glaucoma.* Aug 2004;13(4):319-326.

56. Mitchell P, Smith W, Attebo K, Healey PR. Prevalence of open-angle glaucoma in Australia. The Blue Mountains Eye Study. *Ophthalmology.* Oct 1996;103(10):1661-1669.

57. Drance S, Anderson DR, Schulzer M. Risk factors for progression of visual field abnormalities in normal-tension glaucoma. *Am J Ophthalmol.* Jun 2001;131(6):699-708.

58. The effectiveness of intraocular pressure reduction in the treatment of normal-tension glaucoma. Collaborative Normal-Tension Glaucoma Study Group. *Am J Ophthalmol.* Oct 1998;126(4):498-505.

59. Comparison of glaucomatous progression between untreated patients with normal-tension glaucoma and patients with therapeutically reduced intraocular pressures. Collaborative Normal-Tension Glaucoma Study Group. *Am J Ophthalmol.* Oct 1998;126(4):487-497.

60. Schulzer M. Intraocular pressure reduction in normal-tension glaucoma patients. The Normal Tension Glaucoma Study Group. *Ophthalmology.* Sep 1992;99(9):1468-1470.

61. Danias J, Podos SM. Comparison of glaucomatous progression between untreated patients with normal-tension glaucoma and patients with therapeutically reduced intraocular pressures. The effectiveness of intraocular pressure reduction in the treatment of normal-tension glaucoma. *Am J Ophthalmol.* May 1999;127(5):623-625.

62. Leske MC, Hyman L, Hussein M, Heijl A, Bengtsson B. Comparison of glaucomatous progression between untreated patients with normal-tension glaucoma and patients with therapeutically reduced intraocular pressures. The effectiveness of intraocular pressure reduction in the treatment of normal-tension glaucoma. *Am J Ophthalmol.* May 1999;127(5):625-626.

63. Pang IH, Clark A. Outflow Signaling Mechanisms and New Therapeutic Strategies for the Control of Intraocular Pressure. In: Civan MM, ed. *The Eye's Aqueous Humor.* Vol 62. 2 ed. San Diego: Elsevier; 2008:427-469.

64. Vass C, Hirn C, Sycha T, Findl O, Bauer P, Schmetterer L. Medical interventions for primary open angle glaucoma and ocular hypertension. *Cochrane Database Syst Rev.* 2007(4):CD003167.

65. Krupin T, Liebmann JM, Greenfield DS, Ritch R, Gardiner S. A randomized trial of brimonidine versus timolol in preserving visual function: results from the Low-Pressure Glaucoma Treatment Study. *Am J Ophthalmol.* Apr 2011;151(4):671-681.

66. Sihota R. Lasers in primary open angle glaucoma. *Indian J Ophthalmol.* Jan 2011;59 Suppl:S114-117.

67. Kramer TR, Noecker RJ. Comparison of the morphologic changes after selective laser trabeculoplasty and argon laser trabeculoplasty in human eye bank eyes. *Ophthalmology.* Apr 2001;108(4):773-779.

68. Alvarado JA, Alvarado RG, Yeh RF, Franse-Carman L, Marcellino GR, Brownstein MJ. A new insight into the cellular regulation of aqueous outflow: how trabecular meshwork endothelial cells drive a mechanism that regulates the permeability of Schlemm's canal endothelial cells. *Br J Ophthalmol.* Nov 2005;89(11):1500-1505.

69. Murthy S, Latina MA. Pathophysiology of selective laser trabeculoplasty. *Int Ophthalmol Clin.* Winter 2009;49(1):89-98.

70. Cairns JE. Trabeculectomy. Sub-title: "a surgical method of reducing intra-ocular pressure in chronic simple glaucoma without sub-conjunctival drainage of aqueous humour". *Trans Ophthalmol Soc U K.* 1969;88:231-233.

71. Hara T. [Results of trabeculectomy ab externo as filtrating operation. The method of resecting the trabeculum under direct observation of Schlemm's canal (author's transl)]. *Nihon Ganka Gakkai Zasshi.* May 10 1975;79(5):494-497.

72. Watson PG, Barnett F. Effectiveness of trabeculectomy in glaucoma. *Am J Ophthalmol.* May 1975;79(5):831-845.

73. Benedikt O. [Demonstration of aqueous outflow patterns of normal and glaucomatous human eyes through the injection of fluorescein solution in the anterior chamber (author's transl)]. *Albrecht Von Graefes Arch Klin Exp Ophthalmol.* Apr 1 1976;199(1):45-67.

74. Loewenthal LM. Trabeculectomy as treatment for glaucoma: a preliminary report. *Ann Ophthalmol.* Sep 1977;9(9):1179-1186.

75. Luntz MH, Livingston DG. Trabeculotomy ab externo and trabeculectomy in congenital and adult-onset glaucoma. *Am J Ophthalmol.* Feb 1977;83(2):174-179.

76. Portney GL. Trabeculectomy and postoperative ocular hypertension in secondary angle-closure glaucoma. *Am J Ophthalmol.* Aug 1977;84(2):145-149.

77. Moulin F, Haut J, Abi Rached J. Late failures of trabeculoplasty. *Int Ophthalmol.* Feb 1987;10(1):61-66.

78. Fellenbaum PS, Sidoti PA, Heuer DK, Minckler DS, Baerveldt G, Lee PP. Experience with the baerveldt implant in young patients with complicated glaucomas. *J Glaucoma.* Apr 1995;4(2):91-97.

79. Wilson RP, Cantor L, Katz LJ, Schmidt CM, Steinmann WC, Allee S. Aqueous shunts. Molteno versus Schocket. *Ophthalmology.* May 1992;99(5):672-676; discussion 676-678.

80. Beebe WE, Starita RJ, Fellman RL, Lynn JR, Gelender H. The use of Molteno implant and anterior chamber tube shunt to encircling band for the treatment of glaucoma in keratoplasty patients. *Ophthalmology.* Nov 1990;97(11):1414-1422.

81. Krupin eye valve with disk for filtration surgery. The Krupin Eye Valve Filtering Surgery Study Group. *Ophthalmology.* Apr 1994;101(4):651-658.

82. Law SK, Kalenak JW, Connor TB, Jr., Pulido JS, Han DP, Mieler WF. Retinal complications after aqueous shunt surgical procedures for glaucoma. *Arch Ophthalmol.* Dec 1996;114(12):1473-1480.

83. Freedman J. What is new after 40 years of glaucoma implants. *J Glaucoma.* Oct-Nov 2010;19(8):504-508.

84. Reinthal EK, Rohrbach JM, Grisanti S. [Glaucoma drainage implants]. *Klin Monbl Augenheilkd.* Jan 2010;227(1):49-55.

85. Libre PE. Nonpenetrating filtering surgery and goniopuncture (staged trabeculectomy) for episcleral venous pressure glaucoma. *Am J Ophthalmol.* Dec 2003;136(6):1172-1174.

86. Roche O, Beby F, Parsa A, Orssaud C, Dufier JL, Parsa CF. Nonpenetrating external trabeculectomy for congenital glaucoma: a retrospective study. *Ophthalmology.* Nov 2007;114(11):1994-1999.

87. Kozlova T, Zagorski ZF, Rakowska E. A simplified technique for non-penetrating deep sclerectomy. *Eur J Ophthalmol.* May-Jun 2002;12(3):188-192.

88. Pajic B, Pajic-Eggspuehler B, Haefliger I. New minimally invasive, deep sclerotomy ab interno surgical procedure for glaucoma, six years of follow-up. *J Glaucoma.* Feb 2011;20(2):109-114.

89. Danielson BL, Boisrobert CY. Absolute optical ranging using low coherence interferometry. *Appl Opt.* Jul 20 1991;30(21):2975-2979.

90. Flournoy PA, McClure RW, Wyntjes G. White-Light Interferometric Thickness Gauge. *Appl Opt.* 1972 1972;11(9):1907-1915.

91. Garudadri CS, Choudhari NS, Rao HL, Senthil S. A randomized trial of brimonidine versus timolol in preserving visual function: results from the Low-pressure Glaucoma Treatment Study. *Am J Ophthalmol.* Nov 2011;152(5):877; author reply 877-878.

92. Wojtkowski M. High-speed optical coherence tomography: basics and applications. *Appl Opt.* Jun 1 2010;49(16):D30-61.

93. Oppenheim AV, Willsky AS. *Signals and Systems*. 2 ed. Upper Saddle River, NJ: Prentice Hall; 1996.

94. Fercher AF, Drexler W, Hitzenberger CK, Lasser T. Optical Coherence Tomography-Principles and Applicatons. *Rep Prog Phys.* Jan. 2003 2003;66:239-303.

95. Klein TE, Weiser W, Eigenwillig CM, Biedermann BR, Huber R. Megahertz OCT for ultrawide-field retinal imaging with a 1050nm Fourier domain mode-locked laser. *Opt Express.* 2011;19(4):3044-3062.

96. Swanson EA, Izatt JA, Hee MR, et al. In vivo retinal imaging by optical coherence tomography. *Opt Lett.* Nov 1 1993;18(21):1864-1866.

97. Wojtkowski M, Srinivasan V, Fujimoto JG, et al. Three-dimensional retinal imaging with high-speed ultrahigh-resolution optical coherence tomography. *Ophthalmology.* Oct 2005;112(10):1734-1746.

98. Tearney GJ, Bouma BE, Boppart SA, Golubovic B, Swanson EA, Fujimoto JG. Rapid acquisition of in vivo biological images by use of optical coherence tomography. *Opt Lett.* Sep 1 1996;21(17):1408-1410.

99. Golubovic B, Bouma BE, Tearney GJ, Fujimoto JG. Optical frequency-domain reflectometry using rapid wavelength tuning of a Cr4+:forsterite laser. *Opt Lett.* Nov 15 1997;22(22):1704-1706.

100. Rollins A, Yazdanfar S, Kulkarni M, Ung-Arunyawee R, Izatt J. In vivo video rate optical coherence tomography. *Opt Express.* Sep 14 1998;3(6):219-229.

101. Wojtkowski M, Bajraszewski T, Targowski P, Kowalczyk A. Real-time in vivo imaging by high-speed spectral optical coherence tomography. *Opt Lett.* Oct 1 2003;28(19):1745-1747.

102. Yun S, Tearney G, de Boer J, Iftimia N, Bouma B. High-speed optical frequency-domain imaging. *Opt Express.* Nov 3 2003;11(22):2953-2963.

103. Yun SH, Boudoux C, Tearney GJ, Bouma BE. High-speed wavelength-swept semiconductor laser with a polygon-scanner-based wavelength filter. *Opt Lett.* Oct 15 2003;28(20):1981-1983.

104. Nassif N, Cense B, Park B, et al. In vivo high-resolution video-rate spectral-domain optical coherence tomography of the human retina and optic nerve. *Opt Express.* Feb 9 2004;12(3):367-376.

105. Nassif N, Cense B, Park BH, et al. In vivo human retinal imaging by ultrahigh-speed spectral domain optical coherence tomography. *Opt Lett.* Mar 1 2004;29(5):480-482.

106. Huber R, Adler DC, Fujimoto JG. Buffered Fourier domain mode locking: Unidirectional swept laser sources for optical coherence tomography imaging at 370,000 lines/s. *Opt Lett.* Oct 15 2006;31(20):2975-2977.

107. Huber R, Adler DC, Srinivasan VJ, Fujimoto JG. Fourier domain mode locking at 1050 nm for ultra-high-speed optical coherence tomography of the human retina at 236,000 axial scans per second. *Opt Lett.* Jul 15 2007;32(14):2049-2051.

108. Huber R, Wojtkowski M, Fujimoto JG. Fourier Domain Mode Locking (FDML): A new laser operating regime and applications for optical coherence tomography. *Opt Express.* Apr 17 2006;14(8):3225-3237.

109. Huber R, Wojtkowski M, Fujimoto JG, Jiang JY, Cable AE. Three-dimensional and C-mode OCT imaging with a compact, frequency swept laser source at 1300 nm. *Opt Express.* Dec 26 2005;13(26):10523-10538.

110. Klein T, Wieser W, Eigenwillig CM, Biedermann BR, Huber R. Megahertz OCT for ultrawide-field retinal imaging with a 1050 nm Fourier domain mode-locked laser. *Opt Express.* Feb 14 2011;19(4):3044-3062.

111. Potsaid B, Gorczynska I, Srinivasan VJ, et al. Ultrahigh speed spectral / Fourier domain OCT ophthalmic imaging at 70,000 to 312,500 axial scans per second. *Opt Express.* Sep 15 2008;16(19):15149-15169.

112. Schuman JS, Hee MR, Arya AV, et al. Optical coherence tomography: a new tool for glaucoma diagnosis. *Curr Opin Ophthalmol.* Apr 1995;6(2):89-95.

113. Baumal CR. Clinical applications of optical coherence tomography. *Curr Opin Ophthalmol.* Jun 1999;10(3):182-188.

114. Tanner V, Williamson TH. Watzke-Allen slit beam test in macular holes confirmed by optical coherence tomography. *Arch Ophthalmol.* Aug 2000;118(8):1059-1063.

115. Ko TH, Witkin AJ, Fujimoto JG, et al. Ultrahigh-resolution optical coherence tomography of surgically closed macular holes. *Arch Ophthalmol.* Jun 2006;124(6):827-836.

116. Roh S, Noecker RJ, Schuman JS, Hedges TR, 3rd, Weiter JJ, Mattox C. Effect of optic nerve head drusen on nerve fiber layer thickness. *Ophthalmology.* May 1998;105(5):878-885.

117. Ocakoglu O, Ustundag C, Koyluoglu N, Oguz V, Kendiroglu G, Ozkan S. Long term follow-up of retinal nerve fiber layer thickness in eyes with optic nerve head drusen. *Curr Eye Res.* May 2003;26(5):277-280.

118. Katz BJ, Pomeranz HD. Visual field defects and retinal nerve fiber layer defects in eyes with buried optic nerve drusen. *Am J Ophthalmol.* Feb 2006;141(2):248-253.

119. Choi SS, Zawadzki RJ, Greiner MA, Werner JS, Keltner JL. Fourier-domain optical coherence tomography and adaptive optics reveal nerve fiber layer loss and photoreceptor changes in a patient with optic nerve drusen. *J Neuroophthalmol.* Jun 2008;28(2):120-125.

120. Haritoglou C, Gass CA, Schaumberger M, Gandorfer A, Ulbig MW, Kampik A. Long-term follow-up after macular hole surgery with internal limiting membrane peeling. *Am J Ophthalmol.* Nov 2002;134(5):661-666.

121. Ko TH, Fujimoto JG, Schuman JS, et al. Comparison of ultrahigh- and standard-resolution optical coherence tomography for imaging macular pathology. *Ophthalmology.* Nov 2005;112(11):1922 e1921-1915.

122. Klatt C, Sendtner P, Ponomareva L, et al. [Diagnostics of metamorphopsia in retinal diseases of different origins]. *Ophthalmologe.* Nov 2006;103(11):945-952.

123. Srinivasan VJ, Wojtkowski M, Witkin AJ, et al. High-definition and 3-dimensional imaging of macular pathologies with high-speed ultrahigh-resolution optical coherence tomography. *Ophthalmology.* Nov 2006;113(11):2054 e2051-2014.

124. Hee MR, Izatt JA, Swanson EA, et al. Optical coherence tomography of the human retina. *Arch Ophthalmol.* Mar 1995;113(3):325-332.

125. Schuman JS, Hee MR, Puliafito CA, et al. Quantification of nerve fiber layer thickness in normal and glaucomatous eyes using optical coherence tomography. *Arch Ophthalmol.* May 1995;113(5):586-596.

126. Burk RO, Volcker HE. Current imaging of the optic disk and retinal nerve fiber layer. *Curr Opin Ophthalmol.* Apr 1996;7(2):99-108.

127. Schuman JS, Pedut-Kloizman T, Hertzmark E, et al. Reproducibility of nerve fiber layer thickness measurements using optical coherence tomography. *Ophthalmology.* Nov 1996;103(11):1889-1898.

128. Funk J. Imaging of the optic disc in glaucoma: which way to go? *Curr Opin Ophthalmol.* Apr 1998;9(2):71-76.

129. Gramer E, Tausch M. Measurement of the retinal nerve fiber layer thickness in clinical routine. *Curr Opin Ophthalmol.* Apr 1998;9(2):77-87.

130. Pieroth L, Schuman JS, Hertzmark E, et al. Evaluation of focal defects of the nerve fiber layer using optical coherence tomography. *Ophthalmology.* Mar 1999;106(3):570-579.

131. Blumenthal EZ, Williams JM, Weinreb RN, Girkin CA, Berry CC, Zangwill LM. Reproducibility of nerve fiber layer thickness measurements by use of optical coherence tomography. *Ophthalmology.* Dec 2000;107(12):2278-2282.

132. Geerling G, Muller M, Winter C, et al. Intraoperative 2-dimensional optical coherence tomography as a new tool for anterior segment surgery. *Arch Ophthalmol.* Feb 2005;123(2):253-257.

133. Meyer CH, Rodrigues EB, Mennel S. Anterior segment anomaly on optical coherence tomography. *Acta Ophthalmol Scand.* Feb 2005;83(1):118-119.

134. Radhakrishnan S, Goldsmith J, Huang D, et al. Comparison of optical coherence tomography and ultrasound biomicroscopy for detection of narrow anterior chamber angles. *Arch Ophthalmol.* Aug 2005;123(8):1053-1059.

135. Radhakrishnan S, Huang D, Smith SD. Optical coherence tomography imaging of the anterior chamber angle. *Ophthalmol Clin North Am.* Sep 2005;18(3):375-381, vi.

136. Muller M, Dahmen G, Porksen E, et al. Anterior chamber angle measurement with optical coherence tomography: intraobserver and interobserver variability. *J Cataract Refract Surg.* Nov 2006;32(11):1803-1808.

137. Dawczynski J, Koenigsdoerffer E, Augsten R, Strobel J. Anterior segment optical coherence tomography for evaluation of changes in anterior chamber angle and depth after intraocular lens implantation in eyes with glaucoma. *Eur J Ophthalmol.* May-Jun 2007;17(3):363-367.

138. Li H, Leung CK, Cheung CY, et al. Repeatability and reproducibility of anterior chamber angle measurement with anterior segment optical coherence tomography. *Br J Ophthalmol.* Nov 2007;91(11):1490-1492.

139. Memarzadeh F, Tang M, Li Y, Chopra V, Francis BA, Huang D. Optical coherence tomography assessment of angle anatomy changes after cataract surgery. *Am J Ophthalmol.* Sep 2007;144(3):464-465.

140. Leung CK, Li H, Weinreb RN, et al. Anterior chamber angle measurement with anterior segment optical coherence tomography: a comparison between slit lamp OCT and Visante OCT. *Invest Ophthalmol Vis Sci.* Aug 2008;49(8):3469-3474.

141. Aptel F, Dumas S, Denis P. Ultrasound biomicroscopy and optical coherence tomography imaging of filtering blebs after deep sclerectomy with new collagen implant. *Eur J Ophthalmol.* Mar-Apr 2009;19(2):223-230.

142. Mansouri K, Sommerhalder J, Shaarawy T. Prospective comparison of ultrasound biomicroscopy and anterior segment optical coherence tomography for evaluation of anterior chamber dimensions in European eyes with primary angle closure. *Eye (Lond).* Feb 2010;24(2):233-239.

143. Carpineto P, Ciancaglini M, Zuppardi E, Doronzo E, Stefano ND, Mastropasqua L. Effect of photorefractive keratectomy for myopia on measurement of retinal nerve fiber layer thickness using optical coherence tomography. *J Refract Surg.* Nov-Dec 2001;17(6):676-681.

144. Bagayev SN, Gelikonov VM, Gelikonov GV, et al. Optical coherence tomography for in situ monitoring of laser corneal ablation. *J Biomed Opt.* Oct 2002;7(4):633-642.

145. Kaushik S, Gyatsho J, Jain R, Pandav SS, Gupta A. Correlation between retinal nerve fiber layer thickness and central corneal thickness in patients with ocular hypertension: an optical coherence tomography study. *Am J Ophthalmol.* May 2006;141(5):884-890.

146. Christopoulos V, Kagemann L, Wollstein G, et al. In vivo corneal high-speed, ultra high-resolution optical coherence tomography. *Arch Ophthalmol.* Aug 2007;125(8):1027-1035.

147. Kawana K, Kiuchi T, Yasuno Y, Oshika T. Evaluation of trabeculectomy blebs using 3-dimensional cornea and anterior segment optical coherence tomography. *Ophthalmology.* May 2009;116(5):848-855.

148. Zhang Y, Davidson BR, Stamer WD, Barton JK, Marmorstein LY, Marmorstein AD. Enhanced inflow and outflow rates despite lower IOP in bestrophin-2-deficient mice. *Invest Ophthalmol Vis Sci.* Feb 2009;50(2):765-770.

149. Kagemann L, Wollstein G, Ishikawa H, et al. Identification and assessment of Schlemm's canal by spectral-domain optical coherence tomography. *Invest Ophthalmol Vis Sci.* Aug 2010;51(8):4054-4059.

150. Kagemann L, Wollstein G, Ishikawa H, et al. 3D visualization of aqueous humor outflow structures in-situ in humans. *Exp Eye Res.* Sep 2011;93(3):308-315.

151. Haefliger IO. [Risk factors associated with glaucoma]. *Klin Monatsbl Augenheilkd.* May 1997;210(5):265-268.

152. Allingham RR, de Kater AW, Ethier CR. Schlemm's canal and primary open angle glaucoma: correlation between Schlemm's canal dimensions and outflow facility. *Exp Eye Res.* Jan 1996;62(1):101-109.

153. Kagemann L, Ishikawa H, Wollstein G, et al. Reproducibility of Measurements of Aqueous Velocity Within Schlemm's Canal With Spectral Domain Optical Coherence Tomography. Paper presented at: Association for Research in Vision and Ophthalmology2008; Fort Lauderdale, FL, USA.

154. Kagemann L, Wollstein G, Ishikawa H, Townsend KA, Schuman JS. Validation of spectral domain optical coherence tomographic Doppler shifts using an in vitro flow model. *Invest Ophthalmol Vis Sci.* Feb 2009;50(2):702-706.

155. Ten Hulzen RD, Johnson DH. Effect of fixation pressure on juxtacanalicular tissue and Schlemm's canal. *Invest Ophthalmol Vis Sci.* Jan 1996;37(1):114-124.

156. Wild GJ, Kent AR, Peng Q. Dilation of Schlemm's canal in viscocanalostomy: comparison of 2 viscoelastic substances. *J Cataract Refract Surg.* Aug 2001;27(8):1294-1297.

157. Bloom G, Friberg U. Shrinkage during fixation and embedding of histological specimens. *Acta Morphol Neerl Scand.* 1956;1(1):12-20.

158. Chung HS, Harris A, Kagemann L, Martin B. Peripapillary retinal blood flow in normal tension glaucoma. *Br J Ophthalmol.* Apr 1999;83(4):466-469.

159. Quigley HA. Number of people with glaucoma worldwide. *Br J Ophthalmol.* May 1996;80(5):389-393.

160. Anderson DR. Collaborative normal tension glaucoma study. *Curr Opin Ophthalmol.* Apr 2003;14(2):86-90.

161. Anderson DR, Drance SM, Schulzer M. Factors that predict the benefit of lowering intraocular pressure in normal tension glaucoma. *Am J Ophthalmol.* Nov 2003;136(5):820-829.

162. Linner E. [The outflow pressure in normal and glaucomatous eyes]. *Acta Ophthalmol (Copenh).* 1955;33(2):101-116.

163. Huggert A. Obstruction of the outflow of aqueous humour, produced experimentally. *Acta Ophthalmol (Copenh).* 1957;35(1):1-11.

164. Barany EH. A Mathematical Formulation of Intraocular Pressure as Dependent on Secretion, Ultrafiltration, Bulk Outflow, and Osmotic Reabsorption of Fluid. *Invest Ophthalmol.* Dec 1963;2:584-590.

165. Barany EH. Simultaneous Measurement of Changing Intraocular Pressure and Outflow Facility in the Vervet Monkey by Constant Pressure Infusion. *Invest Ophthalmol.* Apr 1964;3:135-143.

166. Battista SA, Lu Z, Hofmann S, Freddo T, Overby DR, Gong H. Reduction of the available area for aqueous humor outflow and increase in meshwork herniations into collector channels following acute IOP elevation in bovine eyes. *Invest Ophthalmol Vis Sci.* Dec 2008;49(12):5346-5352.

167. Zhang Y, Toris CB, Liu Y, Ye W, Gong H. Morphological and hydrodynamic correlates in monkey eyes with laser induced glaucoma. *Exp Eye Res.* Nov 2009;89(5):748-756.

168. Erickson-Lamy K, Rohen JW, Grant WM. Outflow facility studies in the perfused human ocular anterior segment. *Exp Eye Res.* Jun 1991;52(6):723-731.

169. Bengtsson B. Manifest glaucoma in the aged I: occurrence nine years after a population survey. *Acta Ophthalmol (Copenh).* Jun 1981;59(3):321-331.

170. Uhm KB, Shin DH. Positive family history of glaucoma is a risk factor for increased IOP rather than glaucomatous optic nerve damage (POAG vs OH vs normal control). *Korean J Ophthalmol.* Dec 1992;6(2):100-104.

171. Dielemans I, Vingerling JR, Wolfs RC, Hofman A, Grobbee DE, de Jong PT. The prevalence of primary open-angle glaucoma in a population-based study in The Netherlands. The Rotterdam Study. *Ophthalmology.* Nov 1994;101(11):1851-1855.

172. Iwata K. [Primary open angle glaucoma and low tension glaucoma--pathogenesis and mechanism of optic nerve damage]. *Nihon Ganka Gakkai Zasshi.* Dec 1992;96(12):1501-1531.

173. Sarunic MV, Asrani S, Izatt JA. Imaging the ocular anterior segment with real-time, full-range Fourier-domain optical coherence tomography. *Arch Ophthalmol.* Apr 2008;126(4):537-542.

174. Irshad FA, Mayfield MS, Zurakowski D, Ayyala RS. Variation in Schlemm's canal diameter and location by ultrasound biomicroscopy. *Ophthalmology.* May 2010;117(5):916-920.

175. Zhang K, Kang JU. Real-time 4D signal processing and visualization using graphics processing unit on a regular nonlinear-k Fourier-domain OCT system. *Opt Express.* May 24;18(11):11772-11784.

176. Ellingsen BA, Grant WM. The relationship of pressure and aqueous outflow in enucleated human eyes. *Invest Ophthalmol.* Jun 1971;10(6):430-437.

177. Cense B, Chen TC, Nassif N, et al. Ultra-high speed and ultra-high resolution spectral-domain optical coherence tomography and optical Doppler tomography in ophthalmology. *Bull Soc Belge Ophtalmol.* 2006(302):123-132.

178. Stein DM, Ishikawa H, Hariprasad R, et al. A new quality assessment parameter for optical coherence tomography. *Br J Ophthalmol.* Feb 2006;90(2):186-190.

179. Johnstone MA. The aqueous outflow system as a mechanical pump: evidence from examination of tissue and aqueous movement in human and non-human primates. *J Glaucoma.* Oct 2004;13(5):421-438.

180. Hann CR, Bentley MD, Vercnocke A, Ritman EL, Fautsch MP. Imaging the human aqueous humor outflow pathway in human eyes by three-dimensional micro-computed tomography (3D micro-CT). *Exp Eye Res.* Dec 25.

181. Kagemann L, Wollstein G, Ishikawa H, et al. 3D visualization of aqueous humor outflow structures in-situ in humans. *Exp Eye Res.* Apr 15 2011.

182. Ishikawa H, Gurses-Ozden R, Hoh ST, Dou HL, Liebmann JM, Ritch R. Grayscale and proportion-corrected optical coherence tomography images. *Ophthalmic Surg Lasers.* May-Jun 2000;31(3):223-228.

183. Ishikawa H, Piette S, Liebmann JM, Ritch R. Detecting the inner and outer borders of the retinal nerve fiber layer using optical coherence tomography. *Graefes Arch Clin Exp Ophthalmol.* May 2002;240(5):362-371.

184. Ishikawa H, Stein DM, Wollstein G, Beaton S, Fujimoto JG, Schuman JS. Macular segmentation with optical coherence tomography. *Invest Ophthalmol Vis Sci.* Jun 2005;46(6):2012-2017.

185. Girard MJ, Strouthidis NG, Ethier CR, Mari JM. Shadow removal and contrast enhancement in optical coherence tomography images of the human optic nerve head. *Invest Ophthalmol Vis Sci.* Sep 2011;52(10):7738-7748.

186. Kagemann L, Ishikawa H, Wollstein G, Gabriele M, Schuman JS. Visualization of 3-D high speed ultrahigh resolution optical coherence tomographic data identifies structures visible in 2D frames. *Opt Express.* Mar 2 2009;17(5):4208-4220.

187. Dvorak-Theobald G. Schlemm's Canal: Its Anastomoses and Anatomic Relations. *Trans Am Ophthalmol Soc.* 1934;32:574-595.

188. Dvorak-Theobald G. Further studies on the canal of Schlemm; its anastomoses and anatomic relations. *Am J Ophthalmol.* 1955;39:65-89.

189. Ascher KW. Aqueous veins: physiologic importance of visible elimination of intraocular fluid. *Am J Ophthalmol.* 1942;25:1174-1209.

190. van der Merwe EL, Kidson SH. Advances in imaging the blood and aqueous vessels of the ocular limbus. *Exp Eye Res.* Aug 2010;91(2):118-126.

191. Zhang K, Kang JU. Real-time 4D signal processing and visualization using graphics processing unit on a regular nonlinear-k Fourier-domain OCT system. *Opt Express.* May 24 2010;18(11):11772-11784.

192. Bhutto IA, Amemiya T. Microvascular architecture of the rat choroid: corrosion cast study. *Anat Rec.* Sep 1 2001;264(1):63-71.

193. Morrison JC, Fraunfelder FW, Milne ST, Moore CG. Limbal microvasculature of the rat eye. *Invest Ophthalmol Vis Sci.* Mar 1995;36(3):751-756.

194. Ninomiya H, Inomata T. Microvasculature of the hamster eye: scanning electron microscopy of vascular corrosion casts. *Vet Ophthalmol.* Jan-Feb 2005;8(1):7-12.

195. Ninomiya H, Inomata T. Microvascular anatomy of the pig eye: scanning electron microscopy of vascular corrosion casts. *J Vet Med Sci.* Nov 2006;68(11):1149-1154.

196. Ninomiya H, Inomata T, Kanemaki N. Microvascular architecture of the rabbit eye: a scanning electron microscopic study of vascular corrosion casts. *J Vet Med Sci.* Sep 2008;70(9):887-892.

197. Ninomiya H, Kuno H. Microvasculature of the rat eye: scanning electron microscopy of vascular corrosion casts. *Vet Ophthalmol.* Mar 2001;4(1):55-59.

198. Jocson VL, Sears ML. Channels of aqueous outflow and related blood vessels. I. Macaca mulatta (rhesus). *Arch Ophthalmol.* Jul 1968;80(1):104-114.

199. Morrison JC, DeFrank MP, Van Buskirk EM. Regional microvascular anatomy of the rabbit ciliary body. *Invest Ophthalmol Vis Sci.* Aug 1987;28(8):1314-1324.

200. Fait E, Gnoth S, Dimitropoulou C, et al. Microvascular patterns of the human large intestine: Morphometric studies of vascular parameters in corrosion casts. *Scanning Microsc.* 1998;12:641-651.

201. Miodonski AJ, Litwin JA. Microvascular architecture of the human urinary bladder wall: a corrosion casting study. *Anat Rec.* Mar 1999;254(3):375-381.

202. Reina-De La Torre F, Rodriguez-Baeza A, Sahuquillo-Barris J. Morphological characteristics and distribution pattern of the arterial vessels in human cerebral cortex: a scanning electron microscope study. *Anat Rec.* May 1998;251(1):87-96.

203. Gaudio E, Onori P, Pannarale L, Marinozzi G. Microcirculation of the extrahepatic biliary tree: a scanning electron microscopy study of corrosion casts. *J Anat.* Feb 1993;182 (Pt 1):37-44.

204. Gaasterland DE, Jocson VL, Sears ML. Channels of aqueous outflow and related blood vessels. 3. Episcleral arteriovenous anastomoses in the rhesus monkey eye (Macaca mulatta). *Arch Ophthalmol.* Dec 1970;84(6):770-775.

205. Wojtkowski M, Leitgeb R, Kowalczyk A, Bajraszewski T, Fercher AF. In vivo human retinal imaging by Fourier domain optical coherence tomography. *J Biomed Opt.* Jul 2002;7(3):457-463.

206. Bower BA, Zhao M, Zawadzki RJ, Izatt JA. Real-time spectral domain Doppler optical coherence tomography and investigation of human retinal vessel autoregulation. *J Biomed Opt.* Jul-Aug 2007;12(4):041214.

207. Wang Y, Bower BA, Izatt JA, Tan O, Huang D. In vivo total retinal blood flow measurement by Fourier domain Doppler optical coherence tomography. *J Biomed Opt.* Jul-Aug 2007;12(4):041215.

208. Leitgeb RA, Schmetterer L, Hitzenberger CK, et al. Real-time measurement of in vitro flow by Fourier-domain color Doppler optical coherence tomography. *Opt Lett.* Jan 15 2004;29(2):171-173.

209. Fornaro G, Franceschetti G, Lanari R. Robust Phase-unwrapping techniques: a comparison. *J Opt Soc Am A.* 1996;13:2355-1233.

210. Yun SH, Tearney G, de Boer J, Bouma B. Motion artifacts in optical coherence tomography with frequency-domain ranging. *Opt Express.* Jun 28 2004;12(13):2977-2998.

211. Baker M, Wayland H. On-line volume flow rate and velocity profile measurement for blood in microvessels. *Microvasc Res.* Jan 1974;7(1):131-143.

212. Yoshida A, Feke GT, Mori F, et al. Reproducibility and clinical application of a newly developed stabilized retinal laser Doppler instrument. *Am J Ophthalmol.* Mar 2003;135(3):356-361.

213. Aaslid R, Markwalder TM, Nornes H. Noninvasive transcranial Doppler ultrasound recording of flow velocity in basal cerebral arteries. *J Neurosurg.* Dec 1982;57(6):769-774.

214. Dirnagl U, Kaplan B, Jacewicz M, Pulsinelli W. Continuous measurement of cerebral cortical blood flow by laser-Doppler flowmetry in a rat stroke model. *J Cereb Blood Flow Metab.* Oct 1989;9(5):589-596.

215. Ernst H, Hahn EG, Balzer T, Schlief R, Heyder N. Color doppler ultrasound of liver lesions: signal enhancement after intravenous injection of the ultrasound contrast agent Levovist. *J Clin Ultrasound.* Jan 1996;24(1):31-35.

216. Huang D. "Optical," not "ocular," coherence tomography. *Ophthalmology.* Nov 2008;115(11):2095-2096.

217. Izatt J, Kulkarni MD, Yazdanfar S, Barton JK, Welch AJ. In vivo bidirectional color Doppler flow imaging of picoliter blood volumes using optical coherence tomography. *Opt Lett.* 1997;22:1493-1441.

218. Leitgeb R, Schmetterer L, Drexler W, Fercher A, Zawadzki R, Bajraszewski T. Real-time assessment of retinal blood flow with ultrafast acquisition by color Doppler Fourier domain optical coherence tomography. *Opt Express.* Nov 17 2003;11(23):3116-3121.

219. Zhao Y, Chen Z, Saxer C, Xiang S, de Boer JF, Nelson JS. Phase-resolved optical coherence tomography and optical Doppler tomography for imaging blood flow in human skin with fast scanning speed and high velocity sensitivity. *Opt Lett.* Jan 15 2000;25(2):114-116.

220. Yazdanfar S, Kulkarni M, Izatt J. High resolution imaging of in vivo cardiac dynamics using color Doppler optical coherence tomography. *Opt Express.* Dec 22 1997;1(13):424-431.

221. Mornet S, Vasseur S, Grasset F, Duguet E. Magnetic nanopartical design for medical diagnosis and therapy. *J Mater Chem.* 2004;14:2161.

222. Nahrendorf M, Zhang H, Hembrador S, et al. Nanoparticle PET-CT imaging of macrophages in inflammatory atherosclerosis. *Circulation.* Jan 22 2008;117(3):379-387.

223. Oldenburg AL, Hansen MN, Ralston TS, Wei A, Boppart SA. Imaging gold nanorods in excised human breast carcinoma by spectroscopic optical coherence tomography. *J Mater Chem.* Jan 1 2009;19:6407.

224. Kim J, Oh J, Milner TE, Nelson JS. Imaging nanopartical flow using magneto-motive optical Doppler tomography. *Nanotechnology.* 2007;18:035504.